# A Study of the Higher-Order Cumulants and Correlation Functions of Event-by-Event Proton Multiplicity Distributions in Au + Au Heavy-Ion Collisions from the RHIC Fixed-Target Program at $\sqrt{s_{NN}} = 3.0$ GeV

By

Samuel George Heppelmann

Dissertation

Submitted in partial satisfaction of the requirements for the degree of

Doctor of Philosophy

in

Physics

in the

Office of Graduate Studies

of the

University of California

Davis

Approved:

---

Daniel A. Cebra

---

Manuel Calderón de la Barca Sánchez

---

Ramona Vogt

Committee in Charge

2021

*This work is dedicated to my partner, Priya.*

*Thank you for all of your love and support.*

# Contents

# List of Figures

# List of Tables

## Abstract of the Dissertation

**A Study of the Higher-Order Cumulants and Correlation Functions of Event-by-Event Proton Multiplicity Distributions in $\mathrm{Au}+\mathrm{Au}$ Heavy-Ion Collisions from the RHIC Fixed-Target Program at $\sqrt{s_{NN}} = 3.0$ GeV**

This work reports the cumulants and correlation functions of event-by-event proton multiplicity distributions for the first dedicated fixed-target physics run in $\sqrt{s_{NN}} = 3.0$ GeV Au+Au collisions. Protons are identified within the rapidity ($y$) and transverse momentum ($p_T$) region $-0.9 < y < 0$ and $0.4 < p_T < 2.0$ GeV/$c$ in the center-of-mass frame by the STAR detector. A systematic analysis of the centrality, acceptance, and energy dependence of proton cumulants and correlation functions up to the sixth order are presented. The energy dependence is analyzed with the most central (0-5%) and peripheral (50-60%) data and compared to the UrQMD model and hydrodynamic model calculations. In the most central 5% collisions, one observes a negative value of the proton cumulant ratio of $C_4/C_2$, which is drastically different from the cumulant ratios observed at higher collision energies. Compared to model calculations such as lattice QCD, the hadronic transport model, and the hydrodynamic model, and results from higher energy collisions, the strong suppression in the ratio of $C_4/C_2$ at 3.0 GeV indicates an energy regime dominated by hadronic interactions.

# Acknowledgments

This thesis is the result of years of discussion and mentorship from my advisors and collaborators. I would like to extend my gratitude to the physicists and friends who contributed to the completion of this work.

I would like to thank my advisor, Daniel Cebra, a friend and mentor, for supporting me throughout my graduate studies. More than anyone, Daniel has shaped my understanding of nuclear physics. I would like to thank him for all the great discussions and always promoting my work. Also, I would like to thank Manuel Calderón. Throughout the last six years, I considered Manuel to be my second advisor. His advice was always insightful and challenged my understanding of physics. I appreciate all the time and effort that both Daniel and Manuel gave me throughout my graduate career.

During the last two years of my doctoral studies, I spent a considerable amount of time at Berkeley Lab working with a small group of collaborators. I truly believe the bulk of this work would not have been possible without the contributions from Xin Dong, Nu Xu, and Yu Zhang. I would like to thank each of them for helping me complete this work.

Lastly, I would like to thank my family. Thank you for everything—the love, support, and inspiration. This would not have been possible without them.

# Chapter 1

# Introduction

Understanding matter and how it transforms is a long-standing goal of physicists. A transformation or phase transition occurs with a change of an external variable, such as temperature or pressure, and after a transition, the matter is often physically altered. A common and intuitive example is water for which the three common phases vary drastically, (see Fig. 1.1). Starting from normal conditions (standard temperature and pressure), as the temperature increases water will vaporize into a gas and cross a first-order phase transition. The first-order transition is often characterized by a discontinuity of a state variable and results in a coexistence of water and gas. Above some temperature and pressure threshold, however, the first-order phase transition disappears and only one phase exists. In this region, the transition is classified as continuous.

An analogous phase diagram is often discussed for nuclear matter. Starting from normal conditions, nuclear matter consists of bound protons and neutrons in a nucleus. As temperature or baryon density increases, the nucleus enters a first-order liquid-gas transition and expands into a gas of protons and neutrons [1]. At much higher temperatures and baryon density, the gas of nucleons transforms into a quark-gluon plasma [2]—a near perfect fluid. It is clear that two distinct phases exist, but the location and nature of the transition is not well understood. At low baryon density, theory suggests a continuous phase transition around temperatures $T \sim 155$ MeV [3]. As the baryon density increases, experimental results show hints of critical behavior or a critical endpoint, which would imply the existence of a first-order phase transition.

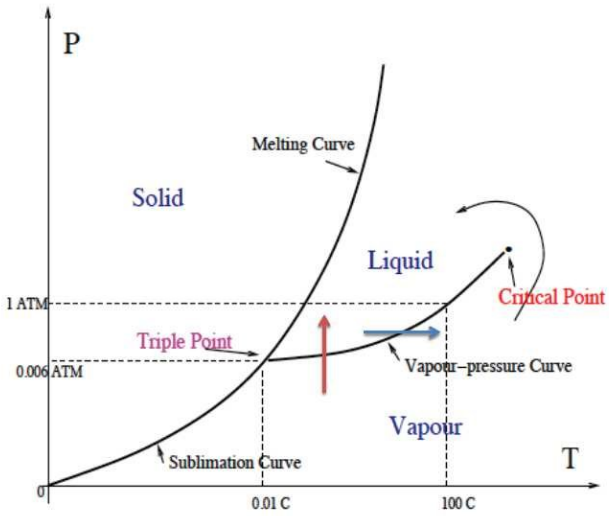


Figure 1.1. Phase diagram of $H_20$ from Ref. [4]. The first-order liquid-gas transition ends at a critical point. Above the critical point, a continuous phase transition exists.

In the laboratory, a QGP is produced by colliding beams of heavy nuclei at relativistic energies. As the nuclei collide, the system reaches thermal equilibrium and a hot, dense QGP forms. The QGP then begins to cool and expand until quarks and gluons condense into hadrons. At some time during this relatively quick process ($\sim$ 2–3 fm/$c$), a phase transition occurs. Due to the short time and length scale, however, physicists cannot directly measure the QGP or its phase transitions and all thermodynamic properties are inferred from measurements of the final state hadrons. While a phase transition cannot be measured, it has been suggested that the fluctuations of conserved quantities may be sensitive to critical phenomena.

Recently, the Beam Energy Scan (BES) program [5] at the Relativistic Heavy Ion Collider (RHIC) probed several temperatures and baryon densities by colliding gold nuclei over a large span of collision energies. A comprehensive study [6] of the higher-order cumulants of the event-by-event net-proton distributions of the BES data showed a fluctuation in energy dependence of the cumulant ratio with respect to a statistical baseline. Specifically, the result showed an enhancement at the lowest measured energy ($\sqrt{s_{NN}} = 7.7$ GeV) which corresponds to the lowest temperature and highest baryon chemical potential.[1] Although the results have large statistical uncertainties, according to certain theoretical

[1]Baryon chemical potential is related to the baryon density and $\mu_B = 0$ when $\bar{p}/p = 1$.

models [7], this enhancement could indicate critical behavior, and consequently, the existence of a first-order phase transition at high baryon density. However, it is imprudent to draw any conclusions from a single experimental observable. Additionally, the cumulant study suffers from large statistical uncertainty.

The results from the first energy scan which covered the center of mass energies ($\sqrt{s_{NN}}$) from 7.7 to 200 GeV of gold on gold collisions (Au+Au), motivated the STAR collaboration to start two programs in conjunction: a second energy scan (BES-II) [8] and a fixed-target program (FXT) [9]. The BES-II program repeats the lower energies ($\sqrt{s_{NN}}$ = 7.7–27 GeV) of BES-I with higher statistics and an upgraded detector. Additionally, the fixed-target program extends the energy range of the detector to $\sqrt{s_{NN}} = 3.0$ GeV.

This thesis is a study of the proton[2] cumulants of the first dedicated fixed-target run with the STAR detector of Au+Au collisions at $\sqrt{s_{NN}} = 3.0$ GeV. This analysis aims to measure the rapidity ($y$), transverse momentum ($p_T$), and centrality dependence of proton cumulants in Au+Au collisions at $\sqrt{s_{NN}} = 3.0$ GeV and compare the $\sqrt{s_{NN}} = 3.0$ GeV measurements to the higher energy BES-I data ($\sqrt{s_{NN}}$ = 7.7–200 GeV). While the scope of this study alone is unlikely to either prove or disprove the existence of a QCD critical point, this work will expand upon our understanding of quantum chromodynamics (QCD) matter and phase transitions in a region of high baryon density.

The first chapter includes a brief history of the soft hadron physics and discussion of the theoretical foundations of QCD phase diagram: asymptotic freedom, color confinement, chiral symmetry, and lattice QCD. In addition, the theoretical models and results of the BES analysis that motivated this work are are presented.

## 1.1 A Brief History of the QCD Phase Diagram

Before hadrons were understood to have substructure, Hagedorn described an excited ensemble of nucleons as a hadron resonance gas (HRG) [11] in which hadrons are composite states or "resonances" of lighter hadrons. The hadron excited states grow exponentially

[2]In heavy-ion collisions at $\sqrt{s_{NN}} = 3.0$ GeV, the anti-proton production is negligible ($\overline{p}/p \sim \exp(-2\mu_B/T_{\rm ch}) < 10^{-6}$) [10]. Therefore, proton and net-proton cumulants are equivalent.

with a continuous mass spectrum [12] described by

$$\rho(m) \propto m^{-5/2} e^{m/T_H}, \tag{1.1}$$

where $T_H$ is a limiting temperature [11]. After the discovery of $J/\psi$ meson and validation of the quark model in the mid-1970s, Hagedorn's notion of a limiting temperature was re-examined as a critical temperature. Specifically, Cabibbo and Parisi described [13] a process in which a hadron gas is heated or compressed until the hadrons overlap. At some critical temperature and pressure, a new phase of matter forms and the quarks can freely move throughout space. This theorized phase of matter would eventually be coined a quark gluon plasma (QGP). In Cabibbo and Parisi's description, there was one phase transition and it was second order. Figure 1.2 is Cabibbo and Parisi's proposed phase diagram.

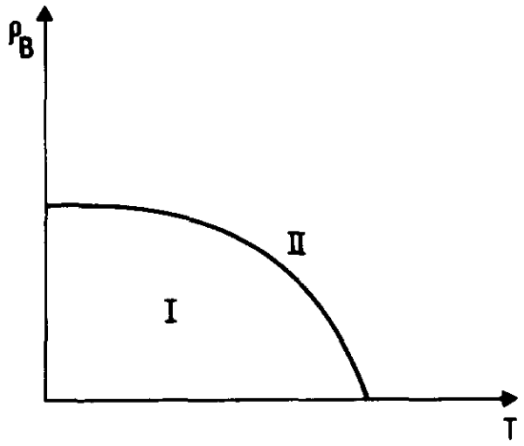


Figure 1.2. Early schematic phase diagram of hadronic matter from Ref. [13]. Here, $\rho_B$ is the baryon density. Phase I consists of hadrons. Quarks can freely move in phase II.

Over the next fifty years, the phase diagram of nuclear physics was studied extensively. Theorists grappled with the idea of asymptotic freedom (see section 1.2.1) and the implication that a QCD phase transition was likely to exist in a nonperturbative region ($T_c \sim$ 100–200 MeV). Thus, the perturbative methods that were successfully applied to high-energy collisions could not describe the strongly coupled fluid. In the 1980s, lattice QCD, a prominent first principles approach, showed theoretical evidence of a quark-gluon

plasma (QGP) [14]. The approach, first introduced by Kenneth Wilson [15] in the 1970s, quantized a gauge field on a discrete lattice in the Euclidean space-time lattice, preserving gauge invariance. The first estimates placed a crossover transition at the pseudo-critical temperature $T_c = 197$–$254$ MeV [14]. Modern calculations place the transition temperatures around $T_c \sim 156$ MeV [3].

On the experimental side, it was proposed that the QCD phase diagram could be accessed through heavy-ion collisions. This led to experimental heavy-ion programs in both the Alternating Gradient Synchrotron (AGS) [16] and the CERN Super Proton Synchrotron (SPS) [17]. The results from the SPS and AGS experiments showed evidence of collectivity [18] and hinted at the existence of a new state of matter. These findings motivated the construction of the Relativistic Heavy Ion Collider (RHIC) and the eventual discovery of the quark-gluon plasma (QGP) at the CERN Super Proton Synchrotron (SPS) [19] and RHIC [20]. The discovery would later be confirmed by the CERN Large Hadron Collider (LHC). The RHIC measurements showed that heavy-ion collisions at high energies quickly thermalize and generate a strongly-coupled plasma which behaves as an ideal fluid. The central observations include large azimuthal anisotropies correlated with the azimuthal angle of the impact parameter [21–24] or elliptic flow $v_2$, and suppression of high-energy jets and heavy quarks [25–27]. Here, the elliptic flow $v_2$ is the Fourier coefficient $\langle\cos(2\Phi)\rangle$ of the azimuthal angle $\Phi$ with respect to the event plane, which is determined by the transverse momenta of produced particles. Additionally, ideal relativistic hydrodynamic predictions reproduced the data well [28, 29]. It was clear that at some threshold of temperature ($T$) and baryon chemical potential ($\mu_B$), a hadron resonance gas[3] transitioned to the liquid-like QGP, which displayed partonic degrees of freedom. Around the same time, evidence was mounting from lattice QCD of a cross over transition at low baryon density. At high baryon density, the order and location of the phase transition is unknown.

[3]Unlike Hagedorn's model, the modern HRG models are described by a discrete mass spectra.

## 1.2 Quantum Chromodynamics

This section introduces a few concepts from QCD which are necessary for the following model discussion. It includes an overview of the QCD coupling constant, color confinement, and chiral symmetry.

### 1.2.1 Running of the Coupling Constant

In both QED and QCD, it is observed that the renormalized effective coupling is dependent on the renormalization scale. The QED coupling increases with the $q^2$ of the virtual photon, from $\alpha \approx 1/137$ at low energies to roughly $\alpha \approx 1/127$ at the energy scale of the $Z$ boson. The QCD effective coupling, however, diverges as the energy scale decreases. One can approximate the QCD coupling constant $\alpha_s$ as

$$\alpha_s(\mu) \equiv \frac{g_s^2(\mu)}{4\pi} \approx \frac{4\pi}{\beta_0 \ln \mu^2/\Lambda_{\mathrm{QCD}}^2}. \tag{1.2}$$

Here, $\mu$ is the momentum transfer scale, $\beta_0 = (11 - \frac{2}{3}n_f)$ is dependent on the number of quark flavors with mass below the $\mu$ scale, and $\Lambda_{\mathrm{QCD}}^2$ is the experimentally determined QCD scale. The $\Lambda_{\mathrm{QCD}}$ parameter for five quarks is $\Lambda_{\mathrm{QCD}} = 213 \pm 8$ MeV [30]. As shown in Eq. (1.2), the strength of the coupling varies considerably with energy, and in the limit of $\mu \to \infty$, the coupling vanishes and the quarks are free. Often, two regimes are discussed: a weak-coupling regime and a strong-coupling regime. The weak regime, where $\mu >> \Lambda_{\mathrm{QCD}}$ and $\alpha_s \sim 0.1$, is the region in which the quarks and gluons appear free inside the nucleus and one can apply perturbation theory. In the strong coupling case, however, where $\mu \sim \Lambda_{\mathrm{QCD}}$ and $\alpha_s \sim 1$, the perturbative expansion is no longer valid.

In the context of the QCD phase diagram, most estimates of the critical temperature are around $T \sim$ 100–200 MeV, a strong coupling region. Therefore, all theoretical descriptions of phase transitions must be nonperturbative.

### 1.2.2 Color Confinement & Chiral Symmetry

Identifying a phase transition requires an order parameter which undergoes a sudden change across a phase boundary. Here, two potential phase transitions are discussed: the onset of deconfinement and the restoration of chiral symmetry, which both have corresponding order parameters.

Color confinement is the observation that all quarks and gluons are confined to a bound baryon or meson and, therefore, quarks cannot be isolated. Unlike QED, if a quark is pulled out of a hadron, the strength of the gluon field increases until eventually pair production occurs. Confinement is a defining quality of a hadron resonance gas and, at some finite temperature and baryon density, confinement breaks down and the gas of color neutral baryons and mesons transitions to a quark gluon plasma. Therefore, the onset of deconfinement is often associated with the QCD phase transition. While confinement is observed in nature, no analytic proof exists in QCD. Models, such as lattice QCD, can characterize the onset of deconfinement with the Wilson line $\langle L \rangle$, and the maximum of Polyakov Loop susceptibility $\chi_L$, where $\chi_L = N^3(\langle L^2 \rangle - \langle L \rangle^2)$. Here, the Wilson line is the product of link variables that are stationary in space but not in time [31, 32] and the Polyakov loop susceptibility is the trace of the Wilson line [33].

Likely the most discussed marker of the QCD phase transition is chiral symmetry restoration. Chiral (handedness in the massless limit) symmetry is defined as invariance under parity transformation. If one assumes that the three lightest quarks obey SU(3) flavour symmetry and are described by $q(x) = (u(x), d(x), s(x))$, then they transform as

$$q \to q' = \exp[i\vec{\alpha} \cdot \vec{\lambda}_F/2]q, \tag{1.3}$$

where $\vec{\alpha}$ is the rotation and the elements of $\vec{\lambda}_F$ are the flavour generators of SU(3). In SU(3), this rotation is invariant under both vector and axial transformations with the respective currents:

$$\bar{q}\gamma^\mu \frac{\lambda_F^\alpha}{2} q, \quad \bar{q}\gamma^\mu\gamma_5 \frac{\lambda_F^\alpha}{2} q. \tag{1.4}$$

It can be shown that the vector transformation requires that all three quark masses to be equivalent in order to preserve this symmetry. In reality, there is a quark mass hierarchy $m_s \gg m_d > m_s$. Thus, the symmetry is broken. While the vector symmetry is broken in SU(3), one can argue an approximate SU(2) symmetry exists for the up and down quark, which results in a proton and neutron isospin doublet. If the SU(2) symmetry were exact, the mass of proton and neutron would be equal. The axial transformation, however, requires all quark masses to be zero. Therefore, the axial symmetry is explicitly

broken in both SU(3) and SU(2). This explains the existence of the three pion states, which are understood to be the Goldstone bosons of a broken SU(2) symmetry[4]. Since the perturbative vacuum is chirally symmetric for massless quarks, the isospin SU(2) symmetry is expected to be restored at finite temperatures, which would indicate a phase transition. In some models, the chiral susceptibility

$$\chi_m = \frac{\partial \langle \bar{q}q \rangle}{\partial m_q}, \tag{1.5}$$

can be described by the change in the vacuum expectation. Here, $m_q$ is the quark mass and $\langle \bar{q}q \rangle$ is the vacuum expectation value of the quark anti-quark pair, also known as the chiral condensate. The critical temperature is determined by the inflection point of $\chi_m$.

## 1.3 Theoretical Models

The study of ultrarelativistic heavy-ion collisions is often categorized into "soft" and "hard" physics by the applicability of pertubative QCD. The distinction is determined the transverse momentum ($p_T$) of the particles or jets with hard processes starting at a $p_T \sim$ 2–3 GeV. In the soft region ($p_T \sim$ 0–2 GeV), nonperturbative models are used to describe the collectivity of particle production. A common approach is to apply relativistic hydrodynamics to the dense nuclear medium. The hydrodynamic models treat the QGP as a locally equilibrated fluid and not a system consisting of individual particles. The approach describes the equation of state well [28, 29] but cannot describe the initial or final state particles. For this reason, the hydrodynamic calculations are often coupled with a hadronization calculation which transforms density elements into final state particles. Alternatively, microscopic transport models, such as UrQMD [34], treat a nuclear collision as an $N$-body problem and simulate each parton or hadron interaction. The microscopic models are restricted to binary collisions and may have limitations in hot dense matter. Typically when studying soft physics, a heavy-ion measurement is compared to hydrodynamic or transport model calculations and the comparison provides a baseline or insight into the nature of the signal. As neither hydrodynamic or transport models contain critical phenomena, both will be used as baselines absent of critical signatures.

[4]If the SU(2) symmetry were exact, the pion masses are expected to be zero.

In this section, three theoretical models which contain critical phenomena are introduced: lattice QCD, the Nambu–Jona-Lasinio (NJL) model, and the linear $\sigma$ model. While there are several other models which contain critical phenomena, an examination of these three particular models provides a balanced insight on the subject. Lattice QCD, a first principles model, has shown to agree well with experimental measurements and the calculation of critical order parameters is straightforward. At the same time, lattice QCD calculations are limited to regions of low $\mu_B$. The NJL model, which is built around chiral symmetry, is selected for its historical relevance and simplicity. Lastly, the linear $\sigma$ model is discussed due to its relevance in the field, which has largely motivated the study of net-proton fluctuations. An overview of each model is provided along with its relevance to nuclear phase transitions.

### 1.3.1 Lattice QCD

Lattice gauge theory is a reformulation of QCD on a lattice of discrete space-time points in which quark fields are placed on the lattice sites and gauge fields are positioned on the links between the sites. The lattice spacing ($a$) acts as a cutoff for ultraviolet divergences. The QCD partition function is constructed by making an analogy between Feynman's path integral formulation of quantum field theory in imaginary time $\tau = it$ and the partition function in statistical mechanics. The system is described with statistical mechanics at temperature $T = 1/\tau$. The QCD partition function of the grand canonical ensemble is

$$\mathcal{Z}(V, T, \mu_q) = \int \mathcal{D}[A, q] \exp\left( - \int_0^{1/T} d\tau \int_V d^3x \times (\mathcal{L}^E_{\mathrm{QCD}} - i\mu q^\dagger q) \right), \tag{1.6}$$

where $A$ is the gauge field, $q$ is the quark field for all color and flavor quantum numbers, and $\mathcal{L}^E_{\mathrm{QCD}}$ is the Euclidean version of the QCD Lagrangian density. In the limit of vanishing $\mu_q$, the path integral can be evaluated with Monte Carlo methods and the temperature dependence of thermodynamic quantities can be calculated.

The change in vacuum expectation value $\langle \bar{q}q \rangle$ can be used as an order parameter and the chiral susceptibility, see Eq. (1.5). The critical temperature is determined by the inflection point of $\chi_m$. Using this method, lattice QCD places a cross over transition at $T_c \sim 156$ MeV [3].

Lattice QCD naturally includes confinement [32] and the onset of deconfinement can be described by the Polyakov Loop susceptibility. Therefore, the phase transition can be characterized by both the onset of deconfinement and chiral symmetry restoration. A comparison of the temperature dependence of confinement order parameters and chiral order parameters is shown in the left panel of Fig. 1.3. In general, lattice QCD does not require the confinement-deconfinement transition and the restoration of chiral symmetry to occur at the same temperature. Nevertheless, the peaks of the susceptibilities of two order parameters are often close in value. The right Fig. shows the temperature dependence of the susceptibility of chiral order parameter for various lattice spacings. The critical temperature is calculated by taking the limit as $N_\tau \to \infty$ and $a \to 0$.

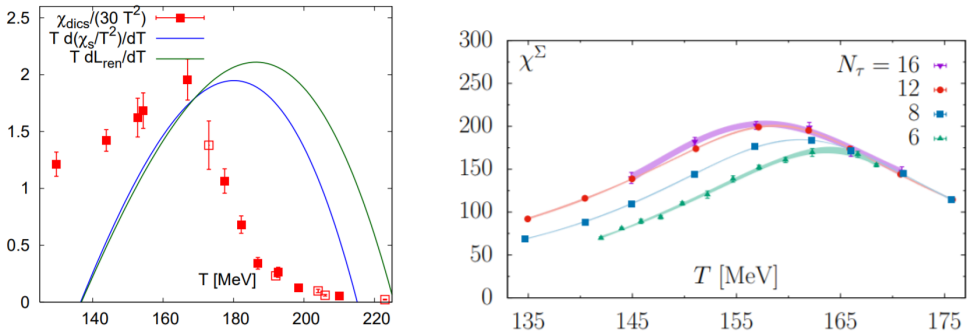


Figure 1.3. Left panel: A comparison of the disconnected chiral susceptibility ($\chi_{\text{disc}}$), derivatives of the Polyakov loop susceptibility ($\chi_S$), and the thermal expectation value of the renormalized Polyakov loop ($L_{\text{ren}}$) [35]. Right panel: The susceptibility of the chiral order parameter for four different lattice spacings [3]. Larger $N_\tau$ indicates a finer spacing.

A chemical freeze-out occurs in an expanding equilibrated medium when the inelastic interactions cease. Similar to the phase transition, the chemical freeze-out line is $T$ and $\mu_B$ dependent. Below both the chemical freeze-out line, the hadron spectra can be described by an HRG. The relation between the temperatures of the chemical freeze-out ($T_{\text{ch}}$) and a chiral phase transition ($T_\chi$) is not well understood, but it is argued that $T_{\text{ch}} \approx T_\chi$ in the low $\mu_B$ limit [36]. Lattice calculations are shown to agree well with experimental data. Figure 1.4 shows the lattice QCD critical temperature as a function of $\mu_B$ compared to the estimated chemical freeze-out temperatures and $\mu_B$ from measured particle spectra in heavy-ion collisions.

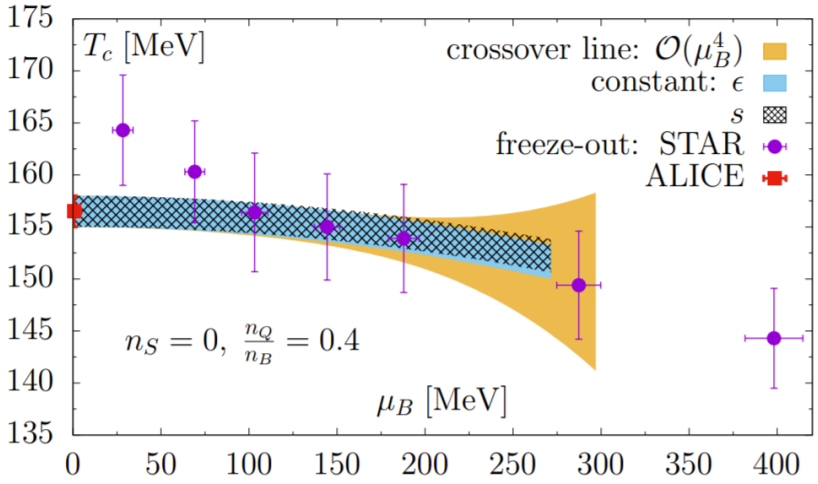


Figure 1.4. The pseudo-critical temperature in the $T$-$\mu_B$ plane for three different $\mu_B$ extrapolations for 2+1 flavor lattice QCD. In the yellow curve, the net strangeness charge-density ($n_S$) is restricted to $n_S = 0$ and the ratio of the net charge-density ($n_Q$) to net baryon-density ($n_B$) is constrained to $n_Q/n_B = 0.4$. The light blue and hatched black curves display a constant energy density ($\epsilon$) of $\epsilon = 0.26(6)$ GeV/fm$^3$ and a constant entropy density ($s$) of $s = 3.7(5)$ fm$^3$ [37] in the $\mu_B$-$T$ plane, respectively. ALICE and STAR data show the $T$ and $\mu_B$ chemical freeze-out parameters for several collision energies [10, 38]. Figure taken from Ref. [3].

The lattice QCD calculations discussed above are restricted to the low $\mu_B$ region. This limitation is due to the last term in Eq. (1.6). If the quark chemical potential ($\mu \approx 3\mu_B$) is nonzero, the path integral becomes oscillatory and is difficult to evaluate. In applied math, this is known as the numerical sign problem. As shown in Fig. 1.4, using expansion methods [3], lattice calculations can be extended to around $\mu_B \sim 270$ MeV, but cannot describe regions of high $\mu_B \sim 700$ MeV.

### 1.3.2 NJL Model

The Nambu–Jona-Lasinio (NJL) model dates back to two papers [39, 40] by Nambu and Jona-Lasinio in 1961. Even before QCD, there were indications of a partially conserved axial vector current and thus an approximate chiral symmetry. This approximate symmetry would imply a near massless fermion $m$ which is at odds with the large nucleon mass $M$. The model introduced a Lagrangian for a nucleon field $q$ with a point-like, chirally

symmetric four-fermion interaction [40, 41] as

$$\mathcal{L} = \bar{q}(i\partial\!\!\!/ - m)q + G\Big\{(\bar{q}q)^2 + (\bar{q}i\gamma_5\vec{\tau}q)^2)\Big\}, \tag{1.7}$$

where $m$ is the bare mass of the nucleon, $\vec{\tau}$ is a Pauli matrix acting in isospin space, and $G$ is a dimensionless coupling constant. The model produces an effective nucleon mass $M$ even with a vanishing fermion mass $m$. Additionally, the model identifies light nucleon-antinucleon excitations in the chiral limit $m \to 0$, which describe the three pion states. This revelation would lead to the pions being identified as the Goldstone bosons of the spontaneously broken chiral symmetry.

With the introduction of QCD, some NJL models replaced the nucleon field $q$ with a quark fields and the effective short-range interaction $G$ describes the gluon field. Therefore, instead of a nucleon mass, a constituent quark mass $M_q$ of 300-400 MeV is generated. The large constituent quark mass and non-zero expectation value of the quark fields $\langle\bar{q}q\rangle$ is produced, which demonstrates a dynamically broken chiral symmetry.

Naturally, NJL models were applied to the $T - \mu$ plane to describe phase transitions. Notably, the first attempt was by Asakawa and Yazaki [42] in 1989. An example phase diagram by Asakawa and Yazaki is depicted in Fig. 1.5. The left and right panels show a phase transition for a massless quark and finite bare quark mass, respectively. This result and many others found two distinct regimes of chiral symmetry restoration for a massless quark: a second-order transition at high $T$ and low $\mu$ and a first-order transition at low $T$ and high $\mu$. Here, $\mu$ is the quark chemical potential and a critical endpoint occurs around $\mu = \mu_B/3 \simeq 308$ MeV. With a finite quark mass, chiral symmetry is only approximately restored and the second-order transition becomes a cross over transition. In either scenario, the first-order transition is limited to a region of high $\mu$ ($\mu_B$). If this is the case, the phase diagram would include a critical endpoint similar to the phase diagram of water (see Fig. 1.1).

These results are in qualitative agreement with lattice QCD. Quantitatively, however, the values of $T_c$ at low $\mu$ appear large. Additionally, it is shown that the first-order transition can become second order depending on the choice of parameters [43]. In general, the NJL model has numerous shortcomings. If the fermion fields describe quarks, the

theory does not have a mechanism of confinement and all high mass mesons would decay into $q\bar{q}$ pairs. In addition, the theory is not renormalizable and requires a regularization prescription, which can vary the order of the transition [43]. Nevertheless, the NJL provides a simple description of QCD phase transitions and introduces the possibility of a critical endpoint.

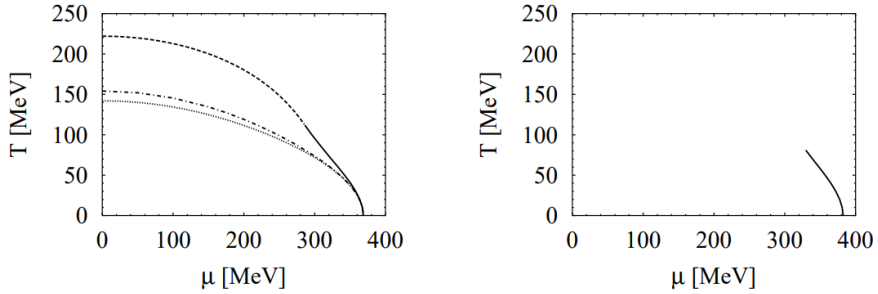


Figure 1.5. An example of two NJL phase diagrams. Left panel: quark mass $m = 0$. Right panel: quark mass $m = 5.6$ MeV. The first and second-order phase transitions are depicted by solid and dashed lines, respectively. The dash-dotted line indicates the location of massless solutions with vanishing pressure. The dotted line corresponds to the zero pressure line in the MIT bag model. Figure from Ref. [42].

### 1.3.3 Linear $\sigma$ Model

The linear $\sigma$ model is a low energy effective field theory, first introduced by Gell-Mann and Levy in 1960 [44]. Unlike the fermionic NJL model, the linear $\sigma$ model is primarily bosonic. Mesons are described by four meson scalar fields corresponding to a three pion ($\pi^+$,$\pi^-$, $\pi^0$) triplet state[5] and an additional sigma ($\sigma$) field singlet state. Fermions can be included as either nucleons or quarks. The four meson fields form a four vector, which acts as the chiral field and obeys an $O(4)$ symmetry. The Lagrangian is given by

$$\begin{aligned}\mathcal{L} =& \frac{1}{2}(\partial_\mu \sigma)^2 + \frac{1}{2}(\partial_\mu \pi)^2 - \frac{\mu^2}{2}(\sigma^2 + \pi^2) - \frac{\lambda}{24}(\sigma^2 + \pi^2)^2 \\ &+ \bar{i}\gamma^\mu \partial_\mu q + ig\bar{q}\gamma_5 \vec{\tau} q \cdot \pi + g\bar{q}q\sigma, \end{aligned} \tag{1.8}$$

[5]Triplet of the isospin SU(2) group, in which the pions have a total isospin $I = 1$ and the $\sigma$ has an isospin of $I = 0$.

where $q$ is the spinor field of either a nucleon or quark field. From the Lagrangian, the classical ground state is determined by the minimum of the potential terms as

$$V(\sigma,\pi) = \frac{\mu^2}{2}(\sigma^2+\pi^2) + \frac{\lambda}{24}(\sigma^2+\pi^2)^2. \tag{1.9}$$

If the mass term $\mu^2$ is negative, there is a minimum of the potential at

$$\sigma^2+\pi^2 = \frac{6\mu^2}{\lambda} \equiv v^2. \tag{1.10}$$

This defines a 3-sphere in the 4-dimensional space. Each point on the 3-sphere is invariant under $O(3)$ rotations. For example, the point ($v$,0,0,0) is invariant under the rotations of the last three components of the vector [45]. In the ground state, the four vector no longer obeys $O(4)$ symmetry but is invariant under[6] $O(3)$. The symmetry is spontaneously broken. The vacuum expectation value $\sigma = v \equiv \sqrt{6\mu^2/\lambda}$ is similar to $\langle\bar{q}q\rangle$ in the NJL model and lattice QCD.

## 1.4 Physics Observables & Fluctuations

While all three models describe a phase transition, the order and location vary considerably. Lattice QCD predicts a smooth crossover at low $\mu_B$ but fails to describe the high density region. The Linear $\sigma$ and NJL models are dependent on the choice of parameters [46, 47] and can describe either a first or second-order transition at high $\mu_B$. Other models not discussed such as a Random Matrix model and the MIT bag model [47], place a first-order phase transition at high $\mu_B$.

While the models are somewhat inconclusive on the existence of a critical point, recent results describe experimental observables that could be sensitive to phase boundaries [7, 48]. Moreover, one could identify the order of the phase transition by testing for the existence of a critical point. Critical points are characterized by the divergence of the correlation length, which is a density correlation in this case. An observable which has been suggested to be sensitive to critical phenomena is the event-by-event fluctuations of particle multiplicities. Below, the motivation for fluctuation measurements is discussed in both the context of the $\sigma$ field and thermodynamic susceptibilities.

[6] $O(3)$ is isomorphic to SU(2)

### 1.4.1 $\sigma$ Field Fluctuations

If one assumes that a first-order phase transition exists, then a critical endpoint exists at some $T$ and $\mu_B$. In general, a critical point is characterized by a diverging correlation length $\xi \to \infty$. While the correlation length can not be directly measured, it is closely related to the order parameter $\langle \bar{q}q \rangle$ or $\sigma$. It can be argued that the critical point is in the same universality class as a 3-dimensional Ising Model [47, 49]. Therefore, a correlation function $\langle \bar{q}q(\mathbf{x})\bar{q}q(\mathbf{0})\rangle_c$ becomes divergent close to the critical point as

$$\langle \bar{q}q(\mathbf{x})\bar{q}q(\mathbf{0})\rangle_c = \begin{cases} \frac{1}{|\mathbf{x}^{1+\eta}|} & |\mathbf{x}| \ll \xi \\ e^{\mathbf{x}/\xi} & |\mathbf{x}| \gg \xi, \end{cases} \tag{1.11}$$

where $\langle \bar{q}q(\mathbf{x})\bar{q}q(\mathbf{0})\rangle_c \equiv \langle \bar{q}q(\mathbf{x})\bar{q}q(\mathbf{0}\rangle - \langle \bar{q}q\rangle^2$ and the parameter $\eta$ is $\eta \approx 0.04$ in the Ising universality class. Furthermore, one can study the probability distribution of the order parameter field $\sigma$. Following Ref. [48], if the maximum of the probability distribution is located at $\sigma = 0$ and is expressed as

$$P[\sigma] \sim \exp\{-\mathbf{\Omega}[\sigma]/T\}, \tag{1.12}$$

where $\Omega$ is the effective action (free energy) functional for the $\sigma$ field. Similar to a field theory, the expectation value of an operator is calculated by integrating over all possible $\sigma$. For example, the 2-point correlator $\langle \sigma(\mathbf{x})\sigma(\mathbf{y})\rangle$ is

$$\langle \sigma(x)\sigma(y)\rangle = \int [\mathcal{D}\sigma(x)]P[\sigma]\sigma(x)\sigma(y). \tag{1.13}$$

Near the critical point $m_\sigma \ll T$, the $\sigma$ field can be treated classically and he functional $\Omega$ can be expanded in powers of $\sigma$ as

$$\Omega = \int d^3x \left[\frac{1}{2}(\nabla\sigma)^2 + \frac{m_\sigma^2}{2}\sigma^2 + \frac{\lambda_3}{3}\sigma^3 + \frac{\lambda_4}{4}\sigma^4 + ...\right]. \tag{1.14}$$

Here, the correlation length can be defined as $\xi = m_\sigma^{-1}$. The integral can be evaluated in the zero momentum mode [48], where $\sigma_0 \equiv \int d^3x\sigma(x)/V$ and the correlation functions

are

$$\begin{aligned}\kappa_2 &= \left\langle \sigma_0^2 \right\rangle = \frac{T}{V}\xi^2 \\ \kappa_3 &= \left\langle \sigma_0^3 \right\rangle = \frac{2\lambda_3 T}{V}\xi^6 \\ \kappa_4 &= \left\langle \sigma_0^4 \right\rangle_c \equiv \left\langle \sigma_0^4 \right\rangle - \left\langle \sigma^2 \right\rangle^2 = \frac{6T}{V}[2(\lambda_3\xi)^2 - \lambda_4]\xi^8.\end{aligned} \tag{1.15}$$

From Eq. (1.15), its clear that fluctuations of $\kappa_{1,2,\ldots} = \left\langle \sigma_{1,2,\ldots}^2 \right\rangle_c$ are sensitive to the correlation length. In the ideal thermodynamic limit, all $\kappa_n$ diverge as $\xi \to \infty$. In a real heavy-ion collision, the maximum correlation length is limited by the system size and finite time effects [50, 51]. The correlation length may increase from the natural length of 1 fm to a maximum of 2–3 fm. Additionally, the fluctuations of the $\sigma$ mode cannot be directly measured but are expected to influence the particle multiplicities and momentum distribution. As the most copiously produced particles, both the net pion ($\Delta\pi = \pi^+ - \pi^-$) and net proton ($\Delta p = p^+ - p^-$) multiplicities are potentially proxies of the $\sigma$ field fluctuations. To illustrate the relation between particle production and the $\sigma$ field, consider a Lagrangian similar to the linear sigma model,

$$\mathcal{L} = 2G\sigma\pi^+\pi^- + g_p\sigma\bar{p}p. \tag{1.16}$$

Let us use the coupling constant $g$ to denote both the pion $g \equiv G/m_\pi$ and proton $g_p\sigma\bar{p}p$ coupling. The infinitesimal change of the field strength $\delta\sigma$ leads to a change of the effective mass of both the pion and proton $\delta m = g\delta\sigma$. While the particle momentum space distribution $f_{\mathbf{p}}$ will contain natural statistical fluctuations $\delta f_{\mathbf{p}}^0$, the change in coupling strength will add an additional term

$$\delta f_{\mathbf{p}} = \delta f_{\mathbf{p}}^0 + \frac{\partial n_{\mathbf{p}}}{\partial m} g\,\delta\sigma. \tag{1.17}$$

Here, $n_{\mathbf{p}}$ is the equilibrium distribution for a particle of mass $m$. The momentum space $f$ is related to the particle yield by $N = Vd\int_{\mathbf{p}} f_{\mathbf{p}}$, where $d$ is the degeneracy factor. The fluctuation in particle yield is

$$\delta N = \delta N_0 + Vg\,\delta\sigma\,d\int_{\mathbf{p}} \frac{\partial n_{\mathbf{p}}}{\partial m}. \tag{1.18}$$

The deviation from the baseline increases with moment order. For example, the fourth order cumulant can be expressed as

$$\left\langle (\delta N)^4 \right\rangle_c = \langle N \rangle + \left\langle \sigma_V^4 \right\rangle_c \left( \frac{gd}{T} \int_{\mathbf{p}} n_p \frac{dm}{dE_p} \right)^4, \tag{1.19}$$

where $dm/dE_{\mathbf{p}}$ is the inverse of the relativistic gamma-factor $\gamma$ of a particle with momentum $\mathbf{p}$ and mass $m$. In the limit of small $n_{\mathbf{p}} \ll 1$, $\delta N_0$ should resemble a classical free gas, obey Poisson statistics, and be uncorrelated with $\sigma$ and $\langle N \rangle$. With Eq. (1.15) and (1.18), the fluctuations of particle multiplicities can be related to the correlation length $\xi$. The $\lambda_3$ and $\lambda_4$ couplings are assumed to vanish with a power of $\xi$ given by

$$\lambda_3 = \tilde{\lambda}_3 T \cdot (T\xi)^{-3/2}, \quad \lambda = \tilde{\lambda}_4 \cdot (T\xi)^{-1}, \tag{1.20}$$

where $\tilde{\lambda}_3$ and $\tilde{\lambda}_4$ are dimensionless couplings from the Ising universality class. The cumulants of the particle distribution are proportional to the correlation length as

$$\begin{aligned} \left\langle (\delta N)^2 \right\rangle &\sim \xi^2 \\ \left\langle (\delta N)^3 \right\rangle &\sim \xi^{4.5} \\ \left\langle (\delta N)^4 \right\rangle_c &\sim \xi^7. \end{aligned} \tag{1.21}$$

The full derivation can be found in Ref. [48].

Particle multiplicities are set in place at the chemical freeze-out. In the high $\mu_B$ regime, there is evidence that the chiral phase transition does not align with the chemical freeze-out temperatures [52]; $T_c$ is systematically higher than $T_{\mathrm{ch}}$. In this scenario, the sensitivity to $\xi$ is dependent on the proximity of the critical point to the chemical freeze-out. Figure 1.6 depicts a critical point and contours of equal $\xi$. If a critical point exists, the fluctuations of $\xi$ should be projected onto the chemical freeze-out line and reflect the fluctuations of particle multiplicities. As discussed in Ref. [7], universality arguments suggest a critical region in which the $\left\langle (\delta N)^4 \right\rangle_c / \langle \delta N \rangle$ rises and falls with increasing collision energy. Figure 1.7 depicts an example of the $4^{\mathrm{th}}$ normalized cumulant $C_4/C_1 \equiv w_4 = \left\langle (\delta N)^4 \right\rangle_c / \langle \delta N \rangle$ as a function of collision energy $\sqrt{s}$. The Linear $\sigma$ model always predicts an oscillation of $w_4$ as a function of $\sqrt{s}$ with respect to a fluctuation baseline, though the magnitude of $w_4$

from the Linear $\sigma$ model depends on the location of the chemical freeze-out curve with respect to the critical point. Furthermore, the energy dependence of $w_4$ (Fig.1.7) does not describe an exact critical point, but a critical region below the fluctuation baseline (red curve). Similar fluctuations are expected for all cumulant ratios, though as shown in Eq. (1.21), the sensitivity of a cumulant to the correlation length increases with cumulant order. A caveat is the non-critical fluctuations $\langle N \rangle$ in Eq. (1.19), which is assumed to follow Poisson statistics. While the assumption that an HRG behaves like a classical free gas is reasonable, it is likely too simplistic. This highlights the importance of comparing the results to models which do not contain critical phenomena such as transport and hydrodynamic models, which will be discussed in later sections. If non-critical effects dilute the proton fluctuations, a signal may only manifest in the higher order cumulants such as $w_4$.

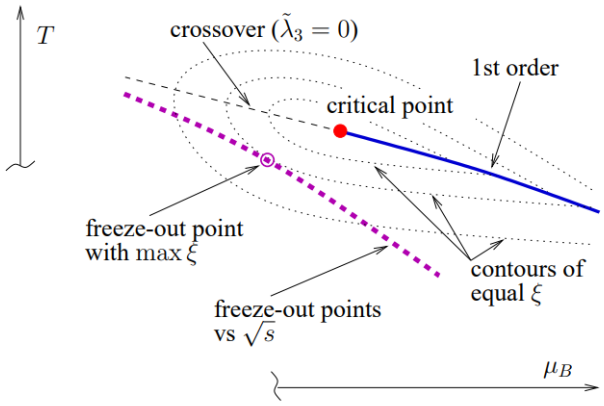


Figure 1.6. Illustration of a possible relative position of the critical point and the locations of the freeze-out line from Ref. [48]. Higher values of $\mu_B$ are probed with lower $\sqrt{s_{NN}}$ values. The dotted lines are contours of equal $\xi$.

### 1.4.2 Susceptibility of Conserved Quantities

While the above discussion was motivated by the coupling to the $\sigma$ field, the cumulants of conserved quantities can be related to thermodynamic susceptibilities. Consider the dimensionless pressure of a QCD partition function [53]

$$\frac{P}{T^4} = \frac{1}{VT^4} \ln[Z(V, T, \mu_B, \mu_Q, \mu_S)], \tag{1.22}$$

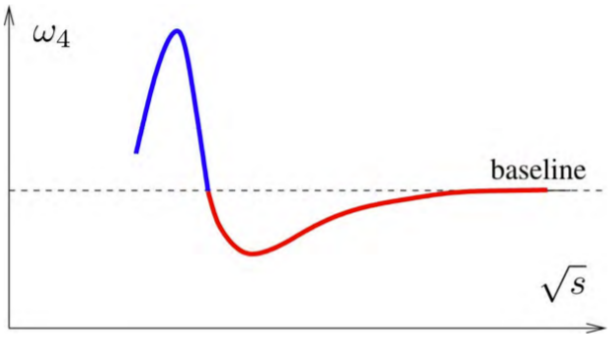


Figure 1.7. An example of the normalized $4^{\text{th}}$ cumulant $w_4$ as a function collision energy $\sqrt{s}$. Figure from Ref. [7].

where $B$, $Q$, and $S$ are the conserved quantities baryon number, charge, and strangeness, respectively. The susceptibilities of the conserved quantities are

$$\chi_{ijk}^{BQS} = \frac{\partial^{i+j+k}[P/T^4]}{\partial\hat{\mu}_B^i \partial\hat{\mu}_Q^j \partial\hat{\mu}_S^k}, \tag{1.23}$$

where $\hat{\mu}_q = \mu_q/T$ and $q = B, Q, S$. As I will show in chapter 8, the $m^{\text{th}}$ cumulant $C_m$ of the probability distribution $P(N)$ is defined as

$$C_m \equiv \langle N \rangle_c = \left. \frac{d^m \log \left\langle e^{\theta N} \right\rangle}{d\theta^m} \right|_{\theta=0}. \tag{1.24}$$

Here, $\log \left\langle e^{\theta N} \right\rangle$ is the cumulant generating function. If applied to the QCD partition function, the cumulants with respect to the conserved quantities are

$$\begin{aligned} C_{ijk}^{BQS} &= \frac{\partial^{(i+j+k)} \ln[Z(V,T,\mu_B,\mu_Q,\mu_S)]}{\partial\hat{\mu}_B^i \partial\hat{\mu}_Q^j \partial\hat{\mu}_S^k} \\ &= VT^4 \chi_{ijk}^{BQS}(T,\mu_B,\mu_Q,\mu_S). \end{aligned} \tag{1.25}$$

By taking the ratios of the cumulants, the volume dependence is cancelled and the ratios of the susceptibilities are

$$\frac{C_X^q}{C_Y^q} = \frac{\chi_X^q}{\chi_Y^q}, \tag{1.26}$$

where $q = B, Q, S$ and $X$ and $Y$ are the cumulant and susceptibility order. The susceptibilities can be calculated for several models. The HRG is often used as the fluctuation

baseline. The dimensionless pressure of an HRG model can be written [54, 55] as[7]

$$\frac{P}{T^4} = \frac{1}{VT^3}\ln[Z(V,T,\mu_B,\mu_Q,\mu_S)] \tag{1.27}$$

$$= \frac{1}{\pi^2}\sum_{i\in X} g_i(\frac{m_i}{T})^2 K_2(\frac{m_i}{T}) \tag{1.28}$$

$$\times \cosh(B_i\hat{\mu}_B + Q_j\hat{\mu}_Q + S_k\hat{\mu}_S), \tag{1.29}$$

where $m_i$ is the hadron mass for each species, $g_i$ is the spin degeneracy, and $K_2$ is the modified Bessel function. While the charge and strangeness susceptibility ratios vary with $\mu_q$ due to multi-charge states, the ratios of the net-baryon number can be reduced [56] to

$$\frac{C^B_{\text{even}}}{C^B_{\text{even}}} = \frac{\chi^B_{\text{even}}}{\chi^B_{\text{even}}} = 1, \quad \frac{C^B_{\text{odd}}}{C^B_{\text{odd}}} = \frac{\chi^B_{\text{odd}}}{\chi^B_{\text{odd}}} = 1 \tag{1.30}$$

and

$$\frac{C^B_{\text{odd}}}{C^B_{\text{even}}} = \frac{\chi^B_{\text{odd}}}{\chi^B_{\text{even}}} = \tanh(\mu_B/T)\Big|_{\mu_Q=\mu_S=0}. \tag{1.31}$$

In the even over odd case of Eq. (1.26), as collision energy decreases, $\mu_B/T$ increases and all cumulant ratios of the baryon number approach unity. Thus, in the high $\mu_B$ limit, a grand canonical ensemble HRG agrees with the Poisson statistics of a free classical gas.

A similar study of the susceptibilities can be applied to an NJL model. Reference [57] calculates the net-baryon moment ratios

$$T\frac{\chi^B_3}{\chi^B_2}, \quad \text{and} \quad T^2\frac{\chi^B_4}{\chi^B_2}, \tag{1.32}$$

for a modified NJL model. The extra factors of $T$ are from the moment definition, see Ref. [58]. Figure 1.8 shows heat maps which describe the sign of both quantities. Similar to Fig. 1.7, the susceptibility ratios can be projected onto the chemical freeze-out line. Figure 1.9 shows $T\chi^B_3/\chi^B_2$ and $T^2\chi^B_4/\chi^B_2$ for several freeze-out conditions.

The NJL model and $\sigma$ field produce strikingly similar results. Assuming $p - \bar{p} \propto B$, both results show a rise and fall of the higher-cumulant ratios as a function of collision

[7]The partition function includes all mesons and baryons, which will obey Bose-Einstein and Fermi-Dirac statistics, respectively. Here, the Boltzmann approximation is used for simplification and the ensemble obeys Maxwell-Boltzmann statistics. See Ref. [54].

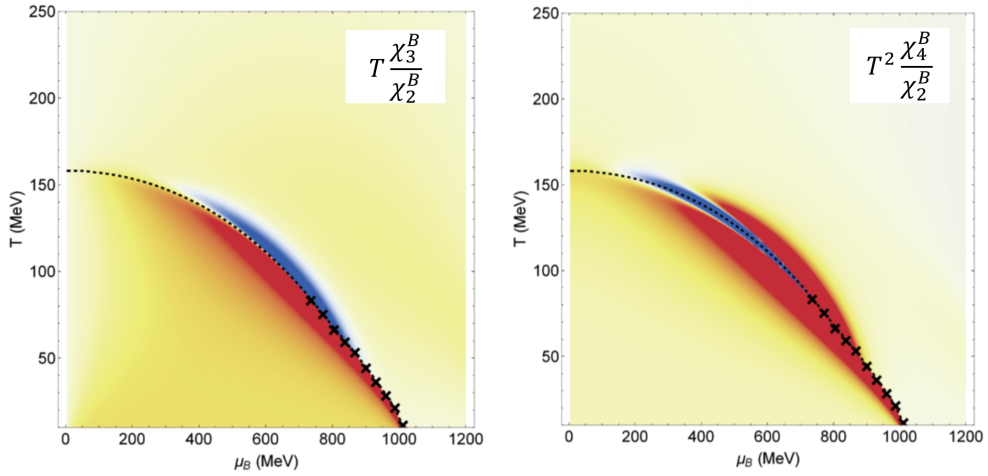


Figure 1.8. Sign of $T\chi_3^B/\chi_2^B$ (left) and $T^2\chi_4^B/\chi_2^B$ (right) which involve baryon number susceptibilities. The red and blue regions represent positive and negative values respectively. The dashed line is a crossover transition and the crosses represent a first-order phase transition. Figure from Ref. [57].

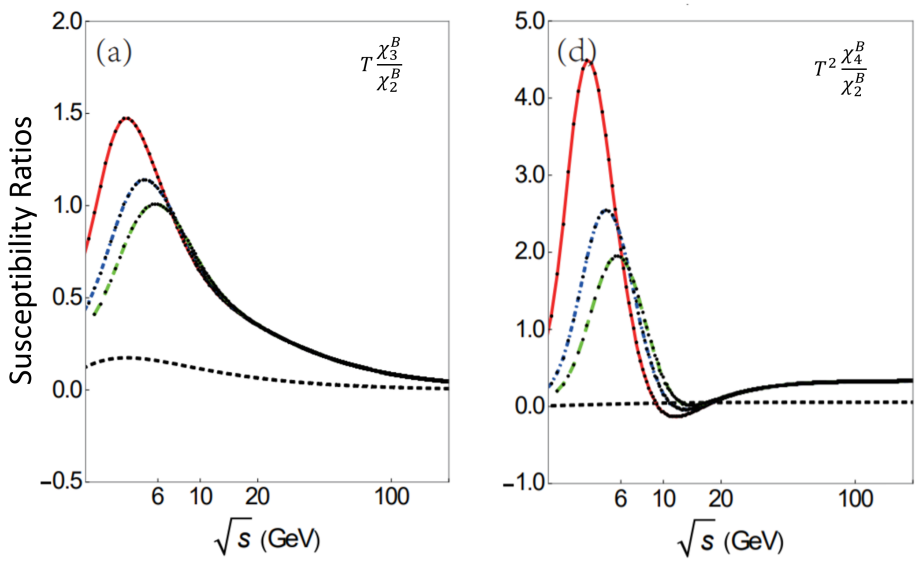


Figure 1.9. The $m_1$ and $m_2$ for three different freeze-out locations. Figure from Ref. [57].

energy. In addition, the fluctuations are more sensitive in the higher-order cumulant ratio $C_4/C_2$. As mentioned, the magnitude of the both Fig. 1.7 and 1.9 are dependent on the location of the critical point with respect to the chemical freeze-out curve, and thus the focus is on the non-monotonic behavior of the energy dependence of the cumulant ratios.

In a similar fashion, the ratios of the susceptibilities of conserved quantities can be calculated for lattice QCD. As discussed above, the lattice calculations are well understood at $\mu_B = 0$. Figure 1.10 [59] shows temperature dependence of the $C_3/C_2$ and $C_4/C_2$ ratios at zero $\mu_b$.

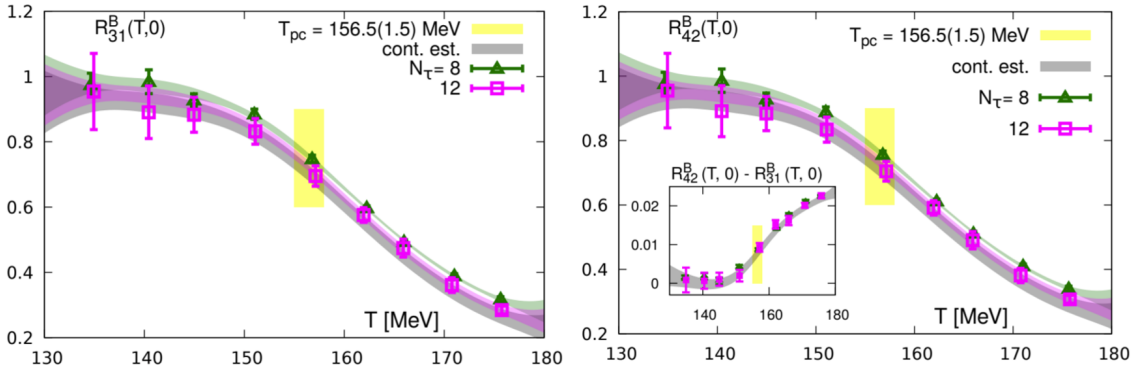


Figure 1.10. Continuum estimates of the cumulants ratios $C_3/C_1 = R_{31}$ and $C_4/C_2 = R_{42}$. The calculation is performed at $\mu_B = 0$ on two lattice sizes: $32^8 \times 8$ and $48^3 \times 12$. The pseudo-critical region is highlighted in yellow. Figure from Ref. [59].

The cumulants from the lattice calculation are below unity at the pseudo-critical/freeze-out temperature. To extend the calculation to higher $\mu_B$, one can take the Taylor expansion of the QCD dimensionless pressure at vanishing chemical potential. The pressure is

$$\frac{P(T,\vec{\mu})}{T^4} = \sum_{i,j,k=0}^{\infty} \frac{1}{i!j!k!} \chi^{BQS}_{ijk}(T) \hat{\mu}^i_B \hat{\mu}^j_Q \hat{\mu}^k_S. \tag{1.33}$$

Following the procedure in Ref. [59, 60], one can calculate the NNLO expansion of the cumulants up to $4^{\text{th}}$ order. Figure 1.11 depicts the cumulant ratios from lattice QCD as a function of $\mu_B/T$ for several temperatures.

The calculation extends to $\mu_B \approx 160$ MeV, which corresponds to a collision energy of $\sqrt{s_{NN}} > 27$ GeV. The lattice calculations show a suppression of both cumulant ratios, which decrease at higher $\mu_B$. Here, "suppression" denotes a value below the Poisson

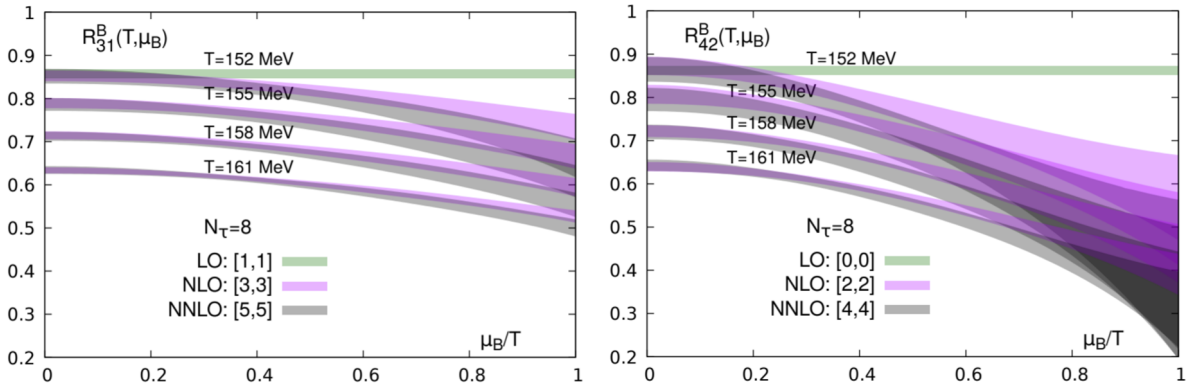


Figure 1.11. The cumulant ratios $C_3/C_1 = R_{31}$ and $C_4/C_2 = R_{42}$ as a function of $\mu_B/T$ for four different temperatures using LO, NLO, and NNLO Taylor expansions. Figure from Ref. [59].

baseline of 1.

### 1.4.3 Net-proton Cumulants & The Beam Energy Scan

It is useful to point out the relation between baryon number and the net-proton number. In general, the dynamics of protons and neutrons are expected to be similar. Additionally, it can be shown that at leading order, net-protons are more sensitive than neutrons to the baryon number [61]. Additionally, the coupling between neutrons and protons is shown to be negligible [62]. Therefore, the baryon number is assumed to be proportional to the net-proton number $p - \bar{p} \propto B$ and ratios of cumulant describe the ratios of QCD susceptibilities. The proportionality between net-proton and net-baryon number is less crucial in the linear $\sigma$ model, which argues that protons are coupled to the $\langle \bar{q}q \rangle$ field. Thus deviations in the chiral order parameter $\langle \bar{q}q \rangle$ will manifest as fluctuations in the proton multiplicities.

The search for critical phenomena motivated the Beam Energy Scan (BES) program at RHIC. The STAR (Solenoidal Tracker at RHIC) experiment collected data in 2010, 2011, and 2014, scanning energies listed in table 1.1 [5].

| Energy (GeV) | 200 | 62.4 | 39 | 27 | 19.6 | 14.5 | 11.5 | 7.7 |
|---|---|---|---|---|---|---|---|---|
| Events (M) | 350 | 67 | 130 | 70 | 36 | 20 | 12 | 4 |

Table 1.1. Overview of energies and events in BES.

The BES program included several areas of study such as elliptic and directed flow [63, 64], jet-quenching effects [65], two-pion interferometry [66], particle spectra [38], and fluctuations. Several event-by-event fluctuations studies were performed which include the energy dependence of net-charge, net-strangeness, and net-proton cumulants. A key finding of BES was the event-by-event measurement of the net-proton multiplicity [6]. Figure 1.12 depicts the BES proton cumulant results. The $C_2/C_1$ and $C_3/C_2$ ratios agree with trends of the transport model (UrQMD) and the canonical ensemble (CE) HRG.

At the same time, $C_4/C_2$ agrees with both UrQMD and CE HRG at high energy but deviates below $\sqrt{s_{NN}} < 27$ GeV. Specifically, the results showed a rise and fall from 7.7 to 27 GeV, (see bottom panel of Fig. 1.12). The BES result showed a striking resemblance to the signal in Fig. 1.7 and the NJL model result in Fig. 1.9 (right panel).

The findings of this data set motivated two additional programs: the Beam Energy Scan II (BES II) [8] and the fixed-target program [9]. BES II re-examines the lower energies, running with higher statistics and improved detector performance, while the fixed-target program extends the energy range of the RHIC collider from 7.7 GeV to 3.0 GeV. The BES-II data analyzers will re-examine the results in Fig. 1.12. With the fixed-target data sets, the cumulants analysis can be performed below the non-monotonic behavior observed at $\sqrt{s_{NN}} = 7.7$ GeV. If a critical region is limited to $7.7 < \sqrt{s_{NN}} < 27$ GeV, one would expect the signal to return to a Poisson or model baseline below 7.7 GeV.

In 2015, STAR performed a test run of the fixed-target program, running a 9.78 GeV gold beam incident on a fixed gold foil target. This initial test run generated a few million events at the center of mass energy of $\sqrt{s_{NN}} = 4.5$ GeV and showed STAR's capability of running a fixed-target program. Due to limited statistics, an event-by-event cumulant analysis was not possible. Motivated by the success of the test run, in 2018, STAR began the first dedicated fixed-target run at the center of mass energy $\sqrt{s_{NN}} = 3.0$ GeV by colliding 3.85 GeV gold ions onto a gold foil sitting at the edge of the STAR Time Projection Chamber (TPC).

This work is a study proton of fluctuations of the fixed-target Au+Au $\sqrt{s_{NN}} = 3.0$ GeV data set. It includes a description of the experimental apparatus, the event centrality

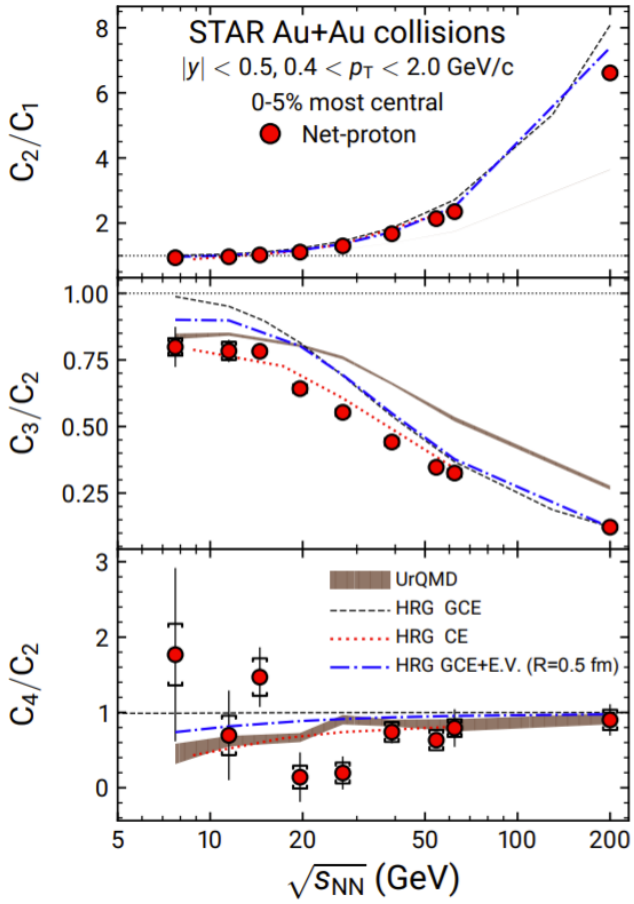


Figure 1.12. Collision energy dependence of $C_2/C_1$, $C_3/C_2$, and $C_4/C_2$ for the proton multiplicity distribution in the 0–5% central Au+Au collisions. The experimental values are compared to UrQMD and HRG models. Figure from Ref. [6].

determination, data collection, and experimental corrections. The centrality, acceptance, and energy dependence of proton cumulants and cumulant ratios are studied. Additionally, from the proton cumulants, the integrated proton correlation functions are calculated and presented. The results are discussed in the context of the QCD critical point and future fluctuation experiments.

# Chapter 2

# Experimental Apparatus

Data for this analysis were recorded by the Solenoidal Tracker at RHIC (STAR) at Brookhaven National Lab (BNL). The STAR detector sits at the 6 o'clock interaction point of the Relativistic Heavy Ion Collider as seen in Fig. 2.1. RHIC has provided collisions to the STAR interaction point since June of 2000, typically running heavy-ion collisions at $\sqrt{s_{NN}} = 200$ GeV and $p+p$ collisions at $\sqrt{s_{NN}} = 500$ GeV. This chapter includes a discussion of the collider facility for the STAR fixed-target Au+Au collisions at $\sqrt{s_{NN}} = 3.0$ GeV, the STAR detector/subsystems and the apparatus/run conditions for heavy-ion collisions in the STAR fixed-target system.

## 2.1 The Relativistic Heavy Ion Collider

The RHIC facility is an accelerator complex at Brookhaven National Lab located in Upton, New York. An overview of the RHIC facility is found here [67, 68]. At the outset, the primary performance goal of RHIC was to provide heavy-ion collision energies up to 100 GeV/$u$ per beam at average store luminosities of $\sim 10^{30}\text{cm}^{-2}\text{s}^{-1}$ for four experiments: STAR, PHENIX, PHOBOS, and BRAHMS. Currently, STAR is the only remaining experiment of the four listed.

To generate a collimated beam of heavy nuclei, the collider facility requires subsystems to strip, accelerate, and store heavy ions. The subsystems are the Electron Ion Beam Source (EBIS), the Booster, the Alternating Gradient Synchrotron (AGS) and the RHIC Ring.

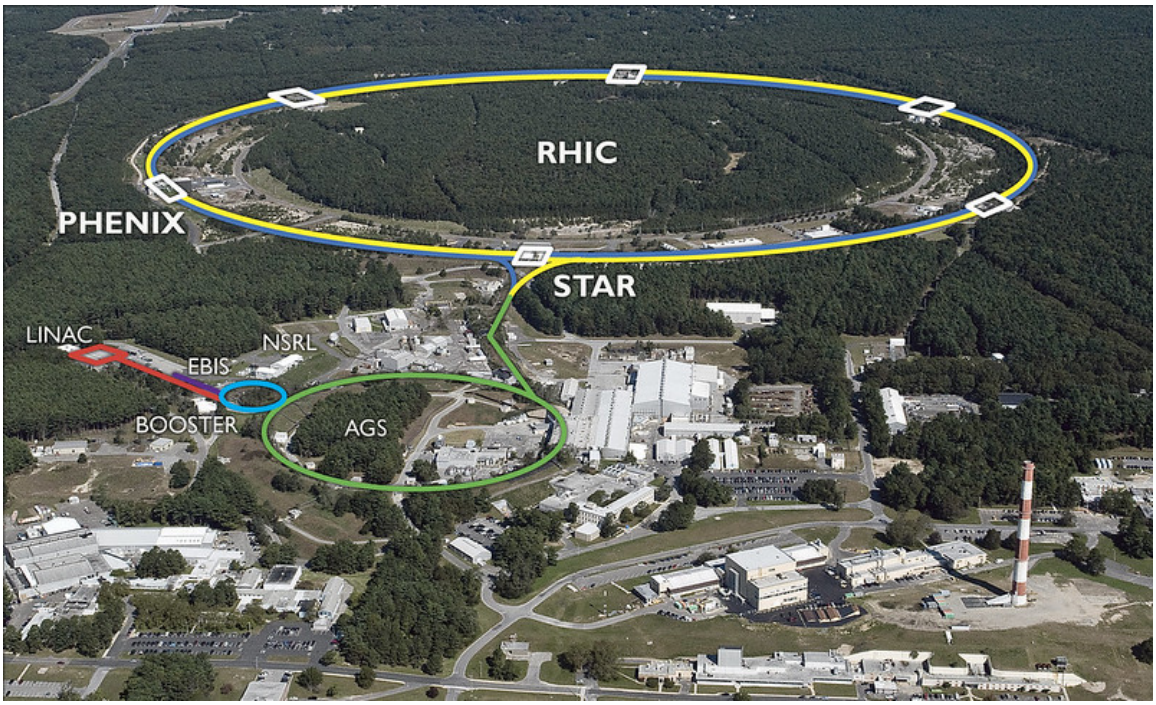


Figure 2.1. Aerial view of RHIC facility [69].

### 2.1.1 Electron Ion Beam Source (EBIS)

The RHIC facility uses an Electron Ion Beam Source (EBIS) [70] to strip the electrons off heavy elements and extract a heavy-ion beam. Previously, the RHIC facility relied on a Tandem Van de Graff accelerator to strip electrons from the element source. However, the EBIS has various advantages over the Van de Graff, most notably its ability to generate a heavy-ion source for all elements/isotopes.

The idea behind an EBIS [71] is to ionize heavy ions by electron impact ionization. An electron gun shoots a highly dense electron beam. The beam is compressed by a magnetic field from a superconducting solenoid and is incident on a heavy element/isotope source. As the heavy element ionizes, the positive nuclei are radially confined by the negative charge of the electron source. The nuclei maintain axial freedom and can be moved/controlled by electrostatic potentials. The electrostatic potentials guide the ions into the booster which is the next accelerator subsystem and the excess electrons are collected by a Faraday cup.

### 2.1.2 The Booster and the Alternating Gradient Sychrotron (AGS)

To achieve the top energies at RHIC ($\sim$ 100 GeV heavy-ion beams), the beams are accelerated in stages, starting with the Booster and AGS. The Booster and AGS are re-purposed accelerators adjacent to the RHIC ring seen in the aeriel view of RHIC in Fig. 2.1. The Booster, a small synchrotron, has a high vacuum capable of accelerating the ions to $\sim 37\%$ the speed of light ($\sim$ 1 GeV). The ions leave the Booster and enter the AGS which further accelerates the ions to the injection energy ($\sim 3 - 10$ GeV). While the ions accelerate in the Booster and AGS, they are incident on stripping foils to remove any excess electrons. In collider run conditions, the ions are piped into both the yellow or blue beams of the RHIC ring. Only a single beam of 3.85 GeV/$u$ was required (yellow beam) for the 2018 fixed-target run. The yellow beam runs counter clockwise around the ring and is in the $-z$ direction at the interaction point, see Fig. 2.3.

### 2.1.3 The RHIC Ring

The RHIC ring is an intersecting synchrotron that can operate as an accelerator, storage ring, and collider. Here, "intersecting" refers to its two beam pipes (yellow and blue), which intersect in the experiment halls. The ring is a 2.4 mile closed loop, housing four experimental halls. Currently, STAR is the only running RHIC experiment. It is located at 6 o'clock on the ring, as shown in Fig. 2.2. RHIC's unique two beam design has allowed the STAR collaboration to study asymmetric collisions such as $p$+Au and $d$+Au, which are otherwise unobtainable in a single beam design.

From the aeriel view of RHIC (Fig. 2.1), the ring appears as a circle. A more appropriate description of the ring, however, would be a hexagon with long straight sections and sharp corners as seen in Fig. 2.2. In the curved sections (corners of the hexagon), the beam pipe passes through dipole magnets which bend the path of the beam. Acceleration occurs in the straight sections, where radio-frequency (RF) cavities boost the beam's energy. RHIC's RF cavitiy sits at 4 o'clock on Fig. 2.2. STAR (6 o'clock) and the other RHIC experiment halls sit in a straight section, where the two beams can intersect.

At low energies ($\sqrt{s_{NN}} < 7$ GeV), the two beams become diffuse and difficult to collide

at high rates. This effectively limits the lowest energy of the collider to $\sqrt{s_{NN}} \approx 7$ GeV. The fixed-target configuration extends the energy range of RHIC to $\sqrt{s_{NN}} = 3.0$ GeV. Of note, a 3.85 GeV gold beam can be produced by the AGS alone and the ring does not provide additional acceleration. Consequently, the RHIC ring acts as a storage ring for the Au+Au collisions at $\sqrt{s_{NN}} = 3.0$ GeV (center of mass energy), which corresponds to a 3.85 GeV beam on a fixed target.

## 2.2 The STAR Detector

The Solenoidal Tracker at RHIC (STAR) is a multi-detector system built within a solenoidal magnet running at 0.5 Tesla. The detector provides full azimuthal and $\eta < 2$ coverage for collisions at the center of the Time Projection Chamber (TPC).

STAR uses a right-handed Cartesian system, where the $y$-axis is opposite the direction of gravity and the origin is located at the center of the solenoid. The positive $z$-axis points in the direction of the blue beam, which circulates clockwise around the ring. The coordinate system can be seen in Fig. 2.3. The origin of the Cartesian coordinate system is located at the center of the STAR TPC.

The event-by-event proton multiplicity analysis primarily relies on two detector subsystems: the Time Projection Chamber (TPC) and the Time of Flight (TOF) system. The TPC provides particle tracking and both detectors provide particle identification. Event triggering requires two additional detectors: the Beam-Beam Counter (BBC) and Event Plane Detector (EPD).

A full description of the STAR detector can be found here [72].

### 2.2.1 The Time Projection Chamber

The primary tracking detector at STAR is the Time Projection Chamber (TPC). The TPC can accommodate the high density of particle tracks for heavy-ion collisions at $\sqrt{s_{NN}} =$ 200 GeV and reconstruct thousands of primary tracks per unit of pseudorapidity [73]. The TPC records both the momentum and energy loss of a track and the vertex location of an event. The track momentum is calculated by measuring the track curvature in the presence of a magnetic field. The momentum is measured from 100 MeV/$c$ to 30 GeV/$c$.

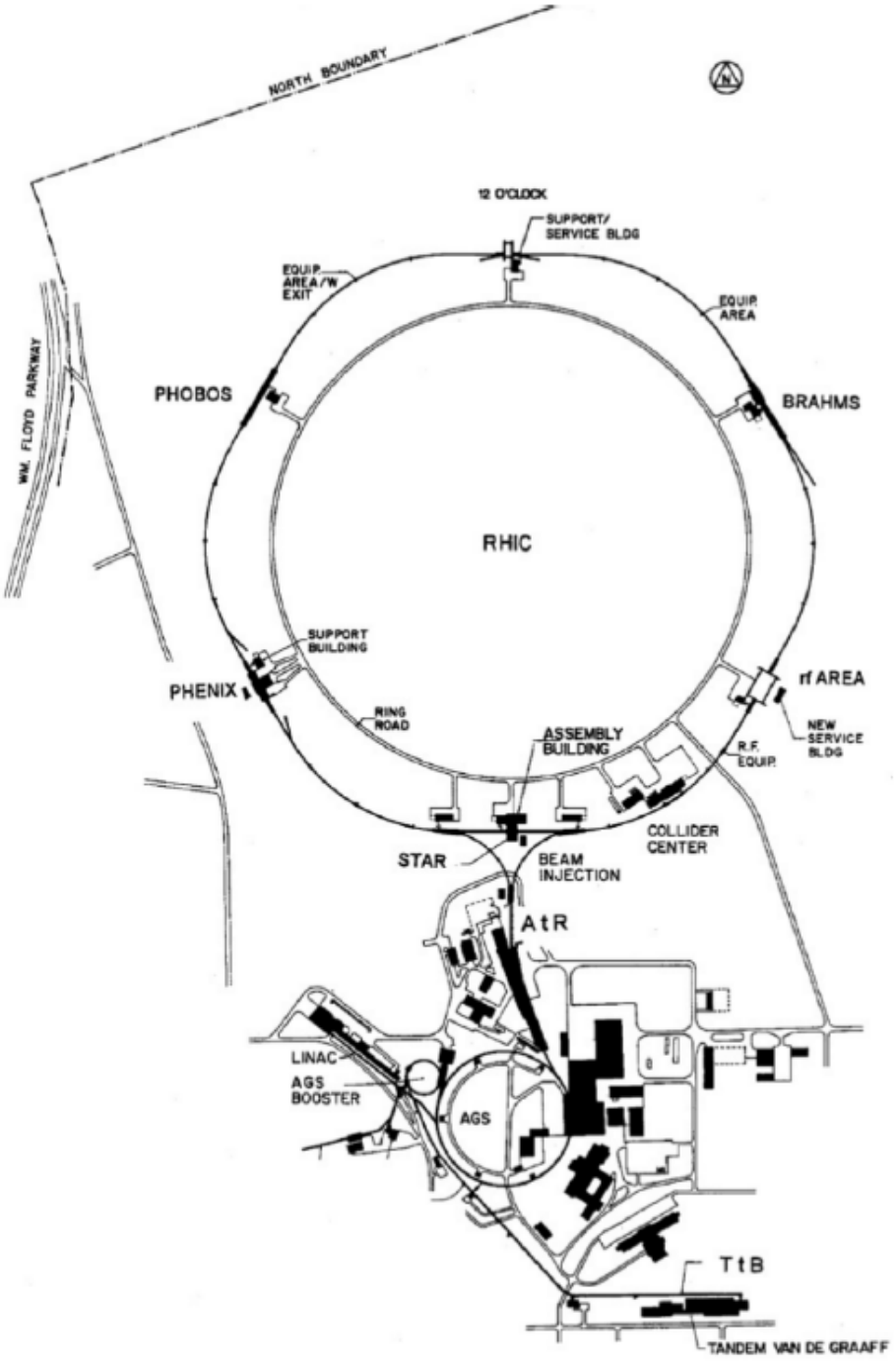


Figure 2.2. Schematic of RHIC [67]

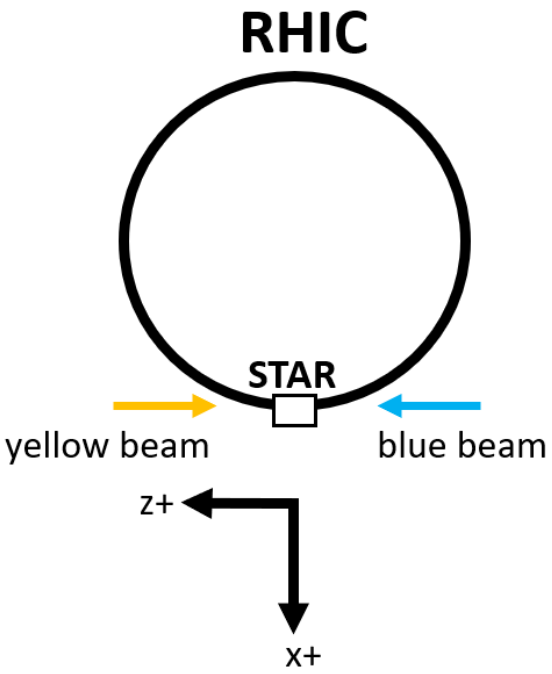


Figure 2.3. STAR coordinate system.

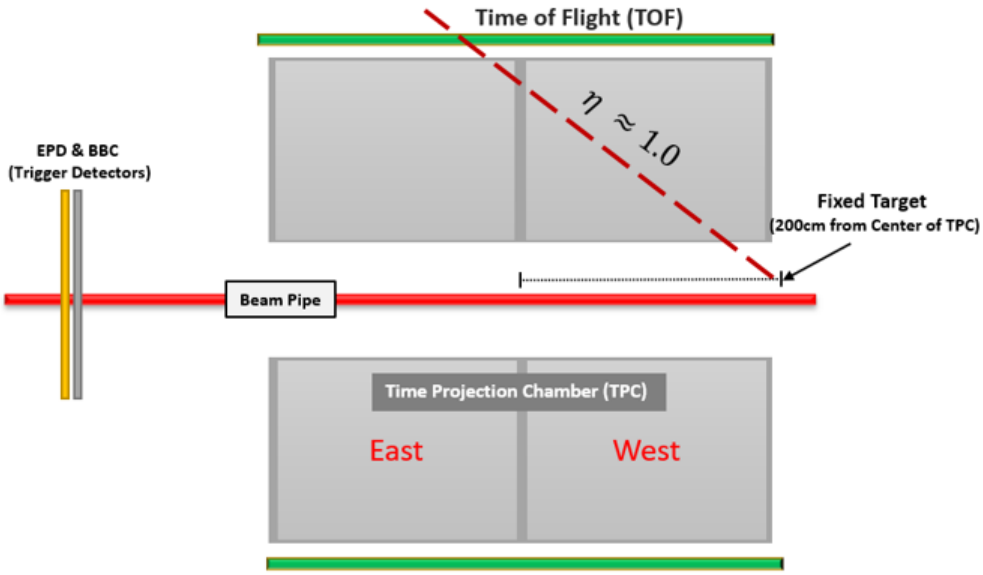


Figure 2.4. Cartoon of the STAR detector subsystems: TPC East/West, TOF, BBC/EPD and Fixed Target.

To calculate track energy loss ($dE/dx$), the ionized electrons from charged tracks passing through the TPC gas are measured. $dE/dx$ is reliably measured up to 1.0 GeV/$c$ (at $\sqrt{s_{NN}} = 200$ GeV).

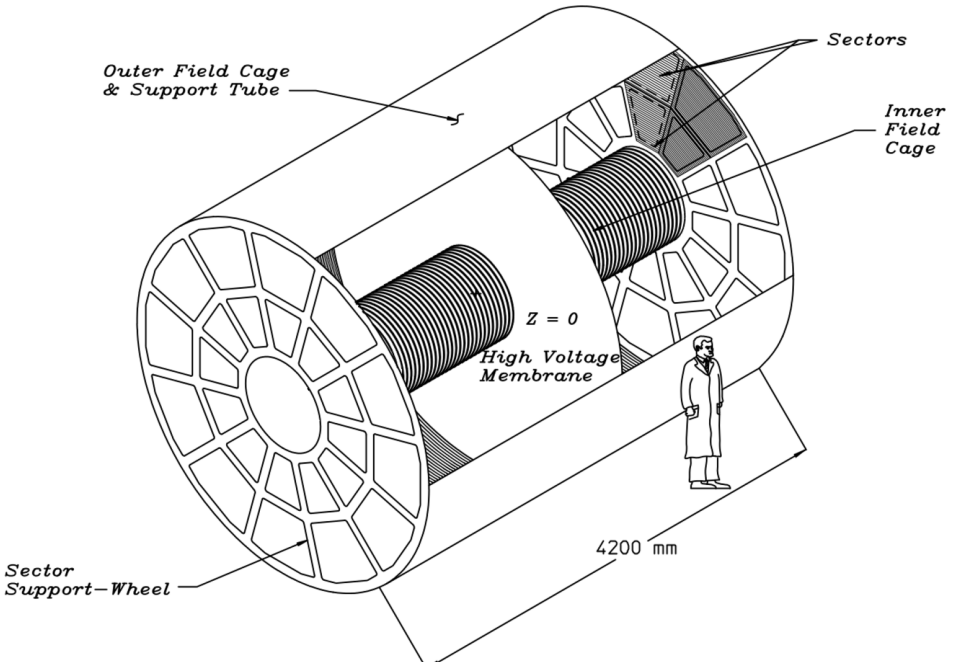


Figure 2.5. Schematic of the STAR TPC [73]

The TPC is a hollow cylinder with an inner radius of 50 cm, outer radius of 200 cm and length of 420 cm. It sits inside a 0.5 Tesla solenoidal magnet. As seen in the schematic of the TPC in Fig. 2.5, the central $x$-$y$ plane is a thin conductive central membrane. The central membrane is held at 28 kV, with both endcaps held at ground (209.3 cm from the center of the TPC). This generates an electric field of $E \approx 135$ V/cm from the central membrane to each anode ground plane. The volume of the TPC is filled with P10 gas (90% Argon and 10% methane). The gas is held 2 mbar above atmosphere to ensure oxygen and water do not enter the volume and contaminate the gas. P10 gas was chosen for its fast drift velocity that peaks at low electric fields. The Argon is a stable gas with a high number of valence electrons, while the methane, a gas with high rotational and vibrational degrees of freedom, absorbs energy and prevents unwanted electron avalanches. At peak velocity, the drift speed of P10 is stable and insensitive to variations in temperature and pressure. The drift speed is measured by injecting a laser into the TPC volume and

ionizing the gas. The electron drift speed is 5.45 cm/$\mu$s.

Charged particles stream through the detector volume and ionize the gas, which generates free electrons. The free electrons drift in the electric field to either endcap ground plane. After passing the ground plane, the electrons are measured by a Multi-Wire Proportional Chamber (MWPC) with readout pads.

The layers of the TPC endcap schematic are shown in Fig. 2.6. The endcap consists of four layers: a gated grid, a shield grid (ground), anode wires and readout pads. After electrons drift past the shield grid, they avalanche to the 20 $\mu$m anode wires providing an amplification factor of 1000-3000. As the electrons avalanche, they temporarily generate positive ions, which produce image charges on the readout pads. The gated grid is switched on/off to prevent the generated positive ions from drifting back into the main volume of the TPC.

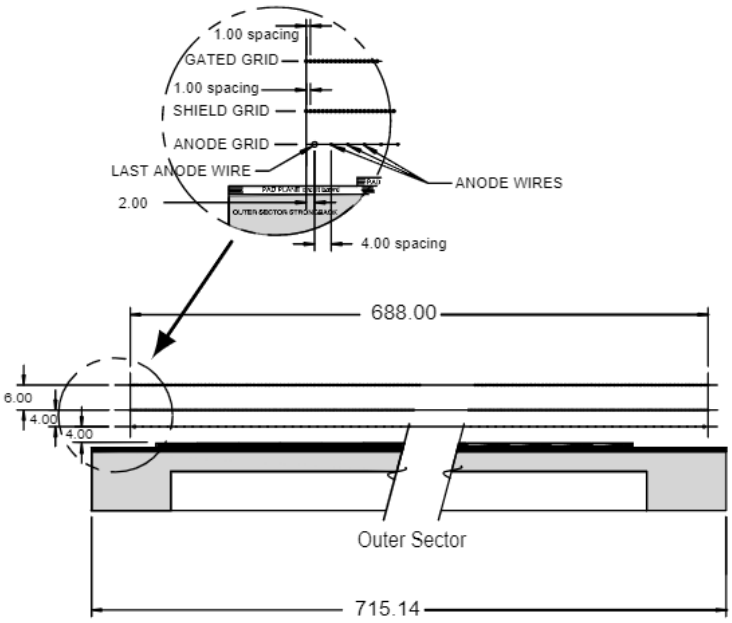


Figure 2.6. Schematic of TPC endcap [73].

The TPC has 12 sectors, each with a pad readout with 13 inner and 32 outer pad rows. Figure 2.7 show a schematic of the pad readout system for a single sector. The outer and inner sectors have a total of 3,942 and 1,750 pads, respectively. The pad rows are perpendicular to the center of the TPC to optimize $p_T$ resolution.

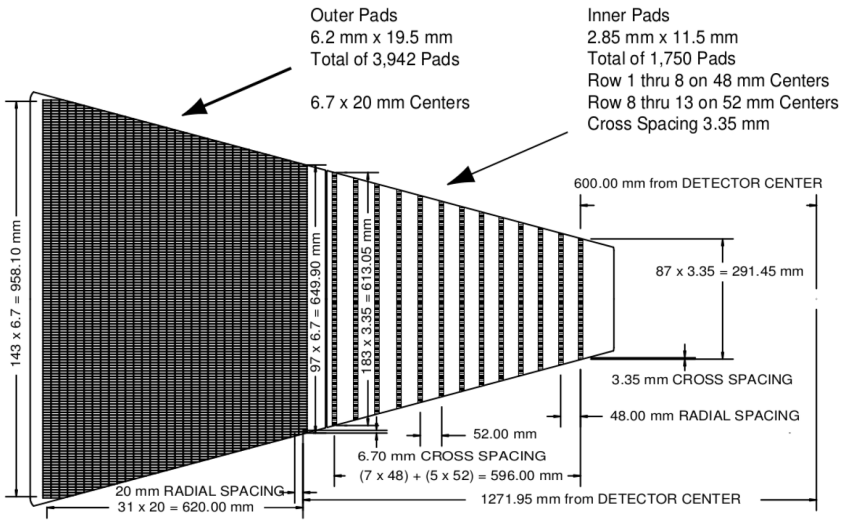


Figure 2.7. Cut-away view of outer sector pad plane [73].

The electron transverse position is measured by the position of the pads in the $x$-$y$ plane. The $z$ position is not directly measured but calculated from time difference between the start of the event and the arrival time of the electron on the pad. With the drift velocity of the gas (5.45 cm/$\mu$s) and the drift time, the $z$ distance is calculated.

The TPC records the spatial data on the ionized electrons but an additional reconstruction procedure is required to form particle tracks. A tracking algorithm is used to generate the charged particle tracks. The pad row hits are fit with a Kalman fitting procedure, which iteratively fits particle helices. This collection of tracks is referred to as the "Global Tracks". Vertices are generated from a vertex algorithm by taking the set of Global tracks and searching for points along the beam line where the helices intersect. The Global tracks are then associated with vertices and refit to include the vertex position, generating sets of primary and secondary tracks. With the track helix, the kinematics of the track can be calculated. While the sign of the charge is determined by direction of the helix in the magnetic field, for simplicity, all tracks are assumed to have unit charge. In a single bunch crossing, the vertex algorithm often finds multiple vertices, either from multiple beam collisions or secondary decays and interactions. In the collider configuration, the vertices are ranked to determine whether they are primary or secondary vertices[1].

[1]Here, the secondary vertex is either a secondary decay or pile-up vertex.

The problem is somewhat simplified for the fixed target by limiting the primary vertices to reside within the fixed target.

In addition to track momenta, the TPC can identify particle species by measuring the energy loss ($dE/dx$) of charged tracks. As charged particles travel through matter, energy is deposited in the traversed material. This energy loss is often referred to as the stopping power of a material and is dependent on both the species and velocity of the charged particle and characteristics of the material. The phenomena of particles traversing matter has been studied at length and, at first approximation, can be well described by the Bethe-Bloch [74] formula. The average energy loss $-\langle dE/dx \rangle$ from the Bethe-Bloch formula for a particle with speed $v$ and charge $z$ is

$$-\langle \frac{dE}{dx} \rangle = \frac{4\pi}{m_e c^2} \frac{nz^2}{\beta^2} \left( \frac{e^2}{4\pi\epsilon_0} \right)^2 \left[ \ln \left( \frac{2m_e c^2 \beta^2}{I(1-\beta^2)} \right) - \beta^2 \right], \tag{2.1}$$

where $c$ is the speed of light, $\epsilon_0$ is the vacuum permittivity and $\beta$ is the relativistic velocity $v/c$. Symbols $e$ and $m_e$ are the electron charge and mass, respectively. The material has an electron number density $n$ and a mean excitation potential $I$.

The Bethe-Bloch formula gives a general formula for the average energy loss in a material. The STAR collaboration, however, uses a more highly tuned model, known as the Bichsel curve [75]:

$$\frac{dE}{dx} = K z^2 \frac{Z}{A} \frac{1}{\beta^2} \left[ \frac{1}{2} \log \left( \frac{2m_e c^2 \beta^2 \gamma^2 T_{\max}}{I^2} \right) - \beta^2 - \frac{\delta(\beta\gamma)}{2} \right] \tag{2.2}$$

$$T_{\max} = \frac{2m_3c^2\beta^2\gamma^2}{1 + 2\gamma(m_e/m_0) + (m_e/m_0)^2} \text{ (Mev)}$$

$$A = \text{Atomic Mass of incident material (g/mol)}$$

$$K = 4\pi N_A r_e^2 m_e c^2 \text{ (cm}^2 \cdot \text{mol)}$$

$$N_A = \text{Avogadro}'\text{s Number}$$

$$r_e = \text{Classical electron radius (fm)}$$

$$m_e = \text{Mass of electron (MeV)}$$

$$m_0 = \text{Mass of incident particle (MeV)}$$

$$Z = \text{Incident particle Atomic Number}$$

$$z = \text{Material Atomic Number}$$

$$I = \text{Mean excitation energy (eV)}$$

$$\delta(\beta\gamma) = \text{Density Effect Correction.}$$

The Bischel differs from the Bethe-Bloch Equation by including a max energy transfer term ($T_{max}$) and a material dependent correction $\delta(\beta\gamma)$. The Bischel curve gives a slightly more realistic energy loss for electrons in P10 gas.

As the track passes through the TPC gas, the argon is ionized. The number of freed electrons is proportional to the energy loss in the argon gas. If the TPC is properly calibrated, the $dE/dx$ can be calculated from the total number of electrons on each pad row hit. In practice, the collection of $dE/dx$ hits looks like a Landau distribution. Therefore, each track is fit with a Landau distribution to estimate the most probable $dE/dx$, a quantity that can be compared to our Bichsel prediction. As seen in Fig. 2.8, the Bichsel predictions nicely predict the particle bands. An $N_\sigma$ value is calculated for each particle species, where

$$N_{\sigma,i} = \frac{1}{\sigma_l} \ln\left(\frac{dE/dx_{\text{meas.}}}{dE/dx_{\text{expect}}}\right) \tag{2.3}$$

for the particle species $i = p^\pm$, $\pi^\pm$, $K^\pm$, $e^\pm$, $d$, and $t$. Here, $dE/dx_{\text{meas.}}$ is the measured $dE/dx$, $dE/dx_{\text{expect}}$ is the Bichsel predicted $dE/dx$, and $\sigma_l$ is a track resolution which

depends on track length. In a region where particles are well separated in $dE/dx$, the $N_\sigma$ of a particle appears Gaussian with a standard deviation of 1. Both particle selection and rejection can be performed by selecting on $N_\sigma$.

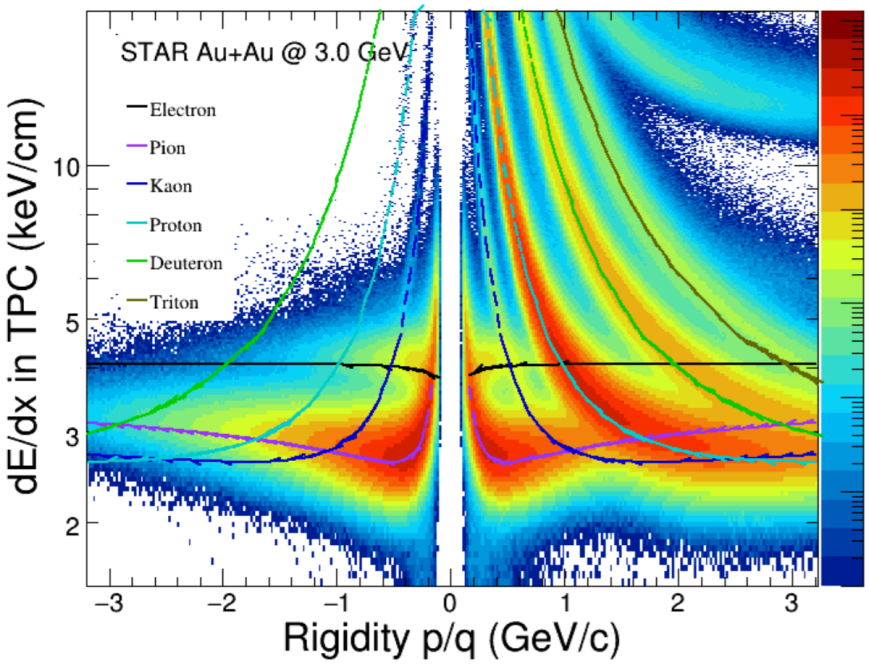


Figure 2.8. $dE/dx$ (keV/cm) versus track rigidity ($|p|/q$ GeV/$c$) for Au + Au $\sqrt{s_{NN}}$ = 3.0 GeV collisions. Both positive and negative electron, pion, kaon, proton, deuteron and triton Bichsel curves are labeled.

Even with the Bichsel curves, protons can only be reliably identified ($\geq$ 97% purity) up to momenta of 2.0 GeV/$c$ at $\sqrt{s_{NN}}$ = 3.0 GeV. Above 2.0 GeV/$c$, the pion, kaon, and deuteron bands begin to merge with the proton band. This band merging produces a considerable amount of contamination in the proton particle identification selection (PID) selection. To improve PID for the higher momenta tracks, an additional TOF cut is implemented.

### 2.2.2 The Time of Flight Detector

The TPC provides $dE/dx$ and rigidity for tracks within the TPC acceptance ($|\eta| < 2.0$ central collisions) but fails to separate particle species above momenta of 2.0 GeV/$c$. To improve PID, the STAR detector includes a Time of Flight system (TOF).

The TOF system consists of two sub detectors, the Barrel TOF modules and the Vertex

Position detector (VPD). The Barrel TOF modules are fast detectors placed around the barrel of the TPC, measuring the hit timing ($\sim$ 60 ps resolution) and position of incident tracks. The VPD, a set of small forward and backward detectors with high timing precision ($\sim$ 28 ps), provides the start time of the event ($t_0$). In central collisions, the VPD calculates the difference in time ($\Delta t$) of luminal particles in the East/West VPD. By comparing the $\Delta t$ to the TPC vertex position, one can identify the start time of the event ($t_0$). This methodology, however, is insufficient in the fixed-target setup in which only one VPD detector can be used; the process requires VPD East/West coincidence. Therefore, a new startless method is designed for the fixed-target configuration, which is described in section 2.2.2.3.

To use the time-of-flight information, TOF hit positions are associated with TPC track helices. With the TOF timing information ($t_{\text{hit}}$) and the start time of the event ($t_0$), one can calculate the charged tracks' time of flight as $\Delta t = (t_{\text{hit}} - t_0)$. The TPC provides the track momentum and track length, while the TOF provides the relativistic velocity. For example, if the track path length is $l$ and track timing from collision to TOF hit is $\Delta t$, then, the relativistic velocity is calculated as $\beta = l/(\Delta t \cdot c)$. Using the definition of relativistic momentum, $p = \gamma m_0 \beta$, the particle mass-squared is

$$m_0^2 = \frac{p^2}{\gamma^2 \beta^2} = p^2 \frac{1 - \beta^2}{\beta^2}. \tag{2.4}$$

The TOF provides PID for tracks with momentum above 200 MeV/$c$ within the pseudorapidity $|\eta| < 1.0$ for collisions in collider mode. The pseudorapidity is shifted by the change in detector geometry and ranges from $0 < \eta < 1.4$ for the fixed-target geometry, see Figure 2.11. Requiring all tracks to have a TOF hit lowers the TPC tracking efficiency by $\sim$ 40%. Therefore, the TOF requirement is limited to high momentum tracks ($p > 2$ GeV/$c$) in which the TPC PID is insufficient.

#### 2.2.2.1 TOF Design

The Barrel Time of Flight (TOF) consists of 60 trays placed around the East and West TPC (120 trays total) providing coverage within $|\eta| < 1.0$ and full azimuthal coverage for collisions in collider mode (center of the TPC). Each TOF tray contains 32 TOF modules. This can be seen in Fig. 2.9, which shows a cross section of a TOF tray. The implications

of the TOF geometry for track acceptance in the fixed-target setup will be discussed in the following section.

The TOF module is based on the multi-gap resistive plate chamber (MRPC) technology. Figure 2.10 shows a side view schematic of a single MRPC module. The MRPC

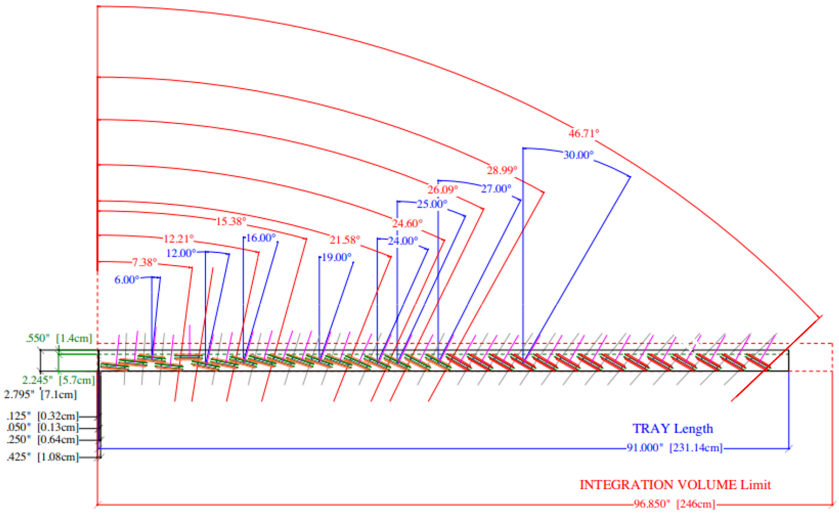


Figure 2.9. TOF tray design. TOf modules are oriented towards the center of the TPC. Figure from Ref. [76].

module is a stack of resistive plates with uniform gas gaps. The module design can be seen in Figure 2.10. In essence, the mechanics of a MRPC are fairly simple. A high voltage is applied to the electrodes on outer plates and a strong electric field is generated in each gas gap. The inner plates are electrically floating. When a charged track passes through the plates, the gas ionizes and produces free electrons. The electrons avalanche towards the resistive plates, where they are deposited and, due to the high resistivity, the charge sticks to the plates. The sum of charge from all plates is read by copper pickup pads. Figure 2.10 shows a schematic of the restive plates, electrodes, copper pickups and a honeycomb support structure.

#### 2.2.2.2 TOF Detector Efficiency for the Fixed Target

Figure 2.12 shows a cartoon cross section of the TOF modules, TPC, and fixed target. TOF module efficiency and hit quality is maximized when track incidence is normal to the

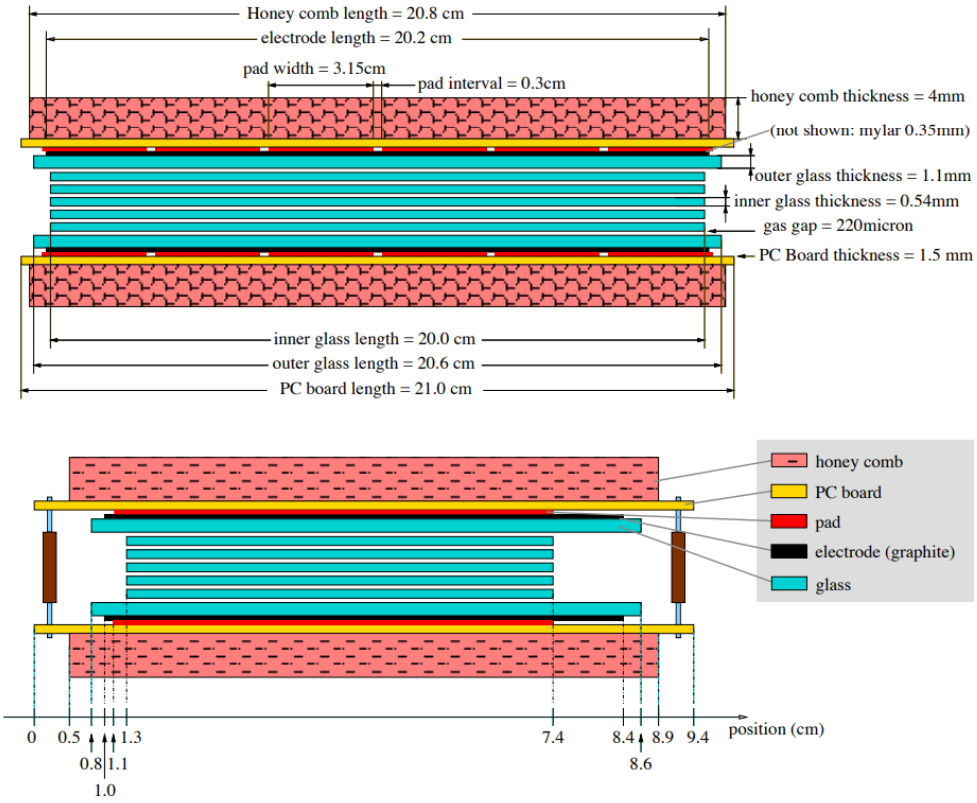


Figure 2.10. TOF module design. Figure from Ref. [76].

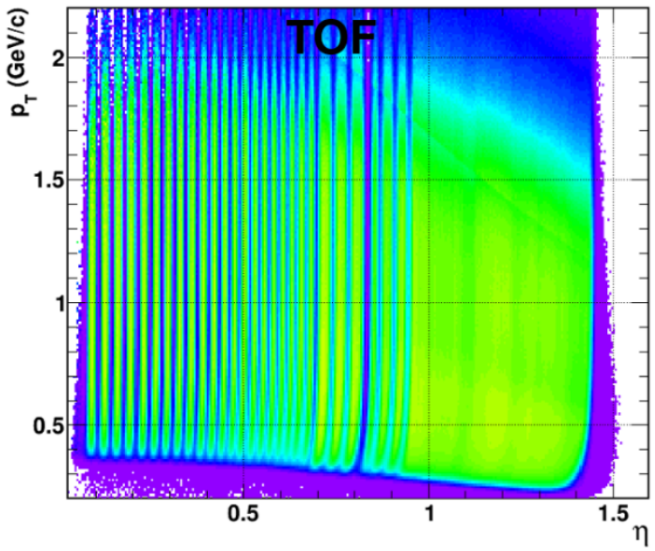


Figure 2.11. Proton track acceptance in the STAR TOF.

TOF module plane. Therefore, the TOF modules are oriented normal to the center of the TPC. In collider mode, this maximizes the number of tracks that are incident normal to the module. A more precise schematic of a single TOF module can be seen in Fig. 2.9. The optimization for collisions in collider mode is problematic for the fixed-target geometry as tracks originate from the edge of the TPC and not the center. The effect can be seen in the efficiency plot 2.11 as an odd striping in efficiency for charged tracks in the West TPC ($\eta \leq 0.75$). Due to this behavior, there is a significant drop in TOF efficiency at low pseudorapidities, when tracks are almost parallel with the TOF module orientation.

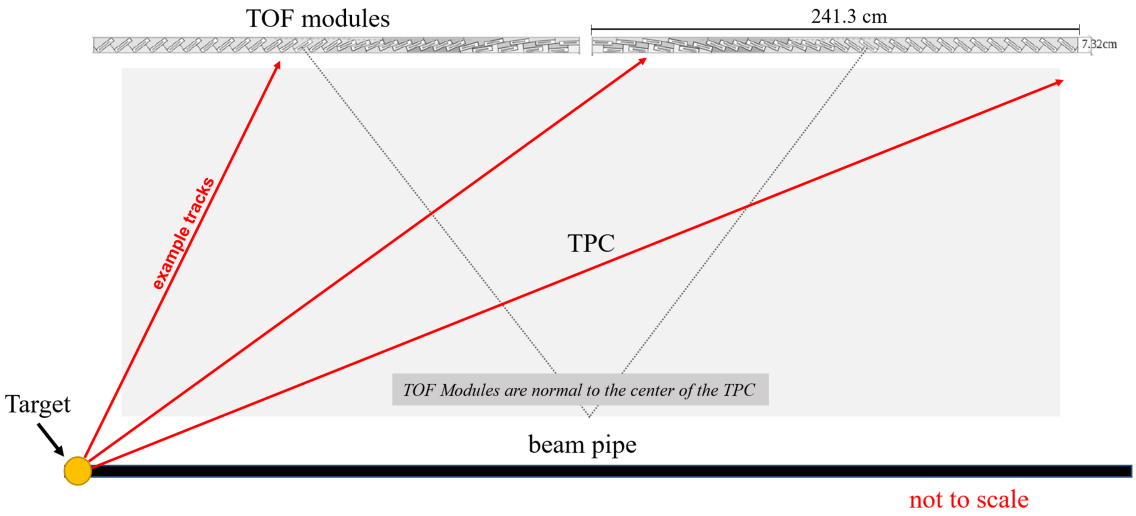


Figure 2.12. Cartoon of TOF and TPC geometry with respect to the fixed target. TOF modules in the figure are from STAR internal documentation. Examples of track projections shown in red.

#### 2.2.2.3 The Startless TOF Algorithm

Typically in the STAR collider configuration, the TOF relies on VPD East/West coincidence and the vertex position of the TPC to determine the start time of the event ($t_0$). Then, the TOF provides the end time for a charged track ($t_{\text{hit}}^{\text{TOF}}$). With the hit time $t_{\text{hit}}^{\text{TOF}}$ and the start time $t_0$, the time-of-flight is calculated by $t_{\text{tof}} = t_{\text{hit}}^{\text{TOF}} - t_0$. Here, there is a distinction between the particle time-of-fight ($t_{\text{tof}}$) and the time measured in the TOF ($t_{\text{hit}}^{\text{TOF}}$) and TPC ($t_{\text{hit}}^{\text{TPC}}$) detectors. If the vertex and module position are known, the particle mass can be calculated, see Eq. (2.4). In the fixed-target configuration, this is an invalid approach, as the collisions do not hit both VPD East and West.

A simple fix is to measure a clean sample of TPC identified pions or protons and calculate the expected time-of-flight ($t_{\rm hit}^{\rm TPC}$) of each track using the TPC path length and assumed mass. By taking the average difference between the TPC and TOF $t_{\rm hit}$ for all candidates, the start time $\langle t_0 \rangle$ is estimated. If the samples are clean and the number of tracks is sufficiently large ($\sim 5$), the $\langle t_0 \rangle$ is fairly accurate. Using pions as an example, if one assumes the mass to be 139.6 GeV/$c^2$, the pion time of flight for each pion track can be calculated as

$$t_{\rm tof}^{\rm TPC,\pi} = l \cdot \sqrt{(m_\pi^2 + p_{\rm tot}^2)/(p_{\rm tot}c)}, \tag{2.5}$$

where $m_\pi$ is the mass of pion, $p_{\rm tot}$ is the TPC total momentum, $c$ is the speed of light, and $l$ is the length of the reconstructed helix. With the collection of pion tracks and the clock time of the TOF modules, the approximate start time is calculated as

$$\langle t_0 \rangle = \frac{\sum_{i=1}^{N_\pi} t_{\rm hit,i}^{\rm TOF} - t_{\rm tof,i}^{\rm TPC,\pi}}{N_\pi}, \tag{2.6}$$

where $t_{\rm tof,i}^{\rm TPC,\pi}$ and $t_{\rm hit,i}^{\rm TOF,\pi}$ are the calculated and measured time-of-flights for the $i^{th}$ pion candidate in the TPC and TOF, respectively. With the calculated $\langle t_0 \rangle$, the time-of-flight is calculated for all TOF hits $t_{\rm tof} = t_{\rm hit}^{\rm TOF} - \langle t_0 \rangle$. To increase the accuracy of the estimation, both pions and protons are used in the calibration.

### 2.2.3 The Beam-Beam Counter & The Event Plane Detector

The Event Plane Detector (EPD) and the Beam-Beam Counter (BBC) are sets of forward/backward detectors. The approximate position can be seen in Fig. 2.4. The BBCs are scintillating tiles paired with photo-multiplier tubes covering the pseudorapidity[2] $3.4 < |\eta| < 5.0$. The EPD, a detector primarily used for measuring the event plane for flow and polarization measurements, shares a similar pseudorapidity space $2.1 < |\eta| < 5.1$. In this analysis, the East BBC and EPD are used as the minimum bias trigger detectors. Specifically, collisions are triggered and recorded if they include a hit in the East BBC or EPD and a hit in the TOF detector.

[2]This is a pseudorapidity in the collider configuration.

## 2.3 The STAR Fixed-Target

The STAR fixed-target program's first test was in 2015, with two small data sets of Au+Au and Al+Au at $\sim 210$ cm from the center of the TPC. With the 2015 test, analyzers were able to perform certain analyses, such as spectra and flow. Figure 2.13 shows the STAR preliminary proton spectra from the test run at $\sqrt{s_{NN}} = 4.5$ GeV. The test run displayed the capacity of the STAR detector to perform well in a fixed-target configuration [77]. The success of the test run motivated the fixed-target program, which would include runs with more statistics at different energies.

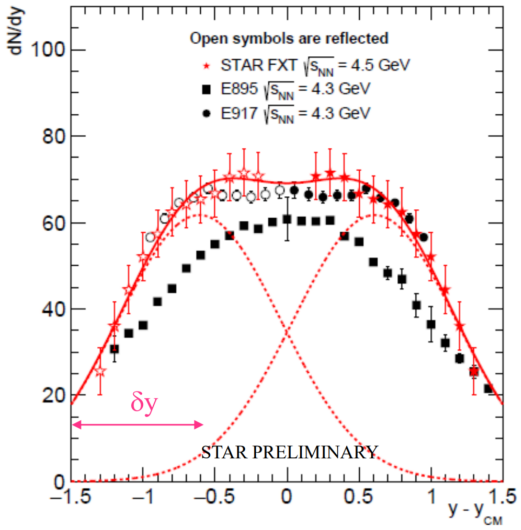


Figure 2.13. Proton $dN/dy$ for the 2015 Au+Au fixed-target test run[78] at $\sqrt{s_{NN}} = 4.5$ GeV. The $\delta y$ exhibits the shift in the proton peak due to baryon stopping.

STAR began a dedicated fixed-target run in 2018 of Au + Au collisions at $\sqrt{s_{NN}} = 3.0$ GeV and the target location was moved to 200.7 cm, closer to the edge of the TPC. This change was possible due to a change in the beam pipe configuration and improves the acceptance at target rapidity.

### 2.3.1 The Target Apparatus

The fixed-target apparatus consists of two long support rods and a half collar to hold the thin gold target. The rods, collar, and gold foil are shown in Fig. 2.15. The original gold foil for the 2015 test run was a 1 mm thick strip. For the dedicated 2018 run, the target thickness was reduced to 0.25 mm.

Figure 2.14. Fixed target apparatus including support beams, holding collar, and gold foil.

### 2.3.2 The Fixed-Target Run Conditions and Geometry

RHIC was setup to run 12 bunches of $7 \times 10^9$ ions. The data acquisition system limited the data taking rate at 1 kHz. The beam was lowered 1.8 cm onto the target until the 1 kHz rate was met. To achieve the event rate, only the edge of the beam was incident on the target.

Typically in the limit $y \approx \eta$, the acceptance of a high energy collider is largely independent of $\sqrt{s_{NN}}$. This is not true for the fixed-target geometry. As the beam energy increases, midrapidity is pushed closer to the beam line. Additionally, midrapidity is different for each particle species. For $\sqrt{s_{NN}} = 3.0$ GeV Au+Au collisions, the proton acceptance[3] is shown in Fig. 2.15. At higher fixed target energies, such as $\sqrt{s_{NN}} = 7.7$ GeV, the midrapidity are outside the TPC acceptance.

[3]To be specific, this is not a true acceptance because the $z$-axis is in counts and not a percentage. A true acceptance is shown in a later chapter (see Fig. 5.3 in chapter 5).

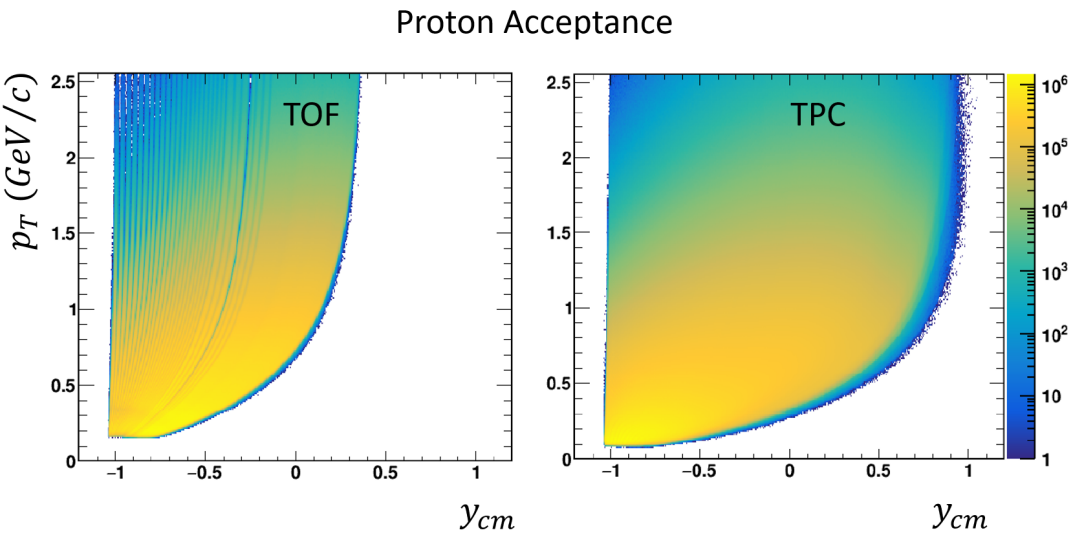


Figure 2.15. TOF (left) and TPC (right) acceptance in $p_T$ and $y$.

# Chapter 3

# Event Centrality Determination

## 3.1 Geometry of Heavy Ion Collisions

The system size, or the number of colliding nucleons, is studied by either changing the species of the colliding ions or studying the dependence of the impact parameter (the distance between the centroids of the two nuclei). An event with a small impact parameter ($\sim$ 0-3 fm for Au+Au collisions) is referred to as a central event, in which the most of the nucleons participate in the collision. As the impact parameter increases, the event centrality decreases to mid-central ($\sim$ 3-6 fm), semi-peripheral ($\sim$ 6-10 fm), and peripheral collisions ($\gtrsim$ 10 fm), respectively. If it were possible to measure the impact parameter directly, experimental observables could be easily studied as a function of system size. However, the impact parameter is inaccessible in high energy experiments and thus one relies on models to estimate the initial geometry of the event. Two models are studied: the Glauber Model [79] and the Ultrarelativistic Quantum Molecular Dynamics model (UrQMD) [34].

The most common model used to determine the event centrality is a Glauber Monte Carlo (GMC) method. The term "Glauber Model" dates back to the 1950s when Roy Glauber presented unpublished work which described the experimental data from $p + d$ collisions with quantum theory. In the 1970s, Maximon and Czyz built off of his work and developed the "wounded nucleon model" to describe inelastic collisions [80]. In the next half century, the Glauber Model would go through several iterations. Eventually with the

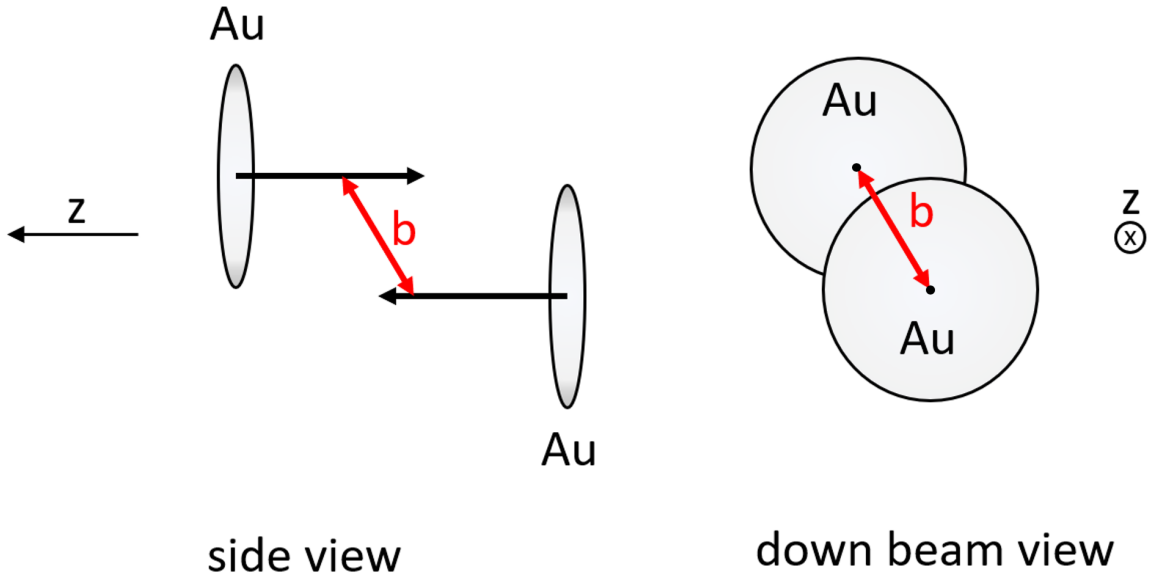


Figure 3.1. Diagram of impact parameter in a Au+Au collision.

advances in modern computers, physicists adapted the Glauber Model to Monte Carlo simulations. Now the term "Glauber Model" is somewhat ambiguous. In the context of this analysis, however, "Glauber Model" will refer to a Glauber Monte Carlo (GMC), in which the nucleus is described as a collection of uncorrelated nucleons. Unlike more sophisticated hydrodynamic and transport models, the GMC model is relatively simple, with few assumptions about the nucleon dynamics. It has been shown that the GMC model agrees well with the measured multiplicity distributions [79].

UrQMD is a microscopic transport model which is tuned to reproduce several particle observables, but does not contain the physics of critical phenomena. Around 80 million events are produced using UrQMD version 3.4 in Au+Au collisions at $\sqrt{s_{NN}} = 3.0$ GeV in cascade mode. The model does not produce an equilibrated system and therefore does not contain any critical phenomena but has been shown to reproduce particle abundance, spectra, and flow at several energies [34]. In comparison to the Glauber Model, the UrQMD model may be more applicable in the low energy range in which nucleons are affected by both elastic and inelastic collisions. Although UrQMD is not used for event centrality, comparisons of both the distributions of the event impact parameter ($b$) and number of participating collisions ($N_{\text{part}}$) are made throughout the analysis.

It should be noted that although $\langle b \rangle$ and $\langle N_{\rm part} \rangle$ are physically different quantities, they are often used interchangeably to describe centrality. Figure 3.2 shows a cartoon example of the relation between the reference multiplicity and the Glauber quantities $b$ and $N_{\rm part}$.

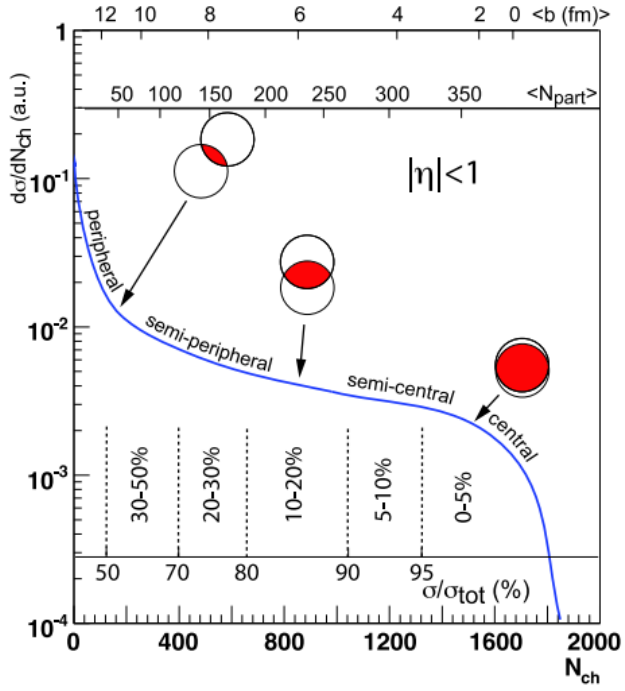


Figure 3.2. Cartoon example of the correlation between the reference multiplicity ($N_{\rm ch}$) and Glauber calculated quantities ($b$,$N_{\rm part}$). This figure was generated by T. Ullrich [79].

## 3.2 Reference Multiplicity

In heavy ion collisions, it has been found that the initial parameters $b$ and $N_{\rm part}$ are monotonically related to particle multiplicity at both forward rapidity and midrapidity [79]. A large particle multiplicity at the midrapidity and a small number of spectators at forward rapidity is expected for an event with a high impact parameter $b$. A commonly used observable is an uncorrected charged track multiplicity within a pseudorapidity window (reference multiplicity). Using the central limit theorem, the average value of a reference multiplicity class should correspond to average $N_{\rm part}$ and $b$ values (Fig. 3.2). The values are determined by a Glauber and particle production model. The full procedure

is discussed in section 3.3.1 and 3.13. This analysis uses a new reference multiplicity (`RefMult3`).

### 3.2.1 Data Collection and Storage

The centrality determination study and the proton analysis are performed on the same data set. The overview of the data collection, file format, and data storage is discussed in chapter 4. This data set contains 147 million minimum bias events. To reduce background, minimum bias events require more than three hits in the Time of Flight (TOF) detector (TOF $> 3$) and a hit in either trigger detector, the EPD or BBC (discussed in section 2.2.3).

### 3.2.2 Event and Track Selection

The event trigger and vertex selection used in the centrality study are outlined in chapter 4. Events in the centrality study require a $z$ vertex location of $199.5 < v_z < 202$ cm with respect to the coordinate system defined in section 2.2 and a radial vertex location of $v_r < 1.5$ cm from the center of the beam spot, $v_{x,y} = (0, -2)$ cm.

In the STAR detector, the beam remnant (spectators) cannot be measured and therefore the choice of reference multiplicity is limited to midrapidity particle production. The conventional STAR run configuration (collider mode) uses the common reference multiplicity `RefMult`. The `RefMult` is defined as the total number of charged tracks in the pseudorapidity acceptance of $|\eta| < 0.5$ with specific detector cuts. However, during BES I, it was shown that `RefMult` is not a suitable reference multiplicity for a proton fluctuation measurement [81]. If protons are included in the reference multiplicity, the analysis will suffer from an artificial enhancement, labeled the "auto-correlation" effect [82]. To suppress the effect, another reference multiplicity (`RefMult3`) was developed which excludes protons. Additionally, the acceptance of the reference multiplicity $|\eta| < 0.5$ was increased to $|\eta| < 1.0$ to offset the lowered particle multiplicity.

The "auto-correlation" effect can be demonstrated with a simple toy model. Consider the random variates $X$ and $Y$ sampled from a normal distribution $N(\mu = 100, \sigma = 10)$, where $\mu$ is the mean and $\sigma^2$ is the variance. If the correlation between $Y$ versus

$X$ and $Y$ versus $X + Y$ are plotted (Fig. 3.3), $Y$ versus $X$ (left panel) will show no correlation and $Y$ versus $X + Y$ (right panel) will display a strong positive correlation. This applies to the proton analysis, in which the observable of interest is the number of protons $Y$ and reference multiplicity is the number of uncorrected tracks excluding protons $X$ (`RefMult3`). The `RefMult3` + protons is $X + Y$ (`RefMult`).

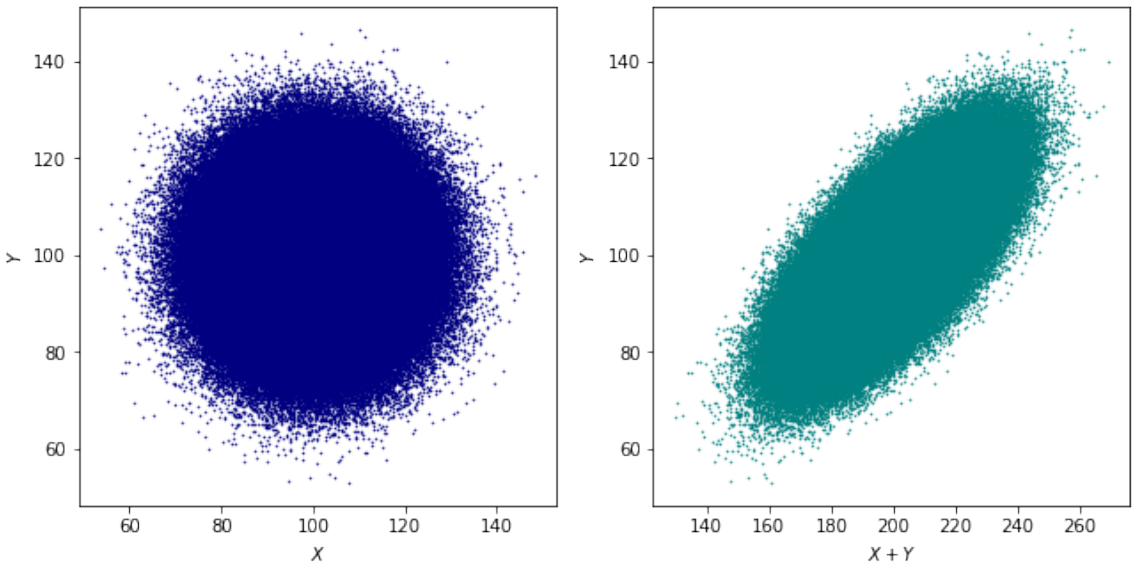


Figure 3.3. Scatter plots of normally distributed random variates $Y$ versus $X$ (left) and $Y$ versus $X+Y$ (right). The plot on the right shows the auto-correlation we would like to avoid.

Two new reference multiplicities are introduced for the fixed-target mode: `FxtMult`, a common reference multiplicity, and `FxtMult3`, a reference multiplicity for the event-by-event protons analysis. Both `FxtMult` and `FxtMult3` are the uncorrected charged tracks in the detector acceptance of $-2 < \eta < 0$, with protons excluded from `FxtMult3` to reduce the effect of auto correlation. To ensure all tracks originate from the primary vertex, additional track quality cuts for `FxtMult` and `FxtMult3` tracks are placed:

1. A track must be associated with the primary vertex (primary track).

2. The distance of closest approach (DCA) of a track to the primary vertex is less than 3 cm (DCA$<$ 3 cm).

3. Both the number of fit points and possible fit points of a track must have a ratio

greater than 0.52.

(`NHitsFit/NHitsPoss` $> 0.52$)

4. The number of $dE/dx$ points of a track is greater than 10 ($dE/dx > 10$).

5. The track is reconstructed with a pseudorapidity between -2.0 and 0.0 ($-2 < \eta < 0$).

6. (`FxtMult3` only) A track's $dE/dx$ versus rigidity is $3\sigma$ below the Bichsel prediction for a proton ($N_{\sigma,p} < -3$).

Items 1-4 of the track selection criteria in the centrality determination are similar to the criteria used for the proton moment analysis, which is discussed later in chapter 4.[1] Figure 3.4 depicts the $dE/dx$ versus $|p|/q$ bands and highlights $3\sigma$ from the proton Bichsel curve [75] ($|N_{\sigma,p}| < 3$).

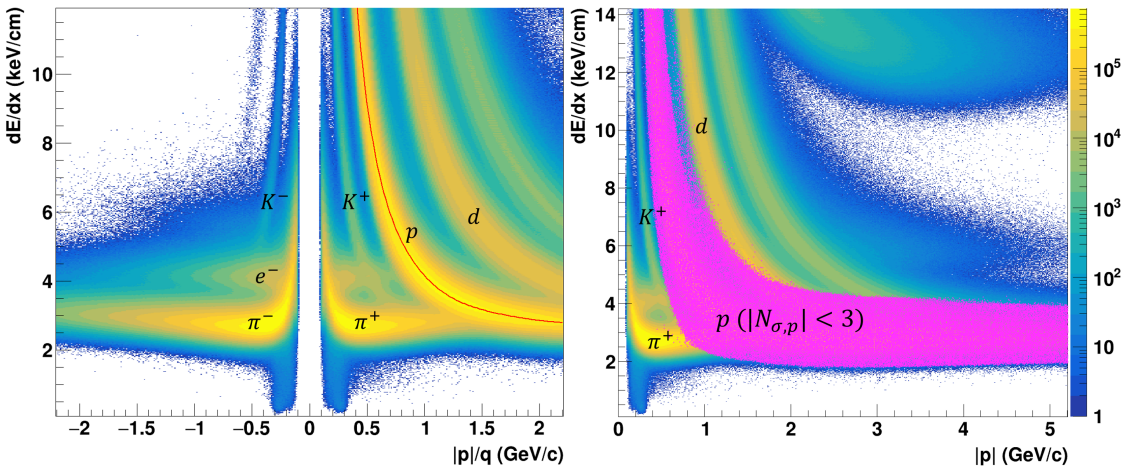


Figure 3.4. $dE/dx$ versus $|p|/q$ (left) and $dE/dx$ versus $|p|$ for positively charged tracks (right). The red line indicates the expected proton energy loss. The magenta section highlights $3\sigma$ from the proton Bichsel curve ($|N_{\sigma,p}| < 3$). Proton, pion, Kaon, deuteron, and electron bands are labeled.

Figure 3.5 shows a comparison of the detector acceptance of the different reference multiplicities: the collider geometry `RefMult` and `RefMult3` and the fixed target `FxtMult` and `FxtMult3`. Both the `FxtMult` and `FxtMult3` have a larger opening angle than `RefMult` and `RefMult3` which increases the particle yield. This is necessary at the fixed-target

[1] This includes definitions of track quality variables.

energies in which particle production is reduced. In general, the centrality resolution scales with the total particle production, see chapter 7.

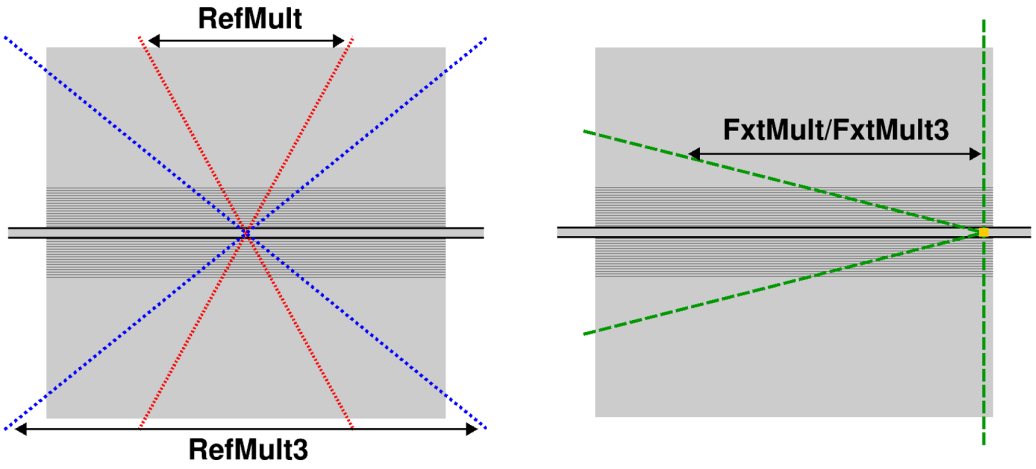


Figure 3.5. Comparison of the pseudorapidity acceptance for `RefMult`, `RefMult3`, `FxtMult` and `FxtMult3`. The left panel shows the acceptance for the collider geometry, where red and blue lines indicate the opening angle of `RefMult` ($|\eta| < 0.5$) and `RefMult3` ($|\eta| < 1$) tracks, respectively. The right panel shows the acceptance for the fixed-target geometry, where green lines indicate the opening angle of `FxtMult` and `FxtMult3` ($-2 < \eta < 0$) tracks. The yellow square indicates position of the fixed target.

### 3.2.3 Reference Multiplicity Simulation Study

With the introduction of a new reference multiplicity `FxtMult3`, it is important to ask whether `FxtMult3` varies monotonically with the initial impact parameter of the event. Although this correlation cannot be directly measured, model calculations may provide insight into the effectiveness of the reference multiplicity. A transport model (UrQMD) is used to test the correlation between `FxtMult3` and the initial collision geometry.

The simulation sample, which consists of 80 million UrQMD events, is generated and stored on the RHIC computing facility. UrQMD is run with a mean-field model at $\sqrt{s_{NN}} = 3.0$ GeV and boosted to the reference frame of the lab. It should be noted that the following study compares the acceptance effects of UrQMD and data, but does not include effects from $dE/dx$ such as the track selection cuts. The events are binned into two dimensional histograms `FxtMult` versus impact parameter $b$ and `FxtMult3` versus impact

parameter $b$, see Fig. 3.6. Dotted black and dashed magenta lines are the centrality classes defined by multiplicity and impact parameter, respectively (0-20%, 20-40%, 40-60% and 60-80%). While both `FxtMult` and `FxtMult3` are correlated with the impact parameter $b$, `FxtMult` has higher resolution and provides a better proxy for $b$. Figure 3.7 show the projections of the correlation plots in Fig. 3.6 for different reference multiplicity selections.

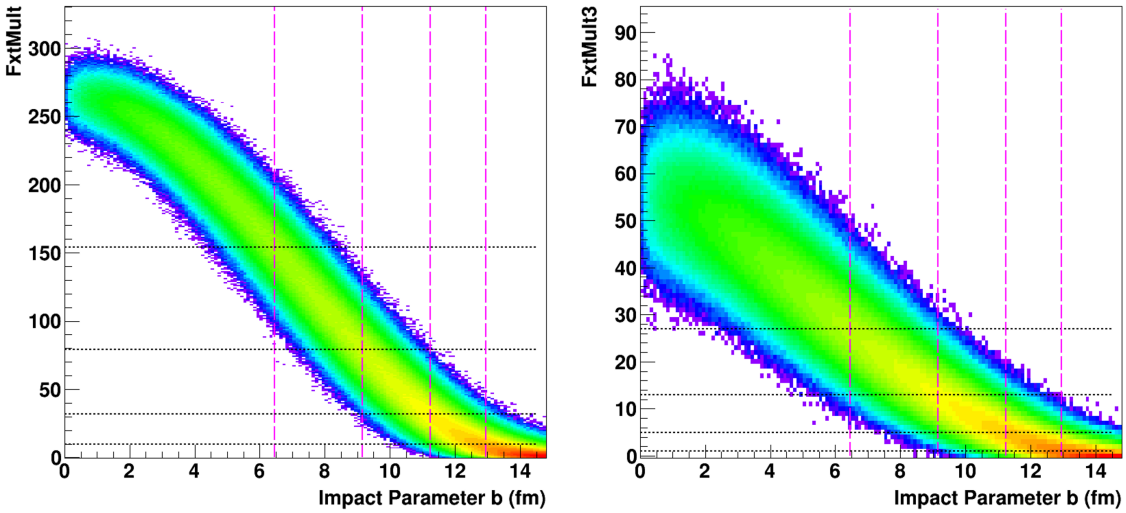


Figure 3.6. Centrality of simulated UrQMD events at $\sqrt{s_{NN}}$ = 3.0 GeV. `FxtMult` versus impact parameter (left) and `FxtMult3` versus impact parameter (right). Black dotted lines separate the 0-20%, 20-40%, 40-60% and 60-80% events binned by event multiplicity. Magenta dashed lines separate the 0-20%, 20-40%, 40-60% and 60-80% events binned by event impact parameter.

The UrQMD simulations show that both `FxtMult` and `FxtMult3` are suitable reference multiplicities. Specifically, both reference multiplicities monotonically vary with the impact parameter. However, `FxtMult` will provide better resolution of impact parameter than `FxtMult3`. This is clear from the Fig. 3.7, which depicts the impact parameters for a given reference multiplicity class. By removing protons from `FxtMult3`, the particle production is lowered and subsequently the centrality resolution is reduced.

## 3.3 Centrality Bin Determination

As previously mentioned, the Glauber Monte Carlo model (GMC) allows one to relate the measured reference multiplicity distribution to the average impact parameter and average number of participating nucleons. To generate the event centrality definition, the GMC

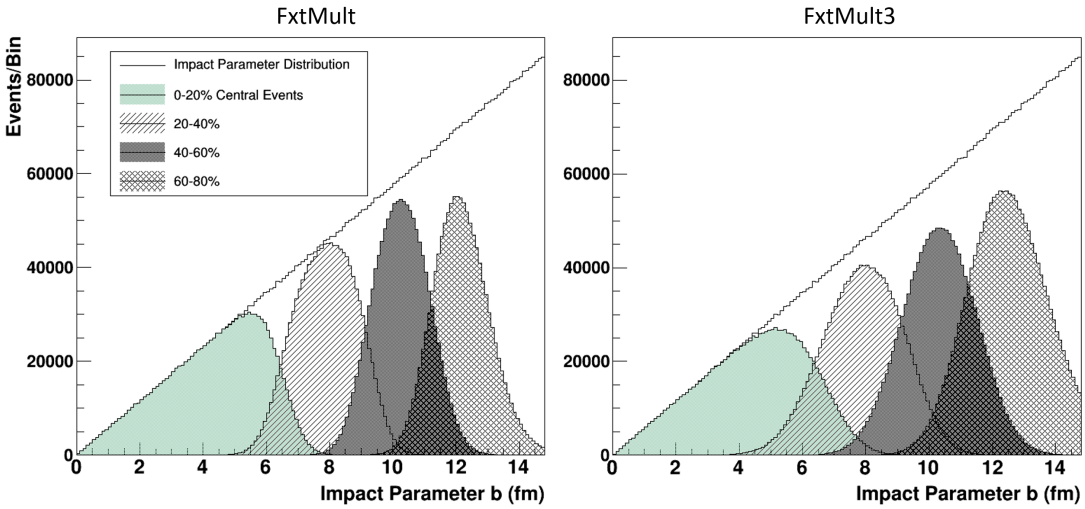


Figure 3.7. Centrality of simulated UrQMD events at $\sqrt{s_{NN}}$ = 3.0 GeV. The histograms show the impact parameter of the event for `FxtMult` (left) and `FxtMult3` (right). Events are separated by event multiplicity (0-20%, 20-40%, 40-60% and 60-80% central events).

requires two additional input parameters: a particle production model and a detector efficiency model.

### 3.3.1 The Glauber Model

The Glauber Monte Carlo model is dependent on two experimental inputs, the nuclear charge density of the nucleus and the nucleon-nucleon cross section. The nuclear charge density, or the probability distribution of nucleons in the nucleus, is well described by a three parameter Fermi distribution. The nucleon-nucleon cross section is inferred from $p+p$ data. Here, both input parameters are discussed in more detail.

#### 3.3.1.1 Three Parameter Fermi Distribution

To populate a nucleus with nucleons in the GMC model, the model requires a nucleon distribution. A common approach is to measure the charge distribution of the nucleon with electron scattering experiments. Then, the charge distribution is parameterized by an empirical model, such as the three parameter Fermi distribution (Wood-Saxon Distribution [83]). The three parameter Fermi distribution is

$$\rho(r) = \rho_0 \frac{1 + w(r/R)^2}{1 + \exp(\frac{r-R}{a})}, \tag{3.1}$$

where $\rho_0$ is the nucleon density in center of the nucleus, $w$ is a spherical deformation parameter, $R$ is the nuclear radius and $a$ is the "skin depth" parameter. The parameters of a gold ion are $R = 6.38$ fm, $a = 0.535$ fm and $w = 0$ [84]. Figure 3.8 depicts a projection of three parameter Fermi distributions for three different nuclei species. With the charge

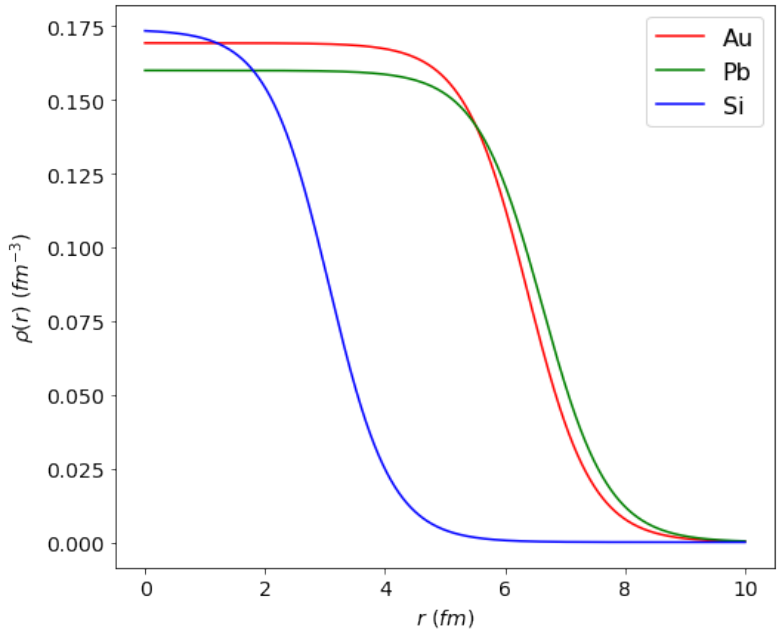


Figure 3.8. Projection of the Wood-Saxon distribution for three nuclei (three parameter Fermi). Au, Pb and Si are plotted with radii of 6.38, 6.62, and 3.07 fm and "skin depth" of 0.353, 0.549, and 0.519 fm, respectively.

density (three parameter Fermi), the nucleon positions are randomly selected and placed in the nucleus until the nucleus is filled.

#### 3.3.1.2 Inelastic Cross Section $\sigma_{inel}^{NN}$

In its simplest form, the GMC model attempts to measure the number of interacting nucleons. Therefore, one must define the criteria for a nucleon-nucleon interaction or collision. In the GMC, a collision occurs if two nucleons are within $\sqrt{\sigma^{NN}/\pi}$ in the transverse plane. At high energies where the center of mass energy is much greater than the difference in mass between a proton and neutron ($\sqrt{s_{NN}} >> m_p - m_n$), the nucleon-nucleon and proton-proton scattering cross sections are expected to be similar. Figure 3.9 shows the $p + p$ cross section versus center of mass energy ($\sigma_p$ versus $\sqrt{s_{NN}}$). The input cross section of the GMC for typical STAR run conditions ($\sqrt{s_{NN}} = 200$ GeV)

is dominated by the inelastic scattering while elastic scattering is negligible. Therefore only the inelastic cross section is considered. At fixed-target energies ($\sqrt{s_{NN}}$ = 3.0 - 7.7 GeV), the elastic contribution is no longer negligible and is comparable to the inelastic cross section, see Fig. 3.9. If elastically-scattered protons are included in the reference multiplicity, the centrality determination is complicated. The GMC model posits that each binary collision act as an independent particle source. The total number of binary collisions is $N_{\text{coll}}$. However, this does not a describe an elastic collision as the collision will not emit additional particles. It is likely a more complex model is required for analyses that include protons in the reference multiplicity. However, the definition of `FxtMult3` excludes elastically-scattered protons and the elastic cross section can be ignored. The inelastic nucleon-nucleon cross section used for the $\sqrt{s_{NN}}$ = 3.0 GeV data is $\sigma^{pp}_{\text{inel}} = 27.28 \pm 0.76(\text{stat.}) \pm 0.3(\text{syst.})$ taken from the PDG summary tables, where $\sigma^{pp}_{tot} = 42.68 \pm 0.04(\text{stat.}) \pm 0.3(\text{syst.})$ and $\sigma^{pp}_{\text{el}} = 15.32 \pm 0.76(\text{stat.} + \text{syst.})$ [74].

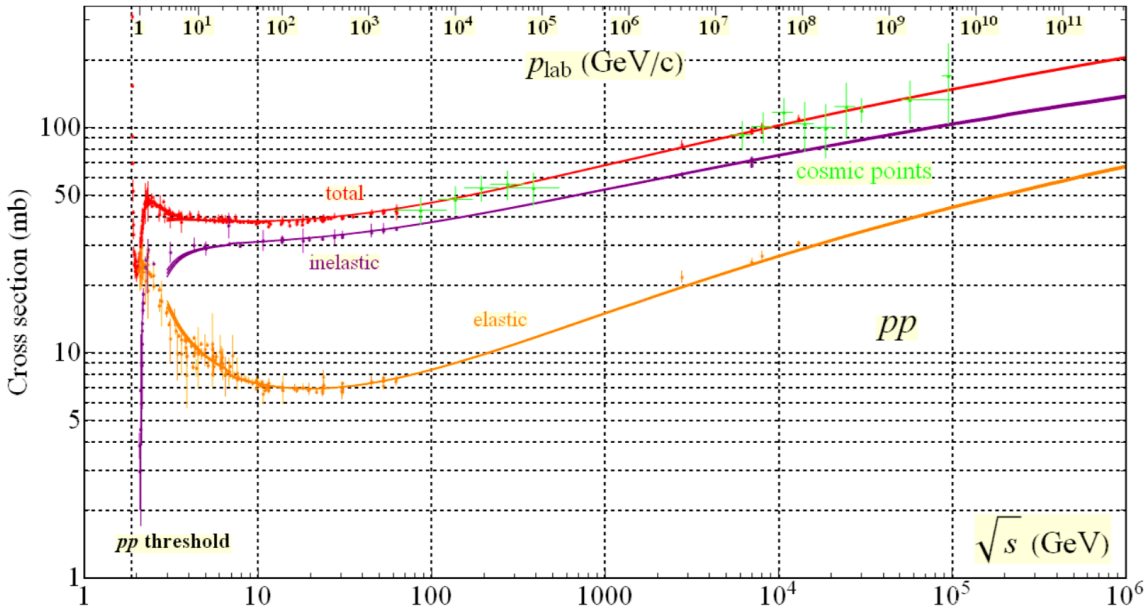


Figure 3.9. $p+p$ cross section versus $\sqrt{s_{NN}}$ (GeV)/projectile momentum ($p_{lab}$ GeV/$c$). Elastic, inelastic and total cross sections are highlighted in orange, purple and red, respectively. Data and figure obtained from PDG [74].

#### 3.3.1.3 Glauber Monte Carlo Procedure

Code to run the Davis Nuclear Group's Glauber Monte Carlo can be found at: `https://bitbucket.org/zsweger/glaubermchardness/src/master/`.

The procedure to generate a GMC event:

1. Randomly populate two gold nuclei,$A = 197$, with nucleons, drawing from $4\pi r^2 \rho(r)$.

2. Randomly select an impact parameter from 0 to $2R$. The distribution of randomly selected impact parameters should be uniform with respect to the area element of a circle ($2\pi bdb$) of radius $2R$, see figure 3.10. Figure 3.1 shows the definition of impact parameter. A distribution of impact parameters is shown in Fig. 3.12.

3. Place nuclei at impact parameter and count the number of overlapping nucleons and the number of binary collisions ($N_{\text{part}}$ and $N_{\text{coll}}$) in the transverse plane.

In the above procedure, the definition of overlap is $d < \sqrt{\sigma_{\text{inel}}^{NN}/\pi}$, where $d$ is the distance between the nucleons in the transverse plane and $\sigma_{\text{inel}}^{NN}$ is the nucleon-nucleon inelastic cross section.

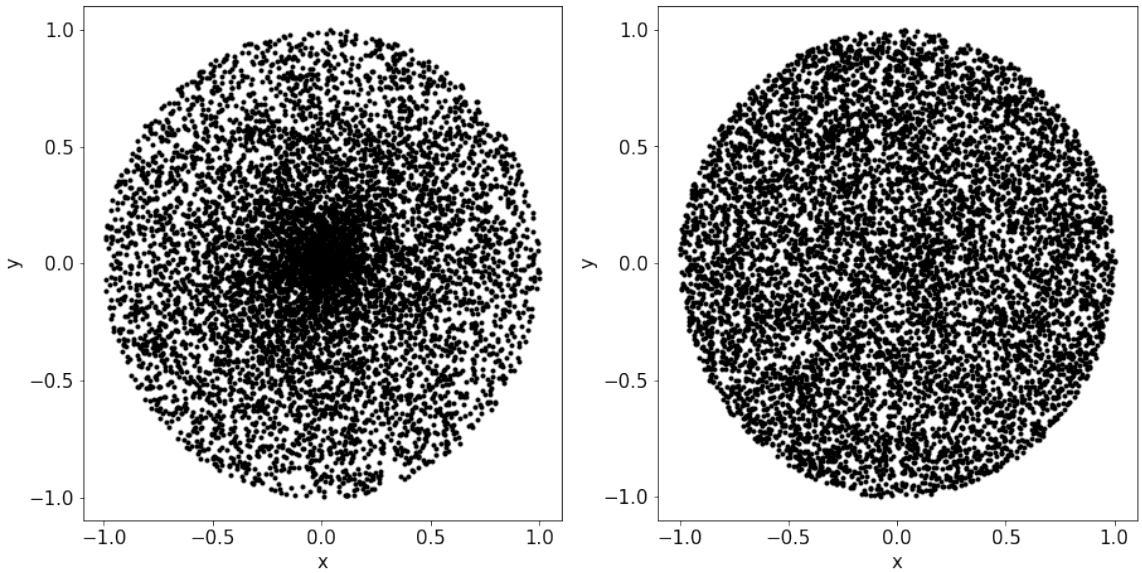


Figure 3.10. An example plot of selecting points on a disk. The left plot incorrectly selects a radius $r$ from 0 to 1 and a $\theta$ from 0 to $2\pi$. This causes an increased density at the center of the circle. The right plot correctly selects a radius $r^2$ from 0 to 1 and a $\theta$ from 0 to $2\pi$.

The output[2] ($N_{\text{part}}$, $N_{\text{coll}}$, and $b$) cannot be related to the reference multiplicity `FxtMult3`. The GMC calculates the probability of interaction but does not generate a final state particle multiplicity. Therefore, estimating the centrality requires an additional particle production model.

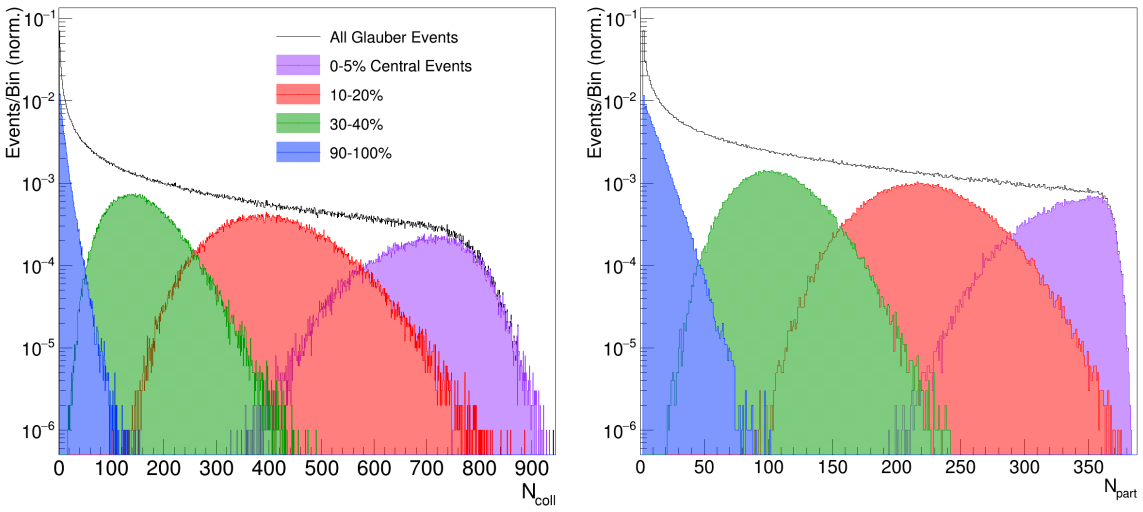


Figure 3.11. $N_{\text{part}}$ (left) and $N_{\text{coll}}$ (right) distributions shown for Glauber Monte Carlo events. Distributions are normalized to unity and shown for various event centralities: 0-5%, 10-20%, 30-40% and 90-100%.

### 3.3.2 Particle Production Model

The model assumes that particles are produced from either soft or hard collisions, in which the total collision energy produced is $E_{\text{tot}} \propto E_{\text{hard}} + E_{\text{soft}}$ [85]. The hard collisions scale with the total number of overlapping collisions and the energy of the system ($E_{\text{hard}} = \sqrt{s_{NN}} N_{\text{coll}}$), while the soft collisions scale with the energy density $\epsilon$ and volume $V$ of the colliding system ($E_{\text{soft}} = \epsilon V$). If one assumes that the volume of the system is proportional to the overlapping nucleons $V \propto N_{\text{part}}$ and the energy per nucleon is proportional to the energy density $\sqrt{s_{NN}}/2 \propto \epsilon$ and $E_{\text{soft}}$ is $\sqrt{s_{NN}} N_{\text{part}}/2$. Together, the total energy is $E_{\text{tot}} \propto \sqrt{s_{NN}}(x N_{\text{coll}} + (x-1)N_{\text{part}}/2)$, in which $x$ is the scaling between hard and soft particle production. Assuming the total energy is proportional to the particle production,

[2]The produced $N_{\text{part}}$, $N_{\text{coll}}$ and $b$ from the GMC are shown in black in Figs. 3.11 and 3.12.

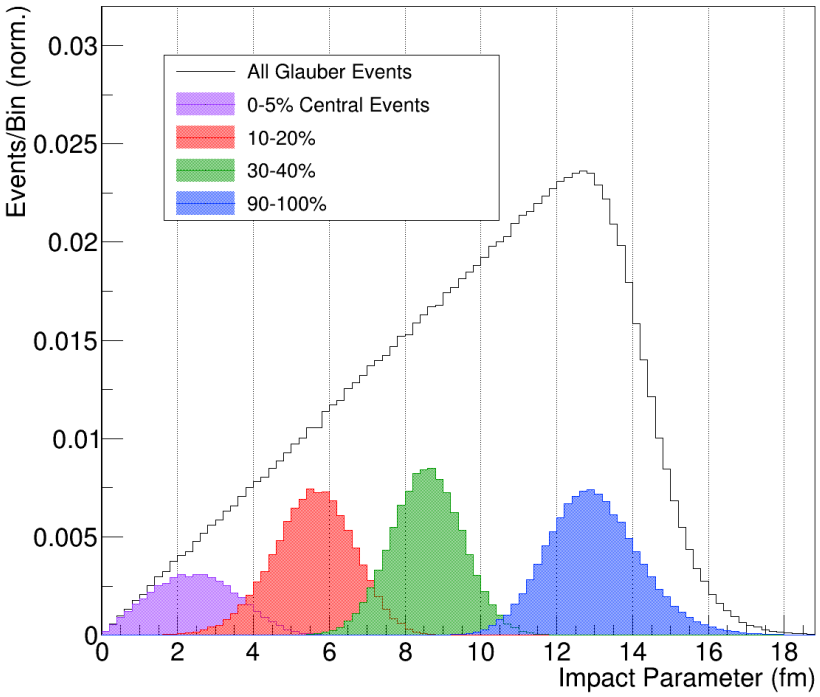


Figure 3.12. Impact parameter distribution shown for Glauber Monte Carlo events. Distribution is normalized to unity and shown for various event centralities: 0-5%, 10-20%, 30-40% and 90-100%.

then the energy ($E_{tot}$) can be converted to the total number of produced particles $N_{\rm ch}$ as

$$N_{ch} = n_{pp}\left(xN_{\rm coll} + (1-x)\frac{N_{\rm part}}{2}\right) \tag{3.2}$$

where $n_{pp}$ is the particle multiplicity of a $p+p$ collision at the same energy per nucleon of the studied system ($\sqrt{s_{NN}} = 3.0$ GeV). This method is known as the two component model [85]. It relies on a few assumptions such as an equivalence between nucleon-nucleon collisions and $p+p$ collisions, and a strict distinction between hard and soft collisions. The methodology agrees well with observed multiplicities at a wide range of energies [86].

The two component model converts the $N_{\rm part}$ and $N_{\rm coll}$ obtained from the Glauber Model to a total multiplicity. It has two free parameters: the event-by-event $p+p$ multiplicity $n_{pp}$ and the hardness parameter $x$. This analysis uses a negative binomial distribution (NBD) to simulate the $p+p$ multiplicity distribution. The UA5 collaboration has demonstrated that $p+p$ multiplicity distributions at 200 and 900 GeV are well described by an NBD, see Fig. 3.13.

An NBD$(n,k)$ describes the number of successes $(n)$ from identical Bernoulli trials before a number of failures occur $(k)$. In this context, the number of successes is the number of generated particles $n_{pp}$ and the $k$ parameter is related to the particle dispersion [87] $D^2 = \langle n_{pp}^2 \rangle - \langle n_{pp} \rangle^2$ by

$$\frac{D^2}{\langle n_{pp} \rangle^2} = \frac{1}{\langle n \rangle} + \frac{1}{k}. \tag{3.3}$$

In full, the NBD for particle production is

$$NBD_{n_{pp}k}(n_{pp}, \langle n_{pp} \rangle, k) = \binom{n_{pp}+k-1}{k-1} \left[ \frac{\langle n_{pp} \rangle / k}{1 + (\langle n_{pp} \rangle / k)} \right]^{n_{pp}} \frac{1}{[1 + (\langle n_{pp} \rangle / k)]^{n_{pp}}}, \tag{3.4}$$

where in the NBD model, the particle multiplicity, $n_{pp}$, is the number of successes produced before $k$ failures. Here, $\langle n_{pp} \rangle$ is the average number of produced particles.

Double NBDs have been considered as alternatives to the single NBD [88], describing particle production from two separate sources. This could be useful for the `FxtMult` reference multiplicity where midrapidity particle multiplicity has two sources, thermal particle production, and scattered participant nucleons (protons). Because `FxtMult3` excludes protons, a single particle source (single NBD) is appropriate.

Lastly, the hardness parameter $x = 0.06$ is obtained by scanning different $x$ values and minimizing a chi-squared $(\chi^2)$ test. The small hardness parameter at $\sqrt{s_{NN}} = 3.0$ GeV is expected.

### 3.3.3 Simulated Detector Efficiency

The NBD takes the Glauber Monte Carlo model output and generates a simulated particle multiplicity distribution. A final caveat is that the reference multiplicity distribution (`FxtMult3`) is uncorrected and should not be directly compared to the NBD result. One should consider the detector efficiency and acceptance effects to the NBD particle multiplicity. Therefore, an efficiency[3] function is generated by placing UrQMD events into a fast detector model. The fast model is a simple Monte Carlo that assumes a binomial detector efficiency with a detection probability $p$. The parameter $p$ varies with $p_T$ and $\eta$ and is calculated from the STAR GEANT detector model. An overview of the STAR GEANT efficiency is discussed in section 5.2. Figure 3.14 shows the raw input UrQMD

[3]Here, "Efficiency" is both detector efficiency and acceptance of the particle $4\pi$ yield.

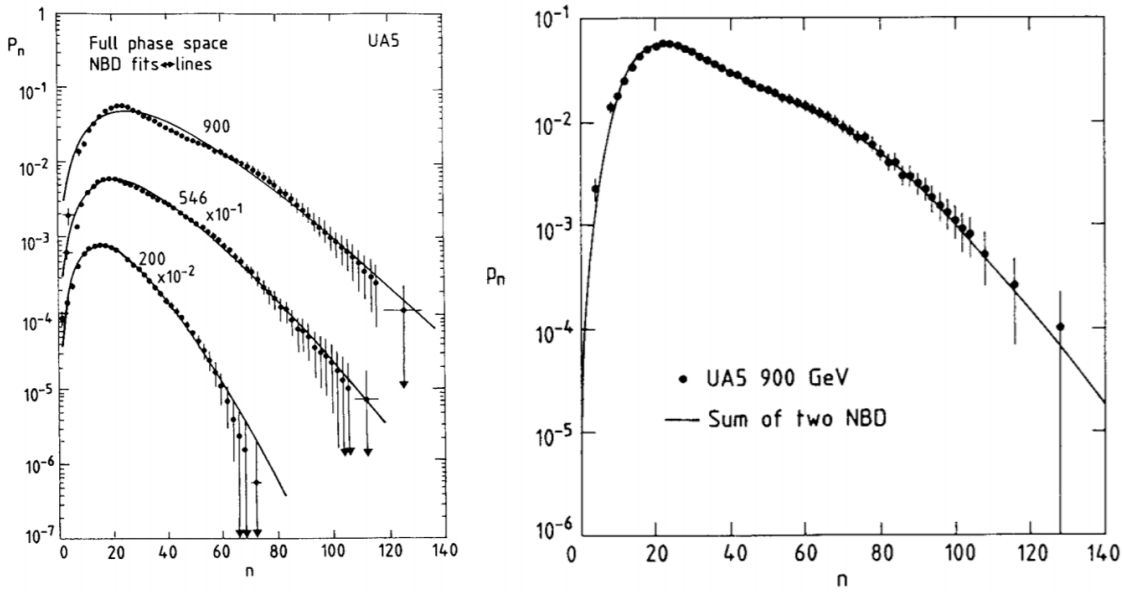


Figure 3.13. Left panel: Negative binomial distribution fit to three energies. Right panel: Double negative binomial distribution. Double NBDs have been considered as alternatives to the NBD. Figure from Ref. [88].

events and the UrQMD "detected" events. The efficiency is calculated by dividing the detected UrQMD events by the input UrQMD events. The pion and Kaon yield is used to approximate `FxtMult3`. Figure 3.15 shows the efficiency as a function of $\langle$`FxtMult3`$\rangle$. A linear fit is applied to interpolate that efficiency at all values of `FxtMult3`.

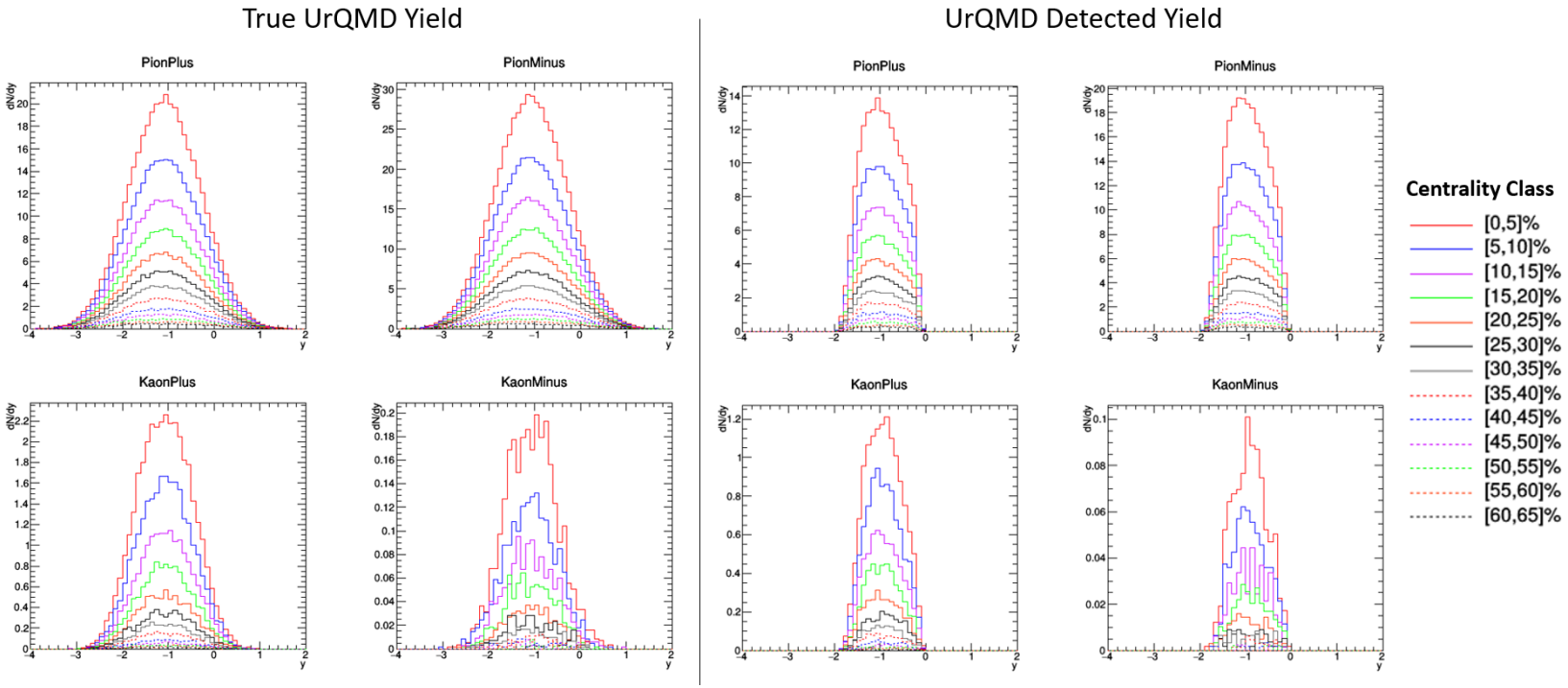


Figure 3.14. Left figures are the true $4\pi$ yield of UrQMD. Right figures are accepted UrQMD particles, where an acceptance $\times$ efficiency model is applied.

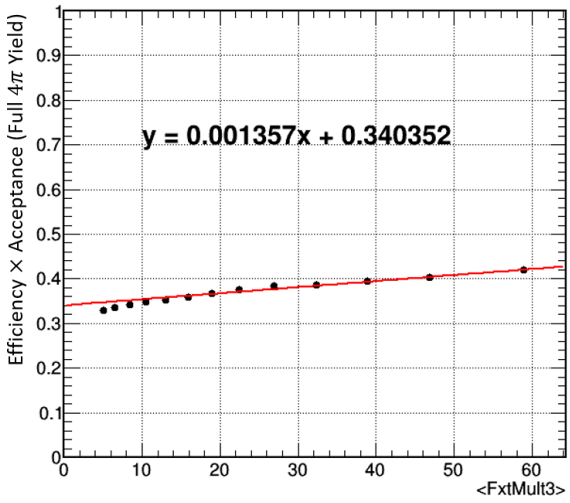


Figure 3.15. Detector Acceptance × Efficiency as a function of `FxtMult3`.

### 3.3.4 Glauber Model + Negative Binomial Distribution

In summary, the GM generates distributions of $N_{\text{part}}$, $N_{\text{coll}}$ and $b$. A two component model and a NBD are used to simulate the particle multiplicity distribution. The simulated multiplicity is piped into a detector model and the free parameters of the NBD $n_{pp}$ and $k$ are randomly sampled to generate an array of simulated multiplicity distributions. The optimal $n_{pp}$ and $k$ are selected by a performing a chi-squared test. Figure 3.16 shows the Glauber + Negative Binomial fit to the reference multiplicity `FxtMult3`. The chi-squared test is performed over a reference multiplicity of twenty to eighty ($20 <$ `FxtMult3` $< 80$). Below multiplicities of twenty, there is a significant drop in the event count. This is due to trigger bias in the data collection. At high multiplicities above eighty, again, there is a disagreement between the data and the model fit. This is due to double collisions in the data (pile up). Below 80, the pile up contamination makes an insignificant[4] contribution to the centrality determination and does not affect the fitting procedure.

To determine the centrality classes, the GM + NBD histogram is integrated and divided into centrality bins (table 3.1). Red dotted lines indicate the centrality bins on Fig. 3.16. The black dashed line is the upper pile up cut at `FxtMult3` $= 80$. The 50-60% centrality bin ($4 \leq$ `FxtMult` $< 6$) is the lowest measured centrality. With the centrality

[4]The pile up is a $\sim 0.5\%$ background effect at all multiplicities but dominates above `FxtMult` $> 80$. Pile up has a large effect on the measured proton cumulants, which is discussed in section 6.2.

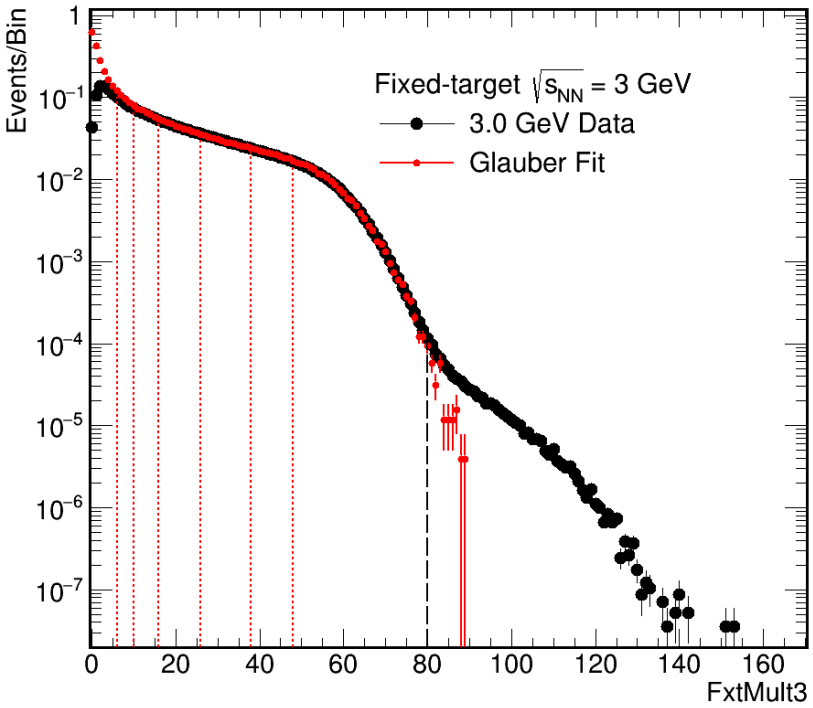


Figure 3.16. `FxtMult3` fit with the Glauber Model + Negative Binomial Distribution. The lowest cut ($N_{\text{ch}} = 4$) is omitted for clarity.

classes and Glauber Model, one can calculate $\langle N_{\text{part}} \rangle$, $\langle N_{\text{coll}} \rangle$ and $\langle b \rangle$ as seen in Fig. 3.11 and in table 3.1.

| % Central | $N_{\text{ch}}$ Cut | $\langle N_{\text{part}} \rangle$ | $\langle N_{\text{coll}} \rangle$ | $\langle b \rangle$ (fm) |
|---|---|---|---|---|
| 0-5 | 48 | $326 \pm 11$ | $679 \pm 24$ | $2.5 \pm 0.3$ |
| 5-10 | 38 | $282 \pm 8$ | $562 \pm 23$ | $3.9 \pm 0.2$ |
| 10-20 | 26 | $219 \pm 8$ | $409 \pm 17$ | $5.5 \pm 0.3$ |
| 20-30 | 16 | $157 \pm 7$ | $259 \pm 16$ | $7.2 \pm 0.3$ |
| 30-40 | 10 | $107 \pm 5$ | $157 \pm 9$ | $8.6 \pm 0.2$ |
| 40-50 | 6 | $70 \pm 5$ | $92 \pm 6$ | $9.7 \pm 0.2$ |
| 50-60 | 4 | $47 \pm 5$ | $56 \pm 7$ | $10.6 \pm 0.4$ |

Table 3.1. Glauber results for each centrality class.

# Chapter 4

# Data Collection, Storage and Selection

This analysis is performed on the first dedicated fixed-target run at RHIC. From May 31$^{\text{st}}$ to June 4$^{\text{th}}$ 2018, the STAR detector triggered on 320 million $\sqrt{s_{NN}} = 3.0$ GeV events. To remove poor-quality data, several checks are performed on both track and event variables. Additionally, due to the sensitivity of the higher-order cumulants, runs or periods of data taking with unusual event and track values are removed. This chapter will outline the procedure for both data collection and storage and the outlier rejection of runs. Additionally, the track and event selection criteria and the selected kinematic acceptance for the proton analysis are covered.

## 4.1 Data Collection

While the experiment is running, raw data from each detector subsystem are recorded in a data acquisition or "DAQ" file. The raw output DAQ files have a large data footprint and therefore are saved on the High Performance Storage System (HPSS), a magnetic tape system. Before a physics analysis can be performed, the "DAQ" file is parsed and calibrated to extract the detector measurements. This includes the TPC track reconstruction process discussed in section 2.2.1. The output from the parsed "DAQ" file is saved in two different "physics ready" file formats: the MuDST and the picoDst. Both file formats are based on the ROOT CERN TTree class [89], in which event information is stored in a

data tree or a list of independent columns (branches). The tree format is well suited for an event-based analysis, allowing for fast retrieval of event and track information. The MuDST is designed to include all quality assurance and calibration information for all detector subsystems and therefore is a more general purpose file format. The picoDst however, is a reduced version of the MuDST and contains more commonly used event and track information. Both the picoDst and MuDST files are stored on the RHIC Computing Facility (RCF). For the proton analysis, it was a priority to run the analysis on a short time scale (less than a day) and store all of the data on a personal computer. Therefore, to further reduce the data footprint, analyzers designed the femtoDst, a reduced picoDst file which only contains event and track information necessary for the proton cumulant analysis. The total picoDst and femtoDst file sizes for the $\sqrt{s_{NN}} = 3.0$ GeV data are $\sim 4.0$ TB and $\sim 127$ GB, respectively. Table 4.1 and 4.2 outline the femtoDst event and track data structure. When possible, event and track variables are saved as char (1 byte) or short integers (2 bytes) to reduce the file size. Using integers reduces the precision of some track variables such as track momentum and DCA. For example, the components of track momentum ($P_x$, $P_y$, $P_z$) values are stored as integers in units of MeV/$c$. Similarly, the DCA values are stored as integers in units of 10 $\mu$m.

## 4.2 Run Selection

From May 31$^{\text{st}}$ to June 4$^{\text{th}}$, 320 million triggers were recorded. The run numbers span from 19151029 to 19155022 for a total of 191 physics runs. Due to the sensitivity of the higher-order cumulants, runs with unusual fluctuations are removed. To identify the poor quality runs, track and event variables averaged over a run are studied.Here, the $\langle ... \rangle$ brackets denote an average over the run. This includes $\langle$`FxtMult`$\rangle$, $\langle V_r \rangle$, $\langle V_z \rangle$, $\langle \eta \rangle$, $\langle \phi \rangle$, $\langle$DCA$\rangle$, and $\langle p_T \rangle$. An example of a run-averaged variable, $\langle p_T \rangle$, is shown in Fig. 4.1. To reject outliers, an iterative procedure is used. First, the RMS is calculated for each run-averaged variable. Next, the runs outside 3×RMS from the mean are removed. The process is repeated until all data points outside the 3×RMS cut are removed. Figure 4.1 plots the various re-calculations of 3×RMS in red. Most of the runs removed during

| FemtoDst Event Information | | |
|---|---|---|
| Branch Name | Data Type | Variable Description |
| RunID | integer | Event run number (19151029 – 19155022) |
| `FxtMult` | short | Uncorrected charged track multiplicity ($-2 < \eta < 0$) |
| `FxtMultTofMatch` | short | `FxtMult` with TOF match required |
| `FxtMult3` | short | `FxtMult` with $\lvert N_{\sigma,p}\rvert < 3$ required |
| Vz | float | $z$ vertex position of the event |
| Vxy | short | Transverse vertex position of the event from the beam spot ($\sqrt{(V_x)^2 + (V_y - 2)^2}$) |
| nMip | float | Number of minimum ionizing particles in the EPD |
| PiPDu | short | Number of TOF identified $\pi^{+/-}$, $p^{+/-}$ and d |
| FemtoTrackArray | FemtoTrack[`FxtMult`] | Array of femto tracks |

Table 4.1. FemtoDst event structure.

the iterative procedure are before run index 110, which indicates a period of poor run conditions. In the beginning of the fixed-target run, beam operators experienced problems with the beam injection, which likely caused the large event and track fluctuations. These runs are noticeably shorter in time, averaging twenty to thirty minutes. Therefore to eliminate the potential background, the first two and a half days are eliminated from the data set. After all cuts, the analysis includes 72 high quality runs.

| FemtoDst Track Information | | |
|---|---|---|
| Branch Name | Data Type | Variable Description |
| Px | short | Track momentum along the $x$-axis ($P_x$) |
| Py | short | $P_y$ |
| Pz | short | $P_z$ |
| `NHitsFit` | char | Number of TPC spatial hit points used in the Kalman fitting procedure |
| DcaX | short | Distance of closest approach along the $x$-axis ($\mathrm{DCA}_x$) |
| DcaY | short | $\mathrm{DCA}_y$ |
| DcaZ | short | $\mathrm{DCA}_z$ |
| NSigmaProton | short | $N_{\sigma,p}$ (See Eq. (2.3)) |
| NSigmaPion | short | $N_{\sigma,\pi}$ |
| TofMass | short | Particle mass using the TOF |
| TofT0 | short | Difference in TOF and TPC calculated time-of-flight |

Table 4.2. FemtoDst track structure.

## 4.3 Event Selection

The fixed-target $\sqrt{s_{NN}} = 3.0$ GeV Au+Au minimum bias trigger requires a hit in either the EPD or BBC detector and three or more hits in the TOF detector. The EPD/BBC are both fast detectors and therefore ideal trigger detectors. The additional TOF requirement reduces the background rate. As seen from the centrality study in chapter 3, the trigger bias drastically increases below the 50-60% centrality classes, see Fig 4.2.

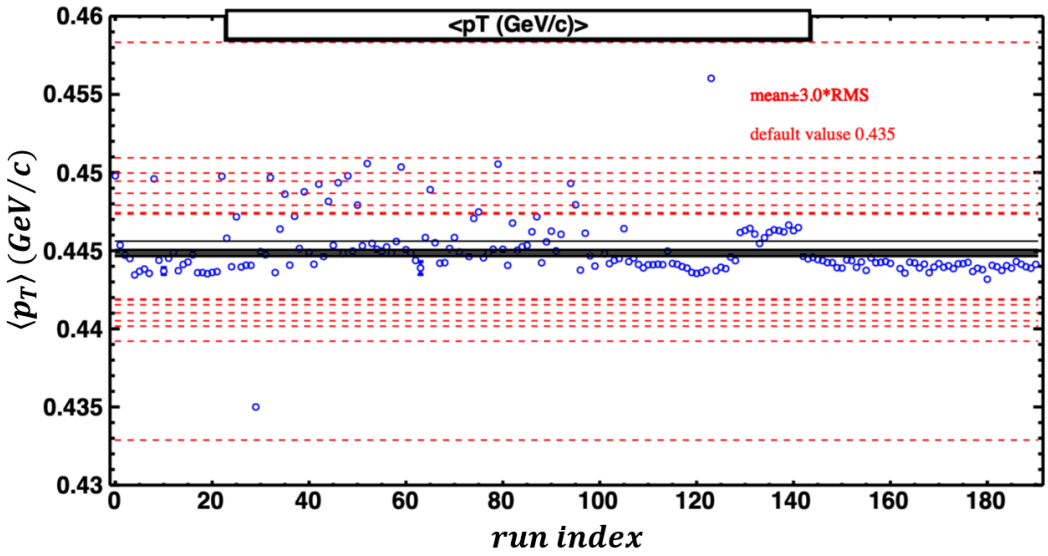


Figure 4.1. The transverse momentum of each track is averaged over the run as a function of the run index. An outlier rejection is applied to the runs outside 3×RMS from the mean average. Plot provided by Guannan Xie.

### 4.3.1 Vertex Selection

The fixed target is placed at 200.7 cm from the center of the TPC along the beam line and the beam spot is centered 2 cm below the center of the beam pipe. Within a fraction of a millimeter, all fixed-target vertices are located at $(0.0, -2.0, 200.7)$ in the STAR coordinate system[1]. To remove potential collisions with the target-support material and events with incorrect timing information, all events in the analysis require a $z$ vertex location of $199.5 < v_z < 202$ cm and a radial vertex location of $v_r < 1.5$ cm from the center of the beam spot, $v_{x,y} = (0, -2)$ cm. The radial and longitudinal vertex distributions are depicted in the left and right panels of Fig. 4.3. In the figure, a red circle and red lines indicate the event selection criteria.

## 4.4 Track Selection

To ensure that the particle tracks contain the correct $dE/dx$ and momentum information, several track-level cuts are implemented. Below, each track variable and the associated track-quality cut is discussed. Tracks that satisfy the outlined requirements will be re-

[1]The coordinate system is defined in section 2.2.

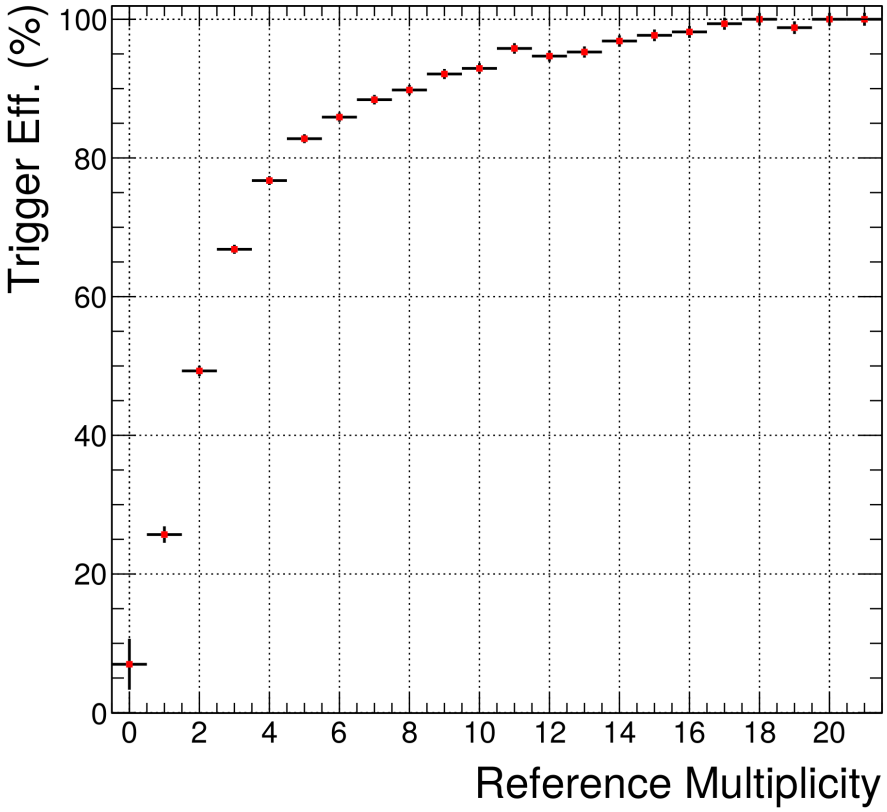


Figure 4.2. Trigger efficiency as a function of reference multiplicity in the low multiplicity region. The efficiency is estimated from the ratio of the multiplicity distributions from the Glauber + two-component model over the data. The lowest centrality bin (50-60%) corresponds to a multiplicity of 4–6.

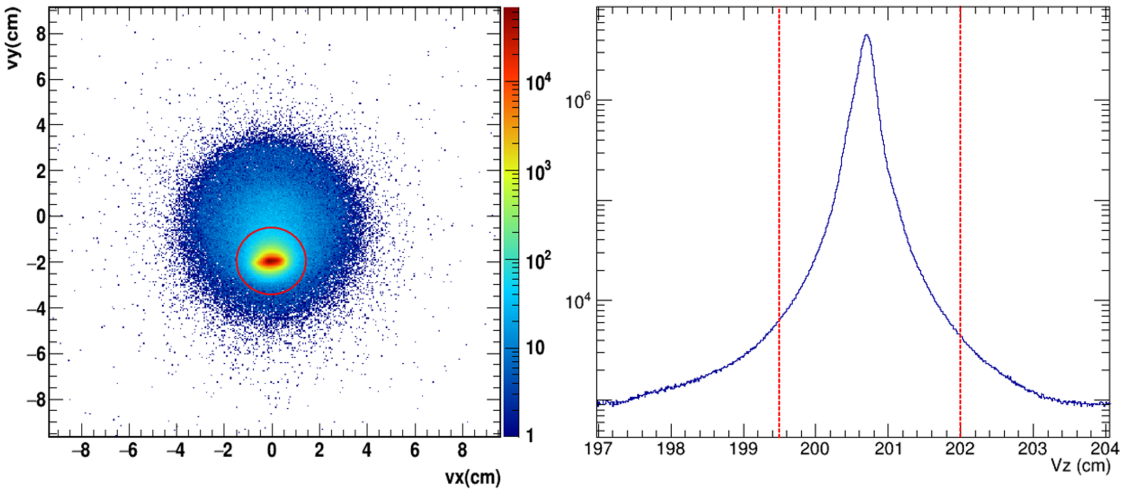


Figure 4.3. Location of the primary vertex for the fixed-target collisions. Left panel: Radial vertex cut ($v_r < 1.5$ cm). The $z$-axis is in a log scale. Right panel: $z$ vertex cut ($199.5 < v_z < 202$ cm).

ferred to as "good" tracks.

### 4.4.1 DCA

As described in chapter 2, the location of an event vertex is determined by projecting the global track helices to the beam line and then searching for track intersections. If multiple tracks intersect within the beam line, a vertex candidate is generated. Then, a vertex ranking algorithm sorts the vertex candidates and defines a primary vertex.

Once the primary vertex location is determined, the minimum distance between a track helix and the vertex position is calculated. If this quantity, the distance of closest approach (DCA) of the track, is below 3.0 cm, the global track is refit with an additional vertex constraint and labelled as a primary track.

In general, tracks with a low DCA ($< 1.0$) are more likely to be associated with the correct vertex and correctly identified as primary tracks. Therefore, by lowering the DCA cut, the background from beam-pipe collisions and secondary decays is decreased. However, lowering the DCA cut will lower the detector efficiency. In the $\sqrt{s_{NN}} = 3.0$ GeV energy regime, the transverse momentum window of the analysis, $0.4 < p_T < 2.0$ GeV/$c$ is expected to remove most secondary decays and beam-pipe interactions. Therefore, an inclusive cut of DCA $< 3.0$ cm is selected. To test the dependence of the DCA cut, the analysis is repeated with different maximum DCA values from 1.0 to 3.0 cm. The left panel of Fig. 4.4 depicts the DCA for both "good" tracks and candidate protons. The difference between the candidate proton and good track DCA distributions is caused by the acceptance cuts applied to the candidate protons ($-0.9 < y < 0$ and $0.4 < p_T < 2.0$ GeV/$c$). In particular, the low $p_T$ tracks of the good tracks have a broader DCA distribution.

### 4.4.2 TPC Spatial Points

#### 4.4.2.1 Minimum `NHitsFit`

To generate tracks, the collection of TPC spatial points are fit with a Kalman fitting procedure, which iteratively fits particle helices. The number of spatial points used to fit each helix is referred to as `NHitsFit`. The right panel of Fig. 4.4 shows the `NHitsFit` distribution for both "good" tracks and analysis protons. Similar to the DCA, the differ-

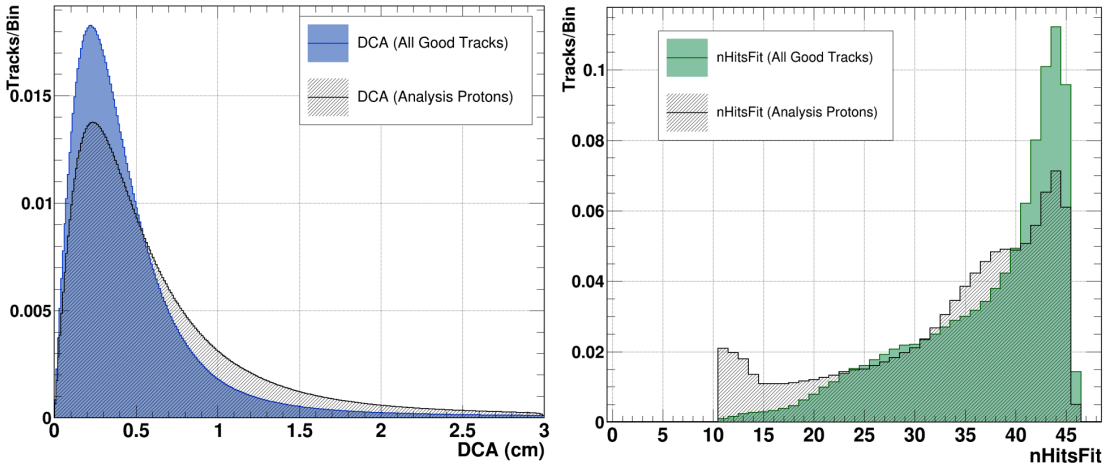


Figure 4.4. Left panel: DCA for "good" primary tracks and analysis protons. Right panel: `NHitsFit` for "good" primary tracks and analysis protons.

ences between the candidate proton and good track `NHitsFit` distribution is caused by the acceptance cuts applied to the candidate protons ($-0.9 < y < 0$ and $0.4 < p_T < 2.0$ GeV/$c$). In particular, the high $y$ tracks near the edge of the TPC have low `NHitsFit` values. The helix fitting procedure requires at least five spatial points which corresponds to the five degrees of freedom of a helix. In general, tracks with a greater number of `NHitsFit` will have an improved momentum resolution. Therefore, placing a cut on the minimum number of `NHitsFit` will increase the overall track quality. However, requiring a high `NHitsFit` will limit the low $p_T$ acceptance and decrease the detector efficiency. All tracks are required to have at least 10 fit points (`NHitsFit` $> 10$). To test the dependence of the minimum `NHitsFit`, two systematic studies are performed in which the minimum `NHitsFit` is increased to 12 and 15.

#### 4.4.2.2 Split Tracks

During reconstruction, a single charged particle can be incorrectly identified as two separate tracks. A useful quantity to help identify duplicate, or split, tracks is the maximum number of possible `NHitsFit` (`NHitsPoss`). This value (`NHitsPoss`) is well defined by the kinematics of the track. If a track passes through the central region of the TPC, the maximum number of spatial points is the number of pad rows (45). A high pseudorapidity track that exits out the endcap of the TPC will have a lower `NHitsPoss`. By requiring all

tracks to have `NHitsFit/NHitsPoss` $> 0.52$, duplicate tracks are eliminated.

### 4.4.3 TOF Requirements

To determine the quality of a hit on a TOF pad, the hit position is expressed in the local coordinate system of the TOF pad active area. The accuracy of the timing information decreases at the edge of the TOF pad, and cuts are placed in the local coordinate system to remove mismatched tracks.

The particle time-of-flight is used to distinguish the particle species of high momentum tracks. The time-of-flight is calculated using both the TPC and TOF detector systems. The mass-squared value of a TOF-matched track is calculated following the procedure outlined in chapter 2. To identify protons, a mass-squared cut of $0.6 < m^2 < 1.2$ $(\mathrm{GeV}/c)^2$ is required for all proton candidates above $|p| > 2.0$ GeV/$c$.

## 4.5 Proton $dE/dx$ Study

With both the track $dE/dx$ from reconstruction and the Bichsel predictions for each particle of interest, the $N_{\sigma,i}$ value can be calculated (see Eq. (2.3)) for each track, where $i$ is the particle species. If the TPC $dE/dx$ calibrations are correct, the $N_{\sigma,i}$ for a given species closely resembles a Gaussian distribution with the Gaussian centroid located at zero. The $N_\sigma$ distribution allows one to determine the probability of a track being a particular species and for the proton analysis, protons are required to be within $|N_{\sigma,p}| < 3$. However, as seen in Fig. 4.5, the centroid of the proton $N_{\sigma,p}$ distribution is offset from zero, which indicates an issue with the calibration. To fix the issue, the protons are binned by momentum and the offset is measured. With the measured offset, all track $N_{\sigma,p}$ values are adjusted as a function of momentum. Additionally with this method, one can estimate the proton purity. The pion and Kaon contamination is estimated by projecting the negatively charged tracks onto the positive $N_{\sigma,p}$ distribution.

At the energy $\sqrt{s_{NN}} = 3.0$ GeV, in which anti-protons are negligible, the negative pions and Kaons are relatively clean. In addition, if one assumes the positive and negative pion and Kaon spectra to be more or less equivalent,[2] the proton purity within $|N_{\sigma,p}| < 3$

[2]The $\pi^+/\pi^-$ ratio is less than one, therefore our estimate is conservative.

is greater than 96% at track momenta less than 2.0 GeV/$c$. Above 2.0 GeV/$c$, the proton yield drops along with the estimated purity. This coincides with the deuteron $dE/dx$ band merging with the proton band, which adds additional contamination. This deuteron merging can be seen in Fig. 4.5, where the two left-most peaks in black begin to merge as the momentum range increases. Therefore above 2.0 GeV/$c$, all proton candidate tracks are required to have a TOF matched hit and a mass-squared value between 0.6 and 1.2 (GeV/$c$)$^2$. The center panel of Fig. 4.6 show the $dE/dx$ as a function of squared mass for all positively charged tracks. A red dashed box indicates the proton requirements for tracks with momentum above 2.0 GeV/$c$.

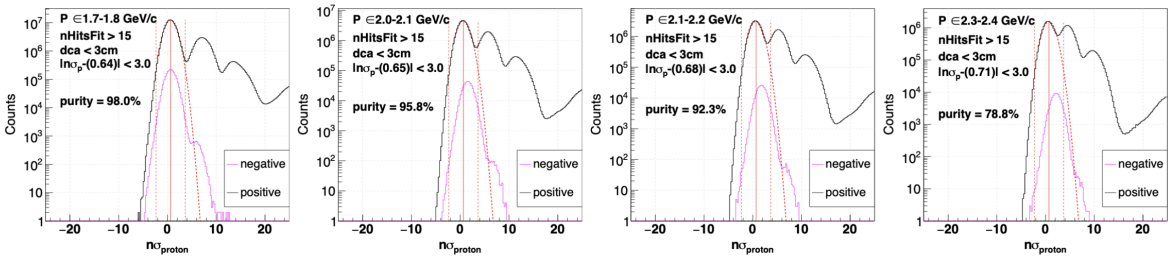


Figure 4.5. Proton track candidate $N_\sigma$ binned by momentum. A non-zero centroid indicates an offset in the TPC $dE/dx$ calibration. The proton peak is centered around zero. The peaks of the black distribution from left to right are the proton, deuteron, and triton bands, respectively. The pink distribution from left to right is the negative pion and negative kaon bands, respectively. The ratio of the area of the pink curve over the area of the black curve within $3\sigma$ around zero provides an estimate of the proton purity.

## 4.6 Analysis Acceptance

The kinematic acceptance for the proton cumulant analysis can have large effects on the measured particle correlations [90–93]. If the acceptance window is too small, the correlations are expected to vanish. If the window covers a large fraction of the proton distribution, the fluctuation is suppressed as the baryon number cannot fluctuate in the $4\pi$ yield due to baryon number conservation. In this study, the rapidity within $-0.5 < y < 0$ is selected as the nominal rapidity window, roughly half the measurable acceptance of $-0.9 < y < 0.1$. All proton candidates are required to have a transverse momentum within $0.4 < p_T < 2.0$ GeV/$c$. The lower transverse momentum limit is selected due

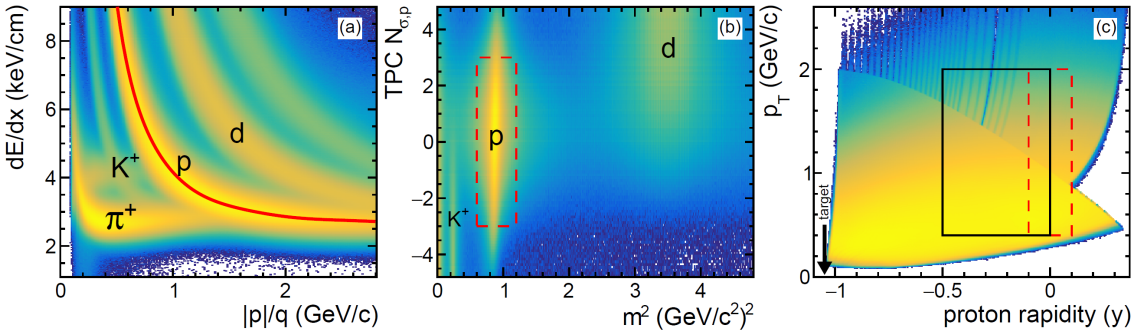


Figure 4.6. Left Panel (a): $dE/dx$ vs. particle rigidity measured in the TPC; pion, Kaon, proton and deuteron bands are labeled. The proton Bichsel curve is plotted in red. Center Panel: (b) TPC $N_{\sigma,p}$ vs mass-squared measured in the TPC and TOF. Kaon, proton and deuteron peaks are labeled. The red dashed box indicates analysis protons above $|p| > 2.0$ GeV/$c$. Right Panel (c): Accepted protons as a function of transverse momentum and proton rapidity ($y$) in the center-of-mass frame Au+Au collisions at $\sqrt{s_{NN}} = 3.0$ GeV. The black box indicates acceptance for rapidity $-0.5 < y < 0$ and momentum $0.4 < p_T < 2.0$ GeV/$c$. The red dashed box indicates a narrower rapidity window $|y| < 0.1$, the largest possible symmetric rapidity window from this data set.

to the drop in tracking efficiency and the increased $\Lambda$ baryon yield below 0.4 GeV/$c$. The high 2.0 GeV/$c$ limit is placed to remove hard-scattered protons[3]. Additionally, the nominal acceptance window is the most similar to the previous BES-I analysis[4] and is used for comparison to the BES-I data.

To study the effect of the selected kinematic acceptance, both the rapidity and transverse momentum are varied. These results are presented in section 9. The rapidity dependence ($y_{min} < y < 0$), $y_{min}$ is varied from $-0.9$ to $-0.2$ with a transverse momentum range of $0.4 < p_T < 2.0$ GeV/$c$. The transverse momentum is $0.4 < p_T < p_T^{max}$, where $p_T^{max}$ is varied from 0.8 to 2.0 GeV/$c$ within the rapidity range of $-0.5 < y < 0$.

[3]Hard-scattered protons may affect the proton cumulants at higher BES-I energies but are unlikely to affect the cumulants at the lowest BES-I energies and the fixed target $\sqrt{s_{NN}} = 3.0$ GeV.

[4]BES-I used a symmetric acceptance window $|y| < 0.5$ with the same transverse momentum $0.4 < p_T < 2.0$ GeV/$c$.

# Chapter 5

# Detector Performance Corrections

If one could measure all particles and generate an event-by-event probability distribution $P(N)$, the cumulant calculation would be trivial. One could simply take the true net-proton distribution in the kinematic region of interest and measure the moments, in which the $i^{\text{th}}$ moment is defined as $\langle N^i \rangle$. From the moments of the distribution, the cumulants can be algebraically constructed

$$C_i = \sum_{k=1}^{n} (-1)^{k-1}(k-1)! B_{n,k}(\langle N \rangle, .... \langle N^{n-k+1} \rangle) \tag{5.1}$$

where $B_{n,k}$ are the incomplete Bell polynomials.

In a real experiment, however, measurements are subject to efficiency and background effects that make the true $P(N)$ unobtainable. Therefore, a sensible methodology must be established to extract $P(N)$ from the measured net proton distribution $\widetilde{P}(N)$. The following section will cover the efficiency correction techniques used in the proton cumulant analysis and methods of estimating the detector efficiency.

## 5.1 Efficiency Correction Technique

### 5.1.1 Constant Efficiency Correction

In the fixed target $\sqrt{s_{NN}} = 3.0$ GeV analysis, a "track-by-track" efficiency correction method [94, 95] is used. However, before the "track-by-track" efficiency correction is discussed, let us start with a simple efficiency correction, which assumes a constant efficiency. In addition, all efficiency correction techniques discussed assume that the STAR detector

has a binomial detector response, such that a track being detected does not affect the probability of an adjacent track being detected. At the highest collider energies, in which track densities affect the detector performance, analyzers were concerned that the detector response appeared non-binomial. Therefore, tests of different non-binomial detector corrections were performed [96]. The effect was minimal and is diminished at the lower collision energies [97].

To extract the true net-proton multiplicity distribution $P(N)$, from a measured net-proton distribution $\widetilde{P}(n)$, one can define

$$\widetilde{P}(n) = \sum_{N} P(N) B_{p,N}(n) \tag{5.2}$$

where $B_{p,N}(n)$ is the binomial efficiency

$$B_{p,N}(n) = \frac{N!}{n!(N-n)!} p^n (1-p)^{N-n}. \tag{5.3}$$

Here, the constant efficiency or probability of detection is $p$ and the number of measured net-protons is $n$.

It is useful for the efficiency correction to express Eq. (5.2) in terms of factorial cumulants. First, one defines the cumulant generating function of the net-proton probability distribution as

$$K(\theta) = \ln \sum_{N} e^{N\theta} P(N) = \ln \left\langle e^{N\theta} \right\rangle \tag{5.4}$$

where the $m^{\text{th}}$ order cumulant is defined as

$$\left\langle N^m \right\rangle_c = \frac{\partial^m}{\partial \theta^m} K(\theta)|_{\theta=0}. \tag{5.5}$$

Next, the factorial cumulants[1] are defined by changing $e^{N\theta} \Rightarrow s^N$. The factorial cumulant generating function becomes

$$K_f(s) = \ln \left\langle s^N \right\rangle. \tag{5.6}$$

With the generating function, one can evaluate the factorial cumulants

$$\left\langle N^m \right\rangle_{fc} = \frac{\partial^m}{\partial^m} K(s)|_{s=1}. \tag{5.7}$$

[1] A discussion of factorial cumulants and factorial moments can be found in chapter 8.

Additionally, if the factorial cumulants of the binomial distribution are defined as

$$\bar{k}_{p.N}(s) = \ln \sum_n s^n B_{p,N}(n) = N \ln(1 - p + ps), \tag{5.8}$$

the factorial cumulant generating function of $\widetilde{P}(n)$ becomes

$$\begin{aligned}
\widetilde{K}(s) &= \ln \sum_n \widetilde{P}(n) s^n = \ln \sum_N P(N) e^{\bar{k}_{p.N}(s)} \\
&= \ln \sum_N P(N)(q - p + ps)^N \\
&= K_f(1 + p(s-1)).
\end{aligned}$$

With the cumulants of $\widetilde{P}(n)$ evaluated, one has a the relation between the measured factorial cumulants and true factorial cumulants

$$\frac{\partial^m}{\partial^m} \widetilde{K}(s)|_{s=1} = p^m \frac{\partial^m}{\partial^m} K(s)|_{s=1}. \tag{5.9}$$

This can be simplified to

$$\langle n^m \rangle_{fc} = p^m \langle N^m \rangle_{fc}. \tag{5.10}$$

By converting to factorial cumulants, the relation between the measured and true distribution is trivial. After calculating the true factorial cumulants, one can convert back to cumulants or moments.

With the simple relation 5.10, the true cumulants of $P(N)$ are constructed in four steps:

1. Calculate the cumulants of $\widetilde{P}(n)$.
2. Convert the cumulants of $\widetilde{P}(n)$ into factorial cumulants.
3. Divide the factorial cumulants of $\widetilde{P}(n)$ by the efficiency to the $m^{\text{th}}$ order to generate the factorial cumulants of $P(N)$.
4. Convert the factorial cumulants of $P(N)$ into cumulants.

Using the above procedure, here are cumulants up to the $4^{\text{th}}$ order:

$$\begin{aligned}
\langle N\rangle_c &= \langle N\rangle_{fc} = \frac{1}{p}\langle n\rangle_{fc} = \frac{1}{p}\langle n\rangle_c \\
\langle N^2\rangle_c &= \frac{1}{p^2}\langle n^2\rangle_c + \left(\frac{1}{p} - \frac{1}{p^2}\right)\langle n\rangle_c \\
\langle N^3\rangle_c &= \frac{1}{p^3}\langle n^3\rangle_c + \left(-\frac{3}{p} + \frac{3}{p^2}\right)\langle n^2\rangle_c + \left(\frac{1}{p^3} - \frac{3}{p^2} + \frac{1}{p}\right)\langle n\rangle_c \\
\langle N^4\rangle_c &= \frac{1}{p^4}\langle n^4\rangle_c + \left(-\frac{6}{p^4} + \frac{6}{p^3}\right)\langle n^3\rangle_c + \left(\frac{11}{p^4} - \frac{18}{p^3} + \frac{7}{p^2}\right)\langle n^2\rangle_c \\
&\quad + \left(\frac{6}{p^4} + \frac{12}{p^3} - \frac{12}{p^3} - \frac{7}{p^2} + \frac{1}{p}\right)\langle n\rangle_c
\end{aligned}$$

This method is effective but limited due to the constant efficiency requirement. As seen in Fig. 5.5, the efficiency of the STAR detector varies with $p_T$. Thus, let us discuss a multivariate efficiency bin correction.

### 5.1.2 Multivariate Efficiency Bin Correction

Let us extend the probability distribution $P(N)$ to a a multivariate distribution $P(\mathbf{N}) = P(N_1, N_2, ..., N_M)$, where $M$ is the number of discrete acceptance bins and $N_i$ is the number of particles entering the $i^{\text{th}}$ acceptance bin. A similar technique was used in BES I, with four discrete efficiency bins, two bins at low $p_T$ and two at high $p_T$ with separate bins for protons and anti-protons.

In the multivariate case, one can extract $P(N_1, N_2, ..., N_M)$ from $\widetilde{P}(n_1, n_2, ..., n_M)$. Unlike the single efficiency case, the efficiency is now a product of binomial distributions. The measured probability distribution $\widetilde{P}(\mathbf{n})$ can be expressed as

$$\widetilde{P}(\mathbf{n}) = \sum_{\mathbf{N}} P(\mathbf{N}) \prod_{i=1}^{M} B_{p_i,N_i}(n_i). \tag{5.11}$$

To simplify the notation, one can define the linear combination of protons and anti-protons in the $i_{th}$ efficiency bin

$$Q_{(a)} = \sum_{i=1}^{M} a_i N_i \tag{5.12}$$

where $a = 1$ and $a = -1$ for protons and anti-protons, respectively.

A cumulant generating function is defined for $P(\mathbf{N}) = P(N_1, N_2, ..., N_M)$ as

$$K(\theta) = \ln\left[\sum_{\mathbf{N}} e^{\theta_{1i}+...+\theta_M N_M} P(\mathbf{N})\right] \tag{5.13}$$

and the $m^{\text{th}}$ order cumulant of $Q_a$ is

$$\left\langle Q_{(a)}^m \right\rangle_c = \partial_{(a)}^m K(\theta)|_{\theta=0} \tag{5.14}$$

with

$$\partial_{(a)} = \sum_{i=1}^{M} a_i \frac{\partial}{\partial\theta_i}. \tag{5.15}$$

One can expand this definition to include mixed cumulants and measure the correlation between two or three conserved quantities such as net-proton, net-strangeness, and net-charge as

$$\left\langle Q_{(a)}Q_{(b)} \right\rangle_c = \partial_{(a)}^m \partial_{(b)}^m K(\theta)|_{\theta=0} \tag{5.16}$$

or

$$\left\langle Q_{(a)}Q_{(b)}Q_{(c)} \right\rangle_c = \partial_{(a)}^m \partial_{(b)}^m \partial_{(c)}^m K(\theta)|_{\theta=0}. \tag{5.17}$$

Next, the factorial cumulant generating function of the $P(\mathbf{N})$ is defined as

$$K_f(\mathbf{s}) = \ln\left[\sum_{\mathbf{N}} P(\mathbf{N}) \prod_{i=1}^{M} s_i^{N_i}\right] \tag{5.18}$$

and the factorial cumulants are defined as

$$\left\langle Q_{(a)} \right\rangle_{fc} = \bar{\partial}_{(a)}^m K_f(s)|_{s=1} \tag{5.19}$$

with

$$\bar{\partial}_{(a)} = \sum_{i=1}^{M} a_i \frac{\partial}{\partial s_i}. \tag{5.20}$$

The mixed factorials cumulants are

$$\left\langle Q_{(a)}Q_{(b)} \right\rangle_{fc} = \bar{\partial}_{(a)}^m \bar{\partial}_{(b)}^m K_f(s)|_{s=1}. \tag{5.21}$$

With the same substitution $s_i = e^{\theta_i}$ used in the constant efficiency case, a similar relation between cumulants and factorial cumulants is derived. The relation between cumulant and factorial cumulant is

$$\left\langle Q_{(a)} \right\rangle_c = \partial_{(a)} K = \sum_{i=1}^{M} a_i \frac{\partial}{\partial\theta_i} K = \sum_{i=1}^{M} a_i \frac{\partial s_i}{\partial\theta_i} \frac{\partial}{\partial s_i} K_f = \bar{\partial}_{(a)} K_f = \left\langle Q_{(a)} \right\rangle_{fc}. \tag{5.22}$$

For the mixed cumulant case,

$$\begin{aligned}
\left\langle Q_{(a)}Q_{(b)}\right\rangle_c &= \partial_{(a)}\partial_{(b)}K = \left(\sum_{i=1}^{M} a_i\frac{\partial}{\partial\theta_i}\right)\left(\sum_{j=1}^{M} b_j\frac{\partial}{\partial\theta_j}\right)K \\
&= \sum_{i=j=1}^{M} a_i b_j\left(\frac{\partial s_i}{\partial\theta_i}\frac{\partial}{\partial s_i}\right)\left(\frac{\partial s_j}{\partial\theta_j}\frac{\partial}{\partial s_j}\right)K_f \\
&= \left(\sum_{i=1}^{M} a_i\frac{\partial s_i}{\partial\theta_i}\frac{\partial}{\partial s_i}\right)\left(\sum_{j=1}^{M} b_j\frac{\partial s_j}{\partial\theta_j}\frac{\partial}{\partial s_j}\right)K_f + \sum_{i=1}^{M} a_i b_i\frac{\partial^2 s_i}{\partial\theta_i^2}\frac{\partial}{\partial s_i}K_f \\
&= (\bar{\partial}_{(a)}\bar{\partial}_{(b)} + \bar{\partial}_{(ab)})K_f \\
&= \left\langle Q_{(a)}Q_{(b)}\right\rangle_{fc} + \left\langle Q_{(ab)}\right\rangle_{fc}
\end{aligned}$$

where $\theta = 0$ and $s = 1$. $\bar{\partial}_{(ab)}$ and $\left\langle Q_{(ab)}\right\rangle_{fc}$ are

$$\bar{\partial}_{(ab)} = \sum_{i=1}^{M} a_i b_i\frac{\partial}{\partial s_i}, \quad \left\langle Q_{(ab)}\right\rangle_{fc} = \sum_{i=1}^{M} a_i b_i N_i. \tag{5.23}$$

With the factorial cumulant generating function of the product of binomial distributions

$$\widetilde{K}_f(\mathbf{s}) = \ln\sum_{\mathbf{N}} P(\mathbf{N})\prod_{i=1}^{M}(1 + p_i(s_i - 1))_i^N = K_f(\mathbf{s'}) \tag{5.24}$$

where $s_i' = 1 + p_i(s_i - 1)$, one arrives at the multivariate version of Eq. (5.10) and can relate multivariate cumulants to multivariate factorial cumulants

$$\bar{\partial}_{(a)}K_f = \bar{\partial}_{(a/p)}\widetilde{K}_f \tag{5.25}$$

$$\bar{\partial}_{(a)}\bar{\partial}_{(b)}K_f = \bar{\partial}_{(a/p)}\bar{\partial}_{(b/p)}\widetilde{K}_f. \tag{5.26}$$

One can calculate the cumulants of $P(\mathbf{N})$ with cumulants of measured distribution $\widetilde{P}(\mathbf{n})$ as follows

1. Calculate the cumulants of $\widetilde{P}(\mathbf{n})$.
2. Convert the cumulants of $\widetilde{P}(\mathbf{n})$ into factorial cumulants.
3. Convert the factorial cumulants of $\widetilde{P}(\mathbf{n})$ into factorial cumulants of $P(\mathbf{N})$ with the efficiency of the $p^i$ efficiency bin.

4. Convert the factorial cumulants of $P(\mathbf{N})$ into cumulants.

Below are the true cumulants expressed as measured cumulants up to $3^{rd}$ order

$$
\begin{aligned}
\left\langle Q_{(a)} \right\rangle_c &= \left\langle Q_{(a)} \right\rangle_{fc} = \left\langle q_{(a/p)} \right\rangle_{fc} = \left\langle q_{(a/p)} \right\rangle_c \\
\left\langle Q^2_{(a)} \right\rangle_c &= \left\langle Q^2_{(a)} \right\rangle_{fc} + \left\langle Q_{(a^2)} \right\rangle_{fc} = \left\langle q^2_{(a/p)} \right\rangle_{fc} + \left\langle q_{(a^2/p)} \right\rangle_{fc} \\
&= \left\langle q^2_{(a/p)} \right\rangle_c - \left\langle q_{(a^2/p^2)} \right\rangle_c + \left\langle q_{(a^2/p)} \right\rangle_c \\
\left\langle Q^3_{(a)} \right\rangle_c &= \left\langle Q^3_{(a)} \right\rangle_{fc} + 3\left\langle Q_{(a)} Q_{(a^2)} \right\rangle_{fc} + \left\langle Q_{(a^3)} \right\rangle_{fc} \\
&= \left\langle q^3_{(a/p)} \right\rangle_{fc} + 3\left\langle q_{(a/p)} q_{(a^2/p)} \right\rangle_{fc} + \left\langle q_{(a^3/p)} \right\rangle_{fc} \\
&= \left\langle q^3_{(a/p)} \right\rangle_c - 3\left\langle q_{(a/p)} q_{(a^2/p^2)} \right\rangle_c \\
&\quad + 2\left\langle q_{(a^3/p^3)} \right\rangle_c + 3(\left\langle q_{(a/p)} q_{(a^2/p)} \right\rangle_c - \left\langle q_{(a^3/p^2)} \right\rangle_c) \left\langle q_{(a^3/p)} \right\rangle_c .
\end{aligned}
$$

Here, $q_{(a)}$ is defined as

$$
q_{(a^r/p^s)} = \sum_{i=1}^{M} \frac{a_i^r}{p_i^s} n_i, \tag{5.27}
$$

where $p_i$ is efficiency of the $i^{\text{th}}$ acceptance bin and $n_i$ is number of net-protons measured in $i^{\text{th}}$ acceptance bin.

The multivariate efficiency correction method is an improvement over the constant efficiency method 5.5 but can still fail to characterize efficiency distributions that vary drastically [98]. Figure 5.1 shows a toy simulation testing the multivariate efficiency bin correction. To simulate a detector with varying efficiency, 50 binomial distributions are generated and applied to simulated events. Using the multivariate efficiency method, the cumulants are calculated with $M$ averaged efficiency bins ($x$-axis). The simulation shows that at least fifty efficiency bins ($M = 50$) are required to accurately reproduce the true cumulants.

### 5.1.3 "track-by-track" Correction Method

The multivariate correction method defines $Q_{(a)}$ from Eq. (5.27) with $M$ efficiency bins. In the multivariate case, the efficiency bins are assumed to have a finite bin size and each bin is weighted by the number of net-protons $n$. To implement the "track-by-track" correction, the bin size is made infinitesimal ($M \to \infty$) and the number of net-protons in

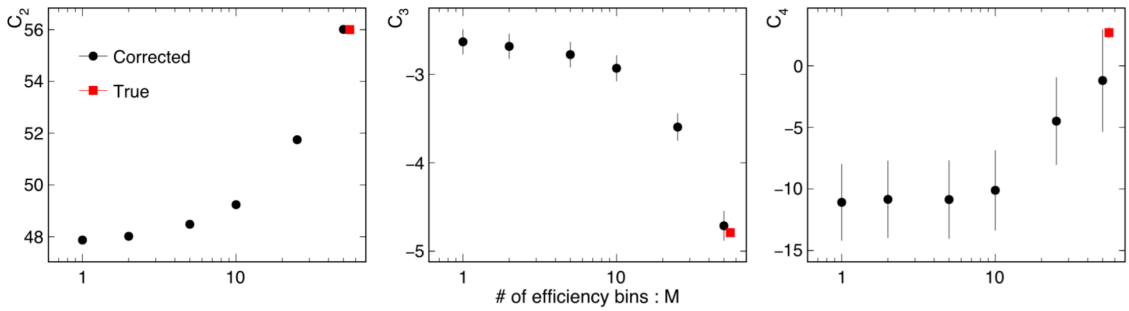


Figure 5.1. Toy simulation to test the multivariate efficiency bin correction. The corrected cumulants approach the true value when the number of efficiency bins increases [98]

.

each bin becomes either $n_i = 0$ or $n_i = 1$. This simplifies the sum in Eq. (5.27), as one only sums over efficiency bins in which a particle is measured and $n = 1$. The efficiency corrected raw moment is

$$q_{(a^r/p^s)} = \sum_{i=1}^{\mathcal{O}} \frac{a_i^r}{p_i^s} \tag{5.28}$$

where $\mathcal{O}$ is the total measured proton/anti-proton yield and $p_i$ is the efficiency at a given rapidity and momentum.

The procedure to calculate $\left\langle Q_{(a)}^r \right\rangle_c$ is the same as described in the previous section. As outlined in [95], the "track-by-track" efficiency correction method agrees with the multivariate efficiency bin method.

A large drawback of the multivariate efficiency bin method is that it requires the proton/anti-proton spectra to properly weight the finite efficiency bins. The "track-by-track" method assumes at maximum one particle per infinitesimal bin and the efficiency is calculated directly from embedding efficiency curves. Figure 5.2 shows 100 toy simulations of the "track-by-track" correction method. The true cumulants are reproduced within statistical uncertainty.

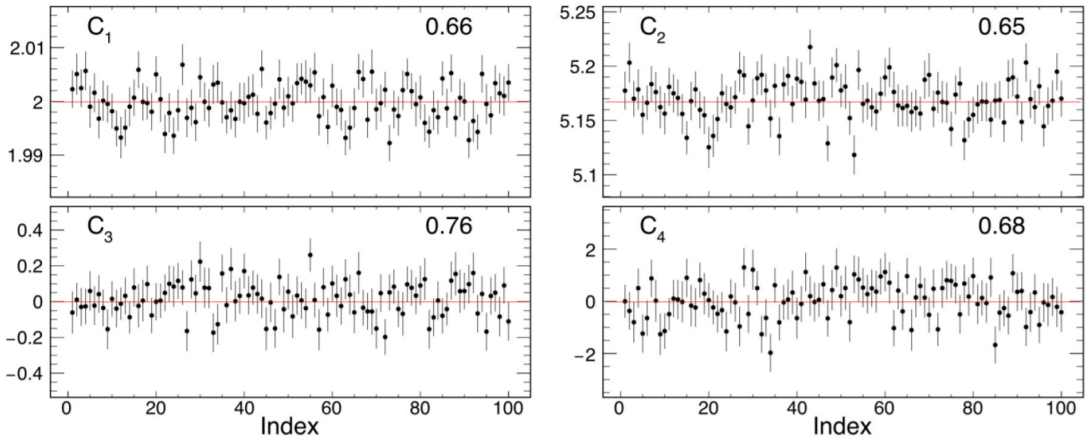


Figure 5.2. Toy simulation to test "track-by-track" correction method. Data points are calculated from 100 different samples. The number in the top right corner is the probability a data point is within the true value. Figure from Ref. [98].

## 5.2 TPC Efficiency

### 5.2.1 Embedding

The STAR collaboration relies on detector simulations to calculate the TPC efficiency. The STAR detector is modeled in GEANT3, a detector framework capable of simulating the passage of particles through matter. To estimate the detector efficiency, simulated tracks are passed through the GEANT3 STAR model, which generates TPC pad positional and $dE/dx$ data. The simulated data is embedded into unprocessed real event data and both the simulated and real detector hits are reconstructed to generate TPC tracks. The reconstruction process is outlined in chapter 2. This process in which the simulated tracks are embedded into real data is referred to as "embedding". With the "embedded" data reconstructed, one can calculate the fraction of simulated tracks that are successfully reproduced. Typically, the ensemble of simulated tracks is generated from a uniform distribution in $p_T$ and $\eta$. In addition, the multiplicity of the real events is varied to study the efficiency as a function of centrality.

### 5.2.2 TPC Efficiency for Au+Au $\sqrt{s_{NN}} = 3.0$ GeV

To apply the single track efficiency correction, the embedding sample is finely binned in transverse momentum and rapidity. The efficiency at a given transverse momentum and

rapidity bin is calculated by dividing the number of reconstructed Monte Carlo proton tracks by the total simulated Monte Carlo proton tracks. The statistical uncertainty is calculated for each bin with a standard Bayesian method, assuming the reconstructed tracks are a subset of the embedded sample.

The 2D efficiency plots as a function of rapidity and transverse momentum are depicted in Fig. 5.3. To reduce the statistical fluctuations, each rapidity slice of the 2D histogram is projected to a 1D histogram, which is the efficiency as a function of $p_T$. Then, each 1D histogram is parameterized by an exponential + 2$^{\text{nd}}$ order polynomial function.

Figure 5.4 depicts the efficiency as a function of $p_T$ for three different centrality classes. The tracking efficiency appears independent of track multiplicity.

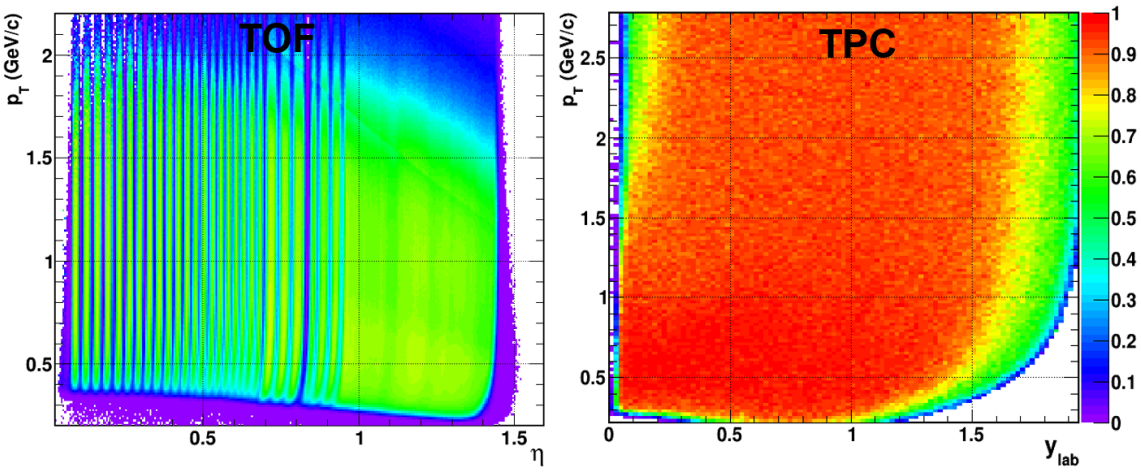


Figure 5.3. Left panel: TOF 2D efficiency histogram binned in transverse momentum and pseudorapidity. Right panel: TPC 2D efficiency histogram binned in transverse momentum and rapidity. Stated rapidity ranges are in the lab frame ($y_{cm} = 1.049$). Efficiency shown is for the nominal cuts `NHitsFit` $\geq 10$ and proton mass of $0.6 < m^2 < 1.2$ (GeV/$c^2$)$^2$.

#### 5.2.2.1 Rapidity Slice Fitting Procedure

To suppress the statistical fluctuations of the embedding sample, each rapidity slice is fit with an exponential + 2$^{\text{nd}}$ order polynomial function

$$f(x) = p_1 e^{-p_2/x} + p_3 x + p_4 x^2. \tag{5.29}$$

The first term in the fitting function, the exponential $p_1 e^{-p_2/x}$, is motivated by the sharp turn-on behavior at $p_T \approx 0.4$ GeV/$c$, as seen in the example fits in Fig. 5.5. The two

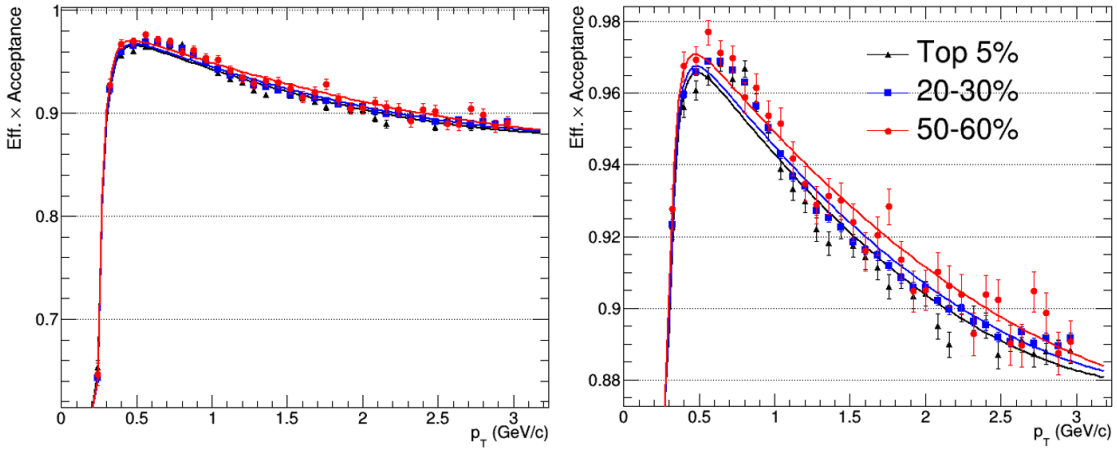


Figure 5.4. Comparison of TPC efficiency as function of $p_T$ for three centrality classes, 0-5%, 20-30%, 50-60%. Efficiency in the analysis window $-0.9 < y < 0.1$ and $0.4 < p_T < 2.0$ varies less than 0.5%. Efficiency slices are fit with an exponential + $2^{\text{nd}}$ order polynomial function.

polynomial terms $p_3 x$ and $p_4 x^2$ capture the small decrease in efficiency with increasing transverse momentum. Figure 5.5 shows an example of the exponential + $2^{\text{nd}}$ order polynomial fit to several rapidity slices.

#### 5.2.2.2 Track Quality Cuts

The TPC detector efficiency varies with the selected track quality cuts `NHitsFit` and DCA. When studying the systematic uncertainty associated with track quality cuts, it is necessary to recalculate the efficiency for each systematic variable studied. In this analysis, the `NHitsFit` track quality variable was studied at 10, 12 and 15. A comparison of the rapidity integrated efficiency for `NHitsFit` $\geq$ 10, and `NHitsFit` $\geq$ 15 is shown in Fig. 5.6. As expected, the more restrictive `NHitsFit` requirement results in an lower efficiency.

#### 5.2.2.3 Centrality Dependence

In BES-I and previous STAR analyses, a sizeable anti-correlation between the total particle multiplicity and the detector efficiency was seen. This effect is understood. When subject to high track densities, the TPC gas volume saturates causing gas occupancy effects and efficiency decreases. Because track multiplicity increases with the center of mass energy $\sqrt{s_{NN}}$, the effect scales with energy. At $\sqrt{s_{NN}} = 3.0$ GeV, the effect is

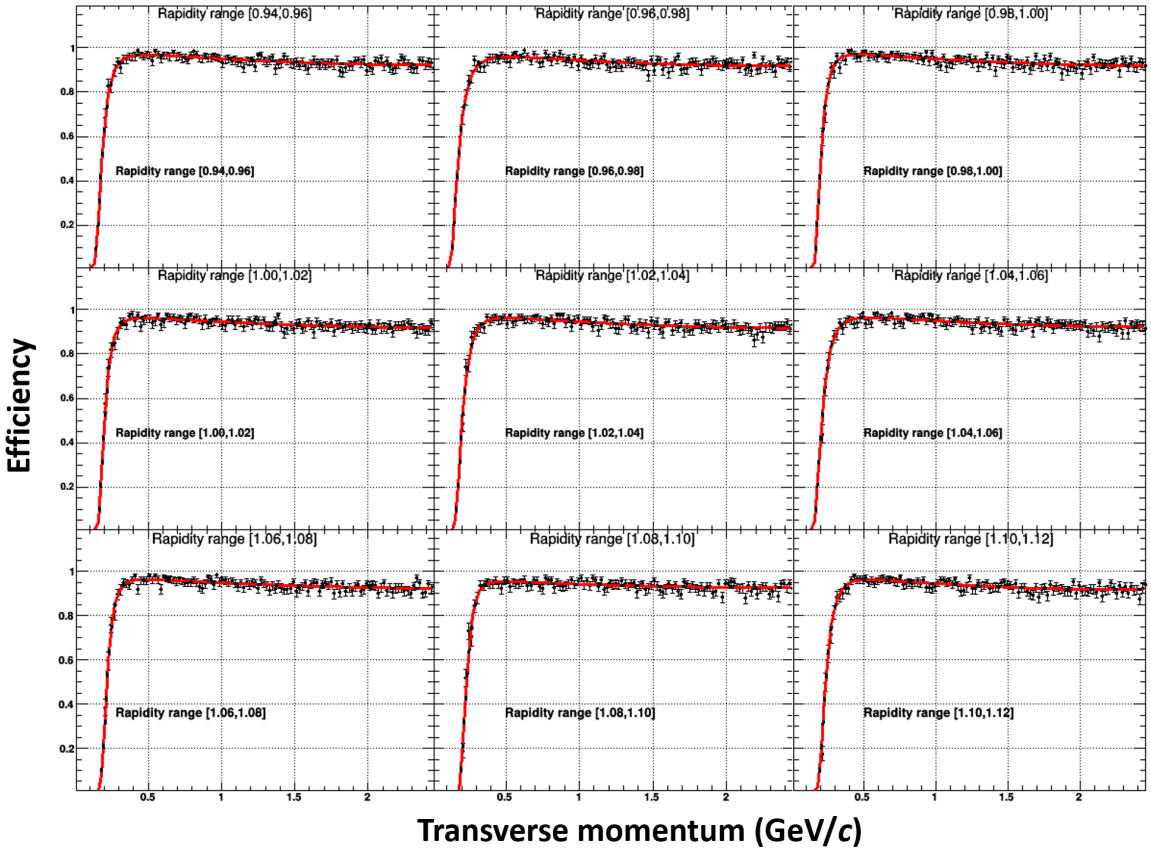


Figure 5.5. Example plot of rapidity slices of TPC detector efficiency with exponential + 2$^{\text{nd}}$ order polynomial fits. Stated rapidity ranges are in the lab frame ($y_{cm} = 1.049$).

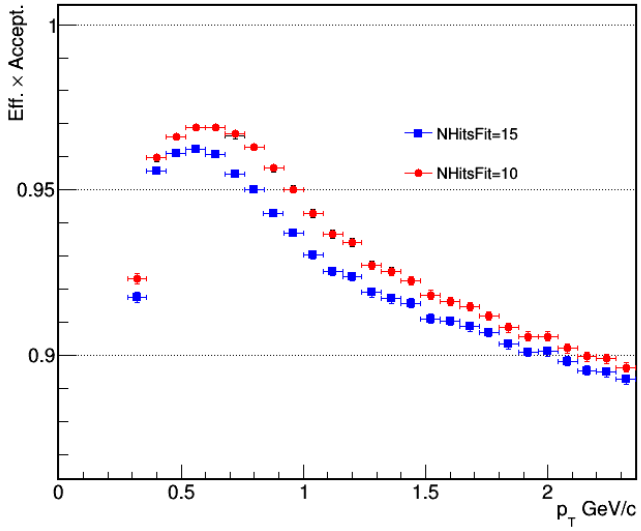


Figure 5.6. TPC detector efficiency from $-0.9 < y < 0.1$ for `NHitsFit` $\geq 10$ and `NHitsFit` $\geq 15$. Integrated efficiency from $0.4 < p_T < 2.0$ is 1% lower for `NHitsFit` $\geq$ 15.

diminished and the efficiency varies less than 0.6% from the highest to lowest centrality classes studied (0-5% to 50-60%).

Figure 5.4 shows the TPC rapidity integrated ($-0.9 < y < 0.1$) detector efficiency at three centralities, top 5%, 20-30% and 50-60%. If the efficiency fits are integrated with respect to rapidity and $p_T$, there is a $\sim 0.5\%$ difference between the top 5% and 50-60% efficiencies. The difference falls within our overall systematic uncertainty for the TPC embedding procedure of $\sim$5% and is therefore ignored.

## 5.3 TOF Efficiency

The TOF efficiency is calculated in $p_T$ and $\eta$ bins. Figure 5.7 displays the TOF $p_T$ versus $\eta$ efficiency map, which has unusual striped acceptance gaps in the $0 < \eta < 1$ region. The TOF modules are positioned for typical collider run conditions, in which the bulk of the collisions occur $\pm$30 cm from the center of the TPC along the beam line. To maximize the efficiency of the TOF detector, the modules are positioned normal to the center of the TPC which causes an acceptance gap for fixed-target vertices which is located $z = 200.7$ cm from the center of the TPC. To calculate the TOF efficiency, a data driven method is used. Below is an outline of the TOF efficiency calculation:

1. Subdivide the acceptance into $p_T$ and $\eta$ bins.
2. Calculate the total number of TPC proton candidate tracks in each bin.[2]
3. Calculate the total number of TPC proton candidate tracks with a matched TOF hit in each bin. The TOF hit must satisfy the proton mass-squared requirement $0.6 < m^2 < 1.2$ $(\mathrm{GeV}/c^2)^2$.
4. Generate an efficiency histogram by dividing the TOF match proton candidates bins by the TPC proton candidate bins.
5. Generate a linear interpolation for each $\eta$ slice.
6. Vary the systematic analysis track requirements and repeat 1–5.

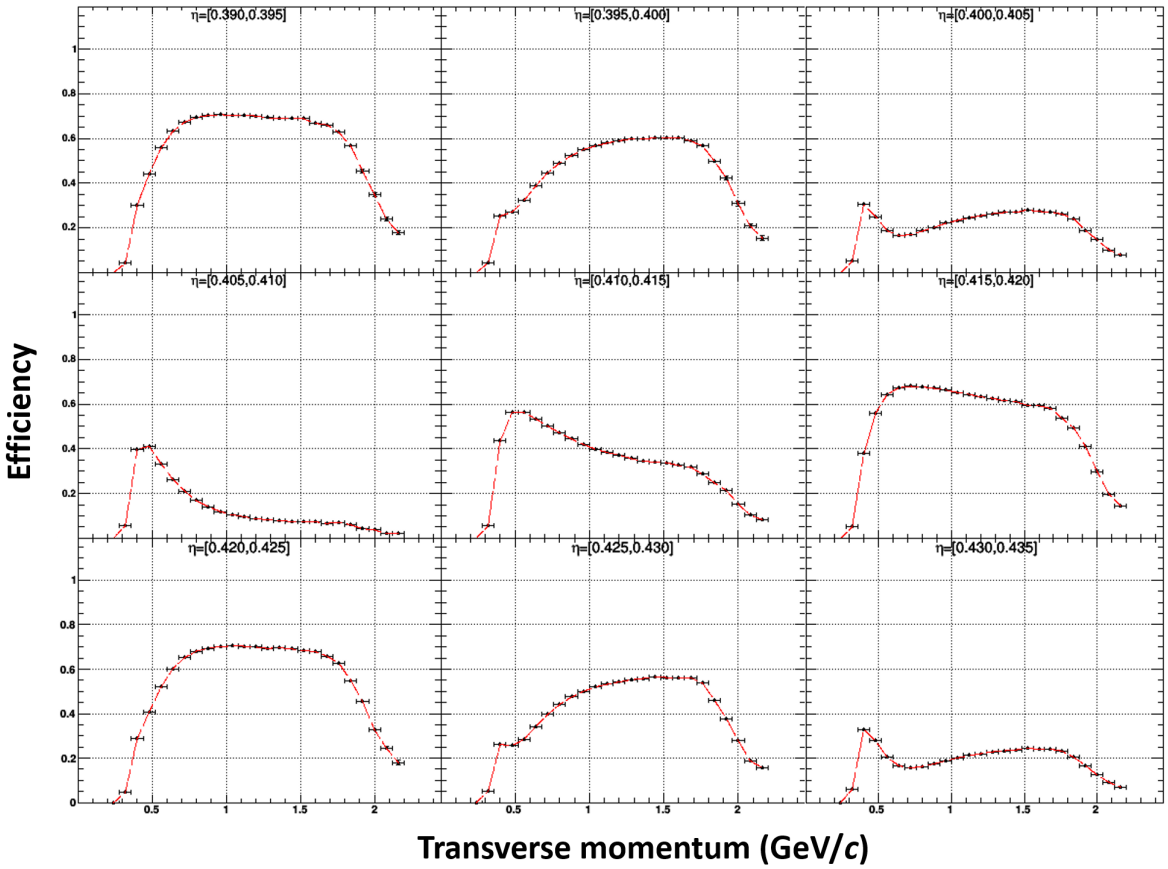


Figure 5.7. Example $\eta$ slices of TOF detector efficiency from $0.390 < \eta < 0.430$. Linear interpolation shown in red.

Figure 5.7 depicts the TOF efficiency as a function of $p_T$ for different $\eta$ slices. The efficiency varies significantly in both $p_T$ and $\eta$. To address the variations in $\eta$, fine binning ($\eta = 0.005$) is used. In $p_T$, a linear interpolation which smooths the bin-by-bin variation is applied.

## 5.4 Applying the Efficiency Correction

With the "track-by-track" efficiency correction from section 5.1 and the efficiency curves from sections 5.2 and 5.3, it is simple to calculate the efficiency:

1. Loop through the $\sqrt{s_{NN}} = 3.0$ GeV events.

[2]TPC track must satisfy proton requirements: $N_{\sigma,p} < 3$, DCA $< 3.0$, `NHitsFit` $\geq 10$, `NHitsFit/NHitsPoss` $> 0.51$.

2. Search for proton/anti-proton tracks within the kinematic acceptance window for each event.

3. Take the collection of proton tracks and calculate $q_{(a^r/p^s)} = \sum_{i=1}^{M}(a_i^r/p_i^s)n_i$, in which $a = \pm 1$ for proton/anti-proton and $p$ is the track efficiency at a given $y/\eta$ and $p_T$.

4. Average the event-by-event $q_{(a^r/p^s)}$ and calculate the cumulants with the procedure outlined in section 5.1.

# Chapter 6

# Background Rejection and Correction Methods

There are three major sources of background in the cumulant analysis: protons ejected from the beam pipe ("knockout protons"), feed down protons from $\Lambda$ decays, and double collisions in the fixed target reconstructed as a single event.

The knockout and feed down protons are largely limited to low momentum tracks which are eliminated by the transverse momentum cut $p_T > 0.4$ GeV/$c$. Both sources are also sensitive to the distance of closest approach (DCA) of the track. Therefore, there is a brief discussion of DCA, and how it relates to knockout and feed down protons. Double collision events (pileup) are the largest source of background and are not be easily removed through analysis cuts. Therefore, this chapter includes a toy model of pileup, an overview of potential background rejection methods, and a pile-up correction method.

## 6.1 Knockout Protons and Feed Down

### 6.1.1 Knockout Protons

As particles fly from the primary collision in the target to the kinematic acceptance of the detector, some tracks interact with the beam pipe and knockout protons are produced. If the knockout protons enter the detector acceptance, they can be misidentified as primary tracks and contaminate the proton signal. Knockout proton contamination is reduced with two analysis cuts. First, all tracks are required to have a DCA less than 3.0 cm. The

DCA cut removes tracks that do not point to the correct vertex. The knockout proton tracks point to the beam pipe, which is the location of the spallation vertex. Additionally, a transverse momentum cut is placed. At lower transverse momenta, the DCA resolution is worse and does not adequately remove the contamination. Therefore, all particle tracks below a transverse momentum of 0.4 GeV are removed.

### 6.1.2 Feed Down

If a particle from a Au+Au collision decays into a proton, the secondary proton can be incorrectly associated with the primary vertex. The two most prominent decays are both weak decays, specifically $\Lambda^0 \rightarrow p + \pi^-$ and $\Sigma^0 \rightarrow p + \pi^0$. This contamination is called feed down. Similar to the knockout protons, the feed down decay produces a secondary vertex and can be removed with the DCA and transverse momentum cut.

To test the effect of the feed down and knockout protons on the proton cumulants, the analysis is run with different DCA cuts. Figure 6.1 shows the results of the systematic DCA study for values of DCA$<$ 1.0 cm to DCA $<$ 3.0 cm. The cumulants and cumulant ratios vary in the most central bins, which contributes significantly to the systematic uncertainty.

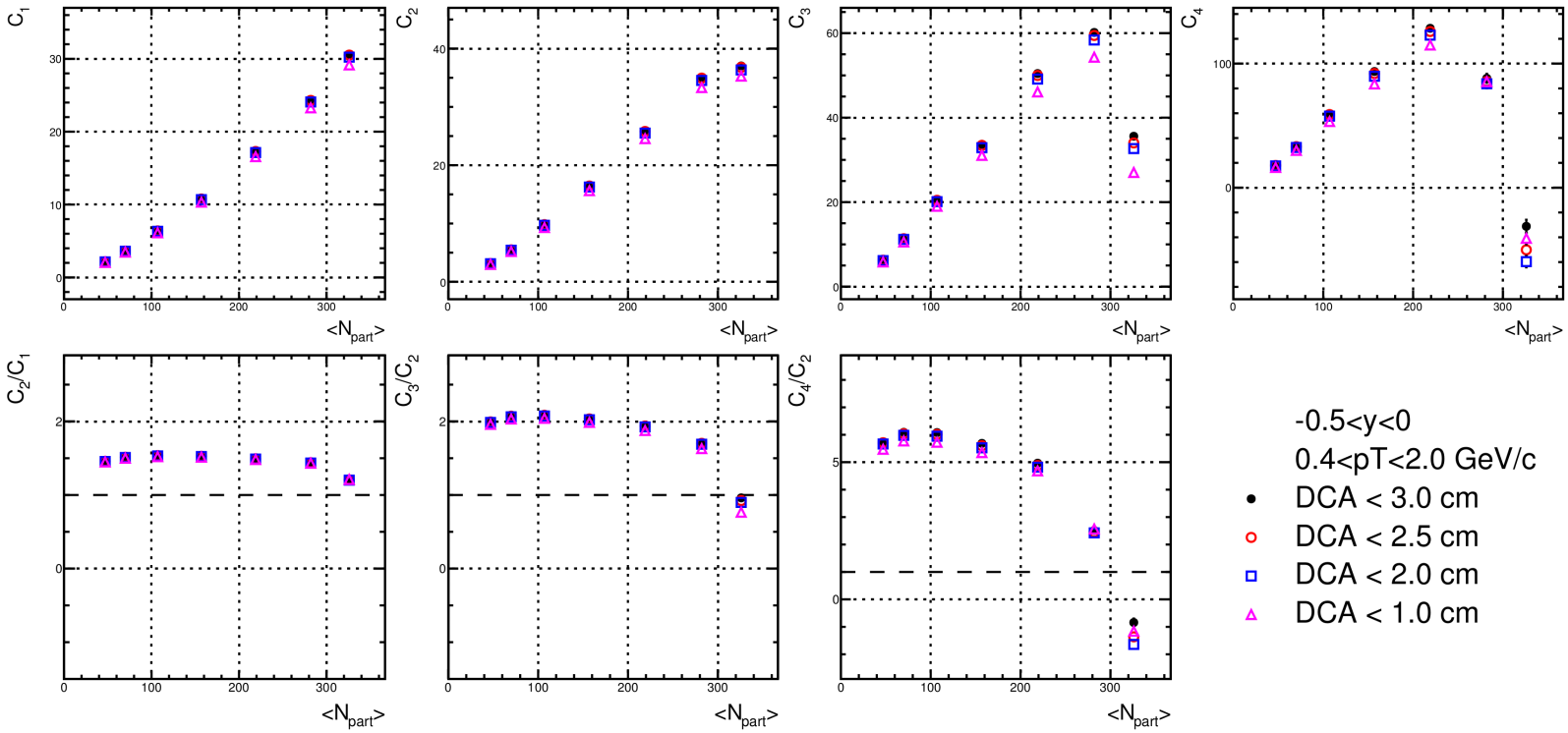


Figure 6.1. The proton cumulants (up to $C_4$) and proton cumulants ratios ($C_2/C_1$, $C_3/C_2$, and $C_4/C_2$) for the fixed-target $\sqrt{s_{NN}} = 3.0$ GeV Au+Au collisions in the rapidity window $-0.5 < y < 0$ and the transverse momentum window $0.4 < p_T < 2.0$ GeV/$c$. The analysis is performed for different maximum DCA cuts.

## 6.2 Pileup

In the 2018 fixed-target run, the largest source of background was pileup, which is defined as two or more collisions reconstructed as a single event. This discussion is limited to two collision pileup as the higher-order collision pileup[1] is negligible [99]. One can see the pileup in the total particle multiplicity distributions. Figure 6.3 shows the $\pi^{\pm}$ and $K^{\pm}$ multiplicity (`FxtMult3`) versus the total particle multiplicity (`FxtMult`). The pileup, a sum of two sub-events,[2] is expected to extend to higher multiplicities. In the figure, there is a main correlation band (yellow) and an underlying pile-up band which emerges at high multiplicities (`FxtMult3` $> 90$ and `FxtMult` $> 200$).

In this data set, there are two distinct types of pile-up events, which are labelled "in-bunch" and "out-of-bunch" pileup. Here, the bunch is the ensemble $7 \times 10^9$ gold ions. As stated in section 2, the RHIC ring held twelve circulating bunches during the 2018 $\sqrt{s_{NN}} = 3.0$ GeV fixed-target run and the bunches passed through the gold target at rate of $\sim 1$ MHz (bunches are separated $\sim 1$ $\mu$s). The "in-bunch" pileup occurs when two ions from the same bunch interact with the target and are reconstructed as a single event. By first approximation the "in-bunch" pileup is similar to the event rate and the probability of a pile-up event is $\sim 0.25\%$.[3] The "out-of-bunch," on the other hand, occurs when two Au+Au collisions from different bunches are reconstructed as a single event. One can see the "out-of-bunch" pileup in the fixed-target vertex distribution. Figure 6.2 shows a vertex distribution with a main peak at $z = 200.7$ cm and multiple secondary "out-of-bunch" pile-up peaks. As discussed in section 2.2.2.3, the start time of the event $t_0$ is used when projecting the $z$ coordinate of the TPC tracks. If the $t_0$ is wrong, the tracks are artificially offset in $z$. The secondary peaks are the "out-of-bunch" vertices artificially displaced. Due to the bunch separation (1 $\mu s$) and the drift velocity of the TPC (5.45 cm/$\mu s$), the offset in $z$ is $\sim 5.45$ cm. In comparison to the "in-bunch" pile-up sub-events, the "out-of-bunch" sub-events are well separated in time ($> 1$ $\mu$s). A large fraction of

[1] Less than 0.01% of events contain three or more collisions.

[2] The sub-event is the single collision event in a pile-up collision.

[3] The STAR detector triggers on 0.2% of all bunch crossings. The pileup estimate is increased to 0.25% to include the contribution from non-triggered events (25% of the hadronic cross section).

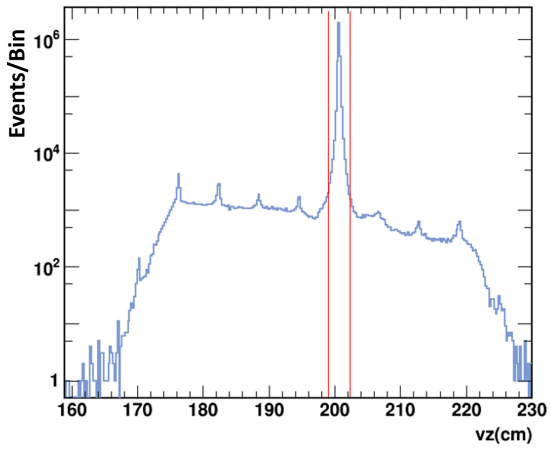


Figure 6.2. Vertex distribution with offset pile-up peaks. Main peak (target location) is highlighted by red lines.

the out-of-bunch pileup is easily rejected by the $z$ vertex cut. However, a persistent background cannot be removed. The out-of-bunch pile-up fraction can be estimated by assuming the background remains flat under the main pile-up peak at $z = 200.7$ cm. Then, the out-of-bunch pile-up fraction is $\sim 0.1$–$0.3\%$. In total, the overall pile-up fraction is is $\sim 0.4$–$0.5\%$.

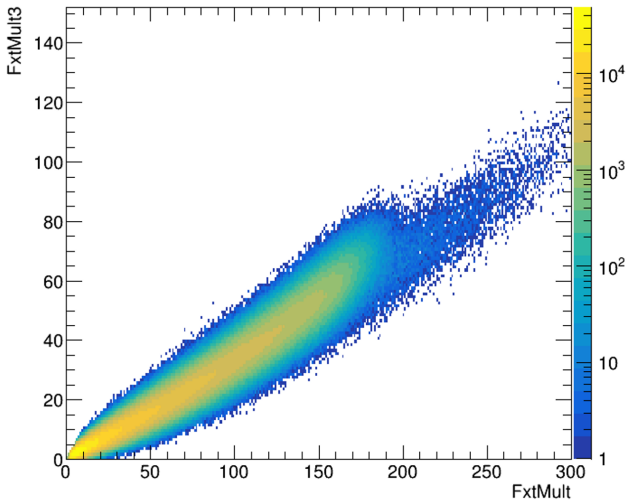


Figure 6.3. `FxtMult3` (primary tracks within $-2 < \eta < 0$ with proton cut $N_{\sigma,p} < -3$) vs `FxtMult` (primary tracks within $-2 < \eta < 0$). Double collisions dominate above `FxtMult` $> 200$.

### 6.2.1 Pile-up Toy Model

One can estimate how pileup affects the proton cumulants by running a toy Monte Carlo of net-proton distributions. To simulate the single collisions, a distribution is generated with no correlations below a multiplicity of 35 and a small anti-correlation from 35 to 40. The uncorrelated and anti-correlated distributions are generated using a Poisson and Gaussian distribution, respectively. To make the average number of net-protons centrality dependent, both the Poisson $P(\lambda = \text{Mult})$ and Gaussian $N(\mu = \text{Mult}, \sigma = 4)$ vary with multiplicity. The left panel of Fig. 6.4 shows the net-proton distributions for single collisions at various multiplicities. Next, a pile-up distribution is generated by convoluting the single collision distribution. For each multiplicity ($\text{Mult}_x$), two single collisions are randomly selected ($\text{mult}_i$ and $\text{mult}_j$) from the multiplicity distribution. If $\text{Mult}_x = \text{mult}_i + \text{mult}_j$, a pile-up event is generated by summing the net-proton and multiplicity values. This process is repeated until the desired pile-up fraction is achieved. In this example, a 1% pile-up signal at all multiplicities is tested. The right panel of Fig. 6.4 shows the pile-up distribution at various multiplicities. Figure 6.5 shows a comparison of the single collision and pile-up distributions at $\text{Mult}_x = 40$.

With the single collision and the pile-up distribution, one can calculate the cumulants and cumulant ratios of the single collision ("true") distribution and the single + pile-up collisions ("measured") distribution. Figure 6.6 shows the average number of net-protons ($C_1$) and the cumulant ratios $C_2/C_1$, $C_3/C_2$ and $C_4/C_2$ of both the true and measured distributions. When $\text{Mult} \leq 35$, the pileup is the sum of two Poisson distributions which creates another Poisson distribution. Therefore when $\text{Mult} \leq 35$, the cumulant ratio is unchanged. The measured $C_4/C_2$ value of the high multiplicity signal ($\text{Mult} > 35$) deviates from the true cumulant ratio. The pileup dilutes the signal and pushes the cumulant ratio closer to the Poisson baseline. The deviation is greatest in the $C_4/C_2$ value. In general, the effect of the pile-up contamination on the cumulants increases with cumulant order.

From the toy model, it is clear that even small levels of pile-up contamination distort the higher-order cumulants. Additionally, if the peripheral events are uncorrelated, the

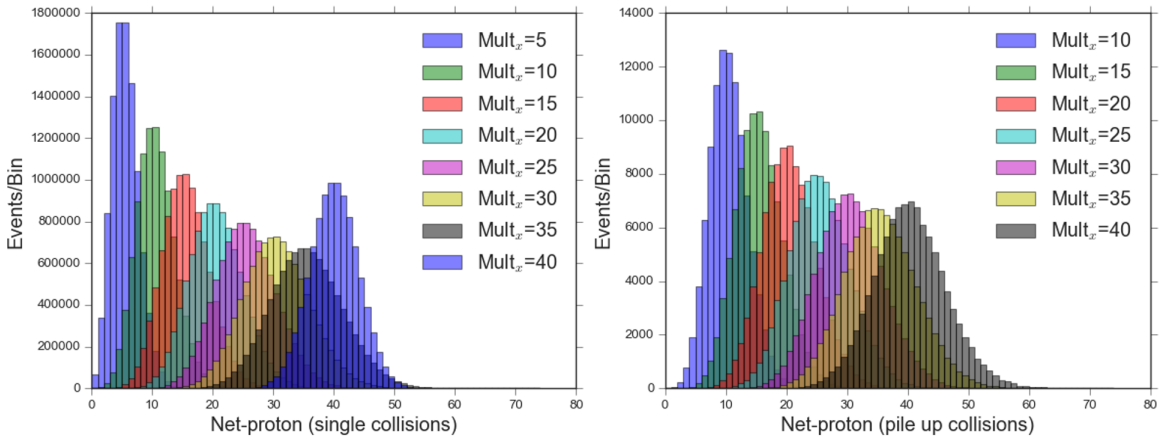


Figure 6.4. Left panel: Toy Monte Carlo single collision net-proton distributions. Right panel: Pile-up distribution generated by convoluting two events from the single collision distribution.

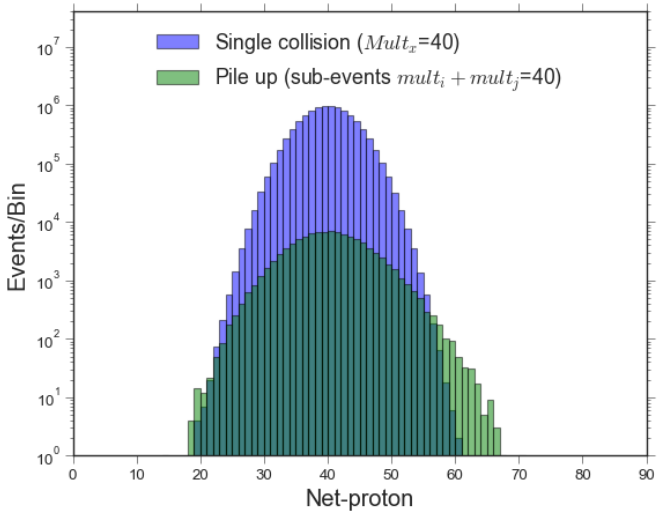


Figure 6.5. Net-proton distribution for Mult = 40 and the underlying pile-up distribution where the sub-event multiplicities sum to Mult = 40 ($\text{mult}_\text{i} + \text{mult}_\text{j} = \text{Mult}$) .

pileup in central collisions dilutes a correlated signal.

### 6.2.2 Pileup Detection in the Fixed Target

Two pile-up rejection techniques were proposed for the 2018 fixed-target data set. Neither cut is used in the final analysis due to incompatibility with the pile-up correction method. However, for completeness, an overview of the proposed cuts along with an estimation of the total rejected pileup is discussed.

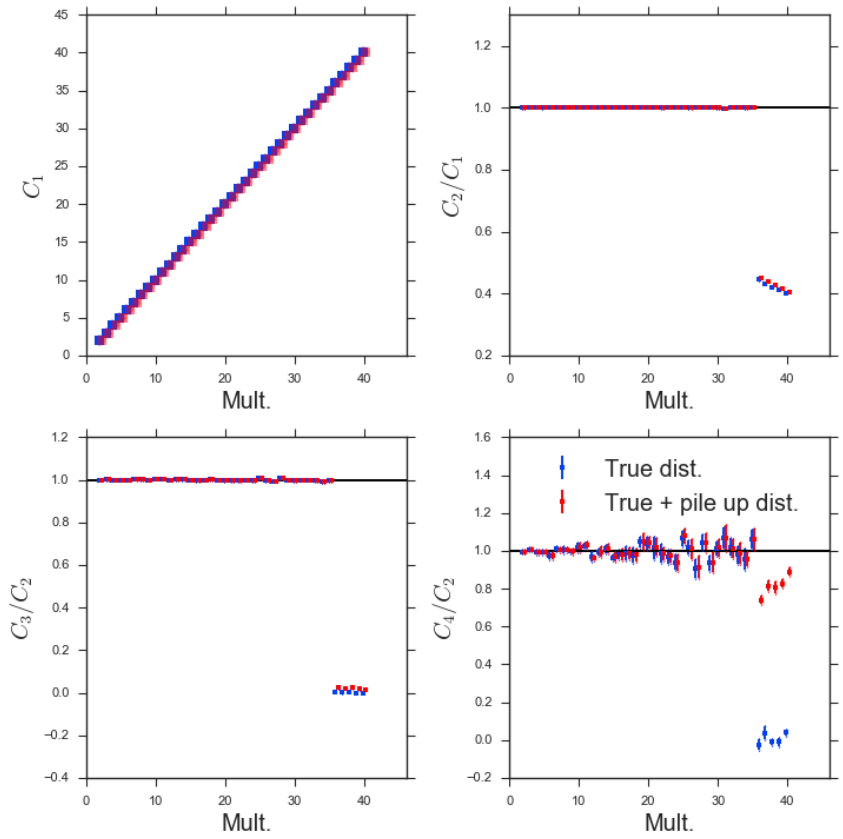


Figure 6.6. $C_1$, $C_2/C/_1$, $C_3/C_2$, and $C_4/C_2$ of a toy Monte Carlo net-proton distribution as a function of multiplicity for both true and measured distributions. The anti-correlation signal is suppressed in the higher cumulant ratios by the 1% pile-up background. Cumulants are offset for visibility.

#### 6.2.2.1 Pile-up Rejection: Event Plane Detector

As discussed in section 2.2.3, the Event Plane Detector (EPD) consists of two rings of scintillating plastic connected to wavelength-shifting fibers and silicon photo-multipliers (SiPMs). An EPD ring sits behind both endcaps of the TPC. However, in the $\sqrt{s_{NN}} = 3.0$ GeV fixed-target geometry, only the east EPD is bombarded with particles. To display the pileup, the total number of minimum ionizing particles (MIPS) in the event ($\mathrm{EPD_{nMip}}$) versus the reference multiplicity is plotted, which is shown in Fig. 6.7. The bulk of the signal (red) appears flat at $50 < \texttt{FxtMult} < 200$ and $0 < \sum \mathrm{EPD_{nMip}} < 130$. Above the main band ($\sum \mathrm{EPD_{nMip}} > 130$), a low statistics cluster of pile-up events is seen. When placing a cut to reject pileup, one should quantify the amount of pileup rejected and the remaining pileup in the signal. This pile-up fraction can be estimated by generating

a convolution of single collision events. Similar to the Toy Model, if one assumes that the pile-up events are the superposition of two sub-events $e_1$ and $e_2$ in which sub-event $e_1$ has $\texttt{FxtMult} = X_1$ and $\mathrm{EPD}_{\mathrm{nMip}} = \mathrm{Y}_1$ and sub-event $e_2$ has $\texttt{FxtMult} = X_2$ and $\mathrm{EPD}_{\mathrm{nMip}} = \mathrm{Y}_2$, the sub-events can be summed to generate a pile-up event with multiplicity $\texttt{FxtMult}^{\mathrm{pu}} = X_1 + X_2$ and EPD $\sum \mathrm{EPD}^{\mathrm{pu}}_{\mathrm{nMip}} = \mathrm{Y}_1 + \mathrm{Y}_2$. The pile-up $\texttt{FxtMult}^{\mathrm{pu}}$ and $\sum \mathrm{EPD}^{\mathrm{pu}}_{\mathrm{nMip}}$ will, on average, be twice as high as the single collision signal. The simulated pile-up distribution is shown in the right panel of Fig. 6.7. By scaling the convolution to the data in region dominated by pileup as indicated in Fig. 6.7, the convolution acts as a proxy of the underlying pileup.

It should be noted that there is additional pileup in Fig. 6.7 (indicated by the magenta oval) which is not described by our model. This is caused by "out-of-bunch" pileup in which one sub-event is outside of trigger window of the EPD. One can simulate the out-of-bunch pileup by summing the `FxtMult` values of two events and only selecting one EPD signal.

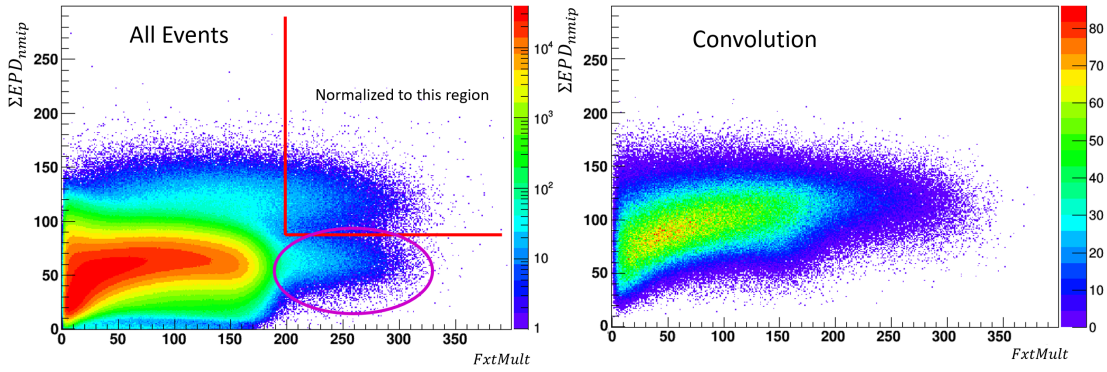


Figure 6.7. Left panel: The sum of EPD nMips vs FxtMult (primary tracks within $-2 < \eta < 0$ ). Right panel: A convolution of two events picked from the left distribution and normalized to the upper right section (indicated by the red line). A magenta circle indicates additional pileup not characterized by the convolution.

Figure 6.8 shows the estimated pileup and measured events as a function of $\mathrm{EPD}_{\mathrm{nMip}}$ for different centrality classes (0-5%, 5-10%, and 10-15%). The vertical lines indicate the different pile-up cuts by percentage of pileup removed. The red and green histograms are the in-bunch and out-of-bunch pileup, respectively. The EPD allows us to remove 80% of the in-bunch pileup with minimal event loss.

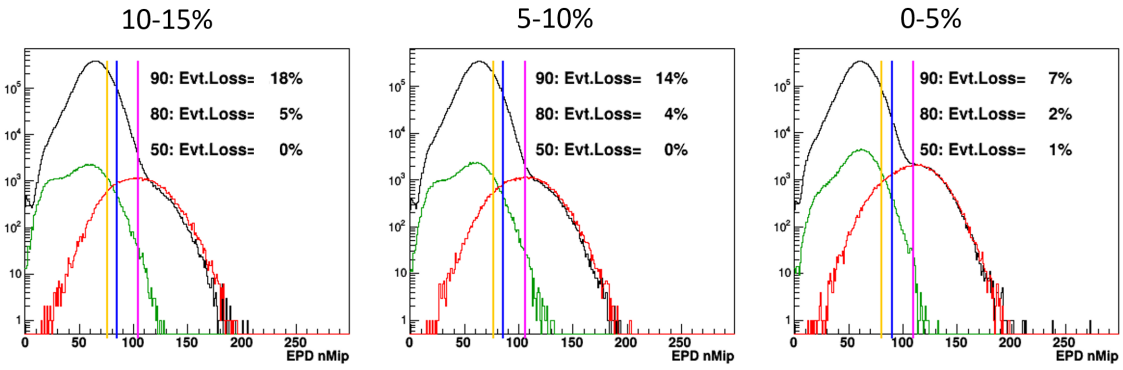


Figure 6.8. Example plots of the sum of EPD nMips for three centralities (0-5%,5-10%, and 10-15%). Vertical lines show different cuts on pileup with magenta, blue, and yellow cutting 50%, 80% and 90% of the pileup, respectively. Percentage of total events rejected is listed. The black, red and green histograms are all collisions, in-bunch and out-of-bunch.

#### 6.2.2.2 Pile-Up Rejection: Time of Flight

The Time of Flight (TOF) timing resolution for a track is 80 ps. Ideally, if the two sub-events in a pile-up event are separated in time by more than 80 ps, one can identify the pileup with the Time-of-Flight (TOF). In the case of in-bunch pileup, the two sub-events occur within the time span of a bunch (1 ns). If one assumes that the two sub-events occur randomly and uniformly within the bunch, 85% of the in-bunch pileup is removed.[4]

In the case of out-of-bunch pileup, identifying sub-events is more difficult. The timing difference between sub-events is often larger (1 $\mu$s) than the TOF trigger window (105 ns). Thus, the timing information for the trailing sub-event is not recorded in the event. However, the out-of-bunch pile-up event will have a large fraction of TPC tracks without TOF information.

Therefore, to remove pileup, one can plot the number of TOF matched pions, protons, and deuterons versus the number of TPC tracks (`FxtMult`). A positive correlation is expected for events with correct timing information, which is indicated by the red oval in Figure 6.9. Below the red oval, there is a second correlation band with roughly half the slope. These events are pileup and have incorrect timing information for, on average, half the TPC tracks. Similar to the method discussed in the previous section, one can estimate the pileup by convoluting the single collision events. First, two sub-events are

[4]Requiring 80 ps to distinguish between two sub-events in the time-of-flight is a conservative estimate.

selected from the main correlation band. The sub-events are combined by summing the `FxtMult` values and selecting the TOF information from one sub-event.

The convoluted pile-up distribution is depicted in the right panel of Fig. 6.9. With the convolution, the pileup is estimated in each centrality class. Figure 6.11 shows projections of the TOF matched pions, protons, and deuterons for three different centrality classes. The underlying pile-up distribution from TOF and EPD convolutions are displayed in red and magenta, respectively. Then, one can select events within the main correlation band and estimate the fraction of underlying pileup. Figure 6.10 displays three levels of pile-up cuts.

In the TOF $\pi+p+d$ versus `FxtMult`, there is an additional band at TOF $\pi+p+d=0$. This is caused by events that have incorrect $t_0$ information, which likely includes pileup. As discussed in section 2.2.2.3, the $t_0$ is calculated by averaging a clean sample of pions and protons in the TPC. If pions and protons are averaged from two sub-events, the $t_0$ will be incorrect and no particles will be identified.

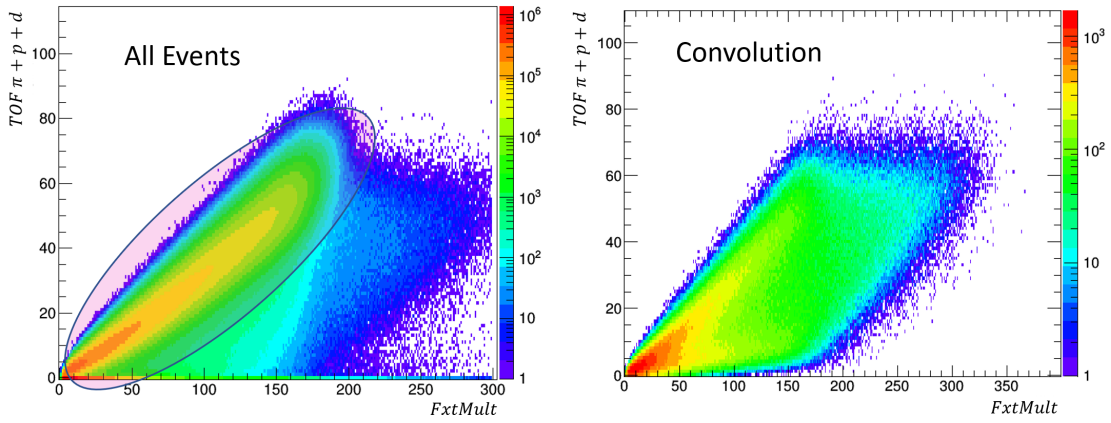


Figure 6.9. Left panel: The sum of protons, pions, and deuterons in the TOF vs FxtMult (primary tracks within $-2<\eta<0$). Right panel: A convolution of two events picked from the left distribution. The expected single collision events are highlighted by a red oval.

### 6.2.2.3 Pile-Up Rejection Summary

If both the EPD and TOF pile-up rejection methods are applied, it is estimated that the overall pile-up fraction decreases by 50%. Interestingly, when applied, the TOF and EPD pile-up methods do not change the proton cumulants up to $4^{\text{th}}$ order (within statistical

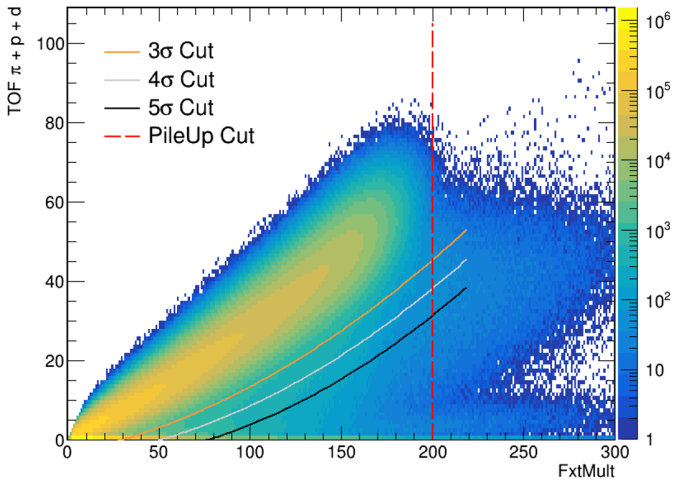


Figure 6.10. The sum of protons, pions and deuterons in the TOF versus FxtMult (primary tracks within $-2 < \eta < 0$). Three lines indicating the $3\sigma$, $4\sigma$, and $5\sigma$ cuts on the single collision band with the an additional pile-up cut at `FxtMult` $= 200$.

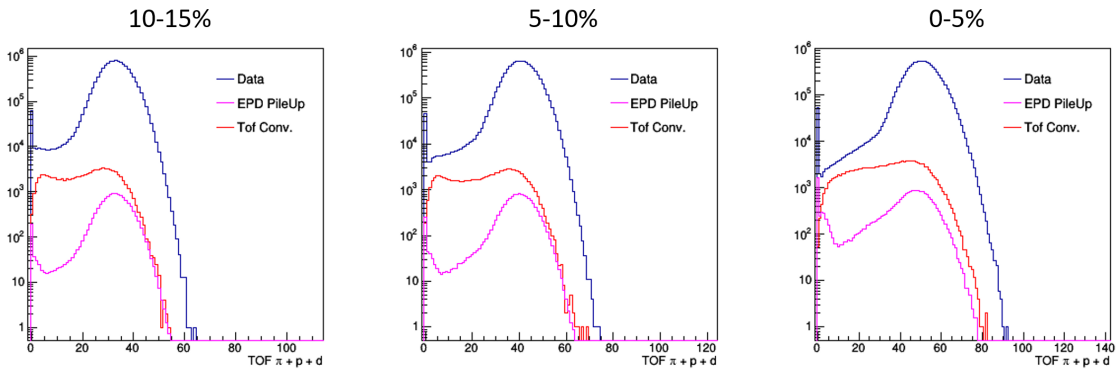


Figure 6.11. Results from 3D convolution of TOF $p$, $\pi$, and $d$ vs. sum of EPD nMips vs. FxtMult, projected onto TOF $p$, $\pi$, and $d$ axis.

significance). However, the cut at `FxtMult` $< 200$ shown in Fig. 6.10, which effectively removes events with unrealistically high proton multiplicities, drastically reduces pile-up contamination in central collisions. This aligns with our understanding of pile-up contamination. The central events are most affected by pileup; specifically pile-up events with the high proton multiplicities dilute the most central collisions.

The rejection methods discussed are not used in the analysis. Instead of the pile-up rejection methods, a pileup corrected method is used. Currently, the correction and rejection techniques are not compatible. Unlike the correction method, the rejection methods, specifically the cut at `FxtMult` $< 200$, are associated with large systematic uncertainties. The value of the cumulants ratio $C_4/C_2$ changes significantly when the `FxtMult` cut is altered.

### 6.2.3 Pile-Up Correction

#### 6.2.3.1 Pile-Up Correction Technique

The pile-up correction method is a data driven approach which separates the proton cumulants of the single collision and pile-up distributions [99]. The correction requires two measured distributions, the particle multiplicity (`FxtMult3`) and the event-by-event proton multiplicity distribution. Here, $P(N)$ is used to denote the net-proton probability distribution. $P_m^{\rm pu}(N)$ and $P_m^t(N)$ will be the probability distributions of the pile-up collisions and true single collisions at the multiplicity bin $m$.

The correction method relies on two assumptions. First, one assumes a pile-up event is the superposition of two single collision events. The higher-order pile-up rate (three or four coincident events) is negligible [99]. Second, it is assumed that each pileup sub-event is independent.

If the probability of a pile-up event at the $m^{\rm th}$ multiplicity bin is $\alpha_m$, then the probability to find $N$ particles of interest at multiplicity $m$ is given by

$$P_m(N) = (1-\alpha_m)P_m^t(N) + \alpha_m P_m^{\rm pu}(N), \tag{6.1}$$

$$P_m^{\rm pu}(N) = \sum_{i,j} \delta_{m,i+j} w_{i,j} P_{i,j}^{\rm sub}(N), \tag{6.2}$$

where $i$ and $j$ are the multiplicities of the sub-events. It is required that the sub-events sum to the $m^{\text{th}}$ multiplicity bin ($m = i + j$). The parameter $w_{i,j}$ is the probability to observe the sub-events with multiplicities $i$ and $j$. The sub-event probability distribution is

$$P^{\text{sub}}_{i,j}(N) = \sum_{N_i,N_j} \delta_{N,N_i+N_j} P^t_i(N_i) P^t_j(N_j). \tag{6.3}$$

Additionally, the sum over $i$ and $j$ runs over non-negative integers, $\sum_{i,j} \delta_{m,i+j} w_{i,j} = 1$, and $w_{i,j} = w_{j,i}$.

Now let us apply the moment generating function to the probability distribution. The moment generating function $G(\theta)$ for the probability distribution $P_m(N)$ is

$$\begin{aligned} G_m(\theta) &= \sum_N e^{N\theta} P_m(N) \\ &= (1-\alpha_m) G^t_m(\theta) + \alpha_m \sum_{i,j} \delta_{m,i+j} w_{i,j} G^{\text{sub}}_{i,j}(\theta) \end{aligned} \tag{6.4}$$

with $G^{\text{sub}}_{i,j}(\theta) = G^t_i(\theta) G^t_j(\theta)$. By applying the generating function, the $r^{\text{th}}$ moment is

$$\begin{aligned} \langle N^r \rangle_m &= \sum_N N^r P_m(N) = \frac{d^r}{d\theta^r} G(\theta)|_{\theta=0} \\ &= (1-\alpha_m) \langle N^r \rangle^t_m + \alpha_m \sum_{i,j} \delta_{m,i+j} w_{i,j} \langle N^r \rangle^{\text{sub}}_{i,j} \end{aligned} \tag{6.5}$$

with $\langle N^r \rangle^t_m = \sum_N N^r P^t_m(N)$. Here, the moment of the sub-event $\langle N^r \rangle^{\text{sub}}_{i,j}$ is

$$\langle N^r \rangle^{\text{sub}}_{i,j} = \sum_N N^r P^{\text{sub}}_{i,j}(N) = \sum_{k=0}^{r} \binom{r}{k} \langle N^{r-k} \rangle^t_i \langle N^k \rangle^t_j \tag{6.6}$$

If the cumulants are used, the sub-event can be expressed as the sum of two single collision events as

$$\langle N^r \rangle^{\text{sub}}_{i,j,c} = \langle N^r \rangle^t_{i,c} + \langle N^r \rangle^t_{j,c}\,. \tag{6.7}$$

Substituting Eq. (6.6) into Eq. (6.5), $\langle N^r \rangle^t_m$ (the single collision moments) are expressed in terms of the measured moments with

$$\langle N^r \rangle^t_m = \frac{\langle N^r \rangle_m - \alpha_m \beta^{(r)}_m}{1 - \alpha_m + 2\alpha_m w_{m,0}}. \tag{6.8}$$

Here, $\beta_m^{(r)}$ is defined as

$$\beta_m^{(r)} = \mu_m^{(r)} + \sum_{i,j>0} \delta_{m,i+j} w_{i,j} \left\langle N^r \right\rangle_{i,j}^{\text{sub}}, \tag{6.9}$$

and

$$\mu_m^{(r)} = \begin{cases} 2w_{m,0} \sum_{k=0}^{r-1} \binom{r}{k} \left\langle N^{r-k} \right\rangle_0^t \left\langle N^k \right\rangle_m^t & (m > 0) \\ \sum_{k=1}^{r-1} \binom{r}{k} \left\langle N^{r-k} \right\rangle_0^t \left\langle N^k \right\rangle_0^t & (m = 0). \end{cases} \tag{6.10}$$

Equation (6.8) is recursive and therefore, it is useful to write out the first few terms of $\mu_m^{(r)}$ and the sub-event moments $\langle N^r \rangle_{i,j}^{\text{sub}}$. The first four $\mu_{m=0}^{(r)}$ are

$$\begin{aligned} \mu_m^{(1)} &= 0, \\ \mu_m^{(2)} &= 2 \left\langle N_0 \right\rangle^t \left\langle N_0 \right\rangle^t, \\ \mu_m^{(3)} &= 6 \left\langle N_0^2 \right\rangle^t \left\langle N_0 \right\rangle^t, \\ \mu_m^{(4)} &= 8 \left\langle N_0^3 \right\rangle^t \left\langle N_0 \right\rangle^t + 6 \left\langle N_0^2 \right\rangle^t \left\langle N_0^2 \right\rangle^t. \end{aligned}$$

The first four $\langle N^r \rangle_{i,j}^{\text{sub}}$ are

$$\begin{aligned} \left\langle N \right\rangle_{i,j}^{\text{sub}} &= \left\langle N \right\rangle_i^t + \left\langle N \right\rangle_j^t, \\ \left\langle N^2 \right\rangle_{i,j}^{\text{sub}} &= \left\langle N^2 \right\rangle_i^t + \left\langle N^2 \right\rangle_j^t + 2 \left\langle N \right\rangle_i^t \left\langle N \right\rangle_j^t, \\ \left\langle N^3 \right\rangle_{i,j}^{\text{sub}} &= \left\langle N^3 \right\rangle_i^t + \left\langle N^3 \right\rangle_j^t + 3 \left\langle N^2 \right\rangle_i^t \left\langle N \right\rangle_j^t + 3 \left\langle N \right\rangle_i^t \left\langle N^2 \right\rangle_j^t, \\ \left\langle N^4 \right\rangle_{i,j}^{\text{sub}} &= \left\langle N^4 \right\rangle_i^t + \left\langle N^4 \right\rangle_j^t + 4 \left\langle N^3 \right\rangle_i^t \left\langle N \right\rangle_j^t + 4 \left\langle N \right\rangle_i^t \left\langle N^3 \right\rangle_j^t + 6 \left\langle N^2 \right\rangle_i^t \left\langle N^2 \right\rangle_j^t. \end{aligned}$$

With Eq. (6.9) and the fact the cumulant $C_0^{(1)} = 0$, one can solve for $\langle N^r \rangle_0^t$. With $\langle N^r \rangle_0^t$, one can recursively solve for any $m$.

The correction is largely data driven and only relies on the total pile-up probability $\alpha$ and the sub-event weight $w_{i,j}$. To calculate $\alpha$ and $w_{i,j}$, both a data-driven unfolding procedure and estimates from simulations are tested. Figure 6.12 are examples of $\alpha$ and the response matrix $w_{i,j}$.

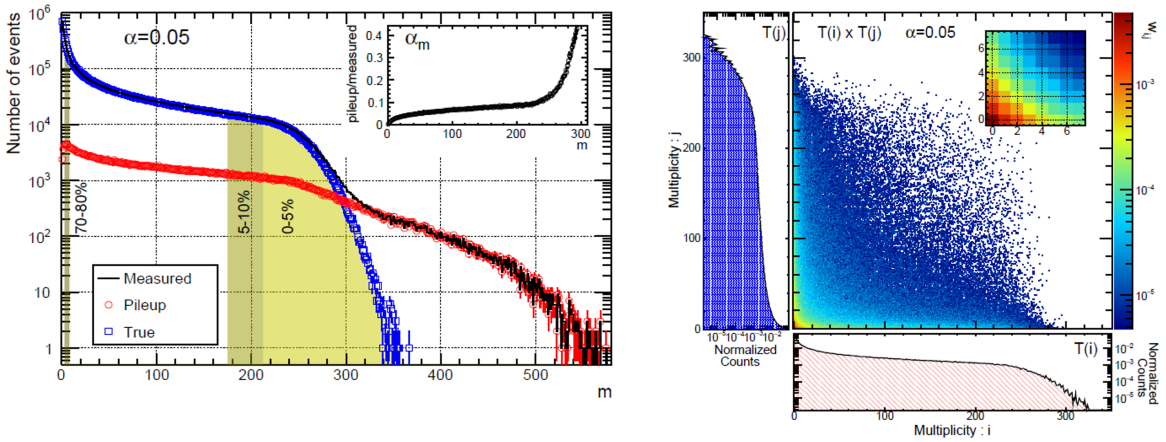


Figure 6.12. Left Panel: Simulated multiplicity distribution generated from Glauber model and two component model. The true distribution, and pile-up distribution, and measured (true + pile-up) distribution are shown in red, blue, and black. The total pile-up ratio is $\alpha = 0.05$ and smaller panel shows $\alpha_m$, where $m$ is our multiplicity. The bands labeled 0-5% and 5-10% indicate centrality. Right Panel: Response matrix $w_{i,j}$. The plot shows the correlation between $i$ and $j$ sub-events. Both figures are from reference [99].

Initially, there was an attempt to estimate the pileup by fitting the multiplicity distribution with both a Glauber Model and UrQMD. However, the estimated pileup varied substantially between the two models. The black and red open circles in Fig. 6.13 show `RefMult3`[5] distributions for UrQMD single collisions and single collisions + pile-up events, respectively. The UrQMD events are fit with the Glauber Model + two component model following a similar procedure outlined in chapter 3. With the Glauber Model, one can generate a correction matrix as seen in the right panel of Fig. 6.12. Results for pileup-corrected cumulant ratios are shown in Fig. 6.14 as a function of centrality. If the correction matrix generated from the Glauber model could reproduce the pileup in our UrQMD sample, the corrected cumulants would return to the true value in Fig. 6.14. Unfortunately, the pile-up correction fails at the most central collisions. The same discrepancy is expected to occur when applying the correction to experimental data, as the neither UrQMD nor the Glauber Model describes the data perfectly. Therefore, a data-driven unfolding method to extract the true single collision distribution from the

[5]`RefMult3` is a common STAR reference multiplicity that excludes protons. `RefMult3` and `FxtMult3` have different kinematic acceptances.

measured multiplicity distribution is applied.

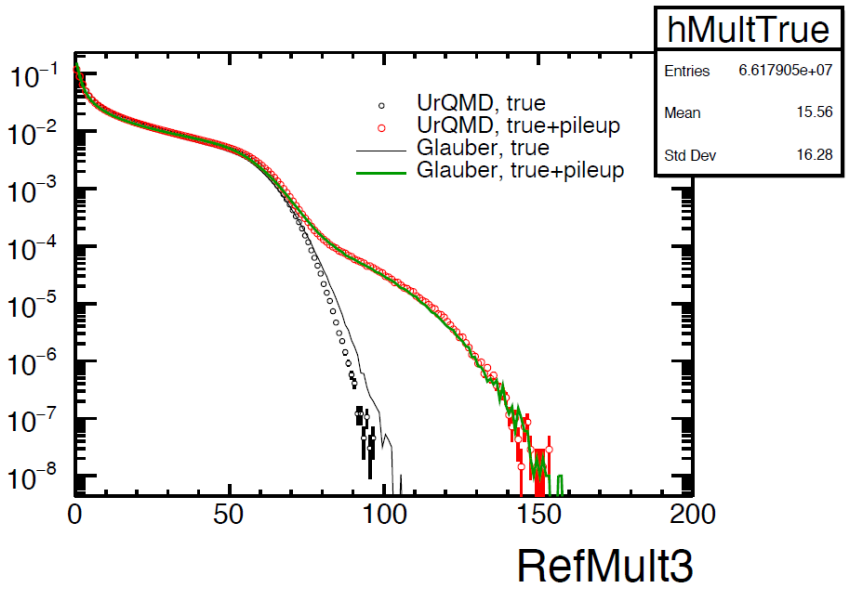


Figure 6.13. `RefMult3` distributions in UrQMD for single-collisions (black circles) and entire events including pileup (red circles) [100]. Solid lines represent fits by Glauber and two-component models.

#### 6.2.3.2 Unfolding for the Pileup Correction

To implement the pile-up correction, one requires the fraction of pileup at each multiplicity bin $\alpha_m$. As discussed in a previous section, the pileup is estimated with a convolution of the single collision distribution. To generate a pile-up event, two events are randomly selected and the multiplicities and net-proton numbers are summed. Like the pileup in the experimental data, one of the sub-events must satisfy the trigger requirements. Therefore, the first sub-event is selected from the `FxtMult3` distribution as the triggered event and a second sub-event is selected from Glauber Model fit. The Glauber Model fit approximates the total cross section. To normalize the pileup, the simulated pile-up events are fit to the high tail of the `FxtMult` distribution (`FxtMult` $> 200$) in Fig. 6.15. However, as seen in Fig. 6.15, the pile-up fit disagrees at high multiplicities. This method does sufficiently describe the data. Therefore, an improved unfolding method is used to extract the single collision distribution.

The unfolding method was originally developed to reconstruct particle multiplicity distributions with non-binomial efficiencies [101]. It estimates the pileup by iteratively

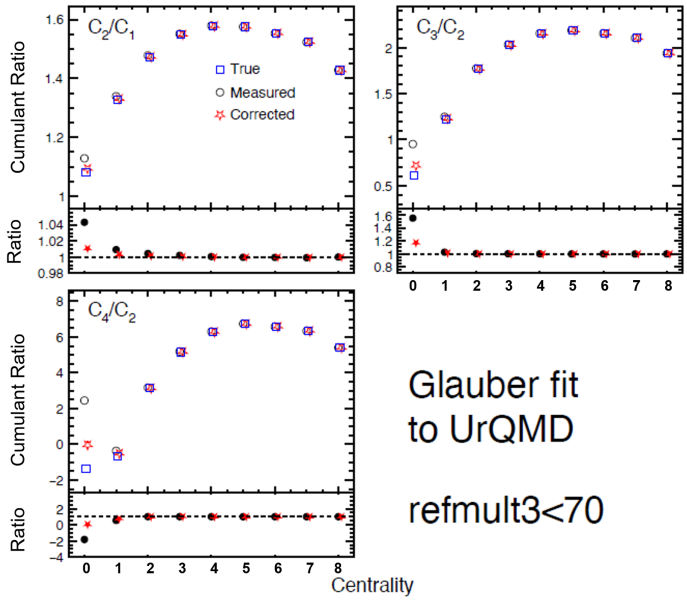


Figure 6.14. Cumulant ratios as a function of centrality for true values for single-collision events (blue squares), measured values for entire events including pileup (black circles), and pile-up corrections (red stars). The ratios of the measured over true (black dots) and corrected over true (red stars) are displayed below each panel. The $x$-axis numbers indicate the centrality bin with zero being the most central collisions. Figure from Ref. [100]. The correction fails at the most central events.

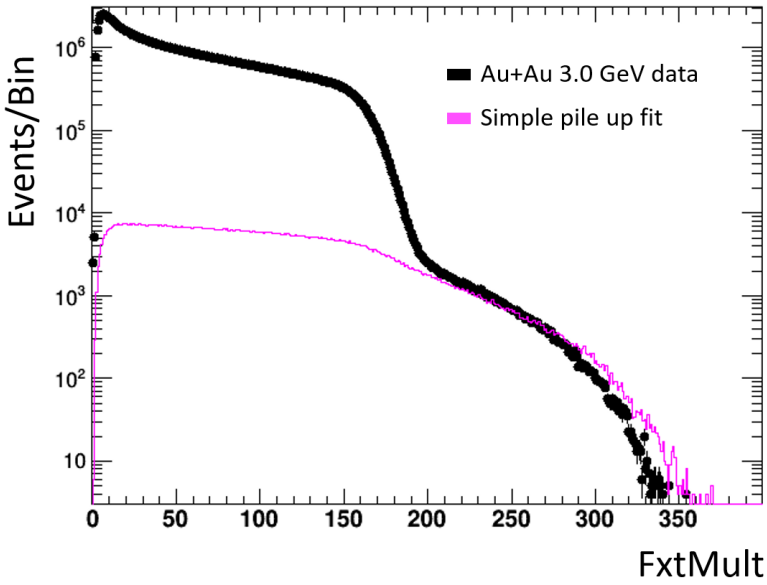


Figure 6.15. Simple top pile-up model. Pile-up events are generated by randomly selecting from `FxtMult` and the Glauber model fit. The shape of the pile-up distribution and the data do not agree at high multiplicities.

altering a simulated single collision distribution until the data is reproduced. The pileup is produced by selecting events from a simulated single collision distribution, which can be arbitrary, and placing the events in a pile-up filter[6]. The difference between the data and the simulated single + pileup are measured and the difference is unfolded back to the single collision coordinates. The simulated single collision distribution is recalculated and the process is repeated. Eventually, the simulated single + pile-up distribution reproduces the data.

The flow chart 6.16 is an overview of the unfolding procedure. To test the method, a closure test is performed using UrQMD events. In the test, the UrQMD events act as the experimental data as shown in (a) and (b) in Fig. 6.16. The goal is to reconstruct the UrQMD true distribution starting from Monte Carlo samples.[7] The procedure is as follows:

1. Generate a Monte Carlo distribution (toy-MC) based on the Glauber and two-component models.

2. Apply the pile-up filter to the toy Glauber distribution (Fig. 6.13) to get the toy-MC measured distributions (Fig. 6.17).

3. Compute a reversed response matrix $\mathcal{R}_{\rm rev}$ numerically (An inversion procedure is not necessary).

4. Calculate the correction function by subtracting the UrQMD from the Glauber distribution (Fig. 6.17).

5. Multiply $\mathcal{R}_{\rm rev}$ by MC-UrQMD to get the correction functions in the true coordinates.

6. Add the correction to the Glauber distribution in the true coordinates.

7. Repeat (**2**)–(**6**) until the correction function becomes close to zero.

[6]The pile-up filter determines how the sub-events are summed together.

[7]In the procedure, "true" is the single collision distribution and "measured" is the single + pile-up distribution.

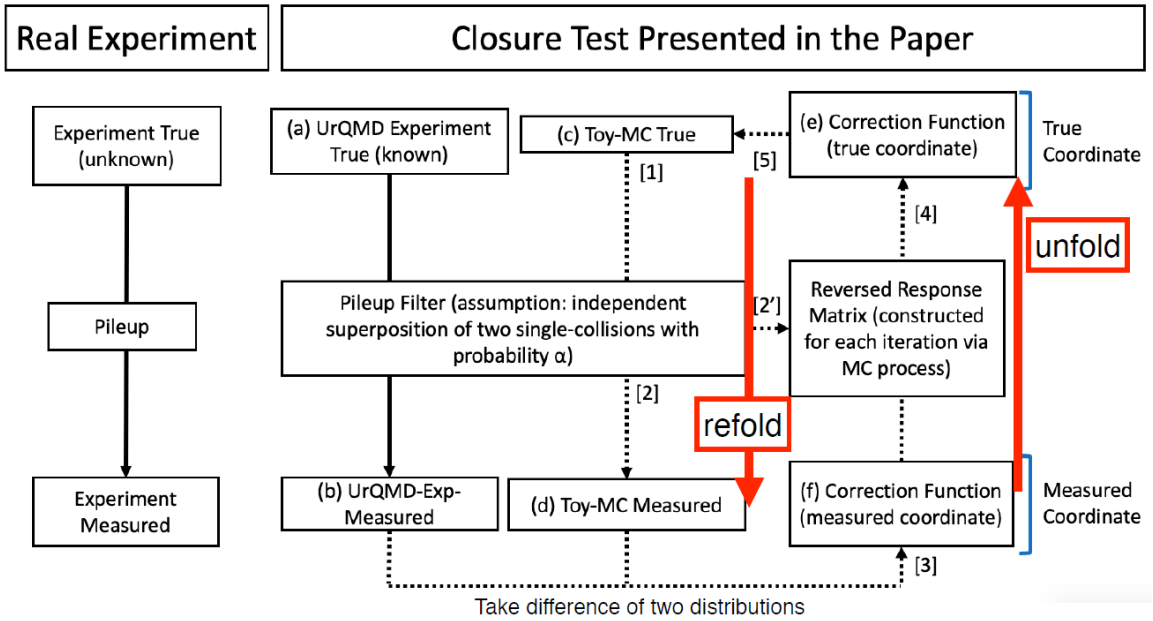


Figure 6.16. Unfolding flowchart used to extract the true multiplicity distribution [100]. The dotted arrows show iteratively repeated steps.

Figure 6.17 shows the multiplicity distributions and correction functions for true and measured coordinates, respectively. The MC samples are generated from the best fit of Glauber to the UrQMD distribution in the true coordinate. If the correction is working, the MC true is modified closer to the UrQMD true with each iteration. Additionally, this method does not require the Glauber fit and would reproduce the UrQMD true distribution with any input. However, using the Glauber Model reduces the number of iterations. The test shows that the UrQMD is reproduced at $\sim 100$ iterations.

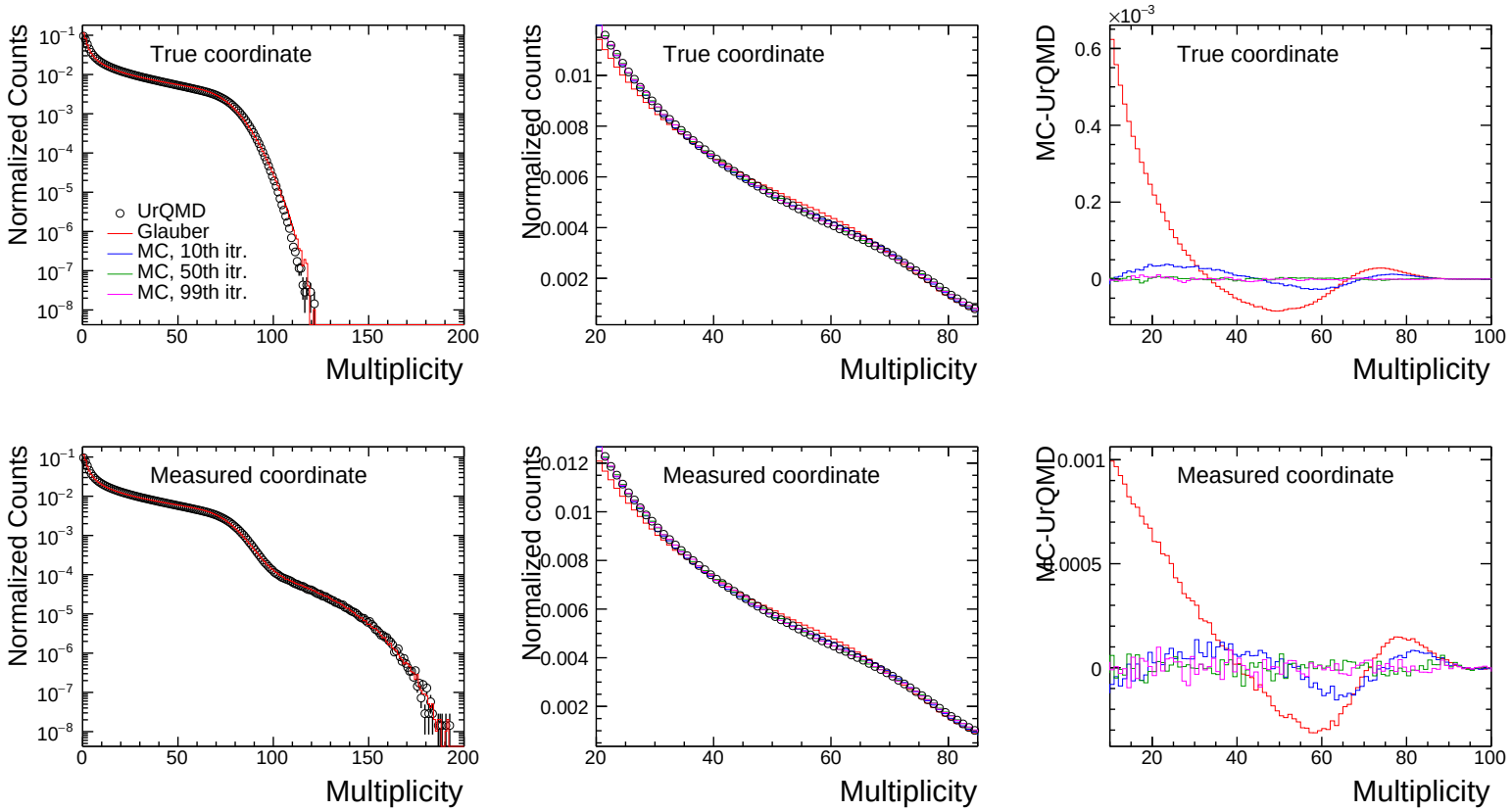


Figure 6.17. Left panels: Multiplicity distributions for UrQMD and Glauber fit. Middle panels: Multiplicity distributions for UrQMD, Glauber fit, and MC samples for 10th, 50th, and 99th iteration. Right panels: Difference between UrQMD and MC samples as a function of multiplicity. Top panels: Distributions in the true coordinates, Bottom panels: Distributions in measured coordinates [100]. Here, "measured" = "true" + "pileup".

UrQMD cumulants up to $4^{\text{th}}$ order are shown in Fig. 6.19 as a function of centrality. As shown, the true values for single-collision events agree with the corrected results. If the initial assumptions for the pile-up filter are correct, the unfolding approach always give the true multiplicity distribution after substantial iterations. For our filter, the only parameter is the pile-up probability $\alpha$. Here, unlike the multiplicity dependent pile-up probability $\alpha_m$ in Eq. (6.8), the pile-up probability $\alpha$ is the total pile-up fraction of all events. The unfolding procedure is run at several $\alpha$ parameters from 0.0025 to 0.07. After 100 iterations, a $\chi^2$ test is performed between the data and Monte Carlo distribution for each $\alpha$ value. To find the optimal $\alpha$ parameter, the $\chi^2$ per degree of freedom ($\chi^2$/ndf) versus $\alpha$ is fit with a $2^{\text{nd}}$ polynomial. The minimum $\chi^2$/ndf of the fit is the optimal $\alpha$ parameter. The fit is shown in Fig. 6.18. The total probability of pileup is $\alpha = 0.0046$. The $\alpha$ parameter is varied by $\alpha = 0.0009$ or $\pm 1$ $\chi^2$/ndf for the systematic analysis, which is indicated by the blue stars on Fig. 6.18.

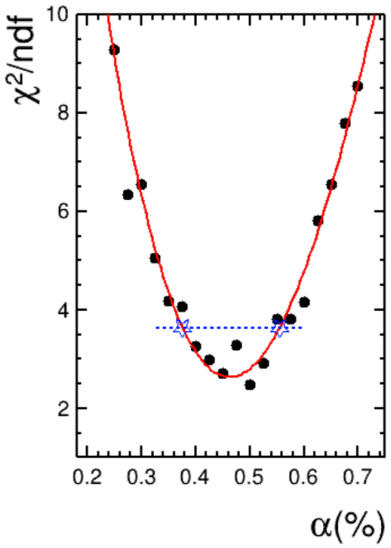


Figure 6.18. $\chi^2$/ndf versus $\alpha$ parameter fit with a 2nd order polynomial.

With the pile-up correction method and the single collision unfolding method, one can obtain the pile-up fraction as a function of multiplicity $\alpha_m$, and the pile-up response matrix $w_{i,j}$. Figure 6.20 shows the `FxtMult3` distribution fit with the Glauber Model and the unfolded single collision and pile-up distribution. Figure 6.21 is the response matrix generated from the unfolding technique.

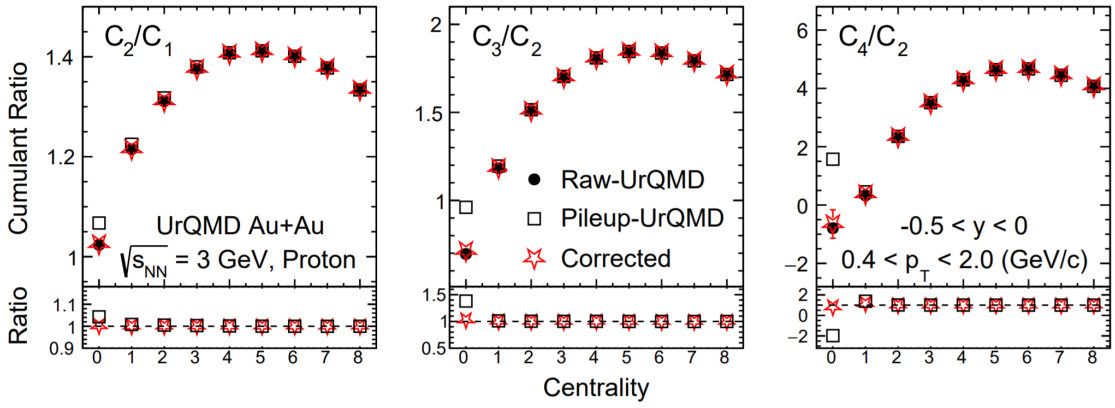


Figure 6.19. Cumulant ratios as a function of centrality for true values for single-collision events (black dots), measured values for entire events including pileups (open squares), and pile-up corrections (red stars) with an improved pile-up unfolding approach. The ratios of the measured over true (black dots) and corrected over true (red stars) are displayed below each panel. The $x$-axis numbers indicate the centrality bin with zero being the most central collisions. Figure from Ref. [102].

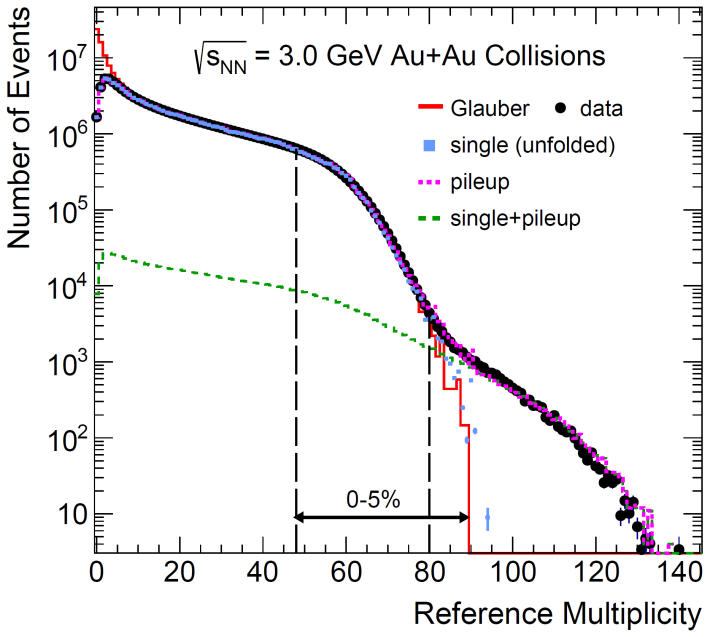


Figure 6.20. `FxtMult3` distributions obtained from $\sqrt{s_{NN}}$ = 3.0 GeV data (black markers), GM (red histogram), and unfolding approach based on a two-component fit in order to separate single and pile-up contributions. Vertical lines represent statistical uncertainties. Single, pileup, and single+pile-up collisions are shown in solid blue markers, green and blue dashed lines, respectively.

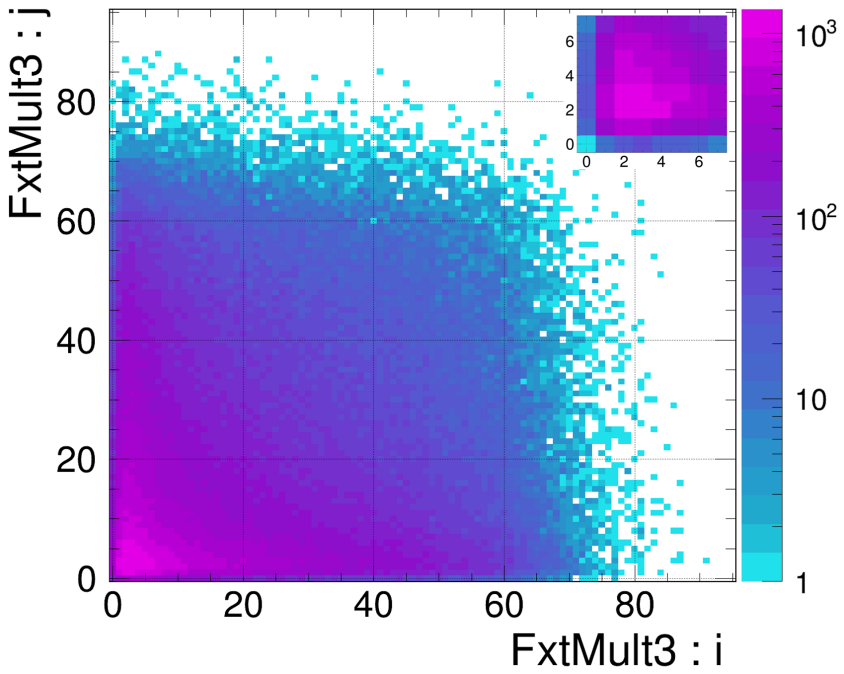


Figure 6.21. Response matrix $w_{i,j}$ generated from the unfolding procedure for Au+Au collisions at $\sqrt{s_{NN}} = 3.0$ GeV.

#### 6.2.3.3 Pile-up Corrected Cumulants

Figures 6.22 and 6.23 are the proton cumulants and cumulant ratios up to $6^{\text{th}}$ order for the Au+Au $\sqrt{s_{NN}} = 3.0$ GeV collisions. The pile-up uncorrected and corrected cumulants are in gray and black, respectively. In both the cumulants and cumulant ratios, the pile-up correction only affects the top multiplicities. Additionally, the correction is larger for higher-order cumulants. Both the corrected and uncorrected cumulants averaged over the centrality class are shown in red and blue, respectively. The averaging is weighted by the number of events in each centrality bin and is outlined in chapter 7. The effect of pileup is diminished when averaged over the centrality class due to the low event count at high multiplicities. Up to the third cumulant, the difference between the corrected and uncorrected is negligible.

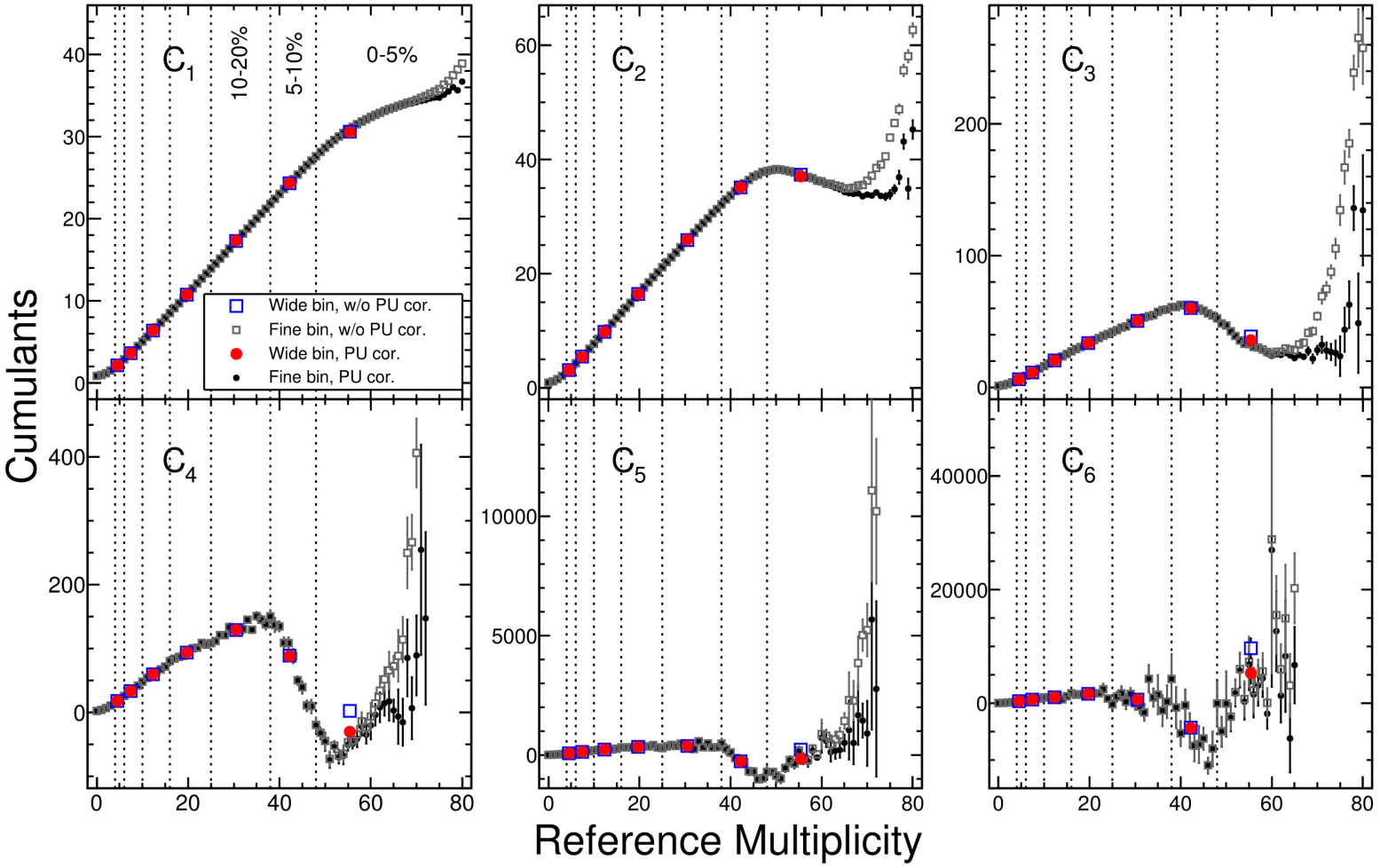


Figure 6.22. Cumulants of the event-by-event proton multiplicity distribution in Au+Au collisions at $\sqrt{s_{NN}} = 3.0$ GeV measured up to $6^{\text{th}}$ order. The corrected and uncorrected cumulants as a function of `FxtMult3` are displayed in black and gray, respectively. The corrected and uncorrected cumulants binned with CBWC are displayed by blue and red, respectively. The CBWC cumulants are plotted at their average `FxtMult3`. Vertical lines indicate the centrality bin edges in Table 3.1.

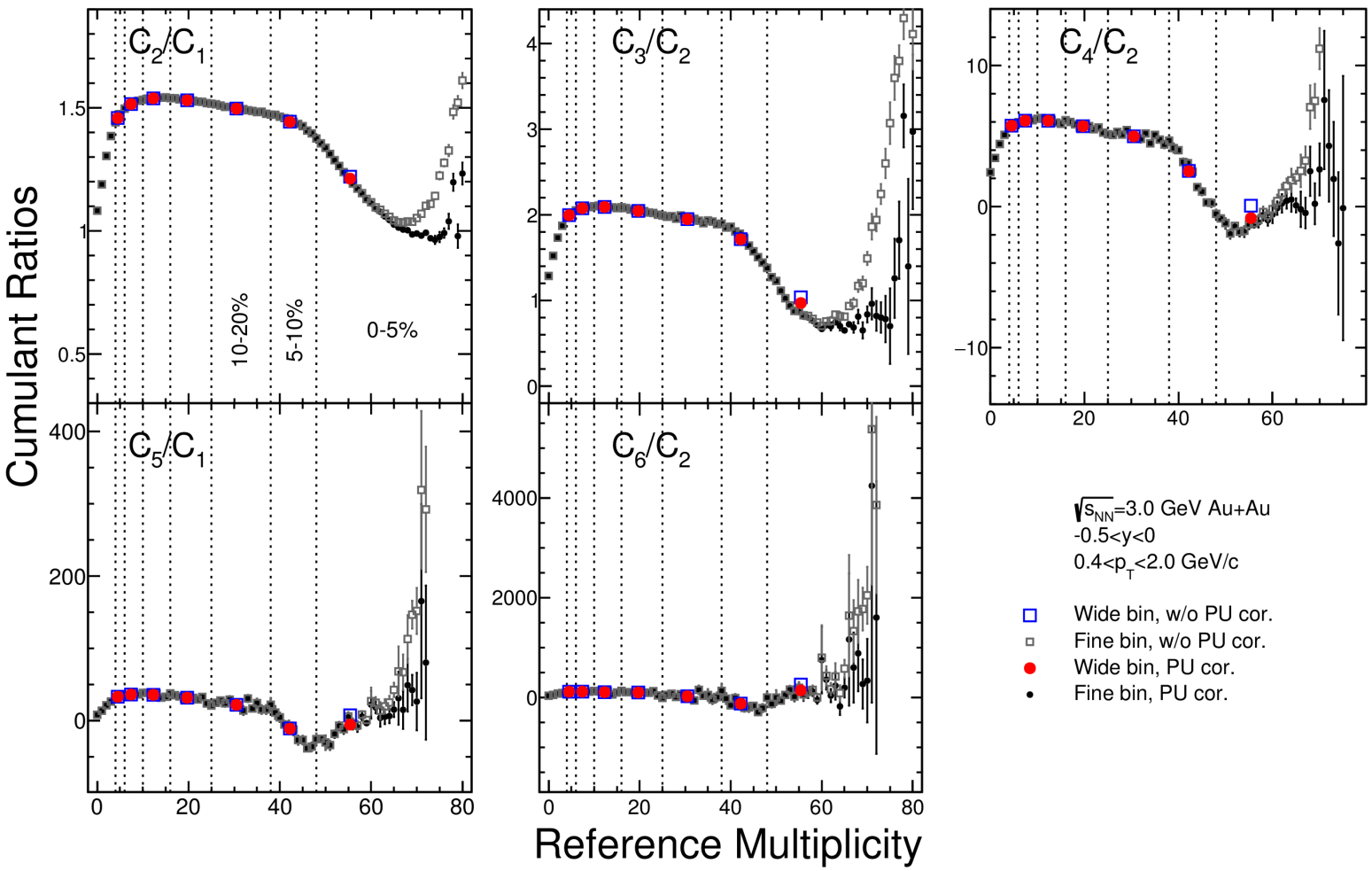


Figure 6.23. Cumulant ratios of the event-by-event proton multiplicity distribution in Au+Au collisions at $\sqrt{s_{NN}} = 3.0$ GeV measured up to $6^{\text{th}}$ order. The corrected and uncorrected cumulants as a function of `FxtMult3` are displayed in black and gray, respectively. The corrected and uncorrected cumulant ratios binned with CBWC are displayed by blue and red, respectively. The CBWC cumulant ratios are plotted at their average `FxtMult3`. Vertical lines indicate the centrality bin edges in Table 3.1.

# Chapter 7

# Volume Fluctuations

In heavy-ion collisions, the volume is defined by either the number of participating nucleons or the impact parameter.[1] For the purposes of this discussion, the $N_{\rm part}$ will define the volume. As discussed in chapter 3, the volume cannot be measured directly, but is inferred through the correlation or anti-correlation of a detector measurement.

In most heavy-ion analyses, the average value of an observable is measured as a function of centrality. The centrality of each event is determined by the reference multiplicity of the event. A range of multiplicities corresponds to a centrality class, see chapter 2. While the multiplicity does not directly measure the impact parameter, the average value of a centrality class is related to an average $b$ and $N_{\rm part}$. By applying the central limit theorem (CLT), the centrality dependence and $\langle N_{\rm part}\rangle$ dependence of an event-averaged observable will converge. This has been confirmed experimentally. Several experiments have measured the same values for various observables using different methodologies for centrality. If the observable is not an event averaged quantity, but instead a higher order moment, the CLT cannot be applied and the centrality dependence and $\langle N_{\rm part}\rangle$ dependence of the observable can vary significantly. This difference or effect is referred to as volume fluctuations (VF). In this chapter, a heuristic description of the VF is provided and the reduction and correction techniques used to reduce VF are discussed.

[1] The highly correlated nature of $b$ and $N_{\rm part}$ is shown in Fig. 7.1.

## 7.1 Heuristic Approach

This heuristic approach is discuss in more detail in Refs. [103, 104]. First, let us assume the volume does not fluctuate and the volume $V$ is fixed. In this case, the net-baryon number $B$ fluctuates with the probability distribution $P(B,V)$, which depends on $\mu$ and temperature $T$. The moments of $P(B,V)$ are

$$\langle B^n \rangle_V = \sum_{B=-\infty}^{\infty} B^n P(B,V), \tag{7.1}$$

where $\langle B^n \rangle_V$ is the $n^{\text{th}}$ order moment. Following the procedure to be discussed in chapter 8, one can easily compute the cumulants from the moments. Dividing by $V$ will generate the volume independent reduced cumulants. The first few reduced cumulants are

$$\begin{aligned} c_1(T,\mu) &= \frac{1}{V}\langle B \rangle_V , \\ c_2(T,\mu) &= \frac{1}{V}\left\langle (\delta B)^2 \right\rangle_V , \\ c_3(T,\mu) &= \frac{1}{V}\left\langle (\delta B)^3 \right\rangle_V , \\ c_4(T,\mu) &= \frac{1}{V}\left\langle (\delta B)^4 - 3(\delta B)^2 \right\rangle_V^2 , \end{aligned} \tag{7.2}$$

where $\delta B = B - \bar{B}$. Both the cumulant ratios and the reduced cumulants are volume independent.

The distribution of protons in a Hadron Resonance Gas model (HRG) follow a Skellam distribution which is defined as the difference between two Poisson distributions. Thus, the even and odd reduced cumulants of a HRG are

$$\begin{aligned} c_{2n+1}^{(HRG)} &= \frac{1}{V}(\langle B \rangle_1 - \langle B \rangle_{-1}), \\ c_{2n}^{(HRG)} &= \frac{1}{V}(\langle B \rangle_1 + \langle B \rangle_{-1}), \end{aligned}$$

where $B_1$ and $B_{-1}$ are for baryons and anti-baryons, respectively. In the absence of anti-protons, the cumulant ratios $C_2/C_1$, $C_3/C_2$, and $C_4/C_2$ equate to one.

Now, let us consider the more realistic fluctuating volume in which the probability distribution of the volume is $\mathcal{P}(V)$ and $n^{\text{th}}$ moment is

$$\langle V^n \rangle = \int V^n \mathcal{P}(V) dV. \tag{7.3}$$

Similarly, one can define a reduced volume cumulant $v_n = (\delta V)^n / \langle V \rangle$. The net-baryon cumulants are

$$\langle B^n \rangle = \int dV \mathcal{P}(V) \sum_{B=-\infty}^{\infty} B^n P(B,V) = \int dV \mathcal{P}(V) \langle B^n \rangle_V . \tag{7.4}$$

The fixed volume $\langle B^n \rangle_V$ can be calculated with Eq. (7.2). From Eq. (7.4) and $\langle B^n \rangle_V$, one can calculate the reduced cumulants with a fluctuating volume as

$$\begin{aligned} \tilde{c}_1 &= c_1, \\ \tilde{c}_2 &= c_2 + c_1^2 v_2, \\ \tilde{c}_3 &= c_3 + 3c_2 c_1 v_2 + c_1^3 v_3, \\ \tilde{c}_4 &= c_4 + (4c_3 c_1 + 3c_2^2) v_2 + 6c_2 c_1^2 v_3 + c_1^4 v_4. \end{aligned} \tag{7.5}$$

Here, $\tilde{c}_n \equiv \langle B^n \rangle$ are the measured cumulants and $c_n$ are the volume independent cumulants. The coefficients in Eq. (7.5) are given by the complete Bell polynomials [103] defined as

$$B_n(x_1, \ldots, x_n) = \sum_{k=1}^{n} B_{n,k}(x_1, x_2, \ldots, x_{n-k+1}), \tag{7.6}$$

where $B_{n,k}(x_1, x_2, \ldots, x_{n-k+1})$ are the incomplete Bell polynomials defined as

$$B_n(x_1, x_2, \ldots, x_{n-k+1}) = \sum \frac{n!}{j_1! j_2! \ldots j_{n-k_1}!} \left(\frac{x_1}{1!}\right)^{j_1} \left(\frac{x_2}{2!}\right)^{j_2} \ldots \left(\frac{x_{n-k+1}}{(n-k+1)!}\right)^{j_{n-k+1}} . \tag{7.7}$$

The heuristic approach describes two different cumulants of the baryon number distribution: a volume independent $c_n(T, \mu)$, which is expected to be sensitive to critical fluctuations [7, 48], and a volume dependent $\tilde{c}_n$, which is also sensitive to the geometry of the collision. Only $\tilde{c_n}$ can be directly measured in heavy-ion collisions.

When the VF are small, the measured cumulants are approximately the volume independent cumulants $\tilde{c}_n \approx c_n$. At first approximation, the effect of VF scales with the width of the correlation band in Fig. 7.2. Note that Eq. (7.5) is only valid when the baryon number and the volume are independent, such that each participant acts as an independent source. From Fig. 7.2, it is shown in the Glauber Model $N_{\text{part}}$ versus `FxtMult3` distribution that particle production linearly scales with $N_{\text{part}}$. Here, each source is an

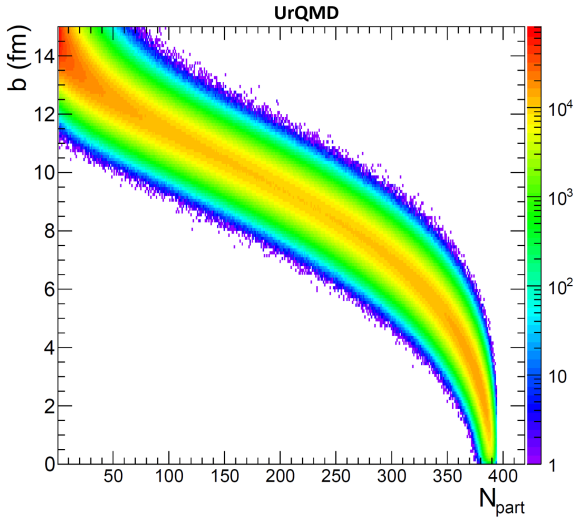


Figure 7.1. Impact parameter versus number of participating nucleons for UrQMD events. Both are measures of the collision volume and are highly correlated.

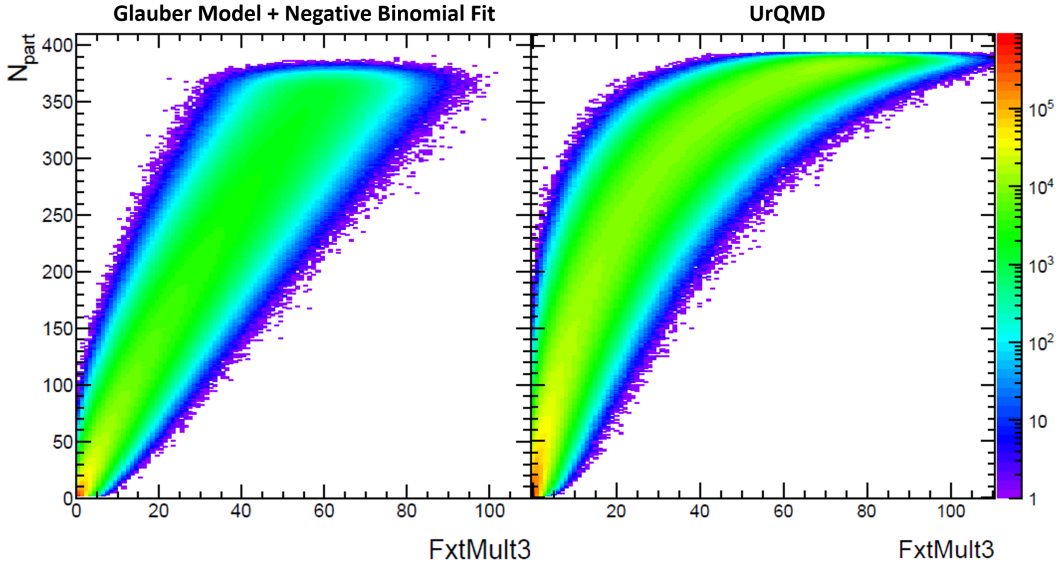


Figure 7.2. Number of participating nucleons versus reference multiplicity (`FxtMult3`) for Glauber Model and UrQMD events.

independent nucleon. This is expected for a Monte Carlo Glauber Model which calculates heavy-ion collisions by superimposing nucleon-nucleon collisions. The UrQMD multiplicity distribution, however, does not linearly scale with $N_{\text{part}}$. Therefore, the VF correction will not describe all of the underlying dynamics.

## 7.2 Volume Fluctuation Correction

### 7.2.1 Data-driven Correction

A simple data-driven method that reduces the VF is the centrality bin width correction (CBWC) [82]. The CBWC reduces the VF by calculating the cumulants in each multiplicity bin and computing a weighted average for each centrality class. The $i^{\text{th}}$ order cumulant for a given centrality class is

$$C_i = \frac{\sum_m n_m C_{i,m}}{\sum_m n_m}, \tag{7.8}$$

where $n_m$ and $C_{i,m}$ are the number of events and the cumulant in the $m_{th}$ multiplicity bin and $m$ spans the multiplicity bins in a centrality class.

At leading order, the effect from VF is proportional to the normalized variance of the $N_{\text{part}}$ distribution ($\langle V_2 \rangle / \langle V_1 \rangle$ in Eq. 7.5). Calculating the cumulants ($C_{i,m}$) at each multiplicity bin, reduces $\langle V_2 \rangle / \langle V_1 \rangle$, which in turn reduces the VF effect. Figure 7.3 shows the $N_{\text{part}}$ distribution for the top centrality class ($48 \leq$ `FxtMult3` $< 80$) and for various multiplicity bins. The corresponding $\langle V_1 \rangle$, $\langle V_2 \rangle$, and $\langle V_2 \rangle / \langle V_1 \rangle$ are in Table 7.1. Both the figure and table show that the fluctuations ($\langle V_2 \rangle / \langle V_1 \rangle$) decrease at higher multiplicities. This is caused by the increase in centrality resolution at higher multiplicities. Figure 7.4 is the Au+Au $\sqrt{s_{NN}} = 3.0$ GeV proton cumulants with and without CBWC applied. With CBWC applied, the wide binned cumulants follow the cumulants as a function of multiplicity.

| Mult. | $\langle V_1 \rangle$ | $\langle V_2 \rangle$ | $v_2$ ($\langle V_2 \rangle$ / $\langle V_1 \rangle$) |
|---|---|---|---|
| 48-79 | 326.50 ± 0.02 | 888.7 ± 0.6 | 2.721 ± 0.001 |
| 48 | 301.0 ± 0.1 | 1035 ± 2 | 3.439 ± 0.002 |
| 52 | 316.2 ± 0.1 | 875 ± 2 | 2.767 ± 0.002 |
| 56 | 328.3 ± 0.1 | 693 ± 2 | 2.111 ± 0.003 |
| 60 | 341.0 ± 0.1 | 526 ± 2 | 1.543 ± 0.004 |
| 64 | 344.1 ± 0.1 | 397 ± 2 | 1.154 ± 0.005 |
| 68 | 349.2 ± 0.1 | 297 ± 2 | 0.851 ± 0.007 |

Table 7.1. The first two cumulants of the Glauber Model $N_{\text{part}}$ distribution ($\langle V_1 \rangle$ and $\langle V_2 \rangle$) in Fig. 7.3.

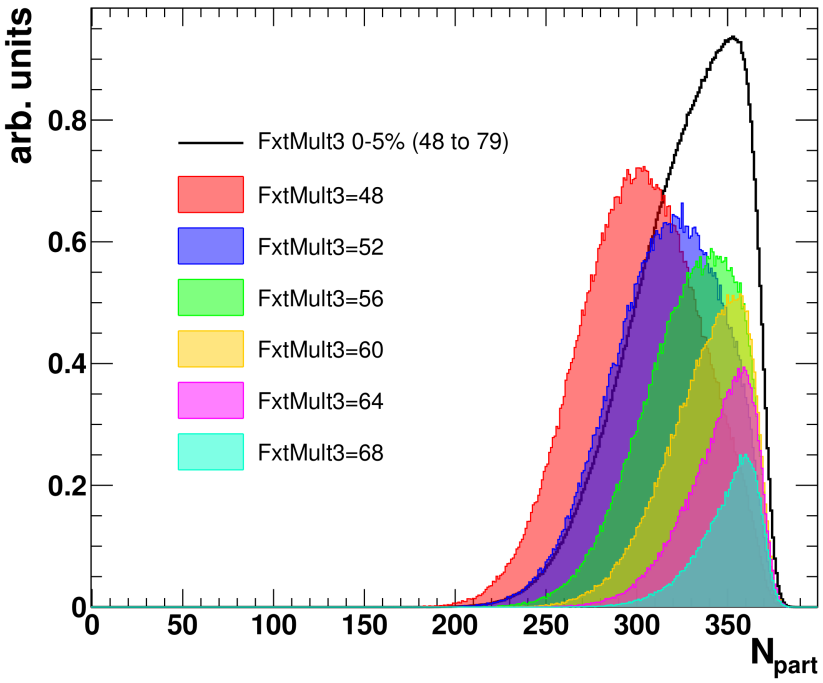


Figure 7.3. The Glauber Model $N_{\text{part}}$ distributions for six different multiplicity bins and the top centrality class 0-5%. The small multiplicity bins and the top centrality class are arbitrarily scaled for clarity.

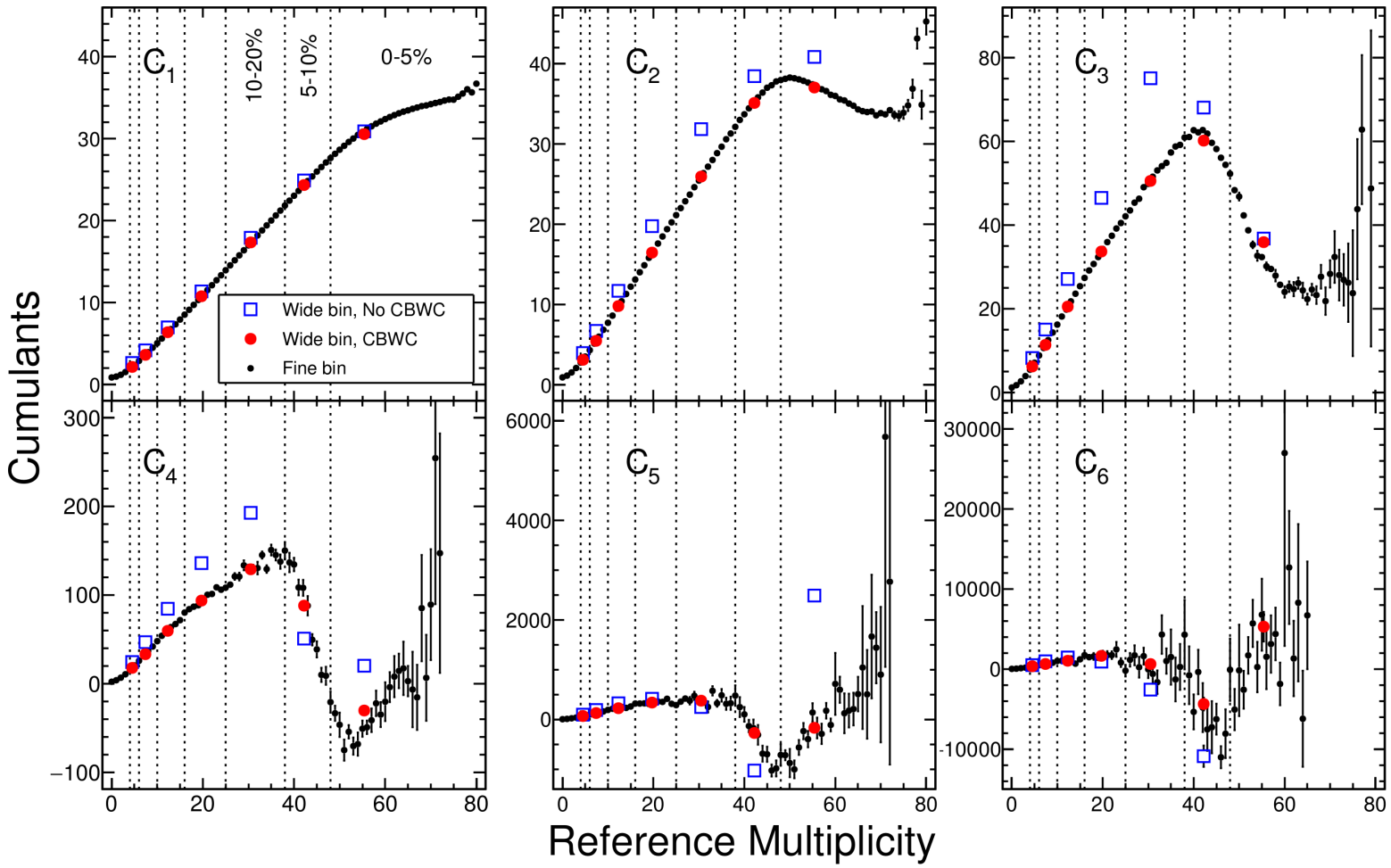


Figure 7.4. Cumulants of the event-by-event proton multiplicity distribution in Au+Au collisions at $\sqrt{s_{NN}} = 3.0$ GeV measured up to $6^{\text{th}}$ order in the kinematic acceptance $-0.5 < y < 0$ and $0.4 < p_T < 2.0$ GeV/$c$. The cumulants as a function of `FxtMult3` are displayed in black. The cumulants with and without CBWC are displayed by red and blue, respectively. The CBWC cumulants are plotted at their average `FxtMult3`. Vertical lines indicate the centrality bin edges in Table 3.1. The pile-up correction is applied to the red circles and black dots and are shown in Fig. 6.22.

### 7.2.2 Model Correction

The CBWC method reduces the centrality bin size, which reduces the VF. If the VF are small, the measured reduced cumulants $\tilde{c_n}$ and volume independent reduced cumulants $c_n$ are approximately equal, see Eq. (7.5). At $\sqrt{s_{NN}} = 3.0$ GeV, however, there were concerns that residual volume fluctuation effects are not significantly reduced by CBWC and an additional model correction may be necessary. The correction is outlined in Refs. [103, 104], but is similar to the heuristic approach discussed in section 7.1. By taking protons as a proxy for baryons and solving for $c_n$ in Eq. (7.5), the first three volume corrected reduced cumulants are

$$\begin{aligned} c_1 &= \tilde{c}_1, \\ c_2 &= \tilde{c}_2 - \tilde{c}_1^2 v_2, \\ c_3 &= \tilde{c}_3 - 3\tilde{c}_2\tilde{c}_1 v_2 + 3\tilde{c}_1^2 v_2^2 - \tilde{c}_1 v_3, \end{aligned} \tag{7.9}$$

where $c_n$ is the $n^{\text{th}}$ volume corrected reduced cumulant and $\tilde{c}_n$ is $n^{\text{th}}$ measured reduced cumulant. The reduced cumulants can be converted to cumulants by multiplying the reduced cumulants by $\langle N_{\text{part}} \rangle$ ($C_n = c_n \langle N_{\text{part}} \rangle$). While the correction appears straightforward, the underlying $N_{\text{part}}$ distribution is not measured in heavy-ion collisions. Therefore, the $N_{\text{part}}$ distribution and the $v_n$ cumulants are calculated from a model. In the first BES, the cumulant values corrected with CBWC and VFC agreed within statistical uncertainty (see Fig. 7.5). This indicated that the VF effect was small and CBWC was sufficient.

Figure 7.6 is the $\sqrt{s_{NN}} = 3.0$ GeV proton cumulants within the kinematic acceptance $-0.5 < y < 0$ and $0.4 < p_T < 2.0$ GeV/$c$ with and without the VFC. Unlike BES-I, the VFC and CBWC do not agree. In comparison to the BES-I data, the larger effect at $\sqrt{s_{NN}} = 3.0$ GeV data set can be explained by the lower centrality resolution. The VF decrease with improved centrality resolution. The boundaries of the $N_{\text{part}}$ distribution are restricted to zero and twice the mass number $2 \times 179$ for gold ions. Assuming $N_{\text{part}}$ and multiplicity vary monotonically, if the boundaries of the multiplicity distribution (0–100 in Fig. 7.2) increase, the widths in Fig. 7.3 will decrease. At $\sqrt{s_{NN}} = 3.0$ GeV, the peak particle multiplicity (excluding pileup) is `FxtMult3` $\approx 80$. The peak particle multiplicity

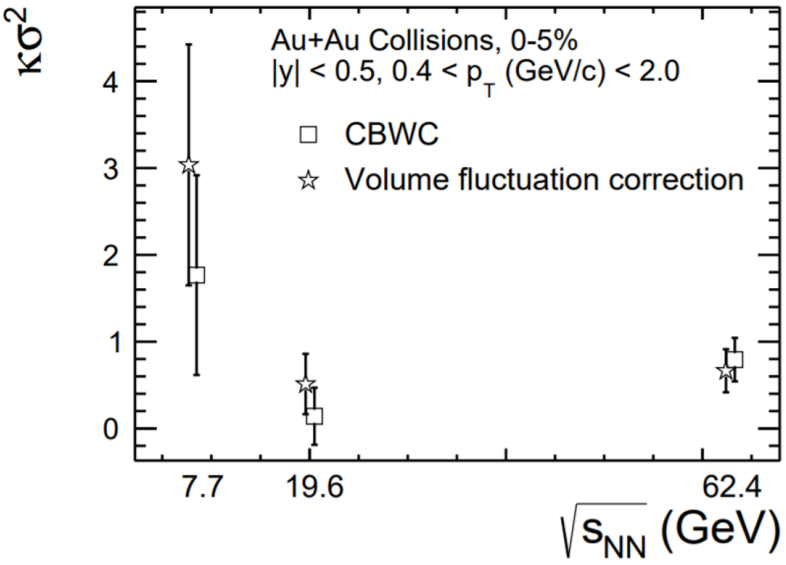


Figure 7.5. BES-I $\kappa\sigma^2$ corrected with either the Centrality Bin Width Correction (CBWC) or the volume fluctuation correction (VFC). The $\kappa\sigma^2$ is equivalent $C_4/C_2$ (see section 8.1). The results agree within statistical uncertainties. Figure from Ref. [6].

is `RefMult3` $\approx 400$ at the lowest energy of the BES-I.

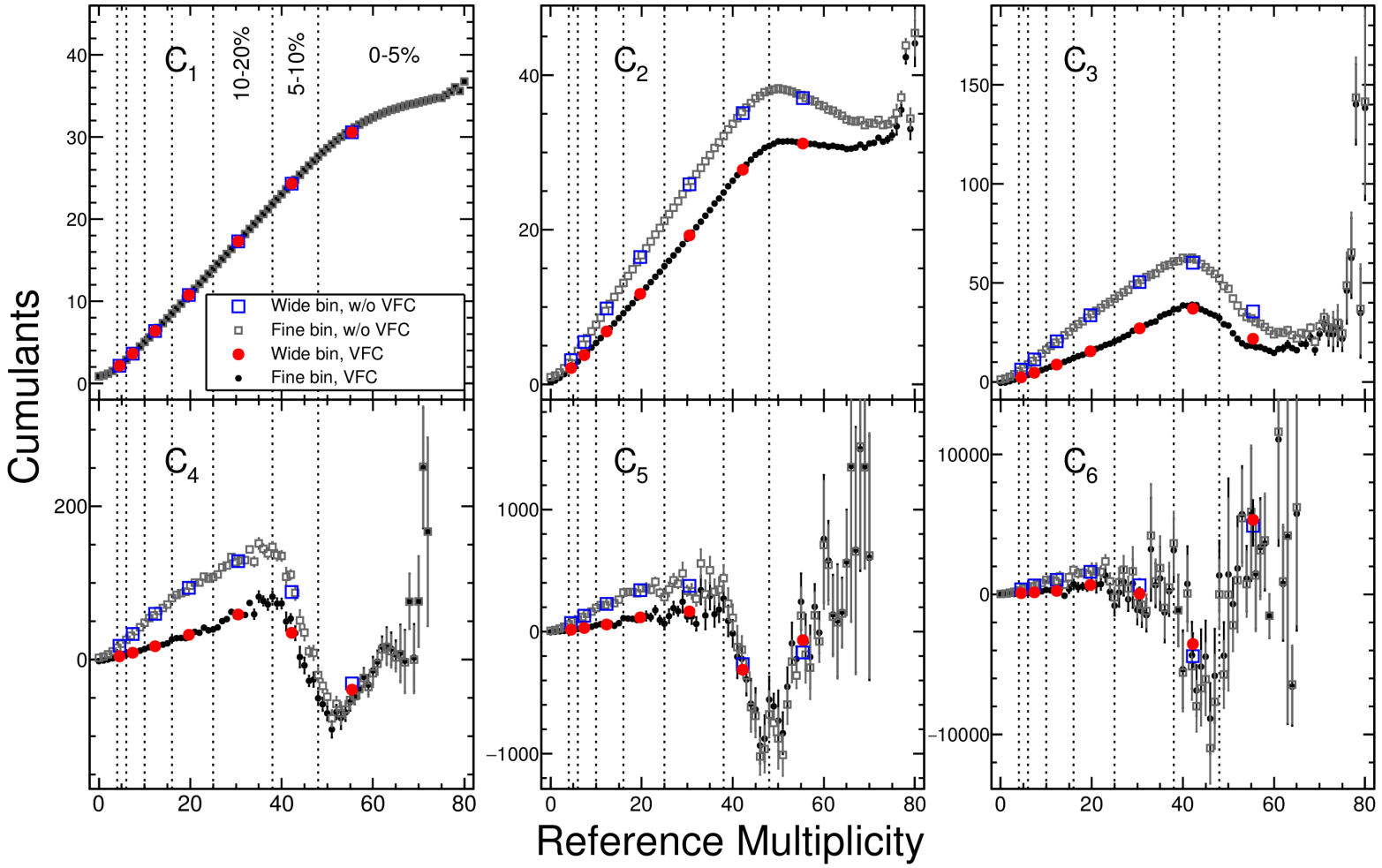


Figure 7.6. Cumulants of the event-by-event proton multiplicity distribution in Au+Au collisions at $\sqrt{s_{NN}} = 3.0$ GeV measured up to $6^{\text{th}}$ order in the kinematic acceptance $-0.5 < y < 0$ and $0.4 < p_T < 2.0$ GeV/$c$. The cumulants as a function of `FxtMult3` are displayed in black. The cumulants with and without VFC are displayed in red and blue, respectively. The CBWC cumulants are plotted at their average `FxtMult3`. Vertical lines indicate the centrality bin edges in Table 3.1.

It should be mentioned that the VFC is applied to the $\sqrt{s_{NN}} = 3.0$ GeV and BES-I data differently. In the BES-I analysis, the VFC cumulants are compared to CBWC cumulants—at $\sqrt{s_{NN}} = 3.0$ GeV, both CBWC and VFC are applied. This is for two reasons. First, the pileup correction requires CBWC and therefore a VFC cumulant without CBWC will contain pileup contamination. Second, the BES-I data was less affected by VFC and thus the additional correction was not necessary.

### 7.2.3 Model Comparison

Figure 7.6 shows the cumulants up to sixth order with a VFC correction. The $N_{\text{part}}$ distribution of the Glauber Model is used to calculate the volume fluctuation terms $v_n$. To test the model dependence, the VFC is also performed using the $N_{\text{part}}$ distribution from a transport model (UrQMD). A comparison of the $N_{\text{part}}$ distributions of the Glauber Model and UrQMD is shown in Fig. 7.7. In the most central events (0-5%), the Glauber Model is wider ($\langle V_2 \rangle$) and has a lower mean ($\langle V_1 \rangle$) with respect the UrQMD $N_{\text{part}}$ distribution. This is likely due to the difference in approach of the two models. The Glauber Model assumes all particles are produced from the binary collisions of overlapping participants in two dimensions. The UrQMD model is a cascade model in which participants can have multiple interactions in 3-dimensions. Thus, the $N_{\text{part}}$ distribution of UrQMD model includes more complex dynamics. Figure 7.8 is a comparison of the cumulants with the VFC using the Glauber and UrQMD $N_{\text{part}}$ distributions. While the two models converge at both low and high multiplicities, the two models disagree in mid-central collisions. Figure 7.9 shows the CBWC cumulants and cumulant ratios with VFC (Glauber and UrQMD) and without VFC.

Algebraically, the $C_2$ and $C_3$ value will always decrease due to the volume correction, see Eq. (7.9).[2] This is also true for higher order cumulants if all lower order cumulants are positive.

If all VF are removed, it is assumed [104] that the cumulant ratio $C_2/C_1$ equals 1 in the absence of proton correlations. This does not occur with either correction for most

[2]The average and variance of a non-negative distribution are positive. Thus $c_1$, $c_2$, $v_1$, and $v_2$ are positive. Therefore, the volume correction to $C_2$ is negative ($-c_1^2 V_2$).

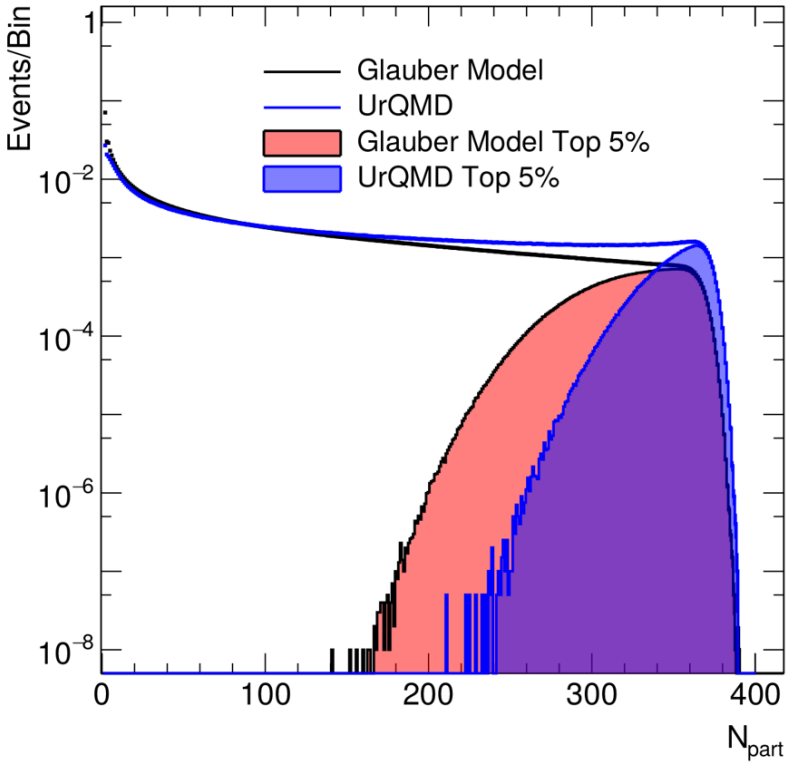


Figure 7.7. Comparison of the $N_{\text{part}}$ distribution for the Glauber Model and UrQMD.

centrality bins. Both VFCs (Glauber and UrQMD) reduce the $C_3/C_2$ ratio from unity ($C_3/C_2 = 0.961 \pm 0.008\,(\text{stat.}) \pm 0.06\,(\text{syst.})$) to a slight suppression ($C_3/C_2 = 0.760 \pm 0.008\,(\text{stat.}) \pm 0.06\,(\text{syst.})$ and $C_3/C_2 = 0.850 \pm 0.008\,(\text{stat.}) \pm 0.06\,(\text{syst.})$ for Glauber and UrQMD, respectively). The higher-order cumulant ratios[3] $C_4/C_2$, $C_5/C_1$, and $C_6/C_2$ in central collisions with and without VFC agree within systematic uncertainty. This is less meaningful for $C_5/C_1$ and $C_6/C_2$ as the systematic uncertainties are very large. The $C_4/C_2$ ratio, however, appears unaffected by the volume fluctuation correction in the top centrality class. In general, the cumulant ratios of the two VFCs (Glauber UrQMD) do not agree, which indicates a significant model dependence in the correction.

[3]The higher-order $C_5/C_1$ and $C_6/C_2$ ratios are studied due to the relation discussed in Eq. (1.30), where both $C_{\text{even}}/C_{\text{even}}$ and $C_{\text{odd}}/C_{\text{odd}}$ equal 1 for an HRG. In contrast, $C_3/C_2$ can be directly related to the normalized skewness (see Eq. (8.10)).

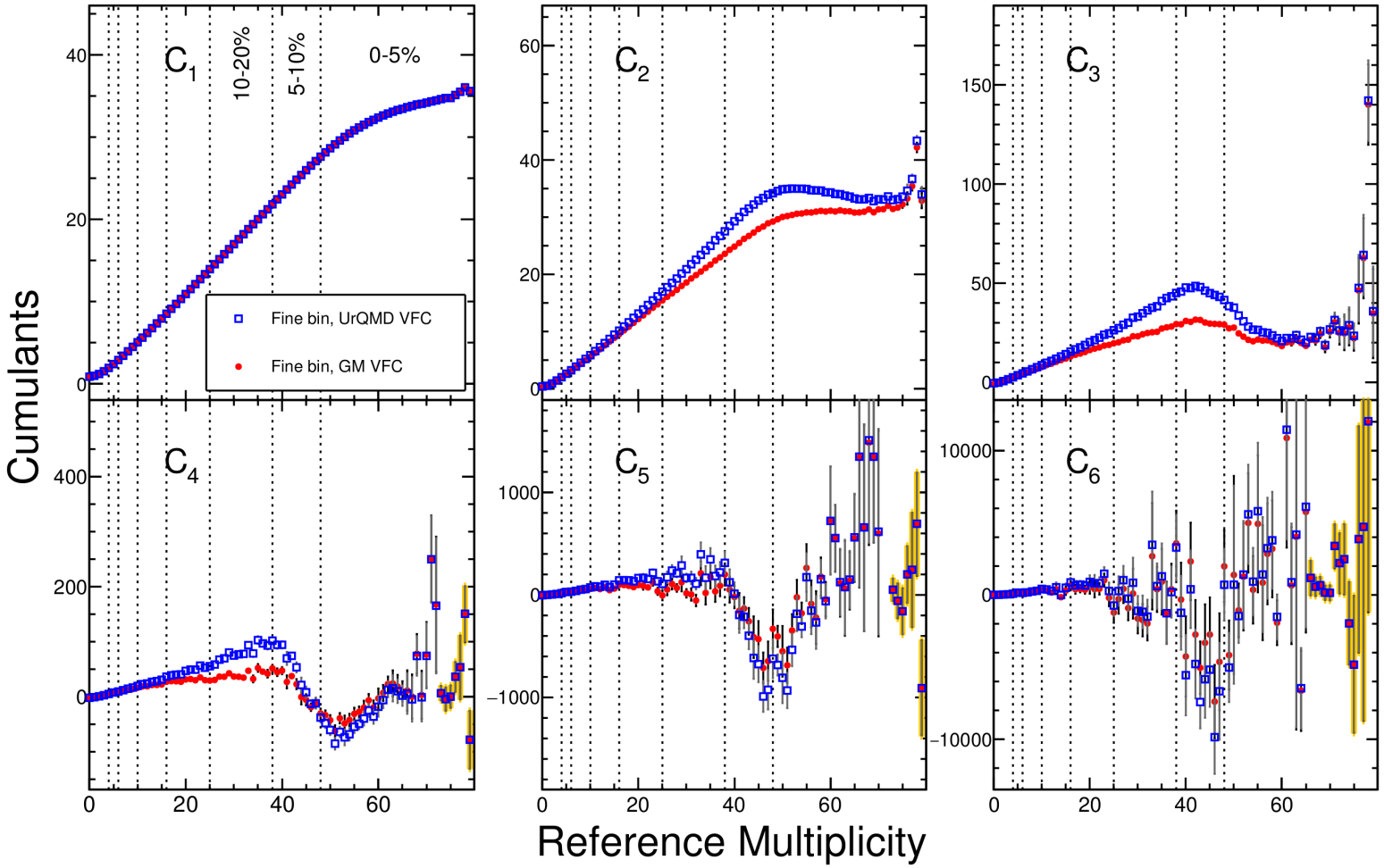


Figure 7.8. Comparison of cumulants of the event-by-event proton multiplicity distribution in Au+Au collisions at $\sqrt{s_{NN}} = 3.0$ GeV corrected for VF with the UrQMD or Glauber Model. Cumulants are measured up to $6^{\text{th}}$ order in the kinematic acceptance $-0.5 < y < 0$ and $0.4 < p_T < 2.0$ GeV/$c$. The cumulants with the VFC using the Glauber and UrQMD model $N_{\text{part}}$ distributions are displayed by red and blue markers, respectively. Vertical lines indicate the centrality bin edges in Table 3.1. Yellow markers indicate a scaling of the data and uncertainties by 0.25.

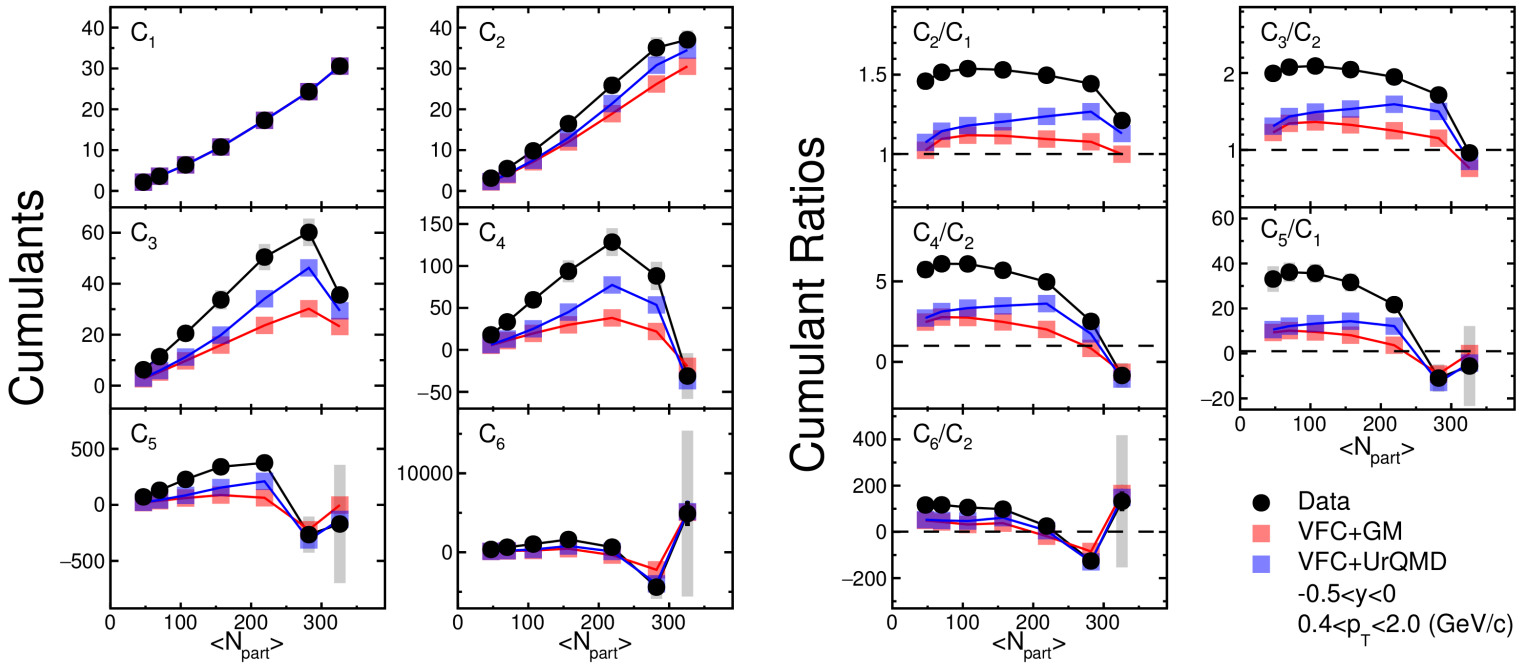


Figure 7.9. Comparison of cumulants and cumulant rations of the event-by-event proton multiplicity distribution in Au+Au collisions at $\sqrt{s_{NN}} = 3.0$ GeV corrected for VF with the UrQMD or Glauber Model. Cumulants are measured up to $6^{\text{th}}$ order in the kinematic acceptance $-0.5 < y < 0$ and $0.4 < p_T < 2.0$ GeV/$c$. The cumulants and ratios without VFC, with VFC using Glauber Model, and with VFC using UrQMD are depicted in black, red and blue, respectively. Statistical and systematic uncertainties are displayed by black and gray bars, respectively. The average $N_{\text{part}}$ is defined by Table 3.1 and corresponds to a centrality class (range of multiplicity) corrected with the CBWC.

# Chapter 8

# Cumulant and Correlation Function Calculations

## 8.1 Moments and Cumulants

Cumulants and moments describe the shape of a probability distribution. The moments can be specified through the moment-generating function. Let $N$ be a random variable of a normalized[1] probability distribution $P(N)$. Provided that an expectation value $\langle . \rangle$ exists for $t$ in some neighborhood of zero, the moment-generating function is

$$M_N(\theta) = \sum_N e^{\theta N} P(N) = \left\langle e^{\theta N} \right\rangle . \tag{8.1}$$

Using the series expansion of $e^{tN}$, $M_N(t)$ is expressed as

$$M_N(\theta) = \langle e \rangle = 1 + t \langle N \rangle + \theta^2 \frac{\langle N^2 \rangle}{2!} + \theta^3 \frac{\langle N^3 \rangle}{3!} + ... + \theta^n \frac{\langle N^n \rangle}{n!} + ..., \tag{8.2}$$

and the $m^{\text{th}}$ raw moment $\mu_m^{'}$ is computed by taking the derivative $m$ times and evaluating at $\theta = 0$. The moments are

$$\mu_m^{'} = M_N^{(m)}(0) = \left. \frac{d^m M_N}{d\theta^m} \right|_{\theta=0} . \tag{8.3}$$

For a probability distribution $P(N)$, in which $N$ is an entry in the data sample, the raw moments are

$$\mu_m^{'} \equiv \langle N^m \rangle = \sum_N N^m P(N). \tag{8.4}$$

[1]Normalized such that $\sum_N P(N) = 1$.

The central moments of a distribution are described by

$$\mu_m \equiv \langle (\delta N)^m \rangle = \sum_N (\delta N)^m P(N), \tag{8.5}$$

where $\langle N \rangle$ is the first moment and $\delta N = N - \langle N \rangle$ is the deviation from the mean value.

Cumulants, which provide an alternative description of a probability distribution, can be constructed from moments. The cumulant-generating function is the natural log of the moment generating function:

$$K_N(\theta) = \log \left\langle e^{\theta N} \right\rangle . \tag{8.6}$$

The cumulants $C_i$ are similarly obtained by expanding $e^{\theta N}$, differentiating $m$ times, and evaluating at $\theta = 0$. The cumulants are defined as

$$C_m \equiv \langle N \rangle_c = \left. \frac{d^m K(\theta)}{d\theta^m} \right|_{\theta=0}. \tag{8.7}$$

In terms of moments, the cumulants are defined as

$$\begin{aligned} C_1 &= \langle N \rangle , \\ C_2 &= \left\langle (\delta N)^2 \right\rangle = \mu_2, \\ C_3 &= \left\langle (\delta N)^3 \right\rangle = \mu_3, \\ C_4 &= \left\langle (\delta N)^4 \right\rangle - 3 \left\langle (\delta N)^2 \right\rangle^2 = \mu_4 - 3\mu_2^2, \\ C_n (n > 3) &= \mu_n - \sum_{m=2}^{n-2} \binom{n-1}{m-1} C_m \mu_{n-m}. \end{aligned} \tag{8.8}$$

The cumulants are related to the various moments as

$$\begin{aligned} M = C_1, \qquad & \sigma^2 = C_2, \\ S = \frac{C_3}{(C_2)^{3/2}}, \quad & \kappa = \frac{C_4}{C_2^2}. \end{aligned} \tag{8.9}$$

The products of moments can be expressed in terms of the cumulant ratios as

$$\sigma^2/M = \frac{C_2}{C_1}, \quad S\sigma = \frac{C_3}{C_2}, \quad \kappa\sigma^2 = \frac{C_4}{C_2}. \tag{8.10}$$

Moments and cumulants are often interchangeable and two probability distributions with the same moments will have identical cumulants. However, some distributions are

more easily expressed by one or the other. A normal distribution $N(\mu, \sigma^2)$ is well described by moments. The $r^{\text{th}}$ central moments of $N(\mu, \sigma^2)$ are

$$\langle (\delta N)^r \rangle = \begin{cases} 0 & \text{if } r \text{ is even,} \\ \sigma^r (r-1)!! & \text{if } r \text{ is odd.} \end{cases} \tag{8.11}$$

On the other hand, a Poisson distribution is more easily described by cumulants. The cumulant generating function is

$$K_N(\theta) = \langle N \rangle \left(e^{\theta} - 1\right) \tag{8.12}$$

and all cumulants are equal ($C_1 = C_2 = ... = C_i = \langle N \rangle$). Thus, all cumulant ratios equate to one.

## 8.2 Factorial Moments and Correlation Functions

The moments and cumulants are closely linked to factorial moments and factorial cumulants (correlation functions). The factorial moment is the expectation value of the falling factorial of a random variable. The $r^{\text{th}}$ factorial moment is defined as

$$\langle N^r \rangle_f = \langle N(N-1)(N-2)...(N-r+1) \rangle \,. \tag{8.13}$$

and similarly, the factorial cumulant is

$$\langle N^r \rangle_{fc} = \langle N(N-1)(N-2)...(N-r+1) \rangle_c \,. \tag{8.14}$$

using the definition of $\langle . \rangle_c$ from Eq. (8.7).

The factorial moment can be expressed by the factorial moment-generating function as

$$M_{f,N}(s) = \sum_N s^N P(N) = \left\langle s^N \right\rangle . \tag{8.15}$$

Likewise, the factorial cumulant-generating function is

$$K_f(s) = \log M_f(s). \tag{8.16}$$

Alternatively, Eq. (8.13) and (8.14) are expressed by

$$\langle N^r \rangle_f = \left. \frac{d^m M_f(s)}{ds^m} \right|_{s=1}, \quad \langle N^r \rangle_{fc} = \left. \frac{d^m K_f(s)}{ds^m} \right|_{s=1}. \tag{8.17}$$

Both the generating functions from Eq. (8.1) and (8.6) are related to Eq. (8.15) and (8.16), respectively, by a change of variable in the generating function $e^{\theta} \to s$ such that

$$K(\theta) = K_f(e^{\theta}), \quad K_f(s) = K(\ln s), \tag{8.18}$$

$$M(\theta) = M_f(e^{\theta}), \quad M_f(s) = M(\ln s). \tag{8.19}$$

Factorial cumulants can describe the multi-particle correlations functions $\kappa_n$. A more thorough description of net-proton correlation functions can be found in Ref. [105]. First, let us introduce the correlation functions with the two particle density $\rho(p_1, p_2)$ for particles with momenta $p_1$ and $p_2$ as

$$\rho_2(p_1, p_2) = \rho(p_1)\rho(p_2) + \kappa(p_1, p_2), \tag{8.20}$$

where $\rho(p_1)$ is the one particle density and $\kappa(p_1, p_2)$ is the two particle correlation function. In general, the two particle density will depend on the particle momentum of both particles. For simplicity, the discussion is restricted to correlations in rapidity and the notation

$$\rho_2(y_1, y_2) = \int dp_{t,1} d\phi_1 dp_{t,2} d\phi_2 \rho_2(p_1, p_2), \tag{8.21}$$

$$\kappa_2(y_1, y_2) = \int dp_{t,1} d\phi_1 dp_{t,2} d\phi_2 \kappa_2(p_1, p_2), \tag{8.22}$$

$$\kappa_2 = \int dy_1 dy_2 C_2(y_1, y_2), \tag{8.23}$$

is adopted. A similar procedure can be performed for higher order $\kappa_n$. Integrating over the momenta of $\rho_2(p_1, p_2)$, one gets

$$\left\langle N^2 \right\rangle_f \equiv \langle N(N-1) \rangle = \int dp_1 dp_2 \rho_2(p_1, p_2) = \langle N \rangle^2 + \kappa_2, \tag{8.24}$$

where $N$ is a particle number. If the procedure is repeated for the three and four particle integrated correlation functions, one gets

$$\left\langle N^3 \right\rangle_f = \langle N \rangle^3 + 3 \langle N \rangle \kappa_2 + \kappa_3, \tag{8.25}$$

$$\left\langle N^4 \right\rangle_f = \langle N \rangle^4 + 6 \langle N \rangle^2 \kappa_2 + 4 \langle N \rangle \kappa_3 + 3\kappa_2^2 + \kappa_4, \tag{8.26}$$

and the correlation functions are

$$\begin{aligned}
\kappa_2 &= \left\langle N^2 \right\rangle_f - \langle N \rangle^2 , \\
\kappa_3 &= \left\langle N^3 \right\rangle_f - 3 \langle N \rangle \left\langle N^2 \right\rangle_f + 2 \langle N \rangle^3 , \\
\kappa_4 &= \left\langle N^4 \right\rangle_f - 4 \left\langle N^3 \right\rangle_f \langle N \rangle - 3 \left\langle N^2 \right\rangle_f^2 + 12 \left\langle N^2 \right\rangle_f \langle N \rangle^2 - 6 \langle N \rangle^4 .
\end{aligned} \tag{8.27}$$

If $\delta N = N - \langle N \rangle$ is used to simplify Eq. (8.27), the correlation functions become

$$\begin{aligned}
\kappa_1 &= \langle N \rangle , \\
\kappa_2 &= \left\langle (\delta N)^2 \right\rangle_f , \\
\kappa_3 &= \left\langle (\delta N)^3 \right\rangle_f , \\
\kappa_4 &= \left\langle (\delta N)^4 \right\rangle_f - 3 \left\langle (\delta N)^2 \right\rangle_f^2 .
\end{aligned} \tag{8.28}$$

The similarity between Eq. (8.28) and (8.8) is due to the fact that the correlation function is equivalent to the factorial cumulant ($\langle N^n \rangle_{fc} = \kappa_n$).

Using Eq. (8.13), the correlation functions are expressed in terms of cumulants as

$$\begin{aligned}
\kappa_1 &= C_1, \\
\kappa_2 &= -C_1 + C_2, \\
\kappa_3 &= 2C_1 - 2C_2 + C_3, \\
\kappa_4 &= -6C_1 + 11C_2 - 6C_3 + C_4, \\
\kappa_5 &= 24C_1 - 50C_2 + 35C_3 - 10C_4 + C_5, \\
\kappa_6 &= -120C_1 + 274C_2 - 225C_3 + 85C_4 - 15C_5 + C_6.
\end{aligned} \tag{8.29}$$

Similarly, the correlation function ratios are

$$\begin{aligned}
\frac{\kappa_2}{\kappa_1} &= \frac{C_2}{C_1} - 1, \\
\frac{\kappa_3}{\kappa_1} &= (\frac{C_3}{C_1} - 1) - 3(\frac{C_2}{C_1} - 1), \\
\frac{\kappa_4}{\kappa_1} &= (\frac{C_4}{C_1} - 1) - 6(\frac{C_3}{C_1} - 1) + 11(\frac{C_2}{C_1} - 1), \\
\frac{\kappa_5}{\kappa_1} &= (\frac{C_5}{C_1} - 1) - 10(\frac{C_4}{C_1} - 1) + 35(\frac{C_3}{C_1} - 1) - 50(\frac{C_2}{C_1} - 1), \\
\frac{\kappa_6}{\kappa_1} &= (\frac{C_6}{C_1} - 1) - 15(\frac{C_5}{C_1} - 1) + 85(\frac{C_4}{C_1} - 1) - 225(\frac{C_3}{C_1} - 1) + 274(\frac{C_2}{C_1} - 1).
\end{aligned} \tag{8.30}$$

### 8.2.1 Statistical Uncertainty Estimation

The lowest energies of the BES-I analysis suffered from low statistics and only around three and seven million events were used for the $\sqrt{s_{NN}} = 7.7$ GeV and $\sqrt{s_{NN}} = 11$ GeV analyses, respectively. Thus, analyzers put in considerable effort to understand the statistical uncertainty. Three different methods for calculating the statistical uncertainty were proposed: the Delta theorem, Sub-sample, and the Bootstrap method. Due to its simplicity and the ease of error propagation, the Bootstrap method is implemented for the $\sqrt{s_{NN}} = 3.0$ GeV analysis. This section includes a description of each method.

**Delta Theorem** [106]

The Delta theorem is closely linked to the central limit theorem (CLT) and allows us to approximate an uncertainty by transforming a distribution with a known uncertainty. For our purposes, it allows us to calculate an analytic expression for cumulants and the cumulant ratios [106]. Before stating the Delta theorem, let us start with the CLT.

***Central Limit Theorem***: Let $\{X_1, ..., X_n\}$ be a random sample of size $n$, where $n$ is a sequence of identically distributed random variables from a distribution with $\mu$, $\sigma^2 < \infty$. As $n \to \infty$, the difference between sample average $\langle X \rangle = \frac{X_1, +..., X_n}{n}$ and $\mu$ when multiplied by $\sqrt{n}$ approximates to a normal distribution with $\langle X \rangle = 0$ and variance $\sigma^2$.

$$\sqrt{n}(\langle X \rangle - \mu) \xrightarrow{d} N(0, \sigma^2) \tag{8.31}$$

Building off of CLT, the Delta theorem states: If there is a sequence of random variables $X_n$ satisfying $\sqrt{n}(\langle X \rangle - \theta) \xrightarrow{d} N(0, \sigma^2)$, then

$$\sqrt{n}(g(\langle X \rangle) - g(\theta)) \xrightarrow{d} N(0, \sigma^2 \cdot g'(\theta)^2), \tag{8.32}$$

for any function $g$, where $g'(\theta)$ exists and is non-zero valued.

It is known [106] that the if the central moments $\mu_{2k} = \left\langle (X - \mu)^{2k} \right\rangle < \infty$, then the random vector $\sqrt{n}(\tilde{\mu}_2 - \mu_2, ..., \tilde{\mu}_k - \mu_k)$ converges in distributions to $(k-1)$-variate normal with mean vector $(0, ..., 0)$ and the covariance matrix $[\sum_{ij}]_{(k-1)\times(k-1)}$, where

$$\sum_{ij} = \mu_{i+j} - \mu_i \mu_j - i\mu_{i-1}\mu_{j+1} - j\mu_{i+1}\mu_{j-1} + ij\mu_{i-1}\mu_{j-1}\mu_2. \tag{8.33}$$

With Eq. (8.33) and the Delta theorem, the limiting distribution central moments transformed by a function $g$ can be calculated. For example, from Eq. (8.33), the limit distribution of the sample variance is

$$\hat{\sigma} \xrightarrow{d} N(\sigma^2, \frac{\mu_4 - \sigma^4}{n}). \tag{8.34}$$

To calculate the limit distribution of the standard deviation $\hat{\sigma}$, one can define the function $g(x) = \sqrt{x}$. Applying the Delta theorem, the limit distribution is

$$\hat{\sigma} \xrightarrow{d} N(\sigma, \frac{\mu_4 - \sigma^4}{4\sigma^2 n}). \tag{8.35}$$

***Multivariate Delta Theorem***:

To calculate the limit distributions of moment and cumulant ratios, a multivariate case of the Delta theorem is required. Suppose that $\mathbf{X} = \{X_1, ..., X_n\}$ is normally distributed as $N(\mu, \Sigma/n)$, where $\Sigma$ is a covariance matrix. Let $\mathbf{g(x)} = (g_1(x_1), ..., (g_m(x_k))$, where $\mathbf{x} = (x_1, ..., x_k)$, be a vector-valued function. Each component function $g_i(x)$ is real valued and has a non-differentiable $g_i(\mu)$, at $\mathbf{x} = \mu$. With the Jacobian determinant

$$\mathbf{D} = \left[ \frac{\partial g_i}{\partial x_j}\Big|_{x=\mu} \right], \tag{8.36}$$

the approximate statistic can be calculated as

$$\mathbf{g(X)} \xrightarrow{d} N(\mathbf{g}(\mu), \frac{\mathbf{D\Sigma D'}}{n}). \tag{8.37}$$

To calculate the standard error or cumulants or cumulant ratios, one can define a random sample moments vector as

$$\hat{T} = \begin{pmatrix} \hat{\mu_2} \\ \hat{\mu_3} \\ \hat{\mu_4} \end{pmatrix} \xrightarrow{d} N( \begin{pmatrix} \mu_2 \\ \mu_3 \\ \mu_4 \end{pmatrix}, \frac{\mathbf{\Sigma}}{n}), \tag{8.38}$$

where $\mathbf{\Sigma}$ is defined by Eq. (8.33).

To calculate cumulant ratios, $\mathbf{g(x)}$ defined by the equations 8.8 and 8.10. With Eq. (8.37), the sample error of the transformed random vector can be calculated.

The calculated variance of the cumulant ratios $C_3/C_2$ and $C_4/C_2$ are

$$\begin{aligned}\mathrm{Var(C_3/C_2)} &= (9 - 6\mu_4 + \mu_3^2(6 + \mu_4) - 2\mu_3\mu_5 + \mu_6)\sigma^2/n \\ \mathrm{Var(C_4/C_2)} &= (-9 + 6\mu_4^2 + \mu_4^3 + 8\mu_3^2(5 + \mu_4) - 8\mu_3\mu_5 \\ &\quad + \mu_4(9 - 2\mu_6) - 6\mu_6 + \mu_8)\sigma^4/n. \end{aligned} \tag{8.39}$$

**Sub-sample Method** [107]

For the Sub-sample method, the data sample is sub-divided into sub samples and the uncertainty is calculated from the variance of the sub-sample measurements. For example, given a data sample $X$, where $\hat{e}$ is a measurement such as mean or $C_4/C_2$, the procedure is:

1. Construct $S$ sub samples $X_1$, ..., $X_S$, each consisting of $n = \frac{N}{S}$ data points randomly selected from the parent sample without replacement.

2. Calculate the value of estimator for each sub sample, $\hat{e_s} = \hat{e}(X_s)$ for $s = 1, ..., S$.

3. The variance estimator is calculated as follows:
   $\mathrm{Var(\hat{e})} = \frac{1}{\mathrm{S(S-1)}} \sum_{\mathrm{s=1}}^{\mathrm{S}} (\hat{\mathrm{e}}_\mathrm{s} - \bar{\hat{\mathrm{e}}})^2$, where $\bar{\hat{e}} = \frac{1}{S} \sum_{s=1}^{S} (\hat{e_s})$

The extra factor of $1/S$ in the variance estimation is used to scale the sub-sample statistics to the statistics of the data sample.

**Bootstrap Method** [107]

The bootstrap method is similar to the Sub-sample method. In both methods, the variance of sample distributions is used to estimate the statistical uncertainty. Unlike the Sub-sample method, $B$ number of statistical samples are generated and each sample size is equivalent to the data set. The samples are generated by randomly selecting events with replacement.

If one has a data sample $X$, where the measurement is $\hat{e}$, the sample error procedure is as follows:

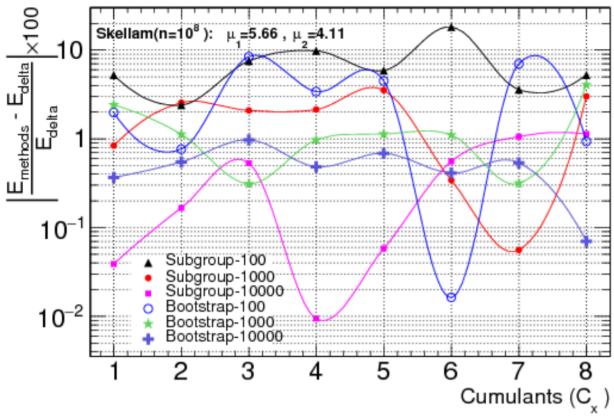


Figure 8.1. Relative percentage deviation of uncertainties obtained in Sub-sample and Bootstrap methods for cumulants up to $8^{\text{th}}$ order. The sample size is $10^8$ with the input parameters $\mu_1$ and $\mu_2$. Figure from Ref. [107].

1. Given a parent sample size $N$, construct $B$ number of independent bootstrap samples $X_1$,...,$X_B$ each consisting of $n$ data points randomly drawn with replacement from the parent sample.

2. Evaluate the estimator in each bootstrap sample, $\hat{e_b} = \hat{e}(X_b)$ for $b = 1, ..., S$.

3. The sample variance of the estimator is given as follows.
   $\text{Var}(\hat{\text{e}}) = \frac{1}{\text{B}-1}\sum_{\text{b}=1}^{\text{B}}(\hat{\text{e}}_\text{b} - \bar{\hat{\text{e}}})^2$, where $\bar{\hat{e}} = \frac{1}{B}\sum_{b=1}^{B}(\hat{e_b})$

The number of bootstraps to accurately characterize the statistical uncertainty is not well defined but studies [107] show agreement between the Delta theorem and Bootstrap method when $B > 1000$.

**Selection of Bootstrap Method**

The differences between the three methods has been studied in detail, see Ref. [107]. Figure 8.1 depicts the percent difference between the cumulant uncertainties from the Delta theorem and different Bootstrap and Sub-sample configurations. The Sub-sample performs worse than the Bootstrap method for the various iterations (100, 1000, 10000). Additionally, the bootstrap and Delta theorem agree at the %1 level if the number of bootstraps $B$ is increased significantly ($B > 10000$).

For this analysis, the Bootstrap method is the selected uncertainty estimation technique. While the Delta theorem is more accurate, the Bootstrap method naturally prop-

| Cut Variable | Nominal Value | Systematic Values |
|---|---|---|
| TPC spatial pts. | `NHitsFit` $< 10$ | 12, 15 |
| Mass-squared ($m^2$) | $0.6 < m^2 < 1.2$ GeV$^2/c^4$ | $\pm 0.1$ GeV$^2/c^4$ |
| Efficiency ($\epsilon$) | $\epsilon \times 1.0$ | $\epsilon \times 1.05$, $\times 0.95$ |
| DCA | DCA $< 3.0$ cm | DCA $< 2.5$, $< 2.0$ cm |
| Pile-up correction | $\min(\chi^2/ndf)$ | $\pm\chi^2/ndf$ |
| Cent. Definition (`FxtMult3`) | Table 3.1 | $\pm 1$ `FxtMult3` |

Table 8.1. Overview of systematic uncertainty variables.

agates through the various background corrections. Additionally, the Delta theorem requires one to calculate $\mu_{2n}$ of the $n^{\text{th}}$ highest moment. This is problematic as background and efficiency corrections become more difficult at higher orders. The number of iterations of the Bootstrap method was $B = 200$. Therefore, the error on the calculated uncertainty of the cumulants and cumulant ratios is likely between 1–7% .

### 8.2.2 Systematic Uncertainty Estimation

The systematic uncertainty of the cumulant calculation can be subdivided into three categories: uncertainty associated with event reconstruction, pileup corrections, and centrality determination. The event reconstruction includes the efficiency in the TPC and TOF, the track reconstruction requirements (DCA, `NHitsFit`), and the PID requirements ($N_{\sigma,p}$ and mass-squared cut). The centrality determination is defined by the centrality class definition in table 3.1. The effect of lowering the $dE/dx$ cut to $N_{\sigma,p} < 2$ was tested but did not affect the final result. To estimate the systematic uncertainty, the analysis was repeated with different analysis requirements which are outlined in table 8.1.

The size of the systematic uncertainties of the cumulants and cumulant ratios are depicted in Figs. 8.2 and 8.3, respectively. In both figures, the gray band is the total uncertainty and the markers represent the uncertainty from each systematic cut (systematic cuts defined in table 8.1).

At central collisions, the systematic uncertainty is dominated by the uncertainty due to reducing the DCA from DCA $< 3.0$ cm to DCA $< 2.0$ cm. Due to the large variation,

additional tests were performed: (DCA $< 1.0$ and DCA $< 1.5$ cm). The difference between DCA $< 2.0$ cm and the nominal DCA $< 3.0$ cm provides the maximum uncertainty. The source of the large variation is unclear. As stated in chapters 4 and 6, the DCA $< 2.0$ cm cut may remove background such as feed down, knockout proton contamination or pileup. However, the large difference only manifests at the highest centrality class and reaches a maximum at DCA $< 2.0$ cm. With either unaccounted feed down or knockout proton contamination, one would expect the difference between DCA $< 1.0$ cm and the nominal analysis to be the same or larger than the difference between DCA $< 2.0$ cm and the nominal analysis. To test for a pileup effect, the pileup unfolding procedure and pileup correction was repeated with the DCA $< 2.0$ cm cut, but the large uncertainty was not reduced. Additionally, the difference could be caused by the TPC efficiency. The TPC reconstruction simulation may not account for the change in efficiency for different DCA cuts. However, this difference is expected to be small. Both background and efficiency were investigated, but no clear evidence of either source was found.

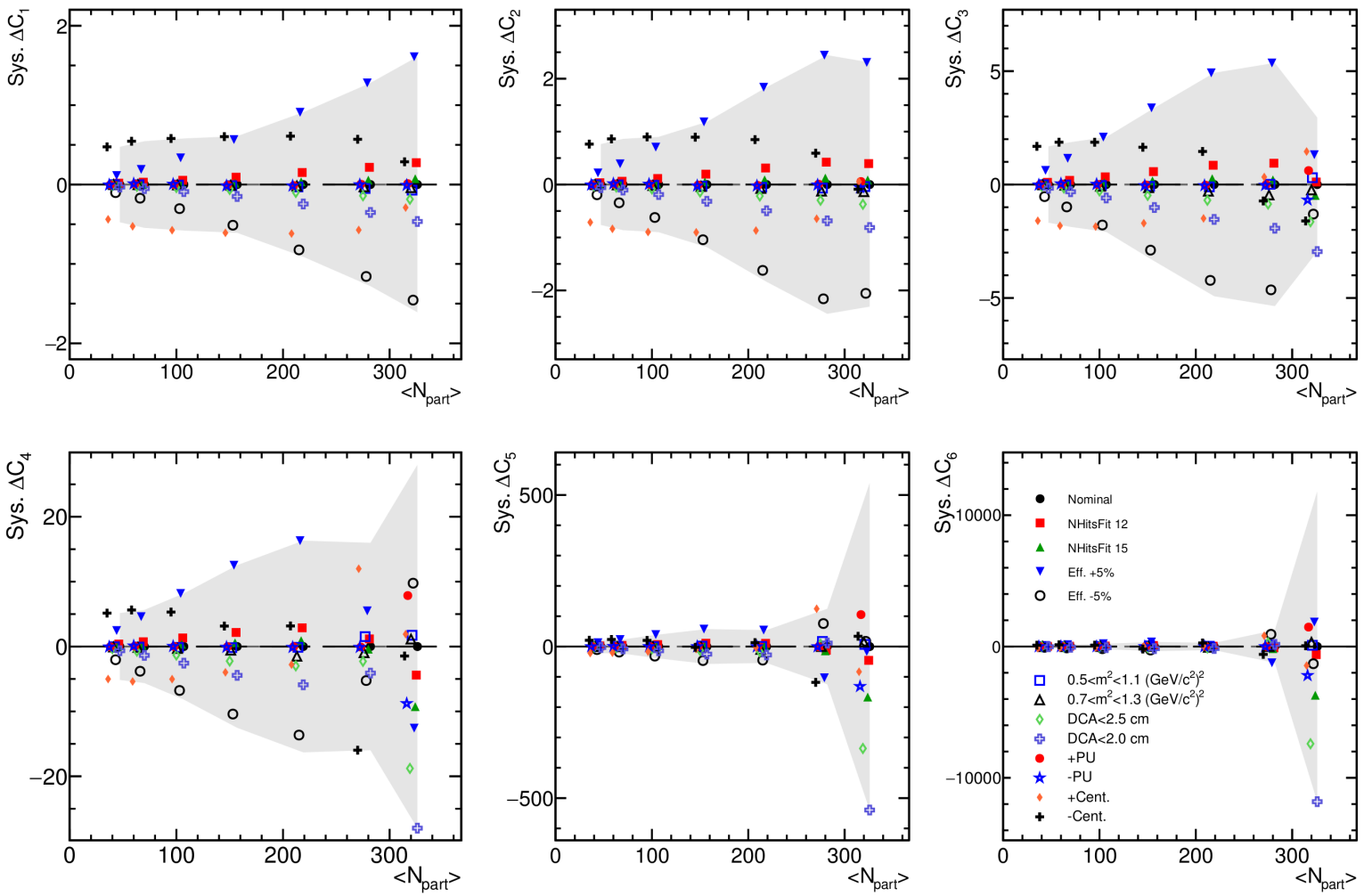


Figure 8.2. The absolute systematic uncertainty of the cumulants up to 6$^{\text{th}}$ order of the proton multiplicity distributions in Au+Au collisions at $\sqrt{s_{NN}} = 3.0$ GeV. The total systematic uncertainty is represented by a gray band. The difference between a systematic analysis and the nominal analysis is displayed by markers. Markers are offset in $\langle N_{\text{part}} \rangle$ for clarity. The systematic analyses are defined in table 8.1.

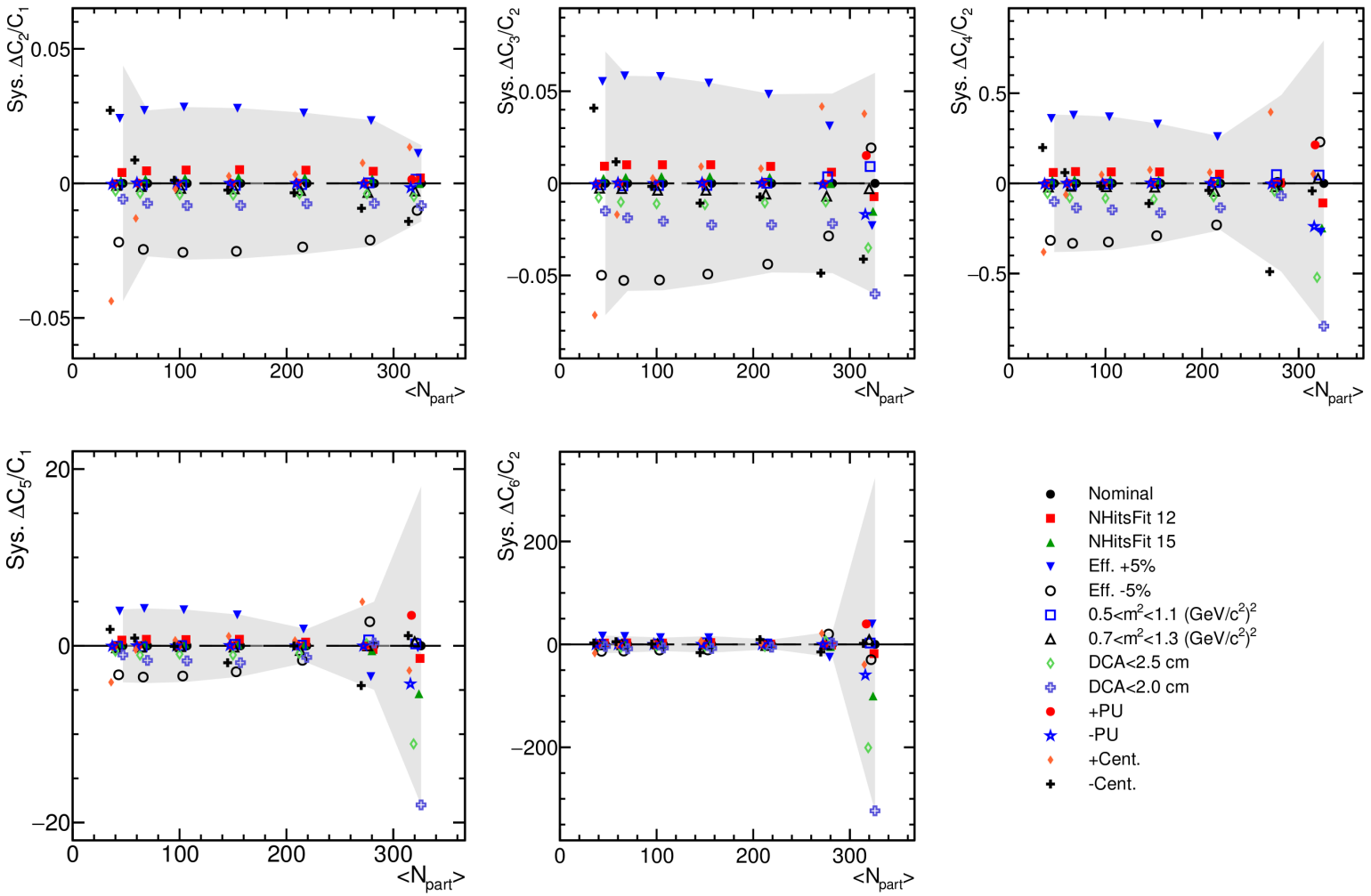


Figure 8.3. The absolute systematic uncertainty of the cumulant ratios up to $6^{\text{th}}$ order of the proton multiplicity distributions in Au+Au collisions at $\sqrt{s_{NN}} = 3.0$ GeV. The total systematic uncertainty is represented by a gray band. The difference between a systematic analysis and the nominal analysis is displayed by markers. Markers are offset in $\langle N_{\text{part}} \rangle$ for clarity. The systematic analyses are defined in table 8.1.

# Chapter 9

# Results and Analysis

In this section, the event-by-event proton cumulants and correlation functions of Au+Au collisions at $\sqrt{s_{NN}} = 3.0$ GeV are presented as a function of rapidity, transverse momentum, and centrality. Additionally, the energy dependence of the cumulants and correlation functions of both the $\sqrt{s_{NN}} = 3.0$ GeV and BES-I data sets are discussed.

In the absence of particle correlations, it is expected that the measured particles behave as a gas of free particles and obey Poisson statistics. As discussed in chapter 8, all orders of cumulants of a Poisson distribution are equal and the ratios equal 1. All cumulant ratios are compared to a Poisson baseline of 1. In the following section, a positive correlation or an enhancement refers to a cumulant ratio greater than 1. Likewise, a suppression is a cumulant ratio below the baseline. The correlation functions behave similarly, however, due to the subtraction of $\kappa_1$ in the definition of the correlation functions (see chapter 8), the Poisson baseline of the $n^{\text{th}}$ correlation function ratio $(\kappa_n/\kappa_1)$ is 0.

All results are compared to UrQMD. The centrality determination is performed similarly in both the data and UrQMD. Therefore, effects from centrality determination, such as volume fluctuations, are expected to be present. A fixed volume UrQMD and hydrodynamic theory [108] calculation are included in the energy dependence comparison, see Fig. 9.10.

## 9.1 Centrality Dependence

In this section, the centrality dependence of the proton cumulant and correlation functions along with the corresponding ratios are discussed. The centrality classes are defined in table 3.1 and plotted as a function of $\langle N_{\rm part} \rangle$. If one assumes that each heavy-ion collision is a superposition of independent proton source distributions that scale with the number of participants ($N_{\rm part}$) [109], the cumulant values should have a linear dependence on $\langle N_{\rm part} \rangle$. In this case, the cumulant ratios would be constant as a function of $\langle N_{\rm part} \rangle$. Furthermore, if each source emits protons isotropically, the proton distribution will behave Poisson-like and the cumulant ratios will equal 1.

The left panel of Fig. 9.1 shows the centrality dependence of the proton cumulants within the kinematic acceptance $-0.5 < y < 0$ and $0.4 < p_T < 2.0$ GeV/$c$. The $C_1$ values increase linearly with $\langle N_{\rm part} \rangle$. The $C_2$ values increases monotonically with $\langle N_{\rm part} \rangle$, but break the linear trend at the highest $\langle N_{\rm part} \rangle$ value. The higher-order cumulants (excluding $C_6$) increase monotonically from the peripheral ($\langle N_{\rm part} \rangle \sim 100$) to the mid-central collisions ($\langle N_{\rm part} \rangle \sim 200$), but decrease in the most central collisions. The right panel of Fig. 9.1 shows the cumulant ratios within the same acceptance. In the peripheral to mid-central collisions ($\langle N_{\rm part} \rangle < 200$), all cumulant ratios are above the Poisson baseline, which indicates a strong positive correlation. The measured protons and UrQMD results have a similar trend. In central collisions, the $C_2/C_1$ ratio is positive, the $C_3/C_2$ ratio is consistent with unity, and the $C_4/C_2$ ratio becomes negative. The behavior of $C_5/C_1$ and $C_6/C_2$ in central collisions is unclear due to the large systematic uncertainty.

As discussed in chapter 7, the strong correlation shown in the cumulant ratios of the peripheral to mid-central collisions could be caused by volume fluctuations. Thus, the strong correlation could be reduced by introducing a model dependent volume fluctuation correction (VFC). The proton cumulants and cumulant ratios are corrected with VFC using two different models: UrQMD (VFC+UrQMD) and Glauber Model (VFC+GM). The VFC cumulants and VFC cumulant ratios are shown in Fig. 9.3. By applying VFC, the cumulant ratios of peripheral to mid-central collisions ($\langle N_{\rm part} \rangle < 200$) are reduced, though a positive correlation still exists. Furthermore, the correction is highly dependent

on the choice of model. The VFC+UrQMD and VFC+GM calculations only agree in the most central or peripheral collisions. While it cannot be concluded that the correction removes the volume fluctuations, the cumulant ratios, specifically $C_4/C_2$ of central collisions, appear unaffected by the VFC.

Figure 9.2 shows the correlation functions within the same kinematic acceptance as Fig. 9.1. The correlation functions and cumulants as a function of centrality behave similarly and increase monotonically with $\langle N_{\rm part} \rangle$ from the peripheral to mid-central collisions. The right panel of Fig. 9.2 shows the normalized correlation functions. In the peripheral to mid-central collisions ($\langle N_{\rm part} \rangle < 200$), the $\kappa_2/\kappa_1$, $\kappa_3/\kappa_1$, and $\kappa_4/\kappa_1$ values are positive, which indicate a positive two, three, and four proton correlation, respectively. In central collisions, the $\kappa_2/\kappa_1$ remains positive, but $\kappa_3/\kappa_1$ and $\kappa_4/\kappa_1$ become negative. The behavior of $\kappa_5/\kappa_1$ and $\kappa_6/\kappa_1$ in central collisions is unclear due to the large systematic uncertainty. The VFC correlation and VFC correlation function ratios are shown in Fig. 9.4. As seen in the cumulant ratios, the large positive correlation of all correlation function ratios is reduced in the peripheral to mid-central collisions, but the two model correction are inconsistent.

In summary, the centrality dependence of both the cumulants ratios and correlation function ratios shows a large correlation in the peripheral to mid-central collisions. VFC reduces the high values, but is highly model dependent. At the same time, the higher cumulant ratios ($C_4/C_2$, $C_5/C_1$, and $C_6/C_2$) of central collisions are least affected by the volume fluctuation correction. The $C_4/C_2$ ratio of the central collisions shows a $2.2\sigma$ suppression with respect to the Poisson baseline.

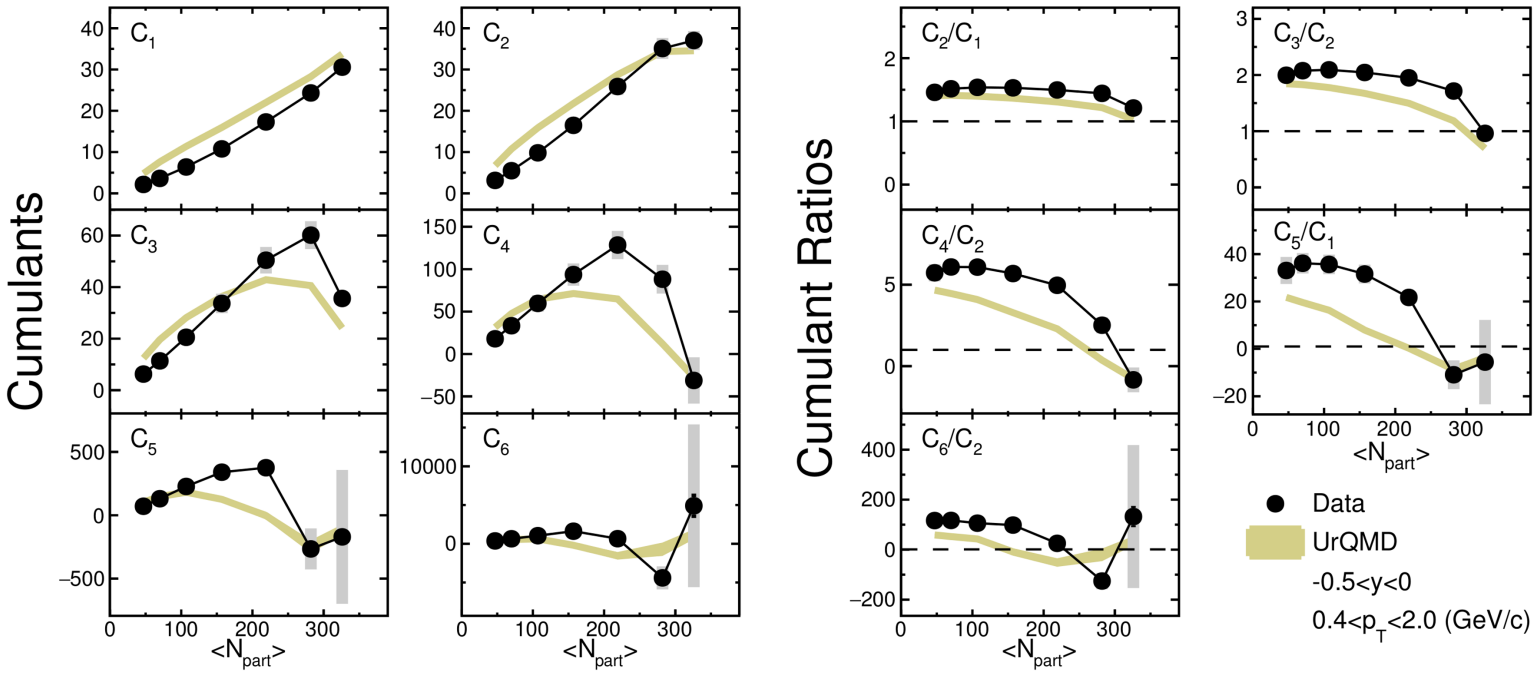


Figure 9.1. Cumulant and cumulant ratios of proton multiplicity distributions in Au+Au collisions at $\sqrt{s_{NN}} = 3.0$ GeV. The kinematic acceptance is within $0.4 < p_{\mathrm{T}} < 2.0$ GeV/$c$ and $-0.5 < y < 0.0$. The statistical and systematic uncertainties are represented by black and gray bars, respectively. The UrQMD result is depicted by gold bands.

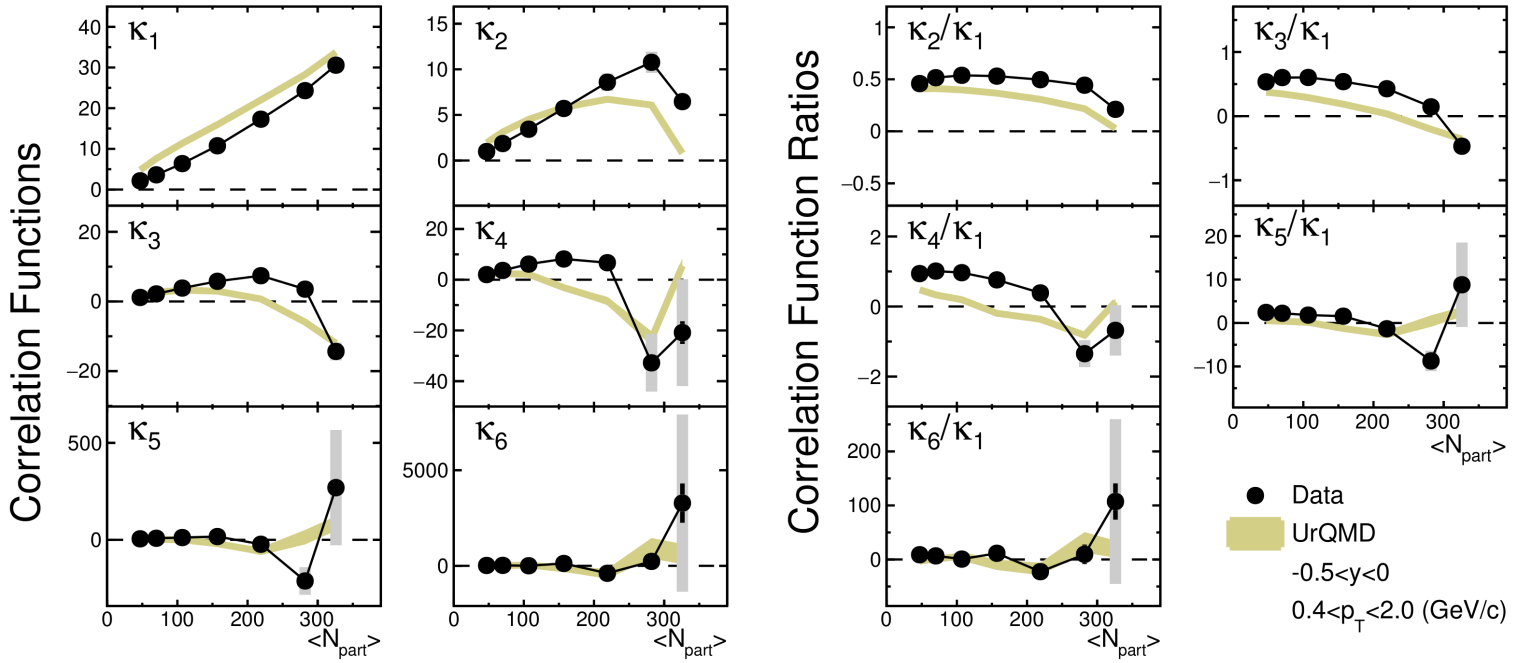


Figure 9.2. Correlation functions and correlation function ratios of proton multiplicity distributions in Au+Au collisions at $\sqrt{s_{NN}} = 3.0$ GeV. The kinematic acceptance is within $0.4 < p_{\mathrm{T}} < 2.0$ GeV/$c$ and $-0.5 < y < 0.0$. The statistical and systematic uncertainties are represented by black and gray bars, respectively. The UrQMD result is depicted by gold bands.

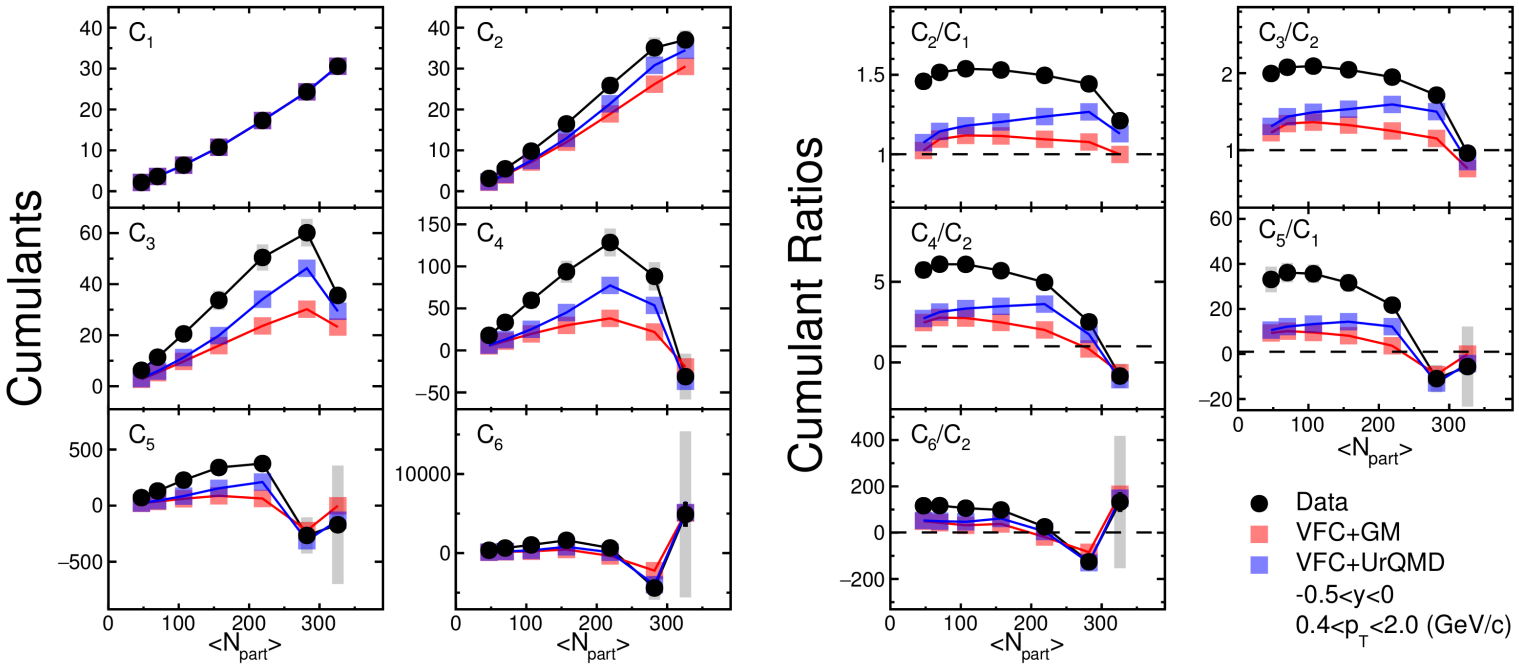


Figure 9.3. Centrality dependence of cumulants and cumulant ratios up to $6^{\text{th}}$ order of the proton multiplicity distributions in Au+Au collisions at $\sqrt{s_{NN}} = 3.0$ GeV. The open squares are correlation functions without VF correction while the red circles and blue triangles are results with VFC using the $N_{\text{part}}$ distributions from the Glauber and UrQMD model, respectively.

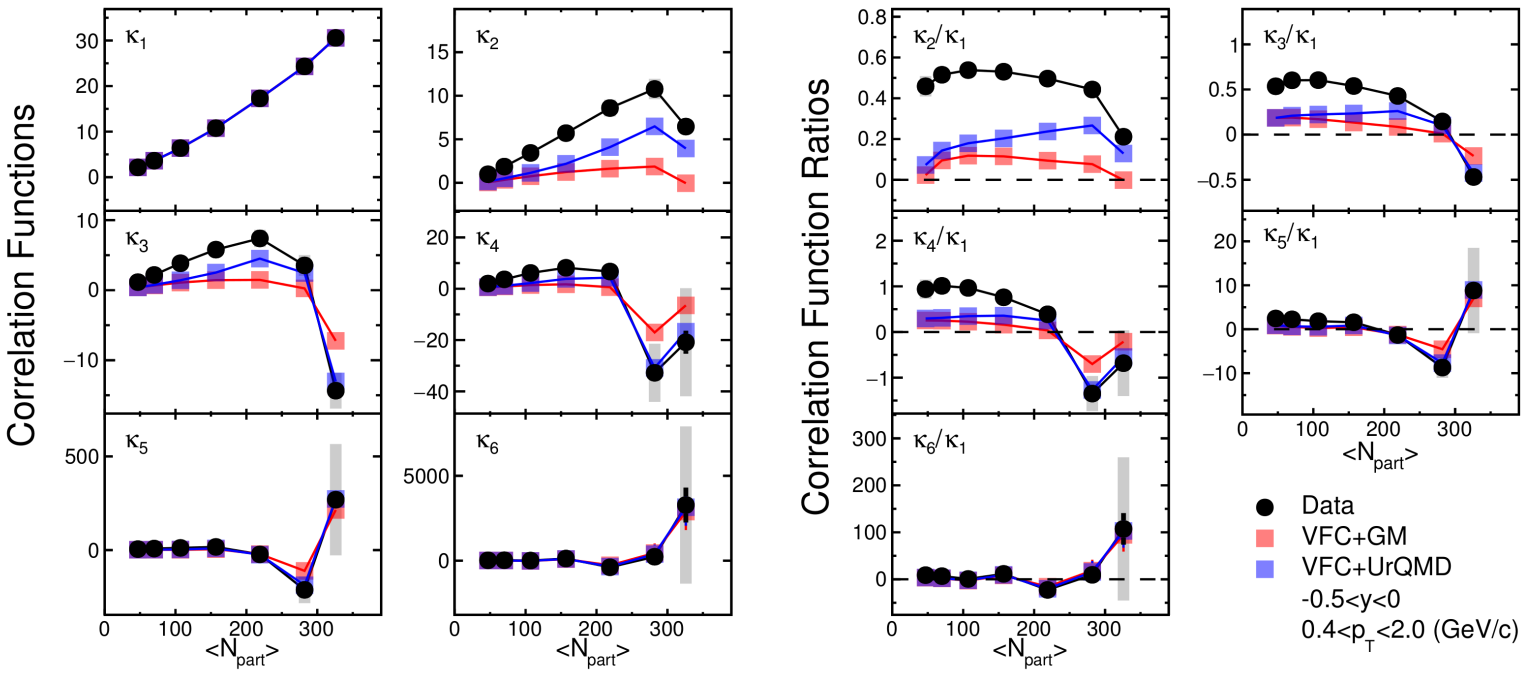


Figure 9.4. Centrality dependence of correlation functions and their normalized ratios up to $6^{\text{th}}$ order of the proton multiplicity distributions in Au+Au collisions at $\sqrt{s_{NN}} = 3.0$ GeV. The open squares are correlation functions without VF correction while red circles and blue triangles are results with VFC using the $N_{\text{part}}$ distributions from the Glauber and UrQMD models, respectively.

## 9.2 Acceptance Dependence

It was pointed out in Refs. [90–93] that there may be two qualitatively different acceptance regimes: $\Delta y \gg \Delta y_{\rm corr}$ and $\Delta y \ll \Delta y_{\rm corr}$, where $\Delta y$ is the width of the kinematic acceptance in rapidity and $\Delta y_{\rm corr}$ is the range of the proton correlations in rapidity. When $\Delta y \ll \Delta y_{\rm corr}$, we expect $\Delta y \sim \langle N \rangle \to 0$ and the cumulant ratios to approach the Poisson limit. Likewise, as $\Delta y \to 0$, we expect the correlation functions to become rapidity independent and approach 0. In the large rapidity window regime $\Delta y \gg \Delta y_{\rm corr}$, cumulants are expected to grow linearly as $\Delta y$ increases. If the cumulants grow linearly, the cumulant ratios will plateau, which indicates a saturation of the physical correlations. If the cumulant ratios continue to increase, this could indicate uncorrelated effects in the measurement, such as volume fluctuations [92]. A similar argument can be made for the transverse momentum dependence. If the transverse momentum window is smaller than the range of proton correlations in $p_T$ ($\Delta y \gg \Delta y_{\rm corr}$), then we expect the cumulant ratios to approach the Poisson limit. Therefore, the rapidity and transverse momentum dependence of proton cumulants and correlation functions may be useful observables in the search for signatures of criticality. It should be noted that the acceptance dependence could be sensitive to non-equilibrium effects, such as smearing due to diffusion, and hadronic rescattering in the expansion of the system [90].

### 9.2.1 Rapidity Dependence

Due to the limitations of the detector acceptance, the rapidity window ($\Delta y$) is varied asymmetrically, where the studied window is $y_{\rm min} < y < 0$. The backwards rapidity cut $y_{\rm min}$ is varied from -0.9 to -0.2. Figure 9.5 depicts the rapidity dependence of the proton cumulants and cumulant ratios within $y_{\rm min} < y < 0$ and $0.4 < p_T < 2.0$ GeV/$c$ for the most central ($0 - 5\%$) and peripheral ($50 - 60\%$) centrality classes.. There are a few notable observations: (i) All cumulant ratios approach unity as the rapidity is decreased. (ii) Central and peripheral collisions behave differently as the rapidity window increases. The cumulants and cumulant ratios in peripheral collisions increase monotonically with $\Delta y$. In the central collisions, the $C_2/C_1$ ratio is largely independent of $\Delta y$ and the $C_3/C_2$ ratio decreases with $\Delta y$. The $C_4/C_2$ of central collisions appears to reach a minimum

around $y_{\min} = -0.6$, though the systematic uncertainties dominate at large $\Delta y$. The higher-order cumulants $C_5$ and $C_6$ are dominated by the large systematic uncertainties. (iii) The trends (not values) of the cumulants and cumulant ratios of both the central and peripheral collisions are reproduced by the transport model (UrQMD).

Figure 9.6 shows the correlation functions within the same kinematic acceptance as Fig. 9.5. The correlation functions behave similarly to the cumulants, specifically observations (i) and (ii). The UrQMD still reproduces the trends (not values) of most correlation functions, however, the two particle correlation ($\kappa_2$) of UrQMD and data are differ significantly.

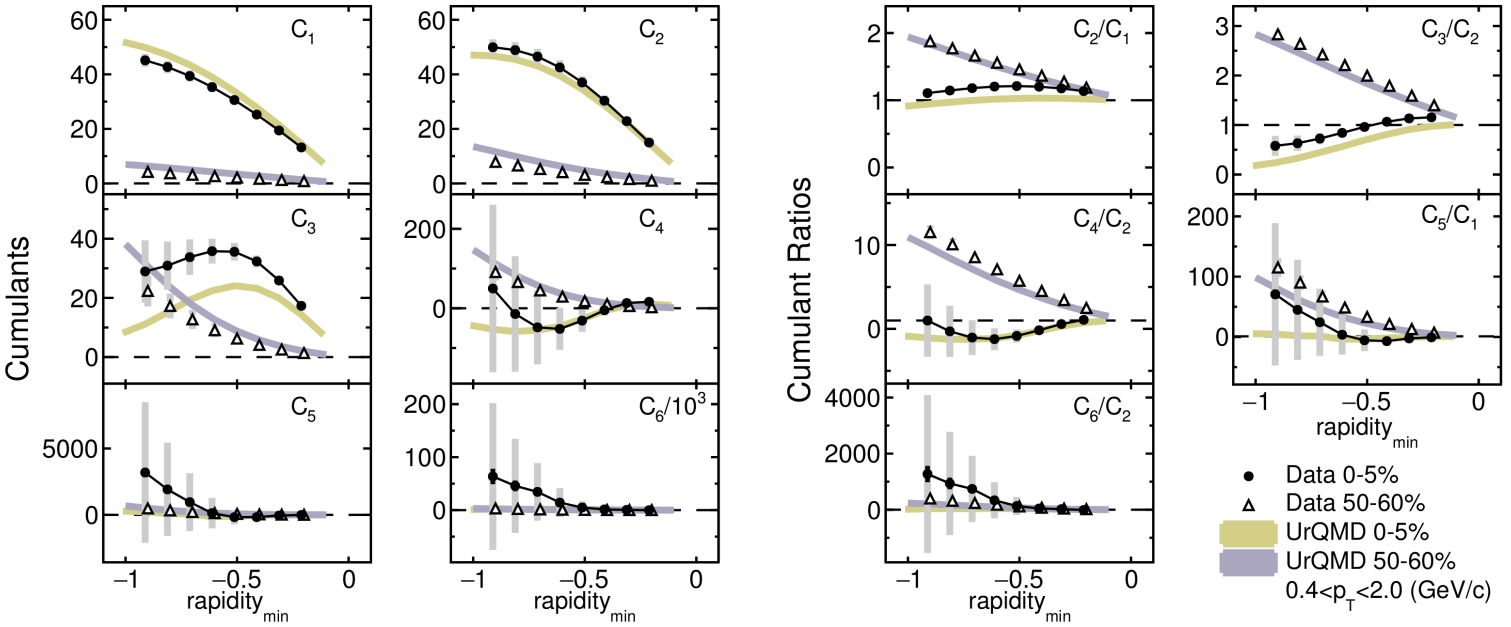


Figure 9.5. Rapidity dependence of cumulant and cumulant ratios of proton multiplicity distributions for Au+Au collisions at $\sqrt{s_{NN}} = 3.0$ GeV. The transverse momentum is within $0.4 < p_{\mathrm{T}} < 2.0$ GeV/$c$ and rapidity is varied from $y_{\mathrm{min}} < y < 0.0$. The cumulants and cumulant ratios of the central (0-5%) and peripheral (50-60%) events are depicted by black circles and white triangles, respectively. The statistical and systematic uncertainties are represented by black and gray bars, respectively. The UrQMD simulations of cumulants and cumulant ratios of the 0-5% and 50-60% collisions are shown by gold and lavender bands, respectively.

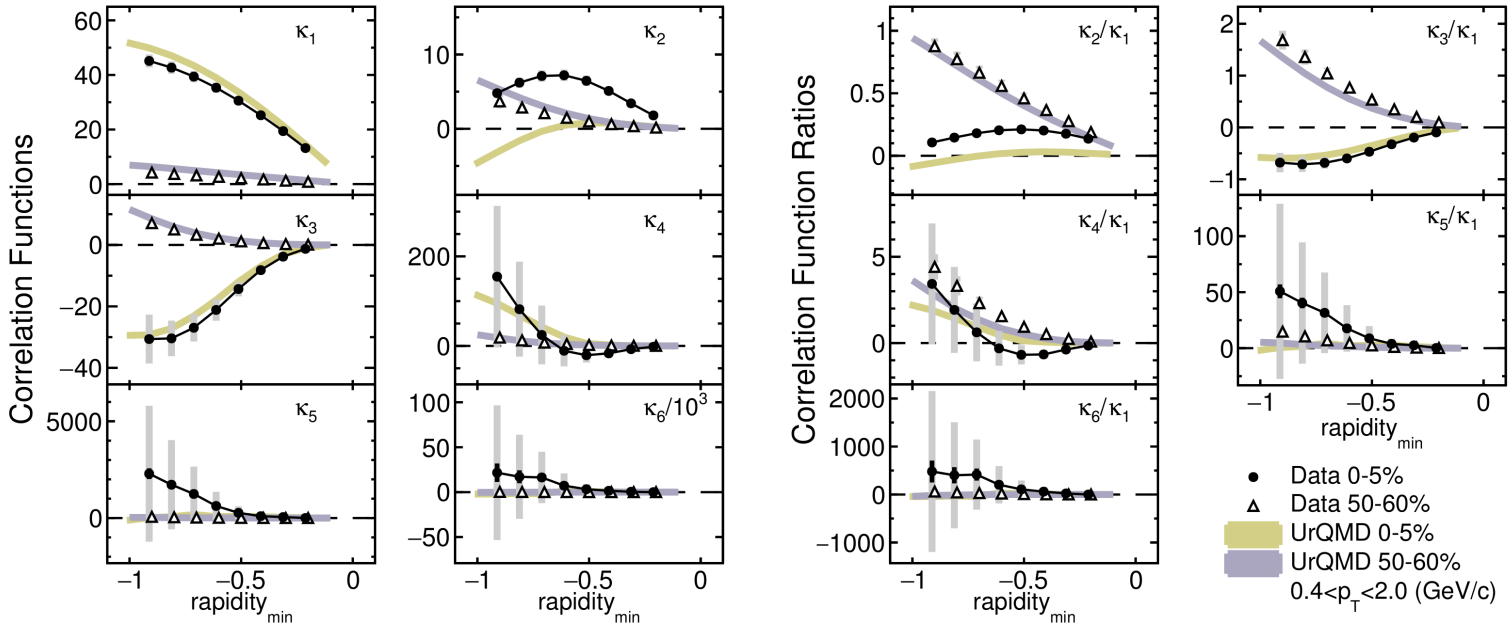


Figure 9.6. Rapidity dependence of correlation functions and correlation function ratios of proton multiplicity distributions for Au+Au collisions at $\sqrt{s_{NN}} = 3.0$ GeV. The transverse momentum is within $0.4 < p_{\mathrm{T}} < 2.0$ GeV/$c$ and rapidity is varied from $y_{\mathrm{min}} < y < 0.0$. The correlation function and correlation function ratios of the central (0-5%) and peripheral (50-60%) events are depicted by black circles and white triangles, respectively. The statistical and systematic uncertainties are represented by black and gray bars, respectively. The UrQMD simulations of correlation function and correlation function ratios of the 0-5% and 50-60% collisions are shown by gold and lavender bands, respectively.

### 9.2.2 Transverse Momentum Dependence

Figure 9.7 depicts the transverse momentum dependence of the proton cumulants and cumulant ratios of the most central $(0-5\%)$ and peripheral $(50-60\%)$ centrality classes within the kinematic acceptance $-0.5 < y < 0$ and $0.4 < p_T < p_T^{\max}$ GeV/$c$, where $p_T^{\max}$ is varied from 0.8 to 2.0. In the most central collisions, the cumulants up to 3$^{\text{rd}}$ order increase with $\Delta p_T$. Meanwhile, $C_4$ decreases with an increased $\Delta p_T$. The $C_4/C_2$ ratio within the smallest $\Delta p_T$ is consistent with the Poisson baseline. As the $\Delta p_T$ increases, $C_4/C_2$ is suppressed. By looking at the increase in $C_1$, one can observe that this suppression is from a relatively small increase in the number of protons. Figure 9.8 depicts transverse momentum dependence of proton correlation functions and correlation function ratios. Similar to the cumulant ratios, the correlation functions approach the Poisson baseline as $\Delta p_T$ is decreased.

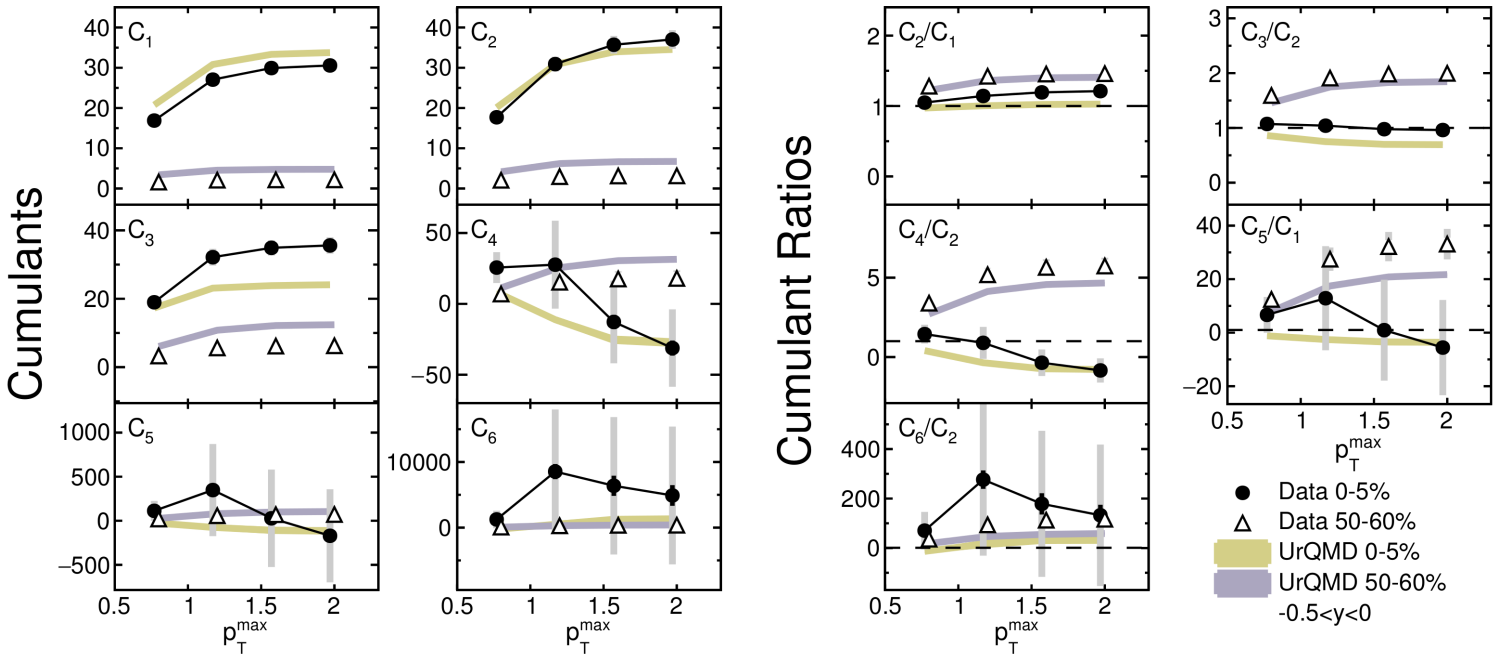


Figure 9.7. The $p_T$ dependence of cumulant and cumulant ratios of proton multiplicity distributions for Au+Au collisions at $\sqrt{s_{NN}} = 3.0$ GeV. The rapidity is within $-0.5 < y < 0$ and the $p_T$ is varied from $0.4 < p_{\rm T} < p_{\rm T}^{\rm max}$ GeV/$c$. The most central (0-5%) and peripheral (50-60%) events are depicted by black circles and white triangles, respectively. The statistical and systematic uncertainties are represented by black and gray bars, respectively. The UrQMD simulations of cumulants and cumulant ratios of the 0-5% and 50-60% collisions are shown by gold and lavender bands, respectively.

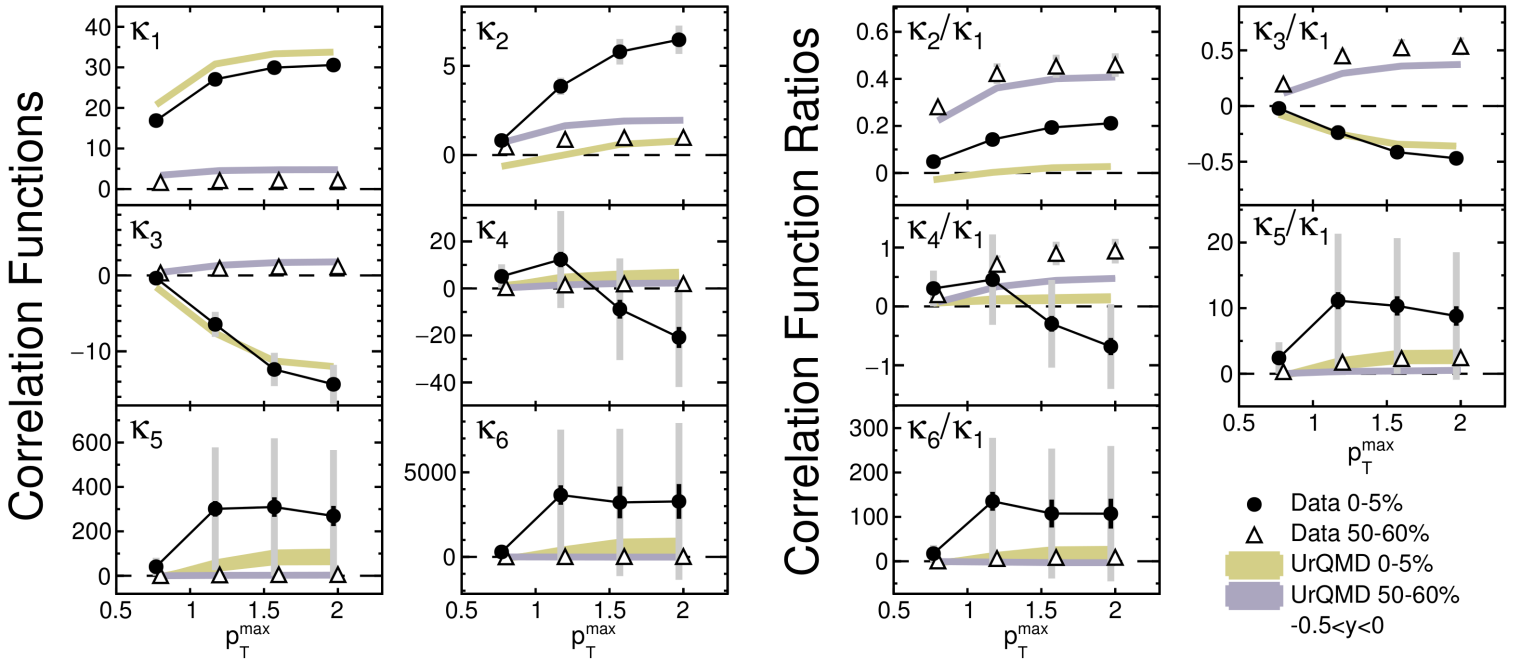


Figure 9.8. The $p_T$ dependence of correlation functions and correlation function ratios of proton multiplicity distributions for Au+Au collisions at $\sqrt{s_{NN}} = 3.0$ GeV. The rapidity is within $-0.5 < y < 0$ and the $p_T$ is varied from $0.4 < p_{\rm T} < p_{\rm T}^{\rm max}$ GeV/$c$. The most central (0-5%) and peripheral (50-60%) events are depicted by black circles and white triangles, respectively. The statistical and systematic uncertainties are represented by black and gray bars, respectively. The UrQMD simulations of correlation function and correlation function ratios of the 0-5% and 50-60% collisions are shown by gold and lavender bands, respectively.

### 9.2.3 Acceptance Dependence Summary

The cumulant ratios as a function of both $\Delta y$ and $\Delta p_T$ approach the Poisson limit in the small acceptance limit. The cumulant ratios and correlation function ratios of peripheral collisions (50–60%) increase monotonically with $\Delta y$, which could indicate a background effect, such as volume fluctuations. The cumulant ratios and correlation function ratios of central collisions (0–5%) do not monotonically increase, though the systematic uncertainty dominates with the large $\Delta y$ and $\Delta p_T$ acceptance. The trends (not values) of cumulants and cumulant ratios of both the central and peripheral collisions are reproduced by the transport model (UrQMD).

## 9.3 Energy Dependence

As discussed in chapter 1, results from the Linear $\sigma$ model suggest that the 3$^{\text{rd}}$ and 4$^{\text{th}}$ cumulants of proton multiplicity distributions are highly sensitive to the correlation length of the system (see Eq. (1.21)) and large deviations of the normalized cumulants ($C_n/C_1$, where $n = 1, ..., 4$) from a model baseline as a function of energy may suggest a region[1] of critical phenomena. The correct model baseline is not known, and thus the cumulant ratios are compared to the Poisson baseline[2], a UrQMD model result, and a hydrodynamic calculation [108]. In addition to the normalized cumulants, the product of higher-order moments such as the $C_3/C_2 \equiv S\sigma$ and $C_4/C_2 \equiv \kappa\sigma^2$ can be constructed from cumulant ratios (see Eq. (8.10)). The $\kappa\sigma^2$ product is of particular interest due to the non-monotonic variation measured in the first BES [6] (see Fig. 1.12). Furthermore, the susceptibility ratios calculated in lattice QCD are equivalent to cumulant ratios and predict a smooth energy dependence. Specifically, lattice QCD predicts a suppression with respect to the Poisson baseline for the $C_3/C_1$ and $C_4/C_2$ ratios as the collision energy decreases, though the calculations are limited to regions below $\mu_B \sim 150$ MeV (see Fig. 1.11).

Figure 9.9 is a comparison of the normalized proton cumulants and the correlation function ratios of the most central Au+Au collisions ($0 - 5\%$) as a function of collision energy. BES-I energies were measured within a kinematic acceptance of $|y| < 0.5$ and

[1] The collision energy can be related to a region of $\mu_B$ and $T$.

[2] All cumulants are equivalent for a Poisson distribution. The cumulant ratios are 1.

$0.4 < p_{\mathrm{T}} < 2.0$, while the $\sqrt{s_{NN}} = 3.0$ GeV data is measured within $-0.5 < y < 0.0$ and $0.4 < p_{\mathrm{T}} < 2.0$. Over the BES energies, both proton and net-proton cumulants are measured. In addition to the data, Fig. 9.9 displays the energy dependence of UrQMD and a hydrodynamic model [108]. At $\sqrt{s_{NN}} = 3.0$ GeV, UrQMD and hydrodynamic calculations are plotted within both the $|y| < 0.5$ and $-0.5 < y < 0.0$ rapidity windows. In addition, a UrQMD calculation with a fixed volume within $-0.5 < y < 0.0$ and $0.4 < p_{\mathrm{T}} < 2.0$ is shown as an open cross. By definition, panels (a) and (b) are equivalent ($C_2/C_1 - 1 = \kappa_2/\kappa_1$). The anti-proton normalized cumulant and correlation function ratios are included for the BES-I energies. As the energy decreases, the proton and anti-proton $\kappa_2/\kappa_1$ ratio diverges and the protons become more negative. The $\sqrt{s_{NN}} = 3.0$ GeV data shows a large positive correlation for the proton $\kappa_2/\kappa_1$ ratios. The UrQMD result shows a similar trend but does not reproduce the values. If the UrQMD is calculated for a fixed volume at $\sqrt{s_{NN}} = 3.0$ GeV (open cross), the ratio flips sign which indicates a suppression in the two particle correlations.

In panel (c), the $C_3/C_1 - 1$ ratio shows a suppression from $\sqrt{s_{NN}} = 7$ GeV to $\sqrt{s_{NN}} = 200$ GeV and an enhancement at $\sqrt{s_{NN}} = 3.0$ GeV. In contrast, the three particle correlation $\kappa_3/\kappa_1$ ratio in panel (d) is suppressed at $\sqrt{s_{NN}} = 3.0$ GeV. This indicates that the enhancement in the $C_3/C_1 - 1$ ratio is caused by contributions from the two particle correlation $\kappa_2/\kappa_1$. The UrQMD $\kappa_3/\kappa_1$ proton ratio agrees with the data at all energies. The fixed-volume UrQMD and hydrodynamic calculations are close to zero.

In panel (e), the trend of the $C_4/C_1 - 1$ ratio of the BES data fluctuates around a suppression, though the uncertainties are large. The $\sqrt{s_{NN}} = 3.0$ GeV shows a relatively large suppression, which agrees with the UrQMD model. In panel (f), $\kappa_4/\kappa_1$ increases relative to $C_4/C_1 - 1$, which indicates the suppression in the $C_4/C_1$ ratio has significant contributions from the lower order particle correlations.

In summary, the differences between $C_3/C_1 - 1$ (c) and $\kappa_3/\kappa_1$ (d) and between $C_4/C_1 - 1$ (e) and $\kappa_4/\kappa_1$ (f) of the $\sqrt{s_{NN}} = 3.0$ GeV data indicate that $C_3$ and $C_4$ have large contributions from the two particle correlation function $\kappa_2$. The flat energy dependence of $\kappa_2$ and $\kappa_3$ is broken by the $\sqrt{s_{NN}} = 3.0$ GeV data. The difference between the UrQMD and

both the fixed-volume UrQMD and hydrodynamic calculations could indicate large effects from volume fluctuations in the lowest collision energy, though no conclusive statements can be made.

Figure 9.10 depicts the energy dependence of the proton and net-proton ($p-\bar{p}$) cumulant ratios for both central (0-5%) and peripheral (50-60%) collisions. The values of the proton and net-proton cumulants converge at the lowest BES energies which marks the antiproton production threshold. At $\sqrt{s_{NN}} = 3.0$ GeV, the anti-proton yield is negligible and proton and net-proton numbers are equivalent.

In both the central and peripheral collisions, the proton $C_2/C_1$ ratio is flat from $\sqrt{s_{NN}} = 7.7$ GeV to $\sqrt{s_{NN}} = 200$ GeV. The $\sqrt{s_{NN}} = 3.0$ GeV data breaks the trend with a positive value in both the $C_2/C_1$ ratios of central and peripheral collisions. Similarly, the $C_3/C_2$ of central collisions ratio appears flat around $\sim 0.8$ for all BES energies while the $\sqrt{s_{NN}} = 3.0$ GeV data is consistent with the Poisson baseline.

The $C_4/C_2$ ratio of peripheral collisions at $\sqrt{s_{NN}} = 3.0$ GeV is larger than $C_4/C_2$ ratio from higher energy collisions by a factor of five. A rapid increase in the energy dependence is confirmed by the UrQMD model calculations. In central collisions, the $C_4/C_2$ ratio from $\sqrt{s_{NN}} = 7.7$ GeV to $\sqrt{s_{NN}} = 27$ GeV shows a slight deviation from both the Poisson and model baselines. However, the statistical uncertainties are large. The $C_4/C_2$ ratio of peripheral collisions at $\sqrt{s_{NN}} = 3.0$ GeV is lower than the Poisson baseline and agrees with the UrQMD model. Additionally, a suppression at $\sqrt{s_{NN}} = 3.0$ GeV is reproduced by the fixed-volume UrQMD and the hydrodynamic model. Recently, at the center of mass energy of 2.4 GeV, HADES reported the values for proton cumulant raios: $C_3/C_2$ = -1.63 $\pm$ 0.09 (stat) $\pm$ 0.34 (sys) and $C_4/C_2 = 0.15 \pm 0.9$ (stat) $\pm$ 1.4 (sys) from ($|y| < 0.4$, $0.4 < p_T < 1.6$ GeV/$c$) [110]. The HADES values are consistent with the $\sqrt{s_{NN}} = 3.0$ GeV data, although the uncertainties are large.

### 9.3.1 Energy Dependence Summary

The cumulant ratios of $C_2/C_1$ and $C_3/C_2$ do not obey the trends seen in higher energy central and peripheral collisions. If one assumes the volume fluctuation corrections in Figure 9.3 are correct, this difference can be partially explained by fluctuations of the

collision volume. This is supported by the large difference between UrQMD with and without a fixed volume. Due to the large model dependence and inconsistencies of the volume correction, however, these claims are speculative.

As discussed in section 4.6, if the measured acceptance is large fraction of the proton $4\pi$ yield, the correlations are suppressed [104]. This effect is expected to increase at lower collision energies due to the lower beam rapidities and therefore, a smaller total rapidity space. The $C_4/C_2$ at $\sqrt{s_{NN}} = 3.0$ GeV is suppressed with respect to the Poisson baseline. This follows the trends of UrQMD and the hydrodynamic calculations which both include baryon conversation. The $C_4/C_2$ ratio at $\sqrt{s_{NN}} = 3.0$ GeV is consistent with fluctuations driven by baryon conservation.

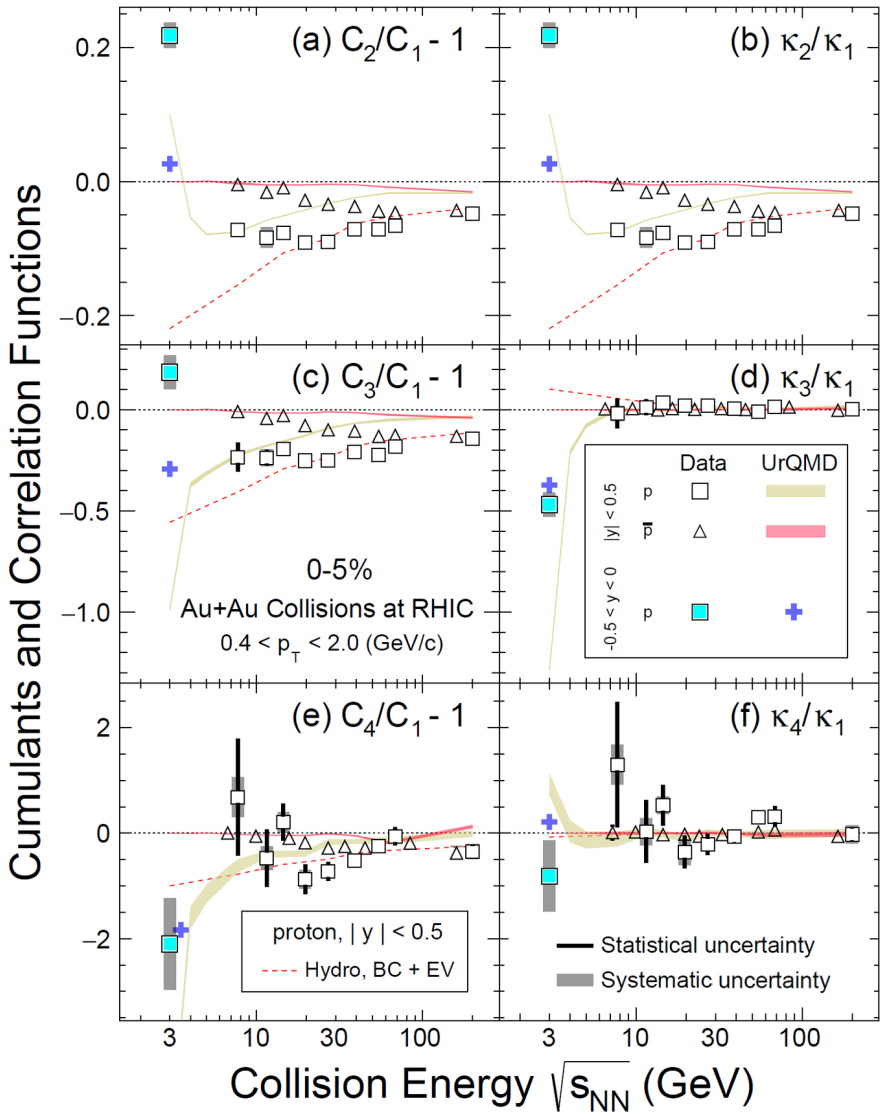


Figure 9.9. Collision energy dependence of the scaled cumulants (left panels) and correlation function ratios (right panels), for protons (open squares) and anti-protons (open triangles), in 0-5% central Au+Au collisions at RHIC. The UrQMD results for protons and anti-protons within $|y| < 0.5$ are shown as gold and pink bands, respectively. At 3 GeV, the model results for protons with $-0.5 < y < 0$ in the top 0-5% central collisions are shown as blue crosses. The open crosses are the results from UrQMD calculated with an impact parameter $b < 3$ fm. Hydrodynamic calculations of the energy dependence for protons within $|y| < 0.5$ are shown as dashed red lines. The results at 3 GeV for protons within $-0.5 < y < 0$ are shown as open stars. For clarity, the $x$-axis position of the open stars are shifted slightly in plots (d) and (f).

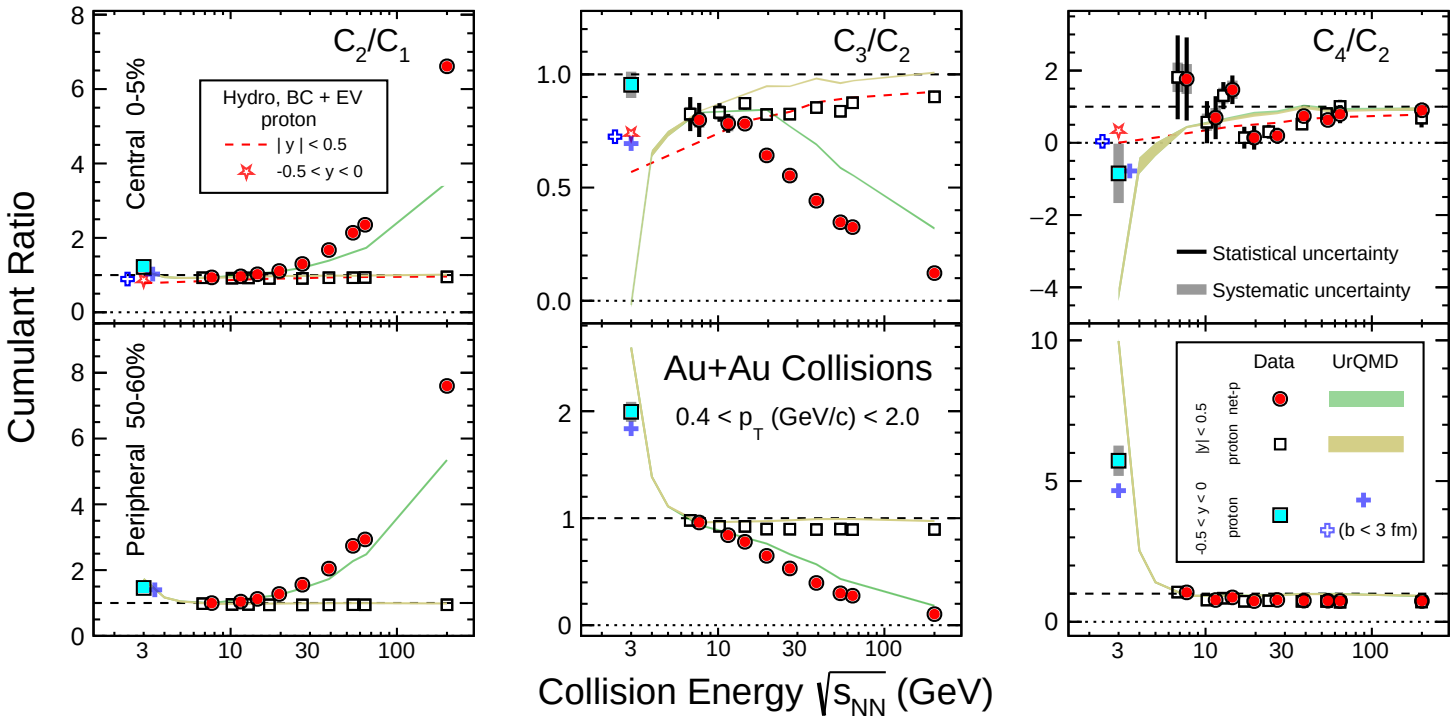


Figure 9.10. Collision energy dependence of the cumulant ratios: $C_2/C_1 = \sigma/M$, $C_3/C_2 = S\sigma$, and $C_4/C_2 = \kappa\sigma^2$, for proton (open squares) and net-proton (red-circles) from top 0-5% (top panels) and 50-60% (bottom panels) Au+Au collisions at RHIC. The points for protons are shifted horizontally for clarity. The proton cumulant ratios from $\sqrt{s_{NN}} = 3.0$ GeV collisions are shown as filled squares. Results for protons and net-protons within $|y| < 0.5$ from the transport model UrQMD are shown as gold and green bands, respectively. At 3 GeV, the model result for protons $(-0.5 < y < 0)$ are shown as blue crosses. Results from UrQMD for the protons and anti-protons $C_4/C_2$, see right panels, are almost totally overlapped. The open cross is the result of the model with a fixed impact parameter $b < 3$ (fm). Similar to Figure 9.9, the hydrodynamic calculations, for top 5% central collisions, for protons within $|y| < 0.5$ are shown as dashed red lines and the result of the 3 GeV protons within $-0.5 < y < 0$ is shown as open red stars.

# Chapter 10

# Conclusion

This thesis describes a systematic study of cumulants and correlation functions of proton multiplicities from Au+Au collisions at $\sqrt{s_{NN}} = 3$ GeV. The data have been collected with the STAR fixed-target mode in 2018 at RHIC. The study includes the proton multiplicities studied as functions of centrality, acceptance, and energy. The protons are identified using the STAR TPC and TOF with greater than 95% purity. The centrality selection is based on pion and kaon multiplicities in the full acceptance of the TPC. The proton tracks are corrected for tracking inefficiencies using a binomial response function and the cumulant values are corrected for pileup contamination. The event-averaged total pileup fraction is determined to be $(0.46 \pm 0.09)\%$. Due to a weak correlation between the measured reference multiplicity and the initial number of participants, a considerable effect from the volume fluctuations is expected. The effects can be suppressed by implementing a model dependent correction procedure [104], however, the results are highly dependent on the choice of model. On the other hand, the most central events of higher order cumulant ratios $C_4/C_2$, $C_5/C_1$, and $C_6/C_2$ appear least affected by volume fluctuation corrections.

The acceptance dependence of the proton cumulants and correlation functions aligns with the theoretical expectations [90–93]. For both central and peripheral collisions, the proton cumulants approach the Poisson limit as the rapidity and transverse momentum window is decreased. One could argue that as the rapidity window increases, the physical correlations should saturate, while uncorrelated effects such as volume fluctuations should grow linearly [91, 92]. The cumulant and correlation function ratios of $\sqrt{s_{NN}} = 3.0$ GeV

peripheral collisions increase monotonically, which indicate the collisions are dominated by uncorrelated effects. This monotonic behavior is not seen in the central collisions, which would indicate physical correlations.

Unlike the $C_2/C_1$ ratios of higher energy collisions, the cumulant ratio $C_2/C_1$ of central collisions at $\sqrt{s_{NN}} = 3.0$ GeV deviate from the Poisson baseline. Similarly, the $C_3/C_2$ ratio appears close to unity, while the $C_3/C_2$ proton ratios of the higher BES energies appear flat around $\sim 0.8$. By applying additional volume corrections, this discrepancy between the $\sqrt{s_{NN}} = 3.0$ GeV and the BES data sets vanishes. However, the correction is highly model dependent, and thus the difference can not be unambiguously attributed to volume fluctuations. The $C_4/C_2$, $C_5/C_1$, and $C_6/C_2$ seem less affected by volume fluctuations, which is likely due to a cancellation of the lower order correlations.

For the $C_4/C_2$ ratio energy dependence, QCD inspired models predict deviations from the Poisson baseline as a function of collision energy [7, 48]. In the first BES, a non-monotonic variation of the energy dependence of the net-proton $C_4/C_2$ in Au+Au collisions was measured. In particular, the behavior from $\sqrt{s_{NN}} = 7.7$ GeV to $\sqrt{s_{NN}} = 27$ GeV hinted towards critical fluctuations. The new $C_4/C_2$ measured in Au+Au collisions at $\sqrt{s_{NN}} = 3.0$ GeV does not return to the Poisson baseline but shows a suppression which agrees well with results from UrQMD and hydrodynamic calculations. In both models, the suppression is attributed to the conservation of baryon number. While baryon number is conserved at all energies, the suppression is expected to increase at lower beam energies.

The results of this analysis suggest that baryon conservation dominates the dynamics in the $\sqrt{s_{NN}} = 3.0$ GeV region of high baryon density. On the other hand, the degree to which the dynamics in Au+Au collisions at $\sqrt{s_{NN}} = 3.0$ GeV are caused by volume fluctuations is not understood. While both model studies and correction techniques indicate that the volume fluctuation effects are reduced for the $C_4/C_2$ in the central collisions, no conclusion can be made.

The cumulant ratios in Au+Au collisions at $\sqrt{s_{NN}} = 3.0$ GeV, which are dominated by fluctuations from baryon conservation, neither support nor contradict the hints of critical fluctuations at higher energies. Calculations from lattice QCD, which support a

smooth crossover transition, predict a suppression with respect to the Poisson baseline at high baryon density, though the calculations are limited to $\mu_B < 150$ MeV and the $\mu_B$ at $\sqrt{s_{NN}} = 3.0$ GeV is likely above $\mu_B \sim 700$ MeV [111]. The Linear $\sigma$ model, a model with a critical point, predicts that the cumulant ratios should return to a baseline below the critical region. The results at $\sqrt{s_{NN}} = 3.0$ GeV are more or less consistent with the suppression seen in the UrQMD results. If UrQMD, a model without critical phenomena, is considered a reasonable baseline for hadronic interactions, both the predictions from lattice QCD and Linear $\sigma$ model calculations are consistent with the $\sqrt{s_{NN}} = 3.0$ GeV result. At the same time, the BES data from $7.7 \leq \sqrt{s_{NN}} < 20$ GeV, shows a non-monotonic energy dependence in $C_4/C_2$ and a clear deviation from the model calculations. While the uncertainties are large, the new $\sqrt{s_{NN}} = 3.0$ GeV data suggests that if a critical region exists and is accessible through heavy-ion collisions, it exists at energies above $\sqrt{s_{NN}} = 3.0$ GeV.

Looking forward, the STAR Collaboration plans to re-analyze both the BES energies and the fixed target $\sqrt{s_{NN}} = 3.0$ GeV energy with significantly higher statistics. The new data sets (BES-II) could shed light on whether the fluctuations in the energy dependence of $C_4/C_2$ is an artifact of high statistical uncertainty or sensitivity to critical phenomena.

# References


[1] Philippe Chomaz. The nuclear liquid gas phase transition and phase coexistence. *AIP Conf. Proc.*, 610(1):167, 2002. doi: 10.1063/1.1469927.

[2] Miklos Gyulassy. The QGP discovered at RHIC. In *NATO Advanced Study Institute: Structure and Dynamics of Elementary Matter*, pages 159–182, 3 2004.

[3] A. Bazavov et al. Chiral crossover in QCD at zero and non-zero chemical potentials. *Phys. Lett. B*, 795:15–21, 2019. doi: 10.1016/j.physletb.2019.05.013.

[4] S. Giorgini. *Lecture Notes on Statistical Mechanics - Course for the Master degree in Physics at the University of Trento from 2010 to 2015 (misprints amended and solution to problems added).* 01 2016.

[5] Grazyna Odyniec. The RHIC Beam Energy Scan program in STAR and what's next. *J. Phys.: Conf. Ser. 455 012037*, 2013.

[6] Mohamed Abdallah et al. Cumulants and correlation functions of net-proton, proton, and antiproton multiplicity distributions in Au+Au collisions at energies available at the BNL Relativistic Heavy Ion Collider. *Phys. Rev. C*, 104(2):024902, 2021. doi: 10.1103/PhysRevC.104.024902.

[7] M. A. Stephanov. On the sign of kurtosis near the QCD critical point. *Phys. Rev. Lett.*, 107:052301, 2011. doi: 10.1103/PhysRevLett.107.052301.

[8] David Tlusty. The RHIC Beam Energy Scan Phase II: Physics and Upgrades. In *13th Conference on the Intersections of Particle and Nuclear Physics*, 10 2018.

[9] Kathryn C. Meehan. The fixed-target experiment at STAR. *J. Phys. Conf. Ser.*, 742(1):012022, 2016. doi: 10.1088/1742-6596/742/1/012022.

[10] Anton Andronic, Peter Braun-Munzinger, Krzysztof Redlich, and Johanna Stachel. Decoding the phase structure of QCD via particle production at high energy. *Nature*, 561(7723):321–330, 2018. doi: 10.1038/s41586-018-0491-6.

[11] R. Hagedorn. Statistical thermodynamics of strong interactions at high-energies. *Nuovo Cim. Suppl.*, 3:147–186, 1965.

[12] Steven C. Frautschi. Statistical bootstrap model of hadrons. *Phys. Rev. D*, 3: 2821–2834, 1971. doi: 10.1103/PhysRevD.3.2821.

[13] N. Cabibbo and G. Parisi. Exponential Hadronic Spectrum and Quark Liberation. *Phys. Lett. B*, 59:67–69, 1975. doi: 10.1016/0370-2693(75)90158-6.

[14] F. Karsch. Lattice QCD at Finite Temperature: A Status Report. *Z. Phys. C*, 38: 147, 1988. doi: 10.1007/BF01574529.

[15] Kenneth G. Wilson. Confinement of quarks. *Phys. Rev. D*, 10:2445–2459, Oct 1974. doi: 10.1103/PhysRevD.10.2445. URL `https://link.aps.org/doi/10.1103/PhysRevD.10.2445`.

[16] R. A. Beth and C. Lasky. The brookhaven alternating gradient synchrotron. *Science*, 128(3336):1393–1401, 1958. doi: 10.1126/science.128.3336.1393.

[17] The Super Proton Synchrotron. Jan 2012. URL `https://cds.cern.ch/record/1997188`.

[18] Ulrich W. Heinz and Maurice Jacob. Evidence for a new state of matter: An Assessment of the results from the CERN lead beam program. 1 2000.

[19] Ulrich W. Heinz. The Little bang: Searching for quark gluon matter in relativistic heavy ion collisions. *Nucl. Phys. A*, 685:414–431, 2001. doi: 10.1016/S0375-9474(01)00558-9.

[20] Rhic scientists serve up 'perfect' liquid, Apr 2005. URL `https://www.bnl.gov/newsroom/news.php?a=110303`.

[21] S. S. Adler et al. Elliptic flow of identified hadrons in Au+Au collisions at s(NN)**(1/2) = 200-GeV. *Phys. Rev. Lett.*, 91:182301, 2003. doi: 10.1103/PhysRevLett.91.182301.

[22] C. Adler et al. Elliptic flow from two and four particle correlations in Au+Au collisions at s(NN)**(1/2) = 130-GeV. *Phys. Rev. C*, 66:034904, 2002. doi: 10.1103/PhysRevC.66.034904.

[23] John Adams et al. Particle type dependence of azimuthal anisotropy and nuclear modification of particle production in Au + Au collisions at s(NN)**(1/2) = 200-GeV. *Phys. Rev. Lett.*, 92:052302, 2004. doi: 10.1103/PhysRevLett.92.052302.

[24] J. Adams et al. Erratum: Azimuthal Anisotropy at the Relativistic Heavy Ion Collider: The First and Fourth Harmonics [Phys. Rev. Lett. 92, 062301 (2004)]. *Phys. Rev. Lett.*, 92:062301, 2004. doi: 10.1103/PhysRevLett.127.069901. [Erratum: Phys.Rev.Lett. 127, 069901 (2021)].

[25] Peter Jacobs and Jennifer Klay. Jets and high p(T) hadrons in dense matter: Recent results from STAR. *AIP Conf. Proc.*, 698(1):667–672, 2004. doi: 10.1063/1.1664324.

[26] David Hardtke. Jets and dijets in Au + Au and p + p collisions at RHIC. *Nucl. Phys. A*, 715:272–279, 2003. doi: 10.1016/S0375-9474(02)01436-7.

[27] C. Adler et al. Disappearance of back-to-back high $p_T$ hadron correlations in central Au+Au collisions at $\sqrt{s_{NN}}$ = 200-GeV. *Phys. Rev. Lett.*, 90:082302, 2003. doi: 10.1103/PhysRevLett.90.082302.

[28] P. Huovinen, P. F. Kolb, Ulrich W. Heinz, P. V. Ruuskanen, and S. A. Voloshin. Radial and elliptic flow at RHIC: Further predictions. *Phys. Lett. B*, 503:58–64, 2001. doi: 10.1016/S0370-2693(01)00219-2.

[29] Peter F. Kolb and Ulrich W. Heinz. Hydrodynamic description of ultrarelativistic heavy ion collisions. pages 634–714, 5 2003.

[30] Siegfried Bethke. The 2009 World Average of alpha(s). *Eur. Phys. J. C*, 64:689–703, 2009. doi: 10.1140/epjc/s10052-009-1173-1.

[31] Ramona Vogt. *Ultrarelativistic Heavy-Ion Collisions*. Elsevier Science B.V., Amsterdam, 2007.

[32] Rajan Gupta. Introduction to lattice QCD: Course. In *Les Houches Summer School in Theoretical Physics, Session 68: Probing the Standard Model of Particle Interactions*, pages 83–219, 7 1997.

[33] Matthias Berwein, Nora Brambilla, and Antonio Vairo. Renormalization of Loop Functions in QCD. *Phys. Part. Nucl.*, 45(4):656–663, 2014. doi: 10.1134/S1063779614040029.

[34] S. A. Bass et al. Microscopic models for ultrarelativistic heavy ion collisions. *Prog. Part. Nucl. Phys.*, 41:255–369, 1998. doi: 10.1016/S0146-6410(98)00058-1.

[35] Alexei Bazavov and Peter Petreczky. Deconfinement and chiral transition with the highly improved staggered quark (HISQ) action. *J. Phys. Conf. Ser.*, 230:012014, 2010. doi: 10.1088/1742-6596/230/1/012014.

[36] P. Braun-Munzinger, J. Stachel, and Christof Wetterich. Chemical freezeout and the QCD phase transition temperature. *Phys. Lett. B*, 596:61–69, 2004. doi: 10.1016/j.physletb.2004.05.081.

[37] A. Bazavov et al. The QCD Equation of State to $\mathcal{O}(\mu_B^6)$ from Lattice QCD. *Phys. Rev. D*, 95(5):054504, 2017. doi: 10.1103/PhysRevD.95.054504.

[38] L. Adamczyk et al. Bulk Properties of the Medium Produced in Relativistic Heavy-Ion Collisions from the Beam Energy Scan Program. *Phys. Rev. C*, 96(4):044904, 2017. doi: 10.1103/PhysRevC.96.044904.

[39] Yoichiro Nambu and G. Jona-Lasinio. Dynamical Model of Elementary Particles Based on an Analogy with Superconductivity. 1. *Phys. Rev.*, 122:345–358, 1961. doi: 10.1103/PhysRev.122.345.

[40] Yoichiro Nambu and G. Jona-Lasinio. DYNAMICAL MODEL OF ELEMENTARY PARTICLES BASED ON AN ANALOGY WITH SUPERCONDUCTIVITY. II. *Phys. Rev.*, 124:246–254, 1961. doi: 10.1103/PhysRev.124.246.

[41] Michael Buballa. NJL model analysis of quark matter at large density. *Phys. Rept.*, 407:205–376, 2005. doi: 10.1016/j.physrep.2004.11.004.

[42] M. Asakawa and K. Yazaki. Chiral Restoration at Finite Density and Temperature. *Nucl. Phys. A*, 504:668–684, 1989. doi: 10.1016/0375-9474(89)90002-X.

[43] S. P. Klevansky. The Nambu-Jona-Lasinio model of quantum chromodynamics. *Rev. Mod. Phys.*, 64:649–708, 1992. doi: 10.1103/RevModPhys.64.649.

[44] Murray Gell-Mann and M Levy. The axial vector current in beta decay. *Nuovo Cim.*, 16:705, 1960. doi: 10.1007/BF02859738.

[45] Nicholas Petropoulos. Linear sigma model at finite temperature. Other thesis, 2 2004.

[46] A. K. Chaudhuri. Phase transition in linear sigma model and disoriented chiral condensate. 7 2000.

[47] Adam Miklos Halasz, A. D. Jackson, R. E. Shrock, Misha A. Stephanov, and J. J. M. Verbaarschot. On the phase diagram of QCD. *Phys. Rev. D*, 58:096007, 1998. doi: 10.1103/PhysRevD.58.096007.

[48] M. A. Stephanov. Non-Gaussian fluctuations near the QCD critical point. *Phys. Rev. Lett.*, 102:032301, 2009. doi: 10.1103/PhysRevLett.102.032301.

[49] Juergen Berges and Krishna Rajagopal. Color superconductivity and chiral symmetry restoration at nonzero baryon density and temperature. *Nucl. Phys. B*, 538: 215–232, 1999. doi: 10.1016/S0550-3213(98)00620-8.

[50] Misha A. Stephanov, K. Rajagopal, and Edward V. Shuryak. Event-by-event fluctuations in heavy ion collisions and the QCD critical point. *Phys. Rev. D*, 60:114028, 1999. doi: 10.1103/PhysRevD.60.114028.

[51] Boris Berdnikov and Krishna Rajagopal. Slowing out-of-equilibrium near the QCD critical point. *Phys. Rev. D*, 61:105017, 2000. doi: 10.1103/PhysRevD.61.105017.

[52] Peter Braun-Munzinger and Johanna Stachel. Dynamics of ultrarelativistic nuclear collisions with heavy beams: An Experimental overview. *Nucl. Phys. A*, 638:3–18, 1998. doi: 10.1016/S0375-9474(98)00342-X.

[53] Heng-Tong Ding, Frithjof Karsch, and Swagato Mukherjee. Thermodynamics of strong-interaction matter from Lattice QCD. *Int. J. Mod. Phys. E*, 24(10):1530007, 2015. doi: 10.1142/S0218301315300076.

[54] Frithjof Karsch and Krzysztof Redlich. Probing freeze-out conditions in heavy ion collisions with moments of charge fluctuations. *Phys. Lett. B*, 695:136–142, 2011. doi: 10.1016/j.physletb.2010.10.046.

[55] Jing-Hua Fu. Higher moments of multiplicity fluctuations in a hadron-resonance gas with exact conservation laws. *Phys. Rev. C*, 96(3):034905, 2017. doi: 10.1103/PhysRevC.96.034905.

[56] Xiaofeng Luo and Nu Xu. Search for the QCD Critical Point with Fluctuations of Conserved Quantities in Relativistic Heavy-Ion Collisions at RHIC : An Overview. *Nucl. Sci. Tech.*, 28(8):112, 2017. doi: 10.1007/s41365-017-0257-0.

[57] Wenkai Fan, Xiaofeng Luo, and Hong-Shi Zong. Mapping the QCD phase diagram with susceptibilities of conserved charges within Nambu–Jona-Lasinio model. *Int. J. Mod. Phys. A*, 32(11):1750061, 2017. doi: 10.1142/S0217751X17500610.

[58] Masayuki Asakawa, Shinji Ejiri, and Masakiyo Kitazawa. Third moments of conserved charges as probes of QCD phase structure. *Phys. Rev. Lett.*, 103:262301, 2009. doi: 10.1103/PhysRevLett.103.262301.

[59] A. Bazavov et al. Skewness, kurtosis, and the fifth and sixth order cumulants of net baryon-number distributions from lattice QCD confront high-statistics STAR data. *Phys. Rev. D*, 101(7):074502, 2020. doi: 10.1103/PhysRevD.101.074502.

[60] A. Bazavov et al. Skewness and kurtosis of net baryon-number distributions at

small values of the baryon chemical potential. *Phys. Rev. D*, 96(7):074510, 2017. doi: 10.1103/PhysRevD.96.074510.

[61] Y. Hatta and M. A. Stephanov. Proton number fluctuation as a signal of the QCD critical endpoint. *Phys. Rev. Lett.*, 91:102003, 2003. doi: 10.1103/PhysRevLett.91.102003. [Erratum: Phys.Rev.Lett. 91, 129901 (2003)].

[62] Masakiyo Kitazawa and Masayuki Asakawa. Relation between baryon number fluctuations and experimentally observed proton number fluctuations in relativistic heavy ion collisions. *Phys. Rev. C*, 86:024904, 2012. doi: 10.1103/PhysRevC.86.024904. [Erratum: Phys.Rev.C 86, 069902 (2012)].

[63] L. Adamczyk et al. Centrality dependence of identified particle elliptic flow in relativistic heavy ion collisions at $\sqrt{s_{NN}}$=7.7–62.4 GeV. *Phys. Rev. C*, 93(1):014907, 2016. doi: 10.1103/PhysRevC.93.014907.

[64] L. Adamczyk et al. Observation of an Energy-Dependent Difference in Elliptic Flow between Particles and Antiparticles in Relativistic Heavy Ion Collisions. *Phys. Rev. Lett.*, 110(14):142301, 2013. doi: 10.1103/PhysRevLett.110.142301.

[65] L. Adamczyk et al. Beam Energy Dependence of Jet-Quenching Effects in Au+Au Collisions at $\sqrt{s_{\rm NN}}$ = 7.7, 11.5, 14.5, 19.6, 27, 39, and 62.4 GeV. *Phys. Rev. Lett.*, 121(3):032301, 2018. doi: 10.1103/PhysRevLett.121.032301.

[66] L. Adamczyk et al. Beam-energy-dependent two-pion interferometry and the freeze-out eccentricity of pions measured in heavy ion collisions at the STAR detector. *Phys. Rev. C*, 92(1):014904, 2015. doi: 10.1103/PhysRevC.92.014904.

[67] H. Hahn, E. Forsyth, H. Foelsche, M. Harrison, J. Kewisch, G. Parzen, S. Peggs, E. Raka, A. Ruggiero, A. Stevens, S. Tepikian, P. Thieberger, D. Trbojevic, J. Wei, E. Willen, S. Ozaki, and S.Y. Lee. The rhic design overview. *Nuclear Instruments and Methods in Physics Research Section A: Accelerators, Spectrometers, Detectors and Associated Equipment*, 499(2):245–263, 2003. ISSN 0168-9002. doi: https://

doi.org/10.1016/S0168-9002(02)01938-1. URL https://www.sciencedirect.com/science/article/pii/S0168900202019381. The Relativistic Heavy Ion Collider Project: RHIC and its Detectors.

[68] M. Harrison, T. Ludlam, and S. Ozaki. Rhic project overview. *Nuclear Instruments and Methods in Physics Research Section A: Accelerators, Spectrometers, Detectors and Associated Equipment*, 499(2):235–244, 2003. ISSN 0168-9002. doi: https://doi.org/10.1016/S0168-9002(02)01937-X. URL https://www.sciencedirect.com/science/article/pii/S016890020201937X. The Relativistic Heavy Ion Collider Project: RHIC and its Detectors.

[69] Brookhaven national lab flickr page, howpublished = https://www.flickr.com/photos/brookhavenlab/, note = Accessed: 2021-7-08.

[70] A. Pikin, J. G. Alessi, E. N. Beebe, A. Kponou, R. Lambiase, R. Lockey, D. Raparia, J. Ritter, L. Snydstrup, and Y. Tan. RHIC EBIS: Basics of design and status of commissioning. *JINST*, 5:C09003, 2010. doi: 10.1088/1748-0221/5/09/C09003.

[71] G. Zschornacka, M. Schmidt, and A. Thorn. Electron Beam Ion Sources. In *CAS - CERN Accelerator School: Ion Sources*, 12 2013. doi: 10.5170/CERN-2013-007.165.

[72] K. H. Ackermann et al. STAR detector overview. *Nucl. Instrum. Meth. A*, 499: 624–632, 2003. doi: 10.1016/S0168-9002(02)01960-5.

[73] M. Anderson et. al (STAR Collaboration). The star time projection chamber: a unique tool for studying high multiplicity events at rhic. *Nuclear Instruments and Methods in Physics Research Section A: Accelerators, Spectrometers, Detectors and Associated Equipment*, 499(2):659–678, 2003. ISSN 0168-9002. doi: https://doi.org/10.1016/S0168-9002(02)01964-2. URL https://www.sciencedirect.com/science/article/pii/S0168900202019642. The Relativistic Heavy Ion Collider Project: RHIC and its Detectors.

[74] P.A. Zyla et al. (Particle Data Group). Prog. theor. exp. phys. 2020.

[75] Hans Bichsel. A method to improve tracking and particle identification in tpcs and silicon detectors. *Nuclear Instruments and Methods in Physics Research Section A: Accelerators, Spectrometers, Detectors and Associated Equipment*, 562(1):154–197, 2006. ISSN 0168-9002. doi: https://doi.org/10.1016/j.nima.2006.03.009. URL https://www.sciencedirect.com/science/article/pii/S0168900206005353.

[76] W.J. Llope. The large-area time-of-flight upgrade for star. *Nuclear Instruments and Methods in Physics Research Section B: Beam Interactions with Materials and Atoms*, 241(1):306–310, 2005. ISSN 0168-583X. doi: https://doi.org/10.1016/j.nimb.2005.07.089. URL https://www.sciencedirect.com/science/article/pii/S0168583X05012267. The Application of Accelerators in Research and Industry.

[77] Kathryn Meehan. STAR Results from Au + Au Fixed-Target Collisions at $\sqrt{s_{NN}} =$ 4.5 GeV. *Nucl. Phys. A*, 967:808–811, 2017. doi: 10.1016/j.nuclphysa.2017.06.007.

[78] Jaroslav Adam et al. Flow and interferometry results from Au+Au collisions at $\sqrt{s_{NN}} = 4.5$ GeV. *Phys. Rev. C*, 103(3):034908, 2021. doi: 10.1103/PhysRevC.103.034908.

[79] Michael L. Miller, Klaus Reygers, Stephen J. Sanders, and Peter Steinberg. Glauber modeling in high-energy nuclear collisions. *Annual Review of Nuclear and Particle Science*, 57(1):205–243, 2007. doi: 10.1146/annurev.nucl.57.090506.123020. URL https://doi.org/10.1146/annurev.nucl.57.090506.123020.

[80] G. Fäldt, H. Pilkuhn, and H.G. Schlaile. Nucleus-nucleus collisions at relativistic energies. *Annals of Physics*, 82(2):326–344, 1974. ISSN 0003-4916. doi: https://doi.org/10.1016/0003-4916(74)90116-X. URL https://www.sciencedirect.com/science/article/pii/000349167490116X.

[81] Mohamed Abdallah et al. Cumulants and Correlation Functions of Net-proton, Proton and Antiproton Multiplicity Distributions in Au+Au Collisions at RHIC, 2021.

[82] Xiaofeng Luo, Ji Xu, Bedangadas Mohanty, and Nu Xu. Volume fluctuation and auto-correlation effects in the moment analysis of net-proton multiplicity distributions in heavy-ion collisions. *J. Phys. G*, 40:105104, 2013. doi: 10.1088/0954-3899/40/10/105104.

[83] Adam B. Jones and B. Alex Brown. Two-parameter fermi function fits to experimental charge and point-proton densities for $^{208}$Pb. *Phys. Rev. C*, 90:067304, Dec 2014. doi: 10.1103/PhysRevC.90.067304. URL https://link.aps.org/doi/10.1103/PhysRevC.90.067304.

[84] H. De Vries, C.W. De Jager, and C. De Vries. Nuclear charge-density-distribution parameters from elastic electron scattering. *Atomic Data and Nuclear Data Tables*, 36(3):495–536, 1987. ISSN 0092-640X. doi: https://doi.org/10.1016/0092-640X(87)90013-1. URL https://www.sciencedirect.com/science/article/pii/0092640X87900131.

[85] Dmitri Kharzeev and Marzia Nardi. Hadron production in nuclear collisions at RHIC and high density QCD. *Phys. Lett. B*, 507:121–128, 2001. doi: 10.1016/S0370-2693(01)00457-9.

[86] B. B. et al. Back. Collision geometry scaling of Au + Au pseudorapidity density from $\sqrt{s_{NN}} = 19.6$ to 200 GeV. *Phys. Rev. C*, 70:021902, Aug 2004. doi: 10.1103/PhysRevC.70.021902. URL https://link.aps.org/doi/10.1103/PhysRevC.70.021902.

[87] Alberto Giovannini and L Van Hove. Negative binomial multiplicity distributions in high energy hadron collisions. *Zeitschrift für Physik C Particles and Fields*, 30 (3):391–400, 1986.

[88] Christer Fuglesang. UA5 MULTIPLICITY DISTRIBUTIONS AND FITS OF VARIOUS FUNCTIONS. In *Conference on Multiparticle Dynamics*, 10 1989.

[89] Rene Brun and Fons Rademakers. ROOT - An Object Oriented Data Analysis

Framework, Proceedings AIHENP'96 Workshop. *Nucl. Inst. Meth. in Phys. Res. A 389*. URL `https://root.cern/`.

[90] Bo Ling and Mikhail A. Stephanov. Acceptance dependence of fluctuation measures near the QCD critical point. *Phys. Rev. C*, 93(3):034915, 2016. doi: 10.1103/PhysRevC.93.034915.

[91] Adam Bzdak, Volker Koch, and Nils Strodthoff. Cumulants and correlation functions versus the QCD phase diagram. *Phys. Rev. C*, 95(5):054906, 2017. doi: 10.1103/PhysRevC.95.054906.

[92] Adam Bzdak and Volker Koch. Rapidity dependence of proton cumulants and correlation functions. *Phys. Rev. C*, 96(5):054905, 2017. doi: 10.1103/PhysRevC.96.054905.

[93] Jasmine Brewer, Swagato Mukherjee, Krishna Rajagopal, and Yi Yin. Searching for the QCD critical point via the rapidity dependence of cumulants. *Phys. Rev. C*, 98(6):061901, 2018. doi: 10.1103/PhysRevC.98.061901.

[94] Toshihiro Nonaka, Masakiyo Kitazawa, and ShinIchi Esumi. More efficient formulas for efficiency correction of cumulants and effect of using averaged efficiency. *Phys. Rev. C*, 95:064912, Jun 2017. doi: 10.1103/PhysRevC.95.064912. URL `https://link.aps.org/doi/10.1103/PhysRevC.95.064912`.

[95] Xiaofeng Luo and Toshihiro Nonaka. Efficiency correction for cumulants of multiplicity distributions based on track-by-track efficiency. *Phys. Rev. C*, 99:044917, Apr 2019. doi: 10.1103/PhysRevC.99.044917. URL `https://link.aps.org/doi/10.1103/PhysRevC.99.044917`.

[96] Toshihiro Nonaka, Masakiyo Kitazawa, and ShinIchi Esumi. A general procedure for detector–response correction of higher order cumulants. *Nucl. Instrum. Meth. A*, 906:10–17, 2018. doi: 10.1016/j.nima.2018.08.013.

[97] Toshihiro Nonaka. Recent Results and Methods on Higher Order and Off-diagonal Cumulants of Identified Net-particle Multiplicity Distributions in Au+Au Collisions at STAR. *Nucl. Phys. A*, 982:863–866, 2019. doi: 10.1016/j.nuclphysa.2018.10.092.

[98] Xiaofeng Luo and Toshihiro Nonaka. Efficiency correction for cumulants of multiplicity distributions based on track-by-track efficiency. *Phys. Rev. C*, 99(4):044917, 2019. doi: 10.1103/PhysRevC.99.044917.

[99] Toshihiro Nonaka, Masakiyo Kitazawa, and ShinIchi Esumi. Pileup corrections on higher-order cumulants. *Nuclear Instruments and Methods in Physics Research Section A: Accelerators, Spectrometers, Detectors and Associated Equipment*, 984:164632, 2020. ISSN 0168-9002. doi: https://doi.org/10.1016/j.nima.2020.164632. URL https://www.sciencedirect.com/science/article/pii/S0168900220310299.

[100] Toshihiro Nonaka. Pile up unfolding and correction figures exchanged through personal correspondence.

[101] ShinIchi Esumi, Kana Nakagawa, and Toshihiro Nonaka. Reconstructing particle number distributions with convoluting volume fluctuations. *Nucl. Instrum. Meth. A*, 987:164802, 2021. doi: 10.1016/j.nima.2020.164802.

[102] Yu Zhang, Yige Huang, Toshihiro Nonaka, and Xiaofeng Luo. Pileup Correction on Higher-order Cumulants with Unfolding Approach. 8 2021.

[103] V. Skokov, B. Friman, and K. Redlich. Volume Fluctuations and Higher Order Cumulants of the Net Baryon Number. *Phys. Rev. C*, 88:034911, 2013. doi: 10.1103/PhysRevC.88.034911.

[104] P. Braun-Munzinger, A. Rustamov, and J. Stachel. Bridging the gap between event-by-event fluctuation measurements and theory predictions in relativistic nuclear collisions. *Nucl. Phys. A*, 960:114–130, 2017. ISSN 0375-9474. doi: https://doi.org/10.1016/j.nuclphysa.2017.01.011. URL https://www.sciencedirect.com/science/article/pii/S0375947417300258.

[105] Adam Bzdak, Volker Koch, and Nils Strodthoff. Cumulants and correlation functions versus the qcd phase diagram. *Phys. Rev. C*, 95:054906, May 2017. doi: 10.1103/PhysRevC.95.054906. URL https://link.aps.org/doi/10.1103/PhysRevC.95.054906.

[106] Xiaofeng Luo. Error Estimation for Moments Analysis in Heavy Ion Collision Experiment. *J. Phys. G*, 39:025008, 2012. doi: 10.1088/0954-3899/39/2/025008.

[107] Ashish Pandav, Debasish Mallick, and Bedangadas Mohanty. Effect of limited statistics on higher order cumulants measurement in heavy-ion collision experiments. *Nucl. Phys. A*, 991:121608, 2019. doi: 10.1016/j.nuclphysa.2019.08.002.

[108] Volodymyr Vovchenko, Volker Koch, and Chun Shen. Proton number cumulants and correlation functions in Au-Au collisions at $\sqrt{s_{NN}} = 7.7 - 200$ GeV from hydrodynamics. 6 2021.

[109] M. M. Aggarwal et al. Higher Moments of Net-proton Multiplicity Distributions at RHIC. *Phys. Rev. Lett.*, 105:022302, 2010. doi: 10.1103/PhysRevLett.105.022302.

[110] Adamczewski-Musch et al. *Phys. Rev. C*, 102:024914, Aug 2020. doi: 10.1103/PhysRevC.102.024914. URL https://link.aps.org/doi/10.1103/PhysRevC.102.024914.

[111] R. Poberezhnyuk, V. Vovchenko, A. Motornenko, M. I. Gorenstein, and H. Stoecker. Chemical freeze-out conditions and fluctuations of conserved charges in heavy-ion collisions within quantum van der Waals model. *Phys. Rev. C*, 100(5):054904, 2019. doi: 10.1103/PhysRevC.100.054904.